Springer Theses
Recognizing Outstanding Ph.D. Research

Hsiang-Hsi Kung

Collective Excitations in the Antisymmetric Channel of Raman Spectroscopy

Springer

Springer Theses

Recognizing Outstanding Ph.D. Research

Aims and Scope

The series "Springer Theses" brings together a selection of the very best Ph.D. theses from around the world and across the physical sciences. Nominated and endorsed by two recognized specialists, each published volume has been selected for its scientific excellence and the high impact of its contents for the pertinent field of research. For greater accessibility to non-specialists, the published versions include an extended introduction, as well as a foreword by the student's supervisor explaining the special relevance of the work for the field. As a whole, the series will provide a valuable resource both for newcomers to the research fields described, and for other scientists seeking detailed background information on special questions. Finally, it provides an accredited documentation of the valuable contributions made by today's younger generation of scientists.

Theses may be nominated for publication in this series by heads of department at internationally leading universities or institutes and should fulfill all of the following criteria

- They must be written in good English.
- The topic should fall within the confines of Chemistry, Physics, Earth Sciences, Engineering and related interdisciplinary fields such as Materials, Nanoscience, Chemical Engineering, Complex Systems and Biophysics.
- The work reported in the thesis must represent a significant scientific advance.
- If the thesis includes previously published material, permission to reproduce this must be gained from the respective copyright holder (a maximum 30% of the thesis should be a verbatim reproduction from the author's previous publications).
- They must have been examined and passed during the 12 months prior to nomination.
- Each thesis should include a foreword by the supervisor outlining the significance of its content.
- The theses should have a clearly defined structure including an introduction accessible to new PhD students and scientists not expert in the relevant field.
- Indexed by zbMATH.

More information about this series at http://www.springer.com/series/8790

Hsiang-Hsi Kung

Collective Excitations in the Antisymmetric Channel of Raman Spectroscopy

Doctoral Thesis accepted by Rutgers University, USA

Springer

Hsiang-Hsi Kung
Quantum Matter Institute
University of British Columbia
Vancouver
BC, Canada

ISSN 2190-5053 ISSN 2190-5061 (electronic)
Springer Theses
ISBN 978-3-030-89331-6 ISBN 978-3-030-89332-3 (eBook)
https://doi.org/10.1007/978-3-030-89332-3

This Springer imprint is published by the registered company Springer Nature Switzerland AG
The registered company address is: Gewerbestrasse 11, 6330 Cham, Switzerland

Supervisor's Foreword

In his Ph.D. work, Dr. Hsiang-Hsi (Sean) Kung made a number of breakthrough contributions to condensed matter physics, including the first observation of broken reflection symmetry in the hidden order phase of the enigmatic heavy fermion material URu_2Si_2, and the discoveries of a novel collective mode – the chiral spin wave – and a novel composite particle – the chiral exciton – in a three-dimensional topological insulator Bi_2Se_3, which adds to the potential of topological insulators as a platform for photonics, optoelectronics, and spintronics devices. Each of the above listed discoveries merits an award on its own; to have three of them within one Ph.D. thesis is an unprecedented fit.

Besides the Springer Thesis Award, his dissertation work has received various recognition from prestigious institutions, including the Northeastern Association of Graduate Schools' Outstanding Doctoral Dissertation Award, and the American Physical Society's Richard L. Greene Dissertation Award in Experimental Condensed Matter or Materials Physics. These achievements highlight the importance of this work and its impact on the broad condensed matter physics community.

Distinguished Professor of Physics Girsh Blumberg
Rutgers University, Piscataway, NJ, USA

Preface

Raman spectroscopy is an inelastic light scattering technique, where a monochromatic light source, typically a laser, is used to exchange energy with the system and thus perturbs the material under study into an excited state. In this process, the energy quanta that the electromagnetic field lose to or gain from the system correspond to specific energy levels that are characteristic to the material, such as lattice vibration modes, aka phonons. That is, each peak in the energy spectrum of the scattered light corresponds to a specific collective excitation of normal modes in the system. Therefore, we gain insights into the material properties by studying the energy spectrum of the scattered light, which is called a Raman spectrum to honor the main discoverer of this effect, Sir C.V. Raman.

One of the most powerful advantages of Raman scattering is that the energy spectra are independent of the incident light energy and only reflect the spectra of the system's excited states. Therefore, experimentalists can pick the excitation energy that maximizes the Raman signal of interest. This effect is also known as resonant Raman scattering, which is done by exciting electrons into an unoccupied band and thus creating an electron–hole pair in the system. There is finite probability that the electron–hole pair decay into an excited state instead of the ground state by emitting a slightly less energetic photon. Another unique property of Raman scattering is its symmetry sensitivity. By using polarized light, one can selectively probe part of the Raman tensor, which in turn reflects collective excitations with a specific symmetry.

My thesis research focuses on using low temperature polarization resolved Raman spectroscopy to identify optically excited collective modes in strongly correlated electron systems and three-dimensional (3D) topological insulators. In particular, we are interested in collective modes present in the pseudovector symmetry channel, such as the A_{2g} representation of D_{4h} group. Although generally forbidden for phononic excitations, it was noted by early workers of the field that contribution from antisymmetric tensors ($A_{2(g)}$ irreducible representation) may arise under special circumstances. Historically, the excitations in the antisymmetric channel have been referred to as the "chiral excitations" due to their intimate relationship with the spin chiral operator. For example, antisymmetric scattering

was predicted for Dirac spin-liquid state in the spin-1/2 kagome system but yet unobserved to date.

Here in this monograph, we discovered two examples of electronic excitations arising from the antisymmetric "chiral" channel. More precisely, we observe sharp $A_{2(g)}$ collective modes in two entirely different nonmagnetic systems: heavy fermion metal URu_2Si_2 and 3D topological insulator Bi_2Se_3. Observation of an antisymmetric collective mode in nonmagnetic systems is highly unusual and rare, and the mechanism is different for different cases. This monograph is dedicated to explore the properties, mechanisms, and physical implications from these two new systems. Due to the recently rising interests on the chiralities in condensed matter physics, we hope that this dissertation will intrigue new insights into the possibility of probing chiral excitations with optical methods.

Vancouver, BC, Canada Hsiang-Hsi Kung

Acknowledgment

This work is dedicated to
the great minds and tireless workers
who strove to understand
the mysterious case of the "hidden order".

I am in debt to many people throughout the course of this monograph, and it is impossible to make a comprehensive list to give proper credits to them all. But, I would like to start by thanking my good friend and thesis advisor, Professor Girsh Blumberg, who patiently and tirelessly guided me in the past five years. It is not uncommon that Ph.D. advisors provide good professional guidance to graduate students. But, Girsh has uplifted the standards for Ph.D. advisory to another level. Besides the useful discussions and insightful comments he offered during this monograph, which would have been impossible to complete without many of his ideas, I am most grateful for his teachings on research attitude and career building. He has always demonstrated high degree of self-discipline and self-motivation toward research—I hope I have learned some of that from him. He showed me that if we push ourselves, we can often achieve more than we originally thought—but, if and only if we start pushing. Because in academia as well as in life, nothing will ever happen unless we try.

I am very grateful to have worked with many talented people in Rutgers, who taught me a lot in many aspects: I would like to thank Professor Kristjan Haule, for patiently teaching me the basics of heavy fermions and strongly correlated materials, helping me improve the writings in the manuscript, and aiding me in many ways in the past 5 years; Professor Piers Coleman and Professor Premi Chandra, for the insightful discussions we had about URu_2Si_2 and also for their friendly support throughout my Ph.D. studies; I am also very thankful to the members of the "Blumberg Lab": Dr. Wei-Lu Zhang, for selflessly sharing her laughter and time when I needed them; Shangfei Wu and Mai Ye, for the lengthy but helpful debates about Raman scattering; Alex Lee and Viktor Krapivin, for their company and help during experiments; and Brian Dennis and Dr. Verner Thorsmølle, for teaching me how to properly run and log experiments. I am also very thankful to

the good friendships I built up with several Rutgers graduate students and postdocs, in particular Alejandro “Ale” Gomez and Aniket ”Po’boy” Patra, for listening to my whining and teaching me to laugh out the stress in life with good friends.

I am fortunate to have collaborated with many great people around the world: I am very thankful to Professor Mydosh from the Leiden University, for tirelessly helping me improve the manuscript and carefully explaining to me the Kondo physics in URu_2Si_2; Professor Bauer at the LANL and Professor Baumbach at the FSU Tallahassee, for providing me with the best crystals of URu_2Si_2; Professor Maple, Dr. Ran, and Dr. Kanchanavatee from the UCSD, for very generously providing me large pieces of $URu_{2-x}Fe_xSi_2$ single crystals and being very forgiving for my slow progress; Professor Cheong (Rutgers) and Professor Wang, for generously sharing with me a very rare batch of ultraclean Bi_2Se_3 single crystal; Professor Oh (Rutgers) and his group members, Matthew, Nikesh, Maryam, and Jisoo, for helping me better understand the basics of 3D topological insulators through many discussions; Professor Smirnov and his student Zhengguang Lu from the FSU Tallahassee, for tirelessly helping my experiments in the MagLab; Professor Merlin and his student Ibrahim Boulares from the University of Michigan, and Professor Kemper from the NC State University who very patiently taught me many things about the surface phonon modes and surface resonance in Bi_2Se_3; and Professor Maslov and Dr. Maiti from the University of Florida who very patiently helped me understand the physics of chiral spin modes in Bi_2Se_3.

Last but not the least, my families who endured my capricious temper during the past 5 years, and probably way before that. My special love to Lingwei, for her selfless sacrifices and for displaying great patience with me.

Regretfully, I have to cut off the 10-page-long list I had in mind at here and express my final gratitude toward the financial supports: The thesis work presented here was done under the support of the NSF grants DMR-1104884 and DMR-1709161 and the US DOE—Basic Energy Sciences grant DE-SC0005463. The financial support of the predoctoral University and Louis Bevier Graduate Fellowship is also acknowledged.

Hsiang-Hsi “Sean” Kung

Parts of This Thesis Have Been Published in the Following Journal Articles

1. H.-H. Kung, R.E. Baumbach, E.D. Bauer, V.K. Thorsmølle, W.-L. Zhang, K. Haule, J.A. Mydosh, G. Blumberg, Chirality density wave of the 'hidden order' phase in URu_2Si_2. Science **347**, 6228 (2015). https://doi.org/10.1126/science.1259729
2. H.-H. Kung, S. Ran, N. Kanchanavatee, V. Krapivin, A. Lee, J.A. Mydosh, K. Haule, M.B. Maple, G. Blumberg, Analogy between the 'Hidden Order' and the orbital antiferromagnetism in URu_2Si_2. Phys. Rev. Lett. **117**, 227601 (2016). https://doi.org/10.1103/PhysRevLett.117.227601
3. H.-H. Kung, S. Maiti, X. Wang, S.-W. Cheong, D.L. Maslov and G. Blumberg, Chiral spin mode on the surface of a topological insulator. Phys. Rev. Lett. **119**, 136802 (2017). https://doi.org/10.1103/PhysRevLett.119.136802
4. H.-H. Kung, M. Salehi, X. Wang, I. Boulares, A.F. Kemper, N. Koirala, M. Brahlek, P. Lostak, C. Uher, R. Merlin, S.-W. Cheong, S. Oh, G. Blumberg, Surface vibrational modes of the topological insulator Bi_2Se_3 observed by Raman spectroscopy. Phys. Rev. B **95**, 245406 (2017). https://doi.org/10.1103/PhysRevB.95.245406
5. H.-H. Kung, A.P. Goyal, D.L. Maslov, X. Wang, A. Lee, A.F. Kemper, S.-W. Cheong, G. Blumberg, Observation of chiral surface excitons in a topological insulator Bi_2Se_3. Proc. Natl. Acad. Sci. **116**, 4006 (2019). https://doi.org/10.1073/pnas.1813514116

Contents

1 Introduction 1
1.1 The Scope of This Thesis 1
1.1.1 Brief History 3
1.2 Inelastic Light Scattering 5
1.2.1 Theory of Raman Scattering 7
1.2.2 Nonresonant Raman Scattering 13
1.2.3 Raman Scattering of Phonon 14
1.3 Symmetry Selection Rules in Raman Scattering 15
1.4 Chiral Excitations in Solids 17
References 19

2 Experimental Setup 23
2.1 Raman Scattering Setup 23
2.1.1 Laser 23
2.1.2 Optical Setup 26
2.2 Data Acquisition and Analysis 33
2.2.1 Instrumental Calibrations 34
2.2.2 Cosmic Ray Rejection 35
2.2.3 Optical Corrections 35
2.2.4 Data Analysis 37
References 40

3 Raman Scattering in URu_2Si_2 41
3.1 Introduction 41
3.1.1 Kondo Effect and Heavy Fermion Systems 41
3.1.2 The Phase Diagrams of URu_2Si_2 and the Enigmatic "Hidden Order" 50
3.2 Material and Methods 56
3.2.1 Raman Studies 57
3.2.2 Characterization of Strain Free Areas 59
3.3 Experiment and Results 60
3.3.1 Phonon Modes 62

3.3.2 Raman Response in the A_{2g} Symmetry Channel 64
3.3.3 The Reflection Symmetry Breaking in the "Hidden Order" State 68
3.3.4 Iron Substitution Dependence of the A_{2g} Collective Mode .. 71
3.3.5 Excitation and Sample Dependence 72
3.4 Discussion 75
3.4.1 The Minimal Model and the Hexadecapole Order Parameter 75
3.4.2 The Ordering Vector 77
3.4.3 The $\chi''_{A2g}(\omega, T)$ Continuum 79
3.4.4 The Chirality Density Wave 80
3.4.5 Ginzburg–Landau Theory 81
3.4.6 Origin of the A_{2g} Collective Modes in URu_2Si_2 83
3.5 Summary 85
References 86

4 Secondary Emission in Bi_2Se_3 95
4.1 Introduction 95
4.1.1 Band Topology in Solids 98
4.1.2 Topological Surface States 100
4.1.3 The Band Structure in Bi_2Se_3 103
4.1.4 Materials and Methods 107
4.2 Surface Phonons 109
4.2.1 Results 110
4.2.2 Discussion 116
4.3 Chiral Spin Modes 119
4.3.1 Results 120
4.3.2 Discussion 125
4.4 Photoluminescence 128
4.4.1 Circular Polarized Photoluminescence 128
4.4.2 Results 129
4.4.3 Chiral 2D Excitons 137
4.5 Summary 141
References 142

5 Conclusion 149
References 150

List of Abbreviations

AFM	Antiferromagnetism
ARPES	Angle resolved photoemission spectroscopy
BCT	Body centered tetragonal
BS	Bismuth selenide (Bi_2Se_3)
BZ	Brillouin zone
CDW	Charge density wave
CP	Circularly polarized
DFT	Density functional theory
DMFT	Dynamical mean field theory
DOS	Density of state
FM	Ferromagnetism
FWHM	Full width at half maximum
FS	Fermi surface
HO	Hidden order
IR	Infrared
IRR	Irreducible representation
KK	Kramers–Kronig
PL	Photoluminescence
QEP	Quasi-elastic peak
RRR	Residual resistivity ratio
SC	Superconductivity
SDW	Spin density wave
SOC	Spin–orbit coupling
ST	Simple tetragonal
STM	Scanning tunneling microscopy
TI	Topological insulator

TMD Transition metal dichalcogenide
TSS Topological surface state
TR Time resolved
TRIM Time reversal invariant momentum
TRS Time reversal symmetry
URS Uranium ruthenium silicide (URu_2Si_2)
UV Ultraviolet

Chapter 1
Introduction

Abstract Polarization resolved Raman spectroscopy is a powerful tool as it simultaneously offers exceptional symmetry and energetic resolution (∼0.1 meV), making it particularly suitable for studying low energy collective modes in systems with nontrivial electron correlation. In the condensed matter physics, Raman spectroscopy has been crucial in understanding superconductivity by studying symmetry of the Cooper pair breaking peak, electron–phonon interaction in semiconductors by studying the plasmon–polaritons, and charge density waves by studying the amplitude modes.

In this chapter, I will first introduce the generic theory of polarization resolved Raman spectroscopy in solids. Focus will be given to electronic Raman scattering, where light scatters with the electronic quantum mechanical states. Minimal group theory will be used to justify the symmetry analysis of polarization resolved Raman scattering data. Then, I will discuss how Raman scattering can be used to probe the "chiral excitations," i.e., collective excitations out of a chiral ground state, by measuring inelastic light scattering in the pseudovector-like antisymmetry channel.

1.1 The Scope of This Thesis

In this thesis, we will focus on using low temperature Raman spectroscopy to identify optically excited collective modes in strongly correlated electron systems and three-dimensional (3D) topological insulators. In particular, we are interested in collective modes presenting in the pseudovector-like symmetry channel, e.g., the A_{2g} representation of D_{4h} group, which is antisymmetric with respect to in-plane reflections. Previously, such excitations are primarily seen in magnetic materials where the time reversal symmetry is broken [1]. Here, we present two examples where A_{2g} collective modes arise from time reversal symmetry preserved ground states.

H.-H. Kung, *Collective Excitations in the Antisymmetric Channel of Raman Spectroscopy*, Springer Theses, https://doi.org/10.1007/978-3-030-89332-3_1

In the first example, we study a heavy fermion metal $URu_{2-x}Fe_xSi_2$, which holds long standing interest in the strongly correlated electron community due to an emergent long range order it exhibits at low temperature and $x < 0.1$, known as the "hidden order" (HO). By studying the temperature dependent Raman response function in all allowed symmetry channels for various iron concentrations x, we found evidences of broken symmetries and a possible order parameter that explains the low temperature phase diagram. In the low Fe concentration HO phase, we observed a sharp in gap mode with A_{2g} symmetry and small leakage into the A_{1g} symmetry. Our results show strong indication of the local reflection symmetries broken at the uranium site in the HO phase [2]. As we increase x, the energy of an A_{2g} collective mode decreases to almost zero at the phase boundary and recovers in a well-known antiferromagnetic (AFM) phase. This is a direct evidence that both HO and AFM phases are related to an A_{2g} type order parameter, which arranges the uranium-5f orbitals into orders breaking either local chirality or time reversal symmetry [3].

In the second example, we study a 3D topological insulator Bi_2Se_3, which has a rhombohedral lattice with the D_{3d} point group symmetry. At the crystal surface characterized by the C_{6v} point group, strong spin orbit coupling and time reversal symmetry conspire to form topologically protect Dirac states with chiral spin texture. While the existence and spin texture of the surface states are mostly understood for Bi_2Se_3 through photoemission and scanning tunneling spectroscopies, very few examples of collective excitations from the Dirac surface states have so far been identified, and therefore interactions between the Dirac particles are yet unclear. In our study, we tune the excitation energy into resonance between two surface bands to enhance the signal contributed by the Dirac electrons. As photon energy tuned to 1.8 eV, we observed a sharp collective mode with energy of about 150 meV appearing below the edge of a gapped continuum, in the pseudovector-like A_2 symmetry of the C_{6v} group. By comparing the data with calculations, we identify this peak as the transverse collective spin mode of surface Dirac fermions: a collective spin–flip excitation from the lower to upper Dirac cone [4]. The chiral properties of the surface states could be further explored by measuring the photoluminescence (PL) spectra. With the excitation photon energy tuned to around 2.7 eV, we observe the appearance of a PL peak centered at 2.26 eV, where the intensity is almost perfectly circularly polarized. By comparing the excitation profile with band structure calculations, we identify this PL peak as 2D excitonic bound states composed of surface massless electrons and surface massive holes, both subject to strong spin–orbit coupling which locks their spins and momenta into chiral textures. Due to the chiral structure, the surface excitons emit circularly polarized PL that preserves the angular momenta of the incident light [5]. These are new and direct optical measurements of the dynamical response from the 2D Dirac fermions in topological materials. Both the spin mode and the chiral exciton survive even at room temperature with decreased intensity, which is likely due to the more available decay channels through interacting with surface phonons [6]. The robustness of the chiral collective modes suggests potential applications in room temperature magnonics and optoelectronic devices.

1.1.1 Brief History

We will start with a brief detour on the history of discovery of inelastic light scattering. Newtonian optics (geometrical optics) states that light always travels in a straight line in empty space and can only be perceived by eyes when directly pointed at from the source. However, interaction with medium can deviate light from its optical path, which is often referred to as diffusion of light. We know by now that the diffusion of light is nothing more than the electromagnetic wave interacting with microparticles in the medium, which behave as tiny oscillating dipoles under the influence of the external field. Thus according to Maxwell's theory of electromagnetism, the scattered light can be deflected into any direction away from the optical path. Depending on whether or not the scattered light maintains the same wavelength as the incident light λ_I, the scattering process can be further separated into elastic and inelastic scatterings.

The elastic scattering of light from dilute particles where λ_I is much smaller than average particle separation has been known to scientists for a long time. However, systematic study was not done until the late nineteenth century by Tyndall. Depending on the nature of the scatterers, the elastic scattering from dilute medium can be further separated into two main categories: when the scatterers have diameter comparable or larger than the light wavelength, they are referred to as Tyndall effect, such as in suspending colloidal liquid; otherwise, they are generally referred to as Rayleigh effect, such as scattering from air molecules. Notice that all of the above treatments on light scattering assume each microparticle as harmonic oscillator, with the dipole moment of each particle, oscillates at the same frequency of the incident light, $\omega_I = 2\pi c/\lambda_I$. Thus the particles always radiate with the same wavelength as the incident light.

The scattering of light by dense medium, such as fluids, requires a different explanation. Since the particle separation is small compared to λ_I, there exists coherence between light scattered by different particles, which can no longer be assumed as independent dipolar emitters in Rayleigh's treatments. A straightforward summation over N identical particles leads to destructive interference in every direction except along the forward light path [7], which is obviously inconsistent with our everyday experience of light penetrating water. For example, one can clearly see sunlight beams underwater in a swimming pool, where the light propagation is orthogonal to the observer's viewing direction. This cannot be attributed simply to impurities or dust in the solution, since the elastic line is always present even at large angles to the optical path, and in the purest solutions [8]. It was later pointed out by Landau and Placzek in 1934 that light scattering from local pressure (density) and entropy (temperature) fluctuations will avoid total cancellation of intensity in destructive interference and leads to nonzero intensity for the elastic scattering component away from the optical path [7, 9]. Note that this unshifted component is usually referred to as the "Rayleigh line" in literatures, but its origin is actually quite different from the Rayleigh effect that is causing the blue sky. More detailed discussion can be found in chapter 8 of Ref. [7].

Progress in understanding the inelastic scattering spectra is first made by Brillouin in 1922, who predicted that light interaction with propagating pressure (density) fluctuation in liquid or solids due to sound waves can lead to modification of scattered light wavelength [10]. Using the newly accepted quantum theory of lattice vibrations by Debye, i.e., phonons [11], Brillouin predicted two inelastic peaks displaced symmetrically on both sides of the elastic Rayleigh line, with energy separations related to the sound speed of the medium. The experimental observation was first reported for scattering of light by various pure and transparent liquids in 1930 [8], and the effect was since dubbed Brillouin scattering.

Shortly after Brillouin's thesis, Smekal predicted in 1923 that scattering of light by a two-level system will lead to oscillatory change of the medium's polarizability that causes inelastic sidebands in the spectra of scattered light [12]. The frequency shift of the sidebands from the excitation light frequency will be exactly the "quanta" of the two-level energy difference divided by Plank's constant. A few years later, Kramers and Heisenberg developed a quantum mechanical version of Smekal's theory using the "correspondence principle," describing inelastic light scattering of atoms [13]. The complete quantum mechanical treatment of light will be given by Paul Dirac two years later [14, 15], and thus the Raman scattering from a simple system is predicted and well understood.

Around the same time of Smekal's prediction, Raman and coworkers in Calcutta, India were studying the light transmission through water, because they do not believe that the "blueness" of the sea is due to reflection of the sky [16]. In the process of their study, they discovered sharp inelastic lines in the scattering spectra of several transparent organic liquids and distilled water. Raman spent the next few years studying this phenomenon and realized that not only the radiation is highly polarized, but also the energy shifts of some new lines are the same as the known absorption lines in infrared spectra. In 1928, Raman finally made the announcement that this is the discovery of a new type of "secondary radiation," where "*the incident quantum of radiation is partially absorbed by the molecule and that the unabsorbed part is scattered*" [17, 18]. Raman's discovery was repeated in quartz and several other materials later that year by R.J. Wood with an improved setup [19].

Raman was soon awarded Nobel prize in 1930 due to the discovery of the new type of light scattering now named after him. However, little is known that around the same time in Moscow, Landsberg and Mandelstam also reported similar effect in quartz [20], and it was correctly interpreted as the inelastic light scattering predicted by Smekal in 1923. Detailed historical account of the discovery in Moscow is given in Ref. [21].

The greatest triumph and significance for the discovery of Raman effect were perhaps due to its successful applications in studying of very low energy excitations in materials. These "ultra red" excitations would otherwise be very difficult to investigate experimentally by absorption spectroscopy due to its long wavelength. Raman effect translates the wavelength of these excitations into the visible range, or any other wavelength convenient to the material and experimental setup, by choosing an appropriate incident light energy. Also, in molecules or crystals with

inversion symmetry, some of the vibration normal modes are forbidden by symmetry in infrared absorption, which could be observed in Raman scattering.

Another interesting implication of Raman scattering is in the development of quantum theory. By 1913, the great success of early quantum mechanics in explaining blackbody radiation, heat capacity, and the emission/absorption spectra of simple atoms has left very little doubt on the validity of quantizing energy levels in matters. However, this only deals with the emission and absorption of light by materials, and nothing to do with the nature of the light itself. Therefore, the quantization of the electromagnetic field proposed by Einstein in 1905 remains a debated issue for many years [22]. In 1916, Millikan finally, rather unwillingly, admitted that his experimental data of photoelectric effect is fully consistent with Einstein's theory [22], which would imply that the energy of electromagnetic wave is quantized with a quanta proportional to its frequency, i.e., $\hbar\omega$. In 1923, the observation of wavelength change in X-ray scattering by electrons in vacuum (Compton effect) finally convinced most people the quantum description of electromagnetic waves [23]. However, both experiments were done with high energy photon (extreme UV to hard X-ray), leaving the generality of the "particle description" of light at question. The Raman effect on the other hand is an extremely general and direct demonstration to the quantum nature of electromagnetic waves. As Robert W. Wood aptly commented on the Raman effect in 1928, "it appears to me that this very beautiful discovery, which resulted from Raman's long and patient study of phenomena of light scattering, is one of the most convincing proofs of the quantum theory of light which we have at the present time" [19].

1.2 Inelastic Light Scattering

We discussed in the previous section that Raman scattering is a type of "secondary radiation" [17], i.e., the emission of electromagnetic waves from matters exposed to an external field—the *primary radiation*—which could be either a beam of particles or electromagnetic waves. If the primary radiation is photon, then there are generally speaking two types of photonic secondary radiation that are observed in solids, i.e., the luminescence and light scattering. While most of the photons are scattered elastically in the light–matter interaction, there is a small fraction of scattered photon having a different energy than the absorbed. The photon is said to scatter *inelastically* with the system, i.e., either loses or gains energy through creating or absorbing a *quanta* of collective excitation, respectively. This inelastic process is coined the *Raman effect*, where the energy difference is known as the *Raman shift*. Traditionally, the Raman shift is often given in the unit of wavenumber (cm^{-1}) or frequency (THz), where 1 THz=33.356 cm^{-1}. The wavenumber is a convenient energy scale, comparable to the thermal fluctuations ($1\,k_B = 0.695\,\text{cm}^{-1}/\text{K}$) and the Zeeman energy ($1\,\mu_B$=0.4668 cm^{-1}/T), but almost an order of magnitude smaller than the most commonly used milli-electron volt (1 meV=8.065 cm^{-1}).

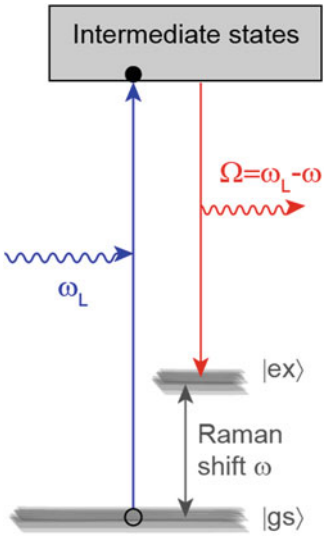

Fig. 1.1 Illustration for the Stokes process, where the incident laser energy is ω_L, and the excited state energy is ω

In order to further distinguish inelastic light scattering from the luminescence, we have to look into the processes of the secondary radiation. In the following, we introduce the 3-step model of secondary radiation typically used to explain the Raman effect [24], also illustrated in Fig. 1.1. First, the incident (primary) photon is absorbed by the material to promote an interband transition into an "intermediate state," which specifies an electron–hole (e–h) pair with the electron in a state of the conduction band and the hole in a state of the valence band. Note that the perturbation theory in quantum mechanics does not require the incident or scattered photon energy to match any of the intermediate state energies in order to acquire nonzero transition probability. If the photon energies are far away from any of the intermediate states, then the transition is said to be *virtual*. This "nonresonant" case is the simplest form of Raman scattering generally discussed in most textbooks and literature [7, 25]. Immediately after the optical absorption and before the band thermalization is fully established, i.e., redistributing electron populations throughout k-space to reach the Fermi–Dirac distribution with a new effective electronic temperature, the e–h pair exchanges energy with the system through inelastic processes such as creating/absorbing phonons, magnons, or other lower energy e–h pairs. Lastly, the e–h pair recombines to emit a "scattered" photon with different energy. Note that these 3 steps can occur in any time orderings.

The differentiation between Raman scattering and luminescence happens in the second step. Generally speaking, if the phase relation of the emitted photons to the absorbed ones is not simply determined by the emission/absorption of collective modes, i.e., the phonons, magnons, plasmons, etc., but containing other unspecified inelastic processes, then we can separate the secondary radiation into two parts. The essentially instantaneous coherent scattering of the e–h pair with elementary excitations is referred to as *Raman scattering*, and the incoherent

processes are known as the *hot luminescence* [26]. These two processes are in principle inseparable if the photon energy matches the intermediate states, i.e., the resonant condition. In some cases, due to the different relaxation processes involved, hot luminescence can still be distinguished from resonant Raman scattering by time resolved experiments [26]. Such differentiation is not present for nonresonant case, where no luminescence is expected as all processes occur virtually and no phase decoherence happens. In reality for most common materials, due to the complexity and broadening of the electronic bands, the visible light excitation almost always falls in the *near resonance* regime, where both nonresonant and resonant Raman scattering, as well as photoluminescence, contribute to the spectra. Therefore, one has to examine the excitation profile and polarization dependence to distinguish these different contributions and to gain understanding of the intermediate states involved in the secondary radiation [27, 28], as we will discuss in more detail in Chap. 4.

It is worth noting that the electron and hole will eventually thermalize independently with the system to regain the Fermi–Dirac distribution, and if momentum conservation allows, the electron and hole may recombine by emitting a less energetic photon, i.e. (cold) photoluminescence. Depending on the band structure, the photoluminescence can sometimes have much longer wavelength than the incident photon. In most metals, the thermalization process is fast ($\ll 1$ ps), and the cold luminescence is generally very broad and featureless in energy. In the typical interesting energy range of Raman scattering, i.e., about 100 meV, cold photoluminescence is a weak almost constant and unpolarized background that can be subtracted from the measured intensity. Due to unscreened Coulomb interaction in insulators and semiconductors, the electron-hole pair often thermalizes to form an exciton with well-defined energy levels [29], which decay back to the ground state by radiating photoluminescence sharply center around the dipole allowed transitions. In this case, the decay time is dominated by the exciton lifetime, which can be as long as nanoseconds and results in very sharp features in the luminescent spectra.

For historical reasons, inelastic light scattering spectra obtained using a Fabry–Pérot interferometer are generally referred to as Brillouin scattering, whereas spectra recorded with grating spectrometers are called Raman scattering. In the rest of this chapter, we will focus on the basic theory of Raman scattering. We will assume that the incident and scattered photon energies are much larger than the Raman shift, but small enough such that the photon momentum is negligible compared to the electronic Brillouin zone.

1.2.1 Theory of Raman Scattering

Depending on the emitted photon energy in an inelastic scattering process, the final state of the system could attain either higher or lower energy than the initial state, known as the Stokes and anti-Stokes processes, respectively. That is, the

scattered photon frequency in a Stokes process is $\omega_s = \omega_I - \omega$, where ω_I is the frequency of the incident photon, and ω is the Raman shift [Fig. 1.1]. In the anti-Stokes process, the scattered photon frequency is then $\omega_{as} = \omega_I + \omega$. In principle, the quasi momenta should also be conserved during scattering, i.e., $\mathbf{k_s} = \mathbf{k_I} - \mathbf{q}$ for the Stokes process and $\mathbf{k_{as}} = \mathbf{k_I} + \mathbf{q}$ for the anti-Stokes process, where $\mathbf{q}$ is the momentum transfer from the photon. However, the photon typically employed in Raman spectroscopy has wavelength of about 0.4–1 μm, which is about 1000 times larger than the lattice parameters of most crystals. Therefore, the photon momentum is about 1000 times smaller than the reciprocal lattice vectors, and thus the momentum transfer between incident and scattered photon, $\mathbf{q}$, can be taken as zero for all practical considerations. In other words, Raman scattering only probes collective modes near the Brillouin zone center.

The experimental observable in scattering experiments is called "differential scattering cross section" (or spectral differential scattering cross section):

$$\frac{d^2\sigma}{d\Omega d\omega_s} = \frac{scattered\ particle\ flux}{incident\ particle\ flux}; \tag{1.1}$$

note that Ω is the solid angle of the collection cone *inside* the sample. Physically, the differential scattering cross section measures the rate energy transfer from the incident beam into a scattered beam within energy range of $d\omega_s$ and detected within the solid angle $d\Omega$, through (Stokes) scattering with a medium. Therefore, we need to do a conversion from the calculated *energy flux* per unit area, $\frac{d^2I_s}{d\Omega d\omega_s}\frac{1}{I_I}$, into the *particle flux* that we measure [7].

$$\frac{d^2\sigma}{d\Omega d\omega_s} = \frac{\omega_I A}{\omega_s}\frac{d^2I_s}{d\Omega d\omega_s}\frac{1}{I_I}, \tag{1.2}$$

where A is the effective scattering area. For light scattering experiments, the photon energy flux is given by the magnitude of Poynting vector [7].

$$\frac{d^2I_s}{d\Omega d\omega_s}\frac{1}{I_I} = \frac{\omega_s^4 V L n_s}{8\pi^2\epsilon_0 c^3}|\epsilon_s \cdot P_s|^2 \frac{1}{2\epsilon_0 c n_I |E_I|^2}, \tag{1.3}$$

where V is the sample volume and E_I is the incident field amplitude, both will eventually cancel with the "power spectrum" $|\epsilon_s \cdot P_s|^2$. P_s is the light induced polarization in the sample, $P_s = \epsilon_0 \chi \cdot \epsilon_I E_I$, where χ is the dynamical charge susceptibility tensor, and ϵ_s and ϵ_I are directional vector for scattered and incident light, respectively. n_I and n_s are the refractive index of the sample at the wavelength of incident and scattered light, respectively. c is speed of light, and L is effective penetration depth of light. Therefore, the scattering cross section can be simplified as

$$\frac{d^2\sigma}{d\Omega d\omega_s} = \frac{\omega_I \omega_s^3 v n_s}{(4\pi\epsilon_0)^2 c^4} V |\epsilon_s \cdot \chi \cdot \epsilon_I|^2, \tag{1.4}$$

where $v = AL$ is the effective scattering volume. In reality, the evaluation of susceptibility should be taken as thermal dynamic average of all finite energy states,

$$|\epsilon_s \cdot \chi \cdot \epsilon_I|^2 \rightarrow \langle |\epsilon_s \cdot \chi \cdot \epsilon_I|^2 \rangle \equiv \frac{1}{V} \sum_f |\langle f|\epsilon_s \cdot \chi \cdot \epsilon_I|i\rangle|^2, \tag{1.5}$$

with $|i\rangle$ and $|f\rangle$ the initial and final states, respectively.

In principle, all of the physics in the scattering event are encrypted in the last term of Eq. (1.4). Namely, the inelastic light scattering probes the dynamical fluctuations of the charge susceptibility due to the perturbation of the incident photon field. The fluctuation could be due to its coupling to lattice vibrations (phonons) [30] or to magnetic excitations [31]. Equation (1.4) is often referred to as the *macroscopic* theory of light scattering. In general, this is not very useful for *ab initio* calculation of the Raman scattering cross section in crystals, which requires a *microscopic* theory.

Microscopic calculation of the scattering cross section is based on time dependent perturbation theory (the "Fermi's Golden Rules") [14] and the "minimal coupling" (excluding electron spin) Hamiltonian of electromagnetic (EM) field to the electrons,

$$H = H_0 + H_{int} = \frac{(\mathbf{p} + e\mathbf{A})^2}{2m} = \frac{\mathbf{p^2}}{2m} + \frac{e^2}{2m}\mathbf{A} \cdot \mathbf{A} + \frac{e}{m}\mathbf{p} \cdot \mathbf{A}, \tag{1.6}$$

where the first term H_0 describes the kinetic motion of the electron in the medium, and the second and third terms are the interaction Hamiltonian H_{int} that governs the coupling between the electron and EM field. Here we have used the Coulomb gauge, $\nabla \cdot \mathbf{A} = 0$, to simplify the equation. Proper microscopic treatment requires rewriting H_{int} with the vector potential in the quantum operator form [7, 30]. The annihilation and creation operators for a photon with energy ω_k, wave vector $\mathbf{k}$, and polarization $\boldsymbol{\epsilon}_k$ are

$$\mathbf{A}(\mathbf{r}) = \sum_k \sqrt{\frac{\hbar}{2\epsilon_0 n^2 V \omega_k}} [\mathbf{a}_k e^{i\mathbf{k}\cdot\mathbf{r}} + \mathbf{a}_k^\dagger e^{-i\mathbf{k}\cdot\mathbf{r}}] \boldsymbol{\epsilon}_k. \tag{1.7}$$

Plugging into Eq. (1.6) and omitting nonlinear terms, the second term becomes [32]

$$H_{AA} = \frac{e^2}{2m} \sum_{k,k'} \left(\frac{\hbar}{2\epsilon_0 n_k n_{k'} V \sqrt{\omega_k \omega_{k'}}} \right) \left[\mathbf{a}_k \mathbf{a}_{k'}^\dagger e^{i(\mathbf{k}-\mathbf{k}')\cdot\mathbf{r}} + \mathbf{a}_k^\dagger \mathbf{a}_{k'} e^{-i(\mathbf{k}-\mathbf{k}')\cdot\mathbf{r}} \right] (\boldsymbol{\epsilon}_k \cdot \boldsymbol{\epsilon}_{k'}). \tag{1.8}$$

To calculate the contributions of Eq. (1.6) in the inelastic light scattering, we need to use the time dependent perturbation theory [14], or more precisely, Fermi's Golden Rule for transition rate between initial state $|i\rangle$ and final state $|f\rangle$,

$$\Gamma_{if} = 2\pi \sum_{i,f} p_i |T|^2 \delta(\omega_I - (\omega_s + \omega_{if})), \tag{1.9}$$

where $\omega_{if} \equiv (E_f - E_i)/\hbar$ is the excitation frequency, commonly called *Raman shift*, and we will simply denote it as ω in the following. $p_i = \exp(-\beta E_i)$ is the probability of being in the initial state, and T is the matrix element that encodes all of the information about interactions between the scattering medium and light. The spectral cross section is proportional to the transition rate by scattered photon density of states per unit solid angle, $\frac{V}{(2\pi)^3} \int d^3\mathbf{k}_s = \frac{V}{8\pi^3} \frac{n_s^3 \omega_s^2}{c^3}$, and then normalize to the incident photon flux. We will drop the prefactors in the following since they are not relevant to this experimental thesis study, and rigorous derivations exist in many books and reviews [7, 27, 30].

The scattering matrix element T can be evaluated perturbatively assuming the interaction Hamiltonian H_{int} is weak compared to H_0,

$$T = \langle f|H_{int}|i\rangle + \sum_m \frac{\langle f|H_{int}|m\rangle \langle m|H_{int}|i\rangle}{\hbar(\omega_i - \omega_m)} + \sum_{m,m'} \frac{\langle f|H_{int}|m\rangle \langle m|H_{int}|m'\rangle \langle m'|H_{int}|i\rangle}{\hbar^2(\omega_i - \omega_m)(\omega_i - \omega_{m'})} + \mathcal{O}(H_{int}^4). \tag{1.10}$$

Inserting H_{AA} term of Eq. (1.6) into Eq. (1.10) and keeping only the leading order, the matrix element for scattering with a collection of particles is

$$T \sim \langle f| \sum_j e^{i\mathbf{q}\cdot\mathbf{r}_j} |i\rangle \, (\boldsymbol{\epsilon}_I \cdot \boldsymbol{\epsilon}_s), \tag{1.11}$$

where $\mathbf{q} = \mathbf{k}_I - \mathbf{k}_s$ is the momentum transfer. In typical Raman scattering experiments, the used wavelength of light is much larger than the lattice parameters, i.e., $\mathbf{q} \approx 0$ compared to the Brillouin zone size, and therefore the exponential term is the order of unity (dipole approximation). Thus, in scattering by electronic transitions, the matrix element is only appreciable with the same initial and final states while conserving the momentum, i.e., the *intraband* transitions. In fact, it can be shown that the cross section of this term is equivalent to the single band electron density–density correlation function close to the Brillouin zone center (at $\mathbf{q} \approx 0$), measuring excitations of conduction electrons and plasmons in crystals [7, 32]. This is why Raman scattering from electrons is often referred to as probing the charge density fluctuation. Following the same argument, Raman response vanishes at zero energy, because there is no charge "fluctuation" in the static limit. Note that H_{AA} does not contribute to the "crossed polarization" scatterings due to the term $(\boldsymbol{\epsilon}_I \cdot \boldsymbol{\epsilon}_s)$ and therefore will never contribute to the antisymmetric symmetry channels, e.g., A_{2g} in D_{4h} group.

The third term in Eq. (1.6) can be written as

$$H_{PA} = \frac{e}{m}\sum_k \sqrt{\frac{\hbar}{2\epsilon_0 n_k^2 V \omega_k}}[\mathbf{a}_k e^{i\mathbf{k}\cdot\mathbf{r}} + \mathbf{a}_k^\dagger e^{-i\mathbf{k}\cdot\mathbf{r}}](\mathbf{p}\cdot\boldsymbol{\epsilon}_k). \tag{1.12}$$

This term obviously does not conserve photon number and thus requires second order perturbation in Eq. (1.10) as an elastic light scattering process. The matrix element then reads

$$T \sim \sum_m \left[\frac{\langle f|\sum_j (\mathbf{p}_j\cdot\epsilon_s)e^{-i\mathbf{k}_s\cdot\mathbf{r}_j}|m\rangle\langle m|\sum_j(\mathbf{p}_j\cdot\epsilon_I)e^{i\mathbf{k}_I\cdot\mathbf{r}_j}|i\rangle}{\omega_i - \omega_m + \omega_I} + \frac{\langle f|\sum_j (\mathbf{p}_j\cdot\epsilon_I)e^{i\mathbf{k}_I\cdot\mathbf{r}_j}|m\rangle\langle m|\sum_j(\mathbf{p}_j\cdot\epsilon_s)e^{-i\mathbf{k}_s\cdot\mathbf{r}_j}|i\rangle}{\omega_i - \omega_m - \omega_s} \right]. \tag{1.13}$$

Note that the matrix element now contains electronic momenta and thus allows scattering between different electronic states, i.e., *interband* transitions [Fig. 1.2b]. Moreover, the incident and scattered photon polarizations need not be parallel as in the H_{AA} term. Therefore, the H_{PA} term is more significant for almost all collective excitations in crystals [7].

We can further draw relation between the experiment (Raman cross section) and the theory (matrix element) by rewriting the T-matrix into correlation functions. Define the single particle states, $|\alpha\rangle$, $|\alpha'\rangle$, $|\beta\rangle$, and $|\beta'\rangle$, and the manybody creation operator $c_\alpha^\dagger$. We can combine and rewrite the T-matrices from H_{AA} and H_{PA} [33],

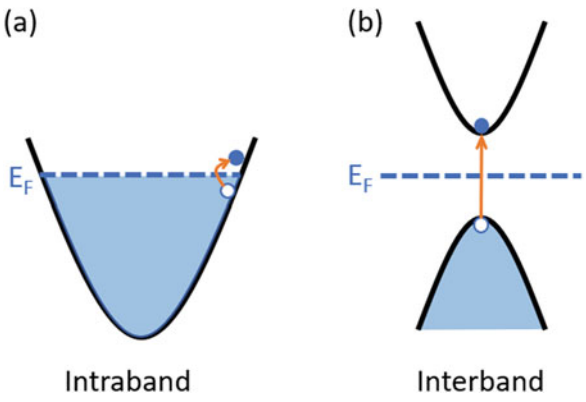

Fig. 1.2 Illustrations of (**a**) intraband and (**b**) interband transitions

$$
\begin{aligned}
T \sim\ & (\epsilon_I \cdot \epsilon_s) \sum_{\alpha,\beta} \rho_{\alpha,\beta}(\mathbf{q}) \langle f|c_\alpha^\dagger c_\beta|i\rangle \\
& + \frac{1}{m_e} \sum_m \sum_{\alpha,\alpha',\beta,\beta'} p_{\alpha,\alpha'}(\mathbf{q}_s) p_{\beta,\beta'}(\mathbf{q}_I) \\
& \times \left[\frac{\langle f|c_\alpha^\dagger c_{\alpha'}|m\rangle \langle m|c_\beta^\dagger c_{\beta'}|i\rangle}{\omega_i - \omega_m + \omega_I} + \frac{\langle f|c_\beta^\dagger c_{\beta'}|m\rangle \langle m|c_\alpha^\dagger c_{\alpha'}|i\rangle}{\omega_i - \omega_m - \omega_s} \right],
\end{aligned}
\tag{1.14}
$$

where $\rho_{\alpha,\beta}(\mathbf{q}) = \langle \alpha|e^{i\mathbf{q}\cdot\mathbf{r}}|\beta\rangle$ is the electron density matrix element, and $p_{\alpha,\alpha'}(\mathbf{q_{I,s}}) = \langle \alpha|\mathbf{p}\cdot\epsilon_{I,s} e^{\pm i\mathbf{q}_{I,s}\cdot\mathbf{r}}|\alpha'\rangle$ is the momentum matrix element.

Shastry and Shraiman further argued that if we only consider correlation effects for the electronic bands with energy comparable to the photon energies, ω_I and ω_s, which are typically around 2 eV, then the interaction Hamiltonian can be rewritten as

$$
H_{int} = \frac{e^2}{2\hbar^2 c^2} \sum_{\alpha\beta} A_\alpha \gamma_{\alpha\beta} A_\beta + \frac{e}{\hbar c} \mathbf{j}\cdot\mathbf{A}, \tag{1.15}
$$

where $\gamma_{\alpha\beta}(\mathbf{q}) = \sum_{\mathbf{k}} \frac{\partial E(\mathbf{k})}{\partial k_\alpha \partial k_\beta} c^\dagger(\mathbf{k}+\mathbf{q}/2) c(\mathbf{k}-\mathbf{q}/2)$ is usually called Maxwell's stress tensor, relating the energy to vector potential, and $j_\alpha(\mathbf{q}) = \sum_{\mathbf{k}} \frac{\partial E(\mathbf{k})}{\partial k_\alpha} c^\dagger(\mathbf{k}+\mathbf{q}/2) c(\mathbf{k}-\mathbf{q}/2)$ is the current operator. Then, the T-matrix can be further generalized to strongly correlated materials [33–35],

$$
\begin{aligned}
T \sim\ & \sum_{\alpha\beta} \epsilon_I^\alpha \epsilon_s^\beta \\
& \times \left[\langle f|\gamma_{\alpha,\beta}(\mathbf{q})|i\rangle + \sum_m \left(\frac{\langle f|j_\beta(\mathbf{q}_s)|m\rangle \langle m|j_\alpha(\mathbf{q}_I)|i\rangle}{\omega_i - \omega_m - \omega_I} + \frac{\langle f|j_\alpha(\mathbf{q}_I)|m\rangle \langle m|j_\beta(\mathbf{q}_s)|i\rangle}{\omega_i - \omega_m + \omega_s} \right) \right].
\end{aligned}
\tag{1.16}
$$

Due to the overall complexity of the problem, Eq. (1.16) needs to be simplified based on specific systems under study before any practical calculation and therefore exceeds the scope of this thesis. These problems are nicely discussed in Refs. [33, 34, 36–38] for several systems.

The scattering rate calculated from Fermi's Golden Rule in Eq. (1.9) is further related to the autocorrelation function of "effective charge density" operator, $\rho(x,t)$

$$
S(\omega,q) = \hbar r_0^2 \frac{\omega_s}{\omega_I} \Gamma_{if} \sim \sum_{\mathbf{k},\mathbf{k}'} \int_{-\infty}^{\infty} \langle c_{\mathbf{k}}^\dagger(t) c_{\mathbf{k}+\mathbf{q}}(t) c_{\mathbf{k}'+\mathbf{q}}^\dagger(0) c_{\mathbf{k}'}(0)\rangle\, e^{i\omega t} dt, \tag{1.17}
$$

which is often referred to as the dynamical electron "effective density–density" correlation function [33]. The fluctuation–dissipation theorem further relates the measured fluctuation (correlation function) to the dissipation of the system (linear response function). The cross section of the Stokes process at zero temperature is simply proportional to the imaginary part of the linear response function (dissipation), $\chi''(\omega, q)$, where ω is the photon energy transfer and q is the momentum transfer. That is, the Stokes intensity will be entirely determined by the *spontaneous scattering* due to quantum fluctuations. Notice that this term is purely quantum mechanical and is irrelevant to the details of the response function under consideration [39].

At finite temperature, the thermal fluctuation will result in an additional term in the correlation function, leading to the *stimulated scattering*. This term is related to the nature of the perturbation, and for Raman scattering, it is determined by the Bose–Einstein factor, $n(\omega, T) = 1/(\exp[\frac{\hbar\omega}{k_B T}] - 1)$. Thus the cross section for the Stokes process in Raman scattering is related to the Raman response function $\chi''(\omega, q)$ by

$$\frac{d^2\sigma}{d\Omega d\omega} \sim S(\omega, q) = [1 + n(\omega, T)]\chi''(\omega, q). \tag{1.18}$$

The details of optical corrections for converting this cross section into the scattering intensity measured by the spectrometer *outside* the sample will be given in the next chapter, Sect. 2.2.3.

For materials without *long range ordered* magnetism, the scattering cross section for the Stokes and anti-Stokes processes is related by the principle of detailed balance [7]:

$$\frac{(d^2\sigma/d\Omega d\omega)_{AS}}{(d^2\sigma/d\Omega d\omega)_S} \sim \frac{n(\omega, T)}{1 + n(\omega, T)} = \exp\left[\frac{-\hbar\omega}{k_B T}\right], \tag{1.19}$$

assuming that the energy shift is much less than the incident laser frequency, $\omega \ll \omega_L$. Therefore, by measuring the ratio of scattering cross section for the Stokes and anti-Stokes processes, we can in principle determine the sample temperature and thus estimate the effect of laser heating.

1.2.2 Nonresonant Raman Scattering

As we discussed earlier in the beginning of this section, if both the incident and scattered photon energies are much smaller than the intermediate state energy, $\omega_{I,s} \ll |\omega_i - \omega_m|$, then the scattering is called "non-resonant," and the intermediate states are called "*virtual* states." If we further limit to *intraband* transitions in weakly interacting systems [Fig. 1.2a], then the Raman cross section can be simplified to the following form [33]:

$$\frac{d^2\sigma}{d\omega d\Omega} \sim |\epsilon_I \cdot \mathbf{M}^{-1} \cdot \epsilon_s|^2 \sum_{\mathbf{k},\mathbf{k}'} \int_{-\infty}^{\infty} \langle c^\dagger_{\mathbf{k}}(t) c_{\mathbf{k}+\mathbf{q}}(t) c^\dagger_{\mathbf{k}'+\mathbf{q}}(0) c_{\mathbf{k}'}(0) \rangle \, e^{i\omega t} dt, \tag{1.20}$$

where $\mathbf{M}^{-1}$ is called the inverse "effective mass tensor" [40],

$$\mathbf{M}^{-1} \equiv \frac{\partial^2 E(\mathbf{k})}{\partial k_\alpha \partial k_\beta} = \frac{1}{m_e}\delta_{\alpha\beta} + \frac{1}{m_e^2} \sum_m \left(\frac{\langle i|p_\beta|m\rangle \langle m|p_\alpha|i\rangle + \langle i|p_\alpha|m\rangle \langle m|p_\beta|i\rangle}{\omega_i - \omega_m} \right). \tag{1.21}$$

This is known as the "effective mass" approximation. This is very useful in metals or large band gap insulators, where the conduction band width or band gap is commonly over 3 eV, such that no *real* interband transitions need to be considered when visible light is used. Within the approximation, by utilizing the symmetry properties of the Raman cross section that we will discuss later, one can even relate symmetry resolved Raman response function to different parts of the Fermi surface [33]. In most metallic materials, unless there exists a singularity in the joint density of states for vertical transitions of visible wavelength, the effective mass approximation is always a good starting point for understanding the Raman scattering spectra.

Up to this point, the Raman scattering cross section has been discussed quite generally without restricted to any specific systems. In the following, we will briefly discuss the most common situations for Raman scattering in solids, i.e., light scattering with lattice vibrations.

1.2.3 Raman Scattering of Phonon

The theory of inelastic light scattering by molecule or lattice vibrations is first developed by Placzek [30], who realized that the vibration of atoms around its equilibrium position creates a time dependent electric polarization, like an oscillating dipole, which as we known leads to emission of electromagnetic waves. In solids, the dominant Raman scattering process is always the one in which the photons interact indirectly with the phonons via the electrons [25]. The photon field interacts with the "deformation potential" induced by the lattice vibrations and thus the energy shift by the phonon energies.

Microscopically, the lattice vibrations modify the dynamical electric susceptibility of the crystal, $\chi(u,t)$ [41]. Note that this is usually called polarizability, $\alpha(u,t)$, for molecule vibrations. Expanding the susceptibility around the equilibrium position of nuclei in the normal coordinates,

$$\chi(u,t) = \chi(0) + (\mathbf{u}(t) \cdot \nabla)\chi(u,t)|_{u=u(0)} + \mathcal{O}(\mathbf{u}^2), \tag{1.22}$$

where $\mathbf{u}(t) = \mathbf{u}_0 e^{-i\omega t} + \mathbf{u}_0^* e^{i\omega t}$ is the lattice displacement due to a phonon mode with frequency ω. The first term in $\chi(u,t)$ does not modify the frequency of

perturbation (elastic scattering), and thus we only keep the second term linear in $\mathbf{u}$. Then the time dependent susceptibility is of the form $\chi(t) = \chi_0 e^{-i\omega t} + \chi_0^* e^{i\omega t}$. Assume that the incoming photon has electric field $\mathbf{E} = \mathbf{E}_0 e^{-i\omega_I t} + \mathbf{E}_0^* e^{i\omega_I t}$, where ω_I is the photon frequency. Then, the induced dipole moment is

$$\mathbf{P}(t) = [\chi_0 \cdot \mathbf{E}_0 e^{-i(\omega_I+\omega)t} + \chi_0^* \cdot \mathbf{E}_0^* e^{i(\omega_I+\omega)t}] + [\chi_0^* \cdot \mathbf{E}_0 e^{-i(\omega_I-\omega)t} + \chi_0 \cdot \mathbf{E}_0^* e^{i(\omega_I-\omega)t}]. \tag{1.23}$$

The first term is oscillating at a slightly lower frequency and thus corresponds to the Stokes process, and the second term is responsible for the anti-Stokes process. The quantum mechanical derivation of phonon scattering turns out to be much more complicated, involving third order perturbation that includes the electron–phonon coupling and neglects the H_{AA} term [7, 25, 42, 43]. However, the conclusion remains the same with simple semi-classical arguments [43, 44]. Therefore we will not reproduce them in this thesis.

The Raman active phonon typically has a Lorentzian lineshape [45]. However, when a sharp phonon mode with energy $\hbar\omega_0$ interacts with a broad electronic continuum, the interference between the transition amplitudes for electronic continuum T_e and the phonon mode T_p results in a "Fano lineshape" [44, 46],

$$I(\omega) = \frac{\pi\rho(\omega)T_e^2(\omega_0 - \omega - VT_p/T_e)^2}{(\omega_0 - \omega + V^2R(\omega))^2 + (\pi V^2\rho(\omega))^2}. \tag{1.24}$$

The electron density of states, $\rho(\omega) = \mathrm{Im}[G(\omega)]$, is usually assumed to be some broad function or even a constant, where $G(\omega) = \sum_e 1/(\omega_e - \omega - i\Gamma)$ is the unperturbed Green's function for the electronic continuum. The electron–phonon interaction is V, and $R(\omega) = \mathrm{Re}[G(\omega)]$. Therefore, the Fano effect is a phonon mode selective probe for studying the electron–phonon coupling in metallic systems, which is especially useful when studying the mechanism of superconductivity in some compounds [47, 48].

1.3 Symmetry Selection Rules in Raman Scattering

The symmetry properties of the scattering cross section, i.e., measured polarization dependences, are determined by the symmetry properties of the Raman response function, $\chi''(\omega)$. Quite generally, the Hamiltonian of a system commutes with the symmetry operators of the crystal's factor group (space group without translational symmetry operators). In other words, the Hamiltonian should transform as the full symmetric irreducible representation of the crystal's factor group. This is called Neumann's Principle [49], first stated by Franz E. Neumann and then later popularized by his student Woldermar Voigt. It was later generalized by Pierre Curie [50], stating that a physical phenomenon may exist and only exist in a medium

that possesses the same symmetry characteristic of the phenomenon or that of a subgroup of that symmetry.

The eigenfunctions of a Hamiltonian can be projected to form basis functions for the irreducible representations of the group. For a certain point group under considerations, let the initial state $|i\rangle$ in a scattering process have symmetry Γ_i and the final state $|f\rangle$ have symmetry Γ_f. The symmetry of the excitation, $|f\rangle\langle i|$, is then equal to $\Gamma_f \otimes \Gamma_i^*$. Let the electric field vector for the incident and scattered light transform as Γ_{ϵ_I} and Γ_{ϵ_s}, respectively. Then, a very general group theoretical statement is that only excitations that satisfy the following relation are allowed [7, 51]:

$$\Gamma_f \otimes \Gamma_i^* \subset \Gamma_{\epsilon_I}^* \otimes \Gamma_{\epsilon_s}. \tag{1.25}$$

Since the algebra and symmetry properties of all irreducible representations for all 32 point groups in 3D are documented [52, 53], we can easily find out the allowed excitation symmetries in a crystal.

Consider now the point group D_{4h}, suitable for the lattice symmetry of URu_2Si_2, which we will discuss in Chap. 3. The electric field vector transforms as Γ_5^- (E_u) along a-axis and Γ_2^- (A_{2u}) along c-axis. Then, $\Gamma_5^- \otimes \Gamma_5^- = \Gamma_1^+ \oplus \Gamma_2^+ \oplus \Gamma_3^+ \oplus \Gamma_3^+$ (in the Bethe notation), or equivalently in the Mulliken notation, $A_{1g} \oplus A_{2g} \oplus B_{1g} \oplus B_{2g}$. This suggests that only excitations with the symmetry of these four irreducible representations are allowed for inelastic light scattering from the ab-surface. In order to access the Γ_5^+ (E_g) excitations, we need to have $\Gamma_5^- \otimes \Gamma_2^- = \Gamma_5^+$, that is, scattering from the ac-surface with incident and scattered light polarization orthogonal to each other (crossed polarization).

The superscript plus sign in the Bethe notation or the subscript g in the Mulliken notation denotes parity even (stands for *gerade*, meaning *even* in German). Similarly, the superscript minus sign and the subscript u mean parity odd (*ungerade*). This distinguish is of course dropped for noncentrosymmetric crystals or 2D wallpaper groups, as we will see in the following for Bi_2Se_3. One immediately notices that, for crystals with inversion symmetry, the multiplication of any two *ungerade* representation will always result in gerade representations. Therefore, only at most half of the irreducible representations are allowed in Raman scattering. This is indeed the case, and these excitations are called Raman active modes. The excitations with *ungerade* symmetries are accessible by absorption or emission spectroscopies, such as infrared spectroscopies.

In Bi_2Se_3, an interesting scenario happens where both excitations from the bulk and from the surface need to be considered [Chap. 4]. The bulk lattice has symmetry of the D_{3d} group, which follows from a similar exercise as above, that only excitations with the symmetries $\Gamma_3^- \otimes \Gamma_3^- = \Gamma_1^+ \oplus \Gamma_2^+ \oplus \Gamma_3^+$ are allowed from ab-plane scattering. Note here that scattering from the ac-plane does not yield any extra symmetry channels. The surface states in Bi_2Se_3 belong to a different symmetry group, C_{6v} [54], which obviously does not have inversion symmetry. The electric field vector in ab-plane transforms as Γ_5 (E_1) and as Γ_1 (A_1) along the c-axis. Thus, the accessible symmetry channels from the ab-plane are $\Gamma_5 \otimes \Gamma_5 = \Gamma_1 \oplus \Gamma_2 \oplus \Gamma_6$

($A_1 \oplus A_2 \oplus E_2$), and the Γ_5 (E_1) symmetry channel is only accessible from the *ac*-surface. Note that in this group, Γ_3 and Γ_4 symmetries will remain silent for two photon scattering process and will only be accessible by nonlinear optics.

The above relations are usually referred to as the Raman selection rules, which determine the allowed excitations symmetries. However, the symmetry properties of each irreducible representation impose much stronger rules on the Raman susceptibility tensors [51], which relates the cross sections for each symmetry channel to the polarizations of light. The bilinear dependence of Raman susceptibility on electric field polarization, $\epsilon_s \cdot \chi \cdot \epsilon_I$, implies the susceptibility tensor to be rank-2. A very general and pedagogical recipe for obtaining the susceptibility tensors for each symmetry channel of the 32 point groups is given by Callen in Ref. [55], and the results for Raman scattering are tabulated first by L.N. Ovander [56] and then cited in several monographs as the "Raman tensors" [7, 27].

We will not repeat the tables here but merely use group D_{4h} as an example for calculating the polarization dependence of cross sections using the Raman tensors.

$$A_{1g}: \begin{bmatrix} a & & \\ & a & \\ & & b \end{bmatrix}; A_{2g}: \begin{bmatrix} & c & \\ -c & & \\ & & \end{bmatrix}; B_{1g}: \begin{bmatrix} d & & \\ & -d & \\ & & \end{bmatrix}; B_{2g}: \begin{bmatrix} & e & \\ e & & \\ & & \end{bmatrix}, \quad (1.26)$$

where the empty spaces in the 3 by 3 matrices are zeros, and the columns and rows are x, y, and z Cartesian coordinates in the *laboratory frame*. The cross section of, for example, the A_{2g} symmetry is then proportional to $|\epsilon_s^x \cdot \mathbf{R} \cdot \epsilon_I^y|^2 \sim c^2$, where $\mathbf{R}$ is the Raman tensor, $\epsilon^x = [1, 0, 0]$, and $\epsilon^y = [0, 1, 0]$. Thus the excitations with A_{2g} symmetry will be contained in the XY scattering geometry. One would need to do this repeatedly for all symmetry channels and for all scattering geometries, to find out the expected polarization dependence of the excitations. Note that due to time reversal symmetry, the circularly polarized light changes chirality on back reflection. Thus, $\epsilon_I^R = [1, -i, 0]/\sqrt{2}$ and $\epsilon_s^R = [1, i, 0]/\sqrt{2}$. As we will see in Chaps. 3 and 4, the circularly polarized light is important to separate A_{2g} symmetry from the other excitations [33, 57].

1.4 Chiral Excitations in Solids

As we introduced above, the phononic Raman cross section is identified as proportional to the electric susceptibility tensor, which is restricted to real and symmetric form [30]. Thus, time reversal symmetry forbids light scattering through the fully antisymmetric Raman tensors, such as collective modes with A_2 or A_{2g} symmetry [58]. Historically, the excitations in the antisymmetric channel are referred to as the "chiral excitations" due to their intimate relationship with the spin chiral operator $\mathbf{s_1} \cdot (\mathbf{s_2} \times \mathbf{s_3})$ [34, 36, 59]. For example, antisymmetric scattering was

predicted for Dirac spin-liquid state in the spin-1/2 kagome system [36], but yet unobserved to date.

It was noted by Placzek at the very end of his book that contribution from antisymmetric tensors ($A_{2(g)}$ irreducible representation) may arise due to breakdown of the polarizability description near resonance conditions [30]. Indeed, this was observed in resonant Raman scattering of heme proteins, such as ferrocytochrome-c [60–62]. Besides resonance scattering, antisymmetric nonresonant vibrational Raman scattering is allowed if one goes beyond the Born–Oppenheimer approximations, such as in systems with exceptionally strong electron–phonon coupling or in the proximity of a phonon mediated phase transition [63]. Generally speaking, magnetic Raman scattering could also couple to the antisymmetric tensor [7]. This is because both the magnetic moments and antisymmetric $A_{2(g)}$ representations transform as a pseudovector (in the lowest order). Many examples exist where sharp magnon or two-magnon peaks were observed in the antisymmetric channel [1, 7, 31]. In magnetic materials, phonon scattering symmetry selection rules are partly relaxed due to Faraday rotation, which also lead to nonzero antisymmetric Raman matrix elements [64, 65].

For nonmagnetic and non-resonance Raman scattering from crystalline samples, much less examples of nonzero signal with A_{2g} symmetry are known. To the best of our knowledge, all of the examples come from electronic Raman scatterings. In general, antisymmetric excitations are allowed for electronic *interband* transitions [56]. For example, transitions between crystal field split states can contribute to the antisymmetric channel. Indeed, the very first observation of Raman scattering in the antisymmetric channel was reported in 1968 from crystal field split states of embedded magnetic ions (Eu^{3+}:YAG) [66] and latter found in several rare earth compounds [67, 68]. However, this is not a common observation, other than very localized $4f$ electrons. Because most systems have full symmetric ground states, and thus an $A_{2(g)}$ interband transition would require a fully antisymmetric $A_{2(g)}$ excited state, which is typically not possible with few exemptions.

The most famous example is perhaps in the insulating cuprates, where an $A_{2(g)}$ symmetry peak slightly below the charge transfer gap edge was observed [32, 69, 70]. This is later understood as excitonic interband transition between B_{1g} and B_{2g} symmetrized copper 3d orbital states [32]. Such transition is in some sense also a crystal field excitation, but the band width is much larger than in $4f$ systems, and therefore the peak is also 2 orders of magnitude broader. An alternative explanation to the peak was given by Khveshchenko and Wiegmann as dynamic chiral spin fluctuations [59], which is a collective zero mode being pulled below the charge transfer gap edge by the exchange interaction J. In this view, the excited state could be thought of as a bound state between the double occupant and the hole sites, where the $A_{2(g)}$ symmetry originates from the local "circular current" induced by the charge transfer.

More recently, antisymmetric continuum was reported from the inter Dirac cones excitations in graphene [71, 72]. Note that the electronic Raman cross section of intraband transitions in metals is usually related to the inverse effective mass tensor, which is always symmetric. That is, Raman scattering cross section of

metals typically does not contain any signal in the fully antisymmetric $A_{2(g)}$ channel. However, the excitations in semi-metallic graphene provided an exception due to its peculiar helical band structure, i.e., the electron momentum locked to pseudo-spin. Similar examples of spin-momentum lock-in can be found in many topological materials [Chap. 4] and therefore provide interesting platforms to look for antisymmetric Raman excitations in future works.

Here in this monograph, we add two more examples of electronic excitations from antisymmetric channel to the above list. More precisely, we observe sharp $A_{2(g)}$ collective modes in two entirely different nonmagnetic systems, heavy fermion metal URu_2Si_2 and 3D topological insulator Bi_2Se_3. Observation of an antisymmetric collective mode in nonmagnetic systems is highly unusual and rare, and the mechanism is different for each case. This monograph is dedicated to explore the properties, mechanism, and physical implications from these two new systems.

References

1. M.G. Cottam, D.J. Lockwood, *Light Scattering in Magnetic Solids* (Wiley, New York, 1986)
2. Kung et al., Science **347**, 6228 (2015). https://doi.org/10.1126/science.1259729
3. Kung et al., Phys. Rev. Lett. **117**, 227601 (2016). https://doi.org/10.1103/PhysRevLett.117.227601
4. Kung et al., Phys. Rev. Lett. **119**, 136802 (2017). https://doi.org/10.1103/PhysRevLett.119.136802
5. Kung et al., Proc. Natl. Acad. Sci. U.S.A. **116**, 4006 (2019). https://doi.org/10.1073/pnas.1813514116
6. Kung et al., Phys. Rev. B **95**, 245406 (2017). https://doi.org/10.1103/PhysRevB.95.245406
7. W. Hayes, R. Loudon, *Scattering of Light by Crystals* (Courier Corporation, Chelmsford, 2012)
8. E. Gross, Change of wave-length of light due to elastic heat waves at scattering in liquids. Nature **126**, 201 (1930)
9. L. Landau, G. Placzek, The structure of undisplaced scattered lines. Physik Z. Sowjetunion **5**, 172 (1934)
10. L. Brillouin, Diffusion of light and X-rays by a transparent homogeneous body. Ann. Phys.(Paris) **17**, 88 (1922)
11. P. Debye, Zur Theorie der spezifischen Wäarmen. Annalen der Physik **344**(14), 789–839 (1912). https://doi.org/10.1002/andp.19123441404
12. A. Smekal, Zur Quantentheorie der Dispersion. Naturwissenschaften **11**(43), 873–875 (1923). https://doi.org/10.1007/BF01576902
13. H.A. Kramers, W. Heisenberg, Über die Streuung von Strahlung durch Atome. Zeitschrift für Physik **31**(1), 681–708 (1925). https://doi.org/10.1007/BF02980624
14. P.A.M. Dirac, The quantum theory of the emission and absorption of radiation. Proc. R. Soc. Lond. A Math. Phys. Eng. Sci. **114**(767), 243–265 (1927). https://doi.org/10.1098/rspa.1927.0039
15. P.A.M. Dirac, The quantum theory of dispersion. Proc. R. Soc. Lond. A: Math. Phys. Eng. Sci. **114**(769), 710–728 (1927). https://doi.org/10.1098/rspa.1927.0071
16. C.V. Raman, On the molecular scattering of light in water and the colour of the sea. Proc. R. Soc. Lond. A **101**(708), 64–80 (1922). https://doi.org/10.1098/rspa.1922.0025
17. C.V. Raman, K.S. Krishnan, A new type of secondary radiation. Nature **121**, 501–502 (1928). https://doi.org/10.1038/121501c0

18. C.V. Raman, A new radiation. Indian J. Phys. **2**, 387–398 (1928)
19. R.W. Wood, Wave-length shifts in scattered light. Nature **122**, 349 (1928). https://doi.org/10.1038/122349d0
20. G. Landsberg, L. Mandelstam, Eine neue Erscheinung bei der Lichtzerstreuung in Krystallen. Naturwissenschaften **16**(28), 557–558 (1928). https://doi.org/10.1007/BF01506807
21. I.L. Fabelinskiĭ, Seventy years of Raman scattering. Physics-Uspekhi **41**(12), 1229 (1998)
22. R.A. Millikan, A direct photoelectric determination of Planck's "*h*". Phys. Rev. **7**, 355–388 (1916). https://doi.org/10.1103/PhysRev.7.355
23. A.H. Compton, A quantum theory of the scattering of X-rays by light elements. Phys. Rev. **21**, 483–502 (1923). https://doi.org/10.1103/PhysRev.21.483
24. A. Pinczuk, E. Burstein, Fundamentals of inelastic light scattering in semiconductors and insulators, in *Light Scattering in Solids I* (Springer, New York, 1983), pp. 23–78
25. R. Loudon, Theory of the first-order Raman effect in crystals. Proc. R. Soc. Lond. A Math. Phys. Eng. Sci. **275**(1361), 218–232 (1963). https://doi.org/10.1098/rspa.1963.0166
26. Y.R. Shen, Distinction between resonance Raman scattering and hot luminescence. Phys. Rev. B **9**, 622–626 (1974). https://doi.org/10.1103/PhysRevB.9.622
27. M. Cardona, Resonance phenomena, in *Light Scattering in Solids II*, ed. by M. Cardona, G. Güntherodt (Springer, Berlin, 1982), pp. 45–49
28. R. Planel, C.B. Guillaume, Optical orientation of excitons, in *Optical Orientation*, Chap. 8, ed. by F. Meier, B.P. Zakharchenya (Elsevier Science Ltd, Amsterdam, 1984), p. 353
29. R.S. Knox, *Theory of Excitons*, vol. 5 (Academic, New York, 1963)
30. G. Placzek, The Rayleigh and Raman scattering, in *Berkeley, Calif: Lawrence Radiation Laboratory* (1959). Translated from the Handbuch der Radiologie, ed. by E. Marx, Leipzig, Akademische Verlagsgesellschaft VI, 2, 209–374 (1934)
31. P.A. Fleury, R. Loudon, Scattering of light by one- and two-magnon excitations. Phys. Rev. **166**, 514–530 (1968). https://doi.org/10.1103/PhysRev.166.514
32. D.V. Salamon, Large-shift Raman scattering in insulating cuprate materials. PhD thesis. University of Illinois at Urbana-Champaign, 1994
33. T.P. Devereaux, R. Hackl, Inelastic light scattering from correlated electrons. Rev. Mod. Phys. **79**, 175–233 (2007). https://doi.org/10.1103/RevModPhys.79.175
34. B.S. Shastry, B.I. Shraiman, Theory of Raman scattering in Mott-Hubbard systems. Phys. Rev. Lett. **65**, 1068–1071 (1990). https://doi.org/10.1103/PhysRevLett.65.1068
35. B.S. Shastry, B.I. Shraiman, Raman scattering in Mott-Hubbard systems. Int. J. Mod. Phys. B **5**, 365–388 (1991). https://doi.org/10.1142/S0217979291000237
36. W.-H. Ko et al., Raman signature of the U(1) Dirac spin-liquid state in the spin-$\frac{1}{2}$ Kagome system. Phys. Rev. B **81**, 024414 (2010). https://doi.org/10.1103/PhysRevB.81.024414
37. A.M. Shvaika et al., Resonant enhancement of inelastic light scattering in strongly correlated materials. Phys. Rev. Lett. **93**, 137402 (2004). https://doi.org/10.1103/PhysRevLett.93.137402
38. A.M. Shvaika et al., Electronic Raman scattering in correlated materials: a treatment of nonresonant, mixed, and resonant scattering using dynamical mean-field theory. Phys. Rev. B **71**, 045120 (2005). https://doi.org/10.1103/PhysRevB.71.045120
39. P. Coleman, *Introduction to Many-Body Physics* (Cambridge University Press, Cambridge, 2015). https://doi.org/10.1017/CBO9781139020916
40. N.W. Ashcroft, N.D. Mermin, *Solid State Physics*. HRW International editions. Holt, Rinehart and Winston, 1976
41. M. Born, K. Huang, *Dynamical Theory of Crystal Lattices*. Oxford Classic Texts in the Physical Sciences (Clarendon Press, Oxford, 1954)
42. R.F. Wallis, M. Balkanski, *Many-body Aspects of Solid State Spectroscopy* (North-Holland Physics, New York, 1986)
43. M.V. Klein, Vibrational Raman scattering from crystals, in *Dynamical Properties of Solids VI: The Modern Physics of Phonons*, ed. by G.K. Horton, A.A. Maradudin (Elsevier, New York, 1990), pp. 65–128

44. M.V. Klein, Electronic Raman scattering, in *Light Scattering in Solids I*, ed. by M. Cardona, G. Güntherodt (Springer, Berlin, 1983), pp. 169–172
45. R Loudon, Theory of the resonance Raman effect in crystals. J. Phys. France **26**(11), 677–683 (1965). https://doi.org/10.1051/jphys:019650026011067700
46. U. Fano, Effects of configuration interaction on intensities and phase shifts. Phys. Rev. **124**, 1866–1878 (1961). https://doi.org/10.1103/PhysRev.124.1866
47. I. Ohana, M.S. Dresselhaus, S. Tanuma, Resonant Raman effect and Fano distortion in the stage-2 graphite donor intercalation compound C/Rb. Phys. Rev. B **43**, 1773–1776 (1991). https://doi.org/10.1103/PhysRevB.43.1773
48. P. Zhou et al., Raman-scattering study of the electron-phonon interaction in M_3C_{60} (M=K,Rb). Phys. Rev. B **48**, 8412–8417 (1993). https://doi.org/10.1103/PhysRevB.48.8412
49. F.E. Neumann, O.E. Meyer, *Vorlesungen über die Theorie der Elasticität der festen Körper und des Lichtäthers: gehalten an der Universität Königsberg*, vol. 4 (BG Teubner, Leipzig, 1885)
50. P. Curie, Sur la symétrie dans les phénomènes physiques, symétrie d'un champ électrique et d'un champ magnétique. Journal de Physique Théorique et Appliquée **3**(1), 393–415 (1894)
51. J.F. Nye, *Physical Properties of Crystals: Their Representation by Tensors and Matrices* (Oxford science publications, Clarendon Press, New York, 1985)
52. G.F. Koster. *Properties of the Thirty-Two Point Groups*. Massachusetts Institute of Technology Press Research Monograph (M.I.T. Press, Cambridge, 1963)
53. E.B. Wilson, J.C. Decius, P.C. Cross, *Molecular Vibrations: The Theory of Infrared and Raman Vibrational Spectra*. Dover Books on Chemistry (Dover Publications, New York, 2012)
54. J. Li, J.J. Tu, J.L. Birman, Symmetry predicted transitions in 3D topological insulators. Solid State Commun. **163**, 11–14 (2013). http://dx.doi.org/10.1016/j.ssc.2013.03.010
55. H. Callen, Crystal symmetry and macroscopic laws. Am. J. Phys. **36**(8), 735–748 (1968). https://doi.org/10.1119/1.1975102
56. L.N. Ovander, The form of the Raman tensor. Opt. Spectrosc **9**, 302 (1960)
57. J. Nestro, T.G. Spiro, Circularly polarized Raman spectroscopy: Direct determination of antisymmetric scattering in the resonance Raman spectrum of ferrocytochrome c. J. Raman Spectrosc. **1**(6), 539–550 (1973). https://doi.org/10.1002/jrs.1250010604
58. F.-C. Liu, A.D. Buckingham, Antisymmetric resonant vibrational Raman scattering. Chem. Phys. Lett. **207**(4), 325–331 (1993). http://dx.doi.org/10.1016/0009-2614(93)89008-6
59. D.V. Khveshchenko, P.B. Wiegmann. Raman scattering and anomalous current algebra in Mott insulators. Phys. Rev. Lett. **73**, 500–503 (1994). https://doi.org/10.1103/PhysRevLett.73.500
60. T.G. Spiro, T.C. Strekas, Resonance Raman spectra of hemoglobin and cytochrome c: inverse polarization and vibronic scattering. Proc. Natl. Acad. Sci. **69**(9), 2622–2626 (1972)
61. L.D. Barron, *Molecular Light Scattering and Optical Activity*, 2nd edn. (Cambridge University Press, Cambridge, 2004)
62. H. Hamaguchi, The resonance effect and depolarization in vibrational Raman scattering, in *Advances in Infrared and Raman Spectroscopy*, ed. by R.J.H. Clark, R.E. Hester (Wiley-Heyden, London, 1985), pp. 273–310
63. F. Liu, Antisymmetric nonresonant vibrational Raman scattering. J. Phys. Chem. **95**(19), 7180–7185 (1991). https://doi.org/10.1021/j100172a017
64. Z. Peng-Xiang, T. An, Influence of Faraday rotation on the selection rule of phonon Raman scattering in magnetic materials. J. Raman Spectrosc. **14**(5), 326–329 (1983). https://doi.org/10.1002/jrs.1250140506
65. R.A. Yadav, Raman scattering in magnetic materials. J. Chem. Sci. **102**(5), 629–634 (1990). https://doi.org/10.1007/BF03040790
66. J.A. Koningstein, O.S. Mortensen, Experimental Observation of an antisymmetric Raman scattering tensor. Nature **217**(5127), 445–446 (1968). https://doi.org/10.1038/217445a0
67. H. Rho, M.V. Klein, P.C. Canfield, Polarized Raman scattering studies of crystal-field excitations in ErNi2B2C. Phys. Rev. B **69**, 144420 (2004). https://doi.org/10.1103/PhysRevB.69.144420

68. H. Rho, M.V. Klein, P.C. Canfield, Crystal-field excitations and spin-phonon interactions in $DyNi_2B_2C$: Raman scattering study. Phys. Rev. B **82**, 064423 (2010). https://doi.org/10.1103/PhysRevB.82.064423
69. R. Liu et al., Novel Raman-active electronic excitations near the charge-transfer gap in insulating cuprates. Phys. Rev. Lett. **71**, 3709–3712 (1993). https://doi.org/10.1103/PhysRevLett.71.3709
70. P.E. Sulewski et al., Observation of chiral spin fluctuations in insulating planar cuprates. Phys. Rev. Lett. **67**, 3864–3867 (1991). https://doi.org/10.1103/PhysRevLett.67.3864
71. E. Riccardi et al., Gate-dependent electronic Raman scattering in graphene. Phys. Rev. Lett. **116**, 066805 (2016). https://doi.org/10.1103/PhysRevLett.116.066805
72. O. Kashuba, V.I. Fal'ko, Signature of electronic excitations in the Raman spectrum of graphene. Phys. Rev. B **80**, 241404 (2009). https://doi.org/10.1103/PhysRevB.80.241404

Chapter 2
Experimental Setup

Abstract Since the days when C.V. Raman and coworkers discovered inelastic light scattering using Calcutta sunlight as the source in the 1920s (Raman, Indian J Phys 2:387–398, 1928), many improvements have been done on Raman spectroscopy apparatus in the past century. Raman scattering setup has evolved into very diverse forms, from portable or even handheld Raman spectrometers widely used by forensic scientists and minefield workers to gigantic state-of-the-art triple-stage grating spectrometers used in research labs. The data collection efficiency has also improved many orders of magnitude, alongside with better spectral resolution and polarization optics. This is due to improvements on almost every single element: laser light source, polarization optics, aberration corrected lens, holographic blazed gratings, off-axis parabolic mirrors, high precision slits, back illuminated CCD detectors, and many other factors (Hayes and Loudon, Scattering of light by crystals. Courier Corporation, Chelmsford, 2012; Palmer, Loewen, Diffraction grating handbook. Newport Corporation, New York, 2005). Given the diversity and breadth of this topic, it is impossible to have a complete account of all involved instrumentations. In this chapter, I will introduce the basic elements common to most low temperature polarization resolved Raman spectroscopic research labs, but focus will be given to the setups we employ here at Rutgers. Then I will discuss the data acquisition, error sources, and data analysis techniques we used in this monograph.

2.1 Raman Scattering Setup

2.1.1 Laser

Although C.V. Raman originally used sun light as excitation source for his pioneering experiments of inelastic light scattering [1], it is more desirable to use monochromatic light source, where the energy is as sharply peaked as possible (monochromaticity). Before the advent of both ruby laser and He–Ne laser in 1960, gas discharge lamps were the only choice of light source for Raman scattering. However, since the cross section of Raman scattering is usually very small,

H.-H. Kung, *Collective Excitations in the Antisymmetric Channel of Raman Spectroscopy*, Springer Theses, https://doi.org/10.1007/978-3-030-89332-3_2

Table 2.1 The list of laser wavelength and typical output power in the Kr^+ laser used in our lab (Coherent Innova 302C), under "single line" configuration, operating at TEM_{00} mode (except for the 752 nm line) under the listed current. Notice that this is the "optimized operating current" that outputs maximum power and was measured by Coherent technician immediately after the replacement of a new plasma tube. The typical operating current we use is around 32–35 A, and the output power is less than listed below

Wavelength (nm)	Energy (eV)	Power (mW)	Operating current (A)
799.3	1.55	103	36
752.5	1.65	200	36
676.4	1.83	190	41
647.1	1.92	760	41
568.2	2.18	340	41
530.9	2.34	440	45
520.8	2.38	272	45
482.5	2.57	155	45
476.2	2.60	195	45
413.1	3.00	650	45
406.7	3.05	415	45
350.7	3.54	500	45

extremely long exposure time is needed to observe the Raman lines, limiting its applicability. In the accounts of Landsberg, Raman scattering in quartz requires more than 15 h exposure time and sometimes more than 100 h [2]. Therefore, it is desirable to have a much more intense and monochromatic light source. The appearance of laser nicely solves both problems and has become an essential tool for most of the Raman scattering experiments nowadays.

For most of the experiments in this thesis, we use a Kr^+ ion laser (Coherent Innova 302C) that allows several lasing lines from UV to NIR range, where the most prominent laser lines are listed in Table 2.1. Notice that the "operating current" tabulated in this table is the "optimized value" that outputs maximum power and was measured by coherent technician immediately after the replacement of a new plasma tube. The typical operating current we use is around 32 A, and the output power is a little less than listed here.

Ion laser is one of the most popular choices for Raman scattering due to its stability, large output power, and monochromaticity. Among them, Ar+ and Kr+ ion lasers are the most popular choices, because both of them have multiple lasing lines in the visible spectrum, convenient for conventional Raman spectroscopy.

In an ion laser, the laser light is produced in the "plasma tube" [Fig. 2.1], which is essentially a sealed cylinder with low pressure Kr gas. During operation, an electric field is supplied to maintain the Kr gas ionized and in a highly excited state, creating a "population inversion" for some atomic states, where the number of particles in a higher energy state exceeds the number of particles in a lower energy state. The energy stored within the population inverted state is eventually released through cascade of "stimulated photon emission," where all ions coherently radiate photons

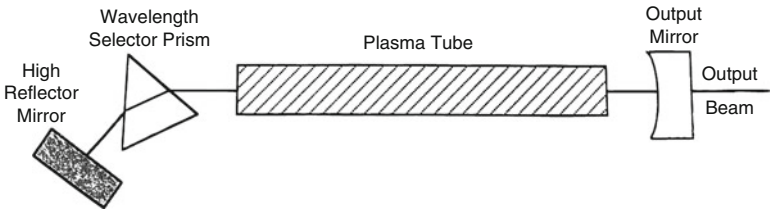

Fig. 2.1 Illustration of the resonance cavity in typical gas ion lasers. The ends of the plasma tube are sealed with "Brewster windows," not shown in the drawing

with the same energy and same phase and thus producing very intense, collimated, and coherent radiation.

The ends of the plasma tube are sealed with "Brewster windows." These are quartz crystals with surface normal oriented at Brewster's angle relative to the light propagation direction. With this geometry, only light with p-polarization can pass through the window and trigger stimulated emission. Thus the output laser light is polarized in the direction that experiences zero loss through the Brewster windows.

Finally, two mirrors are placed outside the plasma tube and on the optical axis, such as drawn in Fig. 2.1. These two mirrors form an optical cavity that stores the electromagnetic energy escaped from the plasma tube. Both the "high reflector" and "output mirror" are quartz coated with dielectric materials to achieve its desired reflectivity within a certain frequency range. While the high reflector has practically 100% reflectivity, the output mirror is designed to have reflectivity slightly less than perfect to allow part of the light intensity to escape the cavity and form the output beam.

Due to the very large number of states in the plasma tube, many laser lines and even much more plasma lines are simultaneously emitting. This is however inconvenient for Raman scattering experiments, where we would like to use monochromatic excitation. This is achieved through placing a "selector prism" in the optical path, known as the "single line" configuration, shown in Fig. 2.1. Light through the prism is dispersed such that only photon wavelength within a small window may reach the high reflector flat mirror and be send back into the optical cavity for further amplification. Thus, by adjusting the prism orientation, we can easily switch between several laser lines.

Apart from the large size, expensive maintenance, requirements for large electric power and water cooling, the main drawback of ion gas lasers is the nuisance of "plasma lines." These are the incoherent, non-lasing, emission lines of the ion plasma. The intensity of the plasma lines are typically comparable to, or even stronger than, many Raman spectroscopic features we are interested in. Furthermore, as an ion laser ages, the once optimized tube condition will unavoidably change slightly, and therefore some weaker laser lines will stop emission after a few years.

Another popular genre is the diode lasers (semiconductor lasers), which due to its high efficiency can be made very compact with appreciable laser output

power without water cooling. Diode lasers with any wavelength across the entire visible spectrum can be found with relatively low price and therefore becoming increasingly popular. The main drawback is its poor collimation, which requires additional lenses outside the laser cavity.

Another common laser source is the solid state laser, which uses solid crystals as lasing medium instead of the plasma tube in ion lasers. The lasing medium needs to be optically pumped by another source, usually a diode laser. One of the most popular solid state lasers is based on neodymium-doped yttrium aluminum garnet (Nd:YAG) crystal, which has a 532 nm line often used for "laser pointers." The first ever built optical laser, the "Ruby laser," is also a type of solid state laser. In our lab, we have an air-cooled 532 nm solid state laser with about 50 mW output power from JDS Uniphase Corporation, a 445 nm laser diode with about 5 mW output power from Lilly Electronics, and a 462 nm laser diode with about 500 mW output power from Thorlabs.

Ti:Sapphire and dye lasers are the most common types of coherent light source with tunable wavelength we have in our lab, however both requiring pumping from another laser source. The author does not use either of the tunable lasers in this monograph.

2.1.2 Optical Setup

Figure 2.2 is an illustration of the basic optical setup for Raman spectroscopy in the "pseudo backscattering" at Rutgers. Notice that the dimensions are not all drawn in scale. All elements are fixed on a large optical table, but adjustments can be easily made depending on the needs of the particular experiment. Several reflective high

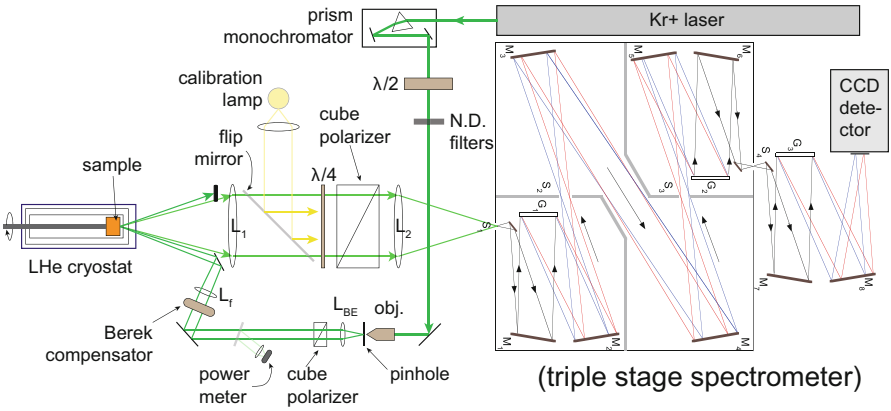

Fig. 2.2 Illustration of the optical setup for Raman spectroscopy at Rutgers. Note that the dimensions are not drawn in scale

power neutral density filters are placed in the optical path to reduce laser power if needed. A complimentary "micro-Raman" setup sharing the optical table, laser source, and spectrometer is not related to this monograph and thus is not shown here.

As we explained in the previous section, the ion lasers typically contain a large amount of plasma lines in the visible range and need to be filtered out as early as possible. In our lab, we place a tunable prism type monochromator immediately behind the laser and then pass the dispersed light through a 5 μm diameter pinhole about 1.5 m behind the monochromator. An objective (obj. in Fig. 2.2) and a thin lens (L_{BE}) are placed across the pinhole as a beam expander, which magnifies the 1.5 mm diameter beam output from the laser to about 10 mm, such that we can conveniently focus into a smaller spot (about 50 μm) on the sample. The pinhole size is chosen to match the diffraction limit of the objective, $D = \frac{4\lambda f}{\pi d}$, where λ is the laser wavelength, $f = 11$ mm is the objective focal length, and $d \approx 1.5$ mm is the laser beam diameter. This combined setup also serves as a "spatial filter" that significantly suppresses the unwanted plasma lines in the laser and also produces a better Gaussian beam profile that propagates along the optical path.

A focusing lens, L_f, is used to focus the beam onto sample. Depending on different operations, this can be an aspheric lens that results in a spherical spot of about 50 μm spot diameter on the sample, or a cylindrical lens that results in a significantly elongated spot, or even a Mitutoyo long working distance objective that produces smaller spots. For most practical usage, it is sufficient to tilt an aspheric lens slightly (about 20°) to produce an elongated elliptical spot with larger area, thus reducing the power density (laser heating) on the sample.

To avoid the elastic reflection from being collected, we employ the "quasi-backscattering" geometry as shown in Fig. 2.2, where the reflected beam is outside the collection cone and blocked. The incident light is at a small angle (about 17°) with respect to the sample surface normal. In all materials studied in this work, the refractive indices are high enough such that the light propagation vector inside the crystals is always less than 10°, which is negligible for all practical concerns.

The secondary emission from the sample is collected by an achromatic lens with $f/2$. After passing the polarization optics ("analyzers"), the light is focused onto the spectrometer's entrance slit by another achromatic lens. A large 50 mm diameter flip mirror is placed in front of the cube polarizer to allow fast switching to calibration lamps as source. The details of the polarization optics, spectrometers, and calibration lamps will be discussed in the following sections.

Polarization Optics

The polarization of laser output is determined by the Brewster windows of the plasma tube, which in our setup is always vertically polarized (out-of-plane direction in Fig. 2.2). Thus a broadband $\lambda/2$ waveplate is placed behind the monochromator to rotate the laser polarization into the direction suitable for the experiment. By design, λ/2 waveplate has the property of rotating the linear polar-

ization of light by 2θ relative to the input polarization, in the plane perpendicular to the optical path, where θ is the angle between input polarization and the waveplate's "slow axis." A broadband Brewster type polarization cube is placed behind L_{BE} to ensure that the degree of linear polarization on the sample is as close to 100% as possible.

Notice that a Berek compensator is basically an adjustable retardation waveplate, and therefore it can also operate in the $\lambda/2$ mode. In this case, the $\lambda/2$ waveplate is unnecessary and can be replaced by the Berek compensator drawn in Fig. 2.2. However, the degree of polarization in a Berek compensator critically depends on its proper alignment and therefore is quite time consuming and troublesome. In most cases, we only use the Berek compensator to produce circularly polarized light. When put into $\lambda/4$ mode with $\theta = 45°$, the Berek compensator transforms linearly polarized light into circular polarization. The advantage of using a Berek compensator over broadband $\lambda/4$ waveplate is its flexibility in wavelength (200–1600 nm) and polarization of incident light. A Berek compensator can be adjusted to produce almost perfect circularly polarized light for a wide range of wavelength, whereas any broadband waveplate suffers finite deviation from $\lambda/4$ retardation, except within some small wavelength window. But because of this flexibility, one has to be careful when aligning the Berek compensator to avoid introducing ellipticity in the output light. This is done by adjusting 4 degrees of freedom (assuming the light beam passes through the center of Berek compensator): 1 rotating axis around optical path ("orientation"), the 2 tilting axis orthogonal to the optical axis, and the retardation of the compensator.

The typical procedures for Berek alignment are the following: First, one has to properly align the compensator to be normal to the optical path by adjusting the 2 tilting degrees of freedom. This is done by looking at the back reflection from the compensator surface when retardation is set to 0. When properly aligned, the reflection should coincide with input beam. One can try to rotate the compensator ("orientation"), and the back reflection spot should not move with changing orientation. Next, one needs to align the slow axis of the Berek compensator with respect to the linear polarization of the incident light, which is determined by the cube polarizer behind L_{BE}. Luckily, the slow axis is usually marked on the compensator mount when bought. As long as the orientation of the cube polarizer is known, it is trivial to orient Berek's slow axis at 45° to the incident light. Usually, one can buy a factory pre-aligned polarizer with markings on the mount and then use it as a reference to align all other linear polarizers in the lab. In typical Raman spectroscopy labs, *all* linear polarizers' orientation is aligned with respect to the gratings' ruling direction, which is typically normal to the plane of incidence, thus normal to the optics table. After the Berek orientation is set to 45°, one rotates the retardation to $\lambda/4$, which is documented for commonly used wavelengths in a pre-calculated table (provided by the company from which the compensator is bought from).

Due to many unavoidable errors in all the previous operations, it is important to check and fine-tune the retardation at this point. This is done by putting a reflective mirror, e.g., Ag coated, behind the Berek compensator and looking at

the back reflection on a "half screen." This screen should be placed between LBE and the cube polarizer and should be positioned such that it blocks exactly half of the incident beam. Needless to say, the reflective mirror has to be tilted in a way such that the back reflected beam has a tiny overlap on the "half screen." If the output beam after Berek is perfect circularly polarized, the mirror reflected beam through the Berek will be a linearly polarized light with polarization orthogonal to the cube polarizer (combined action of reversed helicity by mirror reflection, and the opposite retardation by passing through Berek in the opposite direction) and thus should produce zero intensity on the "half screen."

In the light collection path (lighter green in Fig. 2.2), a broadband ("zero order") $\lambda/4$ waveplate, marked by $\lambda/4$ in Fig. 2.2, is used instead of a compensator because the Raman signal often spans a wide wavelength range. This waveplate must have clear aperture comparable to the collection lens, L_1, which is 38 mm in our lab. Therefore, we use a 50 mm clear aperture mica-type $\lambda/4$ waveplate. The slightly larger diameter ensures that all scattered lights collected by L_1 pass through the waveplate, so that the intensity can be consistently compared between experiments. Sheet mica has the spectacular property of relatively flat retardation profile within the visible spectrum with high transmission and can be made into large diameter. Another popular choice is polymer waveplate, which has lower transmission but can be made into very large size with much lower prices.

The cube polarizer behind the $\lambda/4$ waveplate is often referred to as the "analyzer," with the clear aperture of 50 mm. The cube polarization is oriented in the direction that optimizes the grating throughput in the spectral regime of interest.

Spectrometer

In our lab, we use a custom designed Czerny–Turner triple stage spectrometer by Acton Research Corporation, to collect and disperse the secondary emission from the sample. All of the gratings and slit positions in the spectrometer are motorized and computer controlled. The basic structure and optical paths inside the spectrometer are illustrated in Fig. 2.2 [3], where the black lines denote the optical path of undispersed "white light," the red and blue lines denote the paths of light with longer and shorter wavelength, respectively.

In this design, the dispersion of incident light is entirely achieved by reflective planar gratings, which is basically a more advanced version of double slit interference (in the first order): $\sin\alpha + \sin\beta = \lambda/d$, with α and β being the incident and diffracted light angles (from grating surface normal, thus having opposite signs) for a particular light wavelength λ, and d is the averaged distance between grating grooves [Fig. 2.3]. With elementary trigonometry, we see that the above "grating equation" (diffraction equation for first order) can also be written as

$$2d \sin\left(\frac{\alpha+\beta}{2}\right)\cos\left(\frac{\alpha-\beta}{2}\right) = \lambda. \tag{2.1}$$

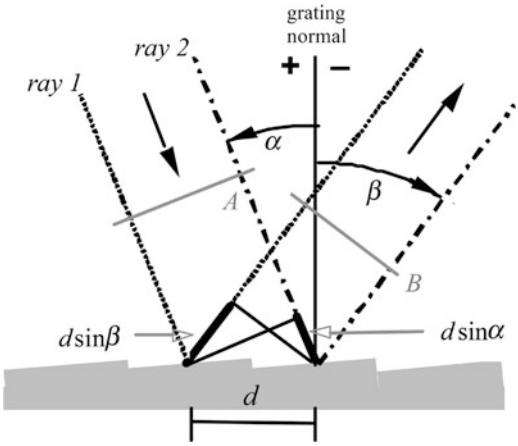

Fig. 2.3 Illustration of the light path for a particular wavelength, λ, by a diffractive planar grating, where the incident light is a parallel beam, and grating grooves are separated by d. Figure adapted from Ref. [4]

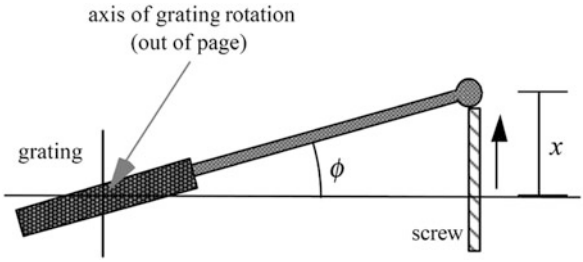

Fig. 2.4 Illustration of the mechanism of a sine bar grating mount. As the screw is extended linearly by the distance x, the grating rotates through an angle ϕ in such a way that $\sin\phi$ is proportional to x. Figure adapted from Ref. [4]

In most designs of spectrometers, the mirrors are fixed, meaning that the angle between incident and diffracted light is a constant, $\alpha - \beta = 2K$. Therefore, it is more convenient to project different parts of the spectrum onto detector by rotating grating about the central axis, i.e., scanning $\alpha + \beta = 2\phi$. The wavelength λ fulfilling Eq. (2.1) is then proportional to $\sin\phi$, which is again proportional to the linear displacement of a device called the "sine bar," shown in Fig. 2.4. Thus by rotating the lead screw connected to the sine bar, we *mechanically* project different parts of the spectrum onto CCD detector.

The angular dispersion of light, which ultimately determines the spectral resolution of the spectrometer, is a function of λ, α, and β. For incident white light at a particular angle α, the first order diffracted light within wavelength regime $\delta\lambda$ is dispersed into a small cone given by $\delta\beta$:

$$\frac{\delta\beta}{\delta\lambda} = \frac{1}{d\cos\beta}. \tag{2.2}$$

For small $\delta\beta$, the linear span of light projected on CCD, $\delta x = f\tan(\delta\beta) \approx f\delta\beta$, with f being the focal length of the spectrometer. Thus the linearly dispersion of light on the CCD, which is one of the most important factors for determining the spectral resolution, is

$$\frac{\delta x}{\delta \lambda} = \frac{f}{d \cos \beta}. \tag{2.3}$$

Thus, a spectrometer's spectral resolution is inversely proportional to the grating grooves distance or proportional to the grooves density. In our lab, we have gratings with three different groove densities: 150, 600, and 1800 grooves/mm. Another way of improving angular dispersion is by having larger β, which corresponds to longer wavelength [Eq. (2.1)].

Another important factor for determining the spectral resolution is the spectrometer's slit size. The entrance slit of the spectrometer, S1, is composed of a pair of horizontal and vertical precision slits. The image on S1 can be thought of a projection of the sample image (confocal image). Thus by controlling the opening of S1, we limit the area on the sample from which we collect the signal. The laser spot should be positioned in the middle of the slits to avoid aberrations and to maximize the signal. The width of the horizontal slit in S1 should match the exit slit, S4, which is also the confocal plane of S1 and the entrance slit of the last stage of spectrometer, and will ultimately determine the spectral resolution. In the design of our spectrometer, the width of the horizontal slits of S1 and S4 should match the pixel size of the CCD detector. In practical operations, we often bin the CCD pixels into superpixels to increase the signal intensity, with the compromise of decreasing spectral resolution. The width of S1 and S4 should be adjusted accordingly to maximize the efficiency.

One of the novel designs of this spectrometer is equipping a removable camera behind S1 (not shown in Fig. 2.2). A computer controlled flat mirror can be translated into the optical path behind S1, which sends the light into a high sensitivity color camera. Thus we can simultaneously see the images of the entrance slits and sample, which ensures the alignment of laser spot as well as collecting data from the sample area of interest.

The first two stages of the spectrometer form a coupled double spectrometer (ARC AM-505F) that usually operates in the "subtractive mode." In this operation, the double spectrometer acts as a spectral block filter of the input light, which is dispersed in the first stage by grating G1 and then recombined by inversely positioned identical grating G2 back into white light. The dispersion of the collected spectra is entirely achieved by the last stage (ARC AM-506), which can be viewed as a separate monochromator with a focal length of 660 mm, and the aperture ratio (defined as the focal length divided by the grating length) is $f/4.7$. The spectral resolution with 1800 g/mm gratings at 532 nm is about $0.9\,\mathrm{cm}^{-1}$. In "additive mode," G1 and G2 are positioned in the same direction, and thus about 3 times better resolution can be achieved.

The advantage of operating in the subtractive mode is for better rejection of elastic line and stray light. Since Raman spectroscopy is only concerned with inelastically scattered light, the typically 8 orders of magnitude stronger elastically scattered laser line needs to be blocked before projecting the spectrum onto CCD camera. Otherwise, not only the CCD could suffer permanent damage, but also all spectral features would be overwhelmed by the "overflow" of the strong elastic line.

There are several ways of blocking the elastically scattered light [5], but triple stage spectrometer has the advantage of the highest resolution (cutoff wavelength being closest to the laser line) and best flexibility and therefore remains the most popular choice among Raman spectroscopist.

The basic working principle of the subtractive stages is that in the first stage, mirrors M1 and M2 focus the dispersed light on a horizontal precision slit, S2. The opening of S2 determines the cutoff wavelength of the spectral range allowed to pass, thus acting as a block filter. Mirrors M3 and M4 form the so-called relay stage, which focus the light onto another precision slit, S3, that is identical to S2. This additional slit allows significantly improved elastic line and stray light rejection. The efficiency of S2 and S3 mainly depends on the resolving power of the first two stages of spectrometer and the focusing power of the mirrors. Therefore, all of the mirrors in the spectrometer are off-axis parabolic mirrors to minimize the spherical aberrations.

The resolving power of a spectrometer is mainly determined by the grating grooves density, focus length, and effective grating area. In our lab, we have three sets of gratings: 150, 600, and 1800 g/mm. In order to optimize the dispersed light intensity, all of the gratings are "blazed," i.e., a specially designed groove profiles to maximize the intensity in the first order diffraction.

Detector

The invention and popularization of charge-coupled device (CCD) detectors are probably the single most important breakthrough for Raman spectroscopy in the past 30 years. The photon to electron conversion (quantum efficiency) is close to 100% in the visible range for the most advanced commercially available CCD detectors. The pixel size is as small as 20 μm while still possessing 200,000 electrons "well depth" (dynamical range), thus allowing both high resolution and high sensitivity.

We have several CCD cameras in our lab for different purposes. The most commonly used one is a back-illuminated silicon-based CCD from Princeton Instrument with 400 vertical pixels and 1340 horizontal pixels. Since a grating spectrometer does not use the vertical degrees of freedom, we always bin the illuminated vertical pixels (typically about 150) into a superpixel. If the signal is very small, we can further bin the horizontal pixels to increase the signal to noise ratio (S/N) at the cost of lowering the spectral resolution.

At liquid nitrogen temperature, the dark current of our CCD is about 0.3 electrons/px/hr, and the readout noise is about 3 electrons. To reduce the noise and maximize S/N, the CCD temperature is locked at −120 °C, and we usually use long exposure times (300 s) to minimize the number of readouts.

Cryostat

Many of the interesting physics and emergent behaviors, e.g., charge/spin/orbital density waves, composite quasiparticles and superconductivity, regretfully only happen at very low temperatures (typically below 50 K). The working principle of most of the cryostats is similar to a Dewar, where one or more "vacuum jackets" separate the sample space from the room temperature atmosphere [6]. The thermal insulation is mainly provided by the vacuum space and thermal radiation shielding. The shielding is connected to a heat reservoir below 100 K, such as a liquid nitrogen jacket, which reduces the thermal radiation on the sample by about 100 times due to Stefan–Boltzmann law. In our design, we utilize the back-flow of cold helium gas to cool down the shielding without additional coolant and thus also able to reach lower temperatures than using liquid nitrogen. In the sample space, the sample under inspection is thermally connected to a cooling source, thermometer and heating coil. These three components together provide a feedback loop for thermal stability at low temperatures.

Depending on the purposes and working temperatures of the cryostat, vastly different designs can be found on the market. In our lab, we use mainly a custom designed continuous flow liquid "helium bath cryostat" made by Oxford Instruments. This cryostat is connected to a small liquid reservoir through a needle valve, which is again connected to external liquid helium Dewars. Therefore, in principle, a temperature of 1.2 K can be reached by pumping on the sample space. In reality, mainly due to radiation heating, the base temperature is about 1.8 K. The main advantage of the bath cryostat is the large temperature adjustability and cooling efficiency. By adjusting the needle valve opening and helium supply rate into the reservoir, temperature between 2 and 300 K can be very easily stabilized with little help of heater. Also, since the sample is in direct contact with the cold helium gas, the cooling is particularly efficient on the sample surface, therefore ideal for Raman spectroscopy where the laser heating is focused on a small region on the sample surface. Since the heat is mainly conducted through the helium gas, the degree of laser heating on the sample is not sensitive to sample thermal conductivity. This is particularly important, because many of the physical phenomena we are interested in are second order phase transitions, across which the thermal conductivity experiences large change.

For most metallic samples, in optical regimes where most of the light is reflected, 1 mW of laser light typically results in about 0.5 K of heating in our cryostat at low temperatures (below 20 K).

2.2 Data Acquisition and Analysis

The double spectrometer and the cryostat temperature are controlled by two LabView programs, where the detailed spectrometer settings, response ratios, backgrounds, temperatures, and laser powers are automatically recorded for each

experiment. The third stage monochromator is coupled to the CCD camera, and both controlled by Winspec (commercial program by Princeton Instruments), which records raw counts in each frame, spectral calibrations, grating positions, exposure times, etc. With all the information, we can convert the recorded counts per CCD pixel into Raman response function, after accounting for several calibrations and corrections listed below.

2.2.1 Instrumental Calibrations

The reliability of the data produced by a Raman spectroscopy lab depends a lot on how the system is being calibrated. In our lab at Rutgers, we calibrate our system in the following ways.

The temperature fluctuations of the room and cooling water may introduce drifting of laser power during experiments, which has to be accounted for before further data analysis. A thin quartz plate is placed behind the cube polarizer in the excitation light path (darker green in Fig. 2.2) to reflect about 5% of light intensity into a power meter. This reading is constantly recorded during the experiments, and all spectra are automatically normalized to the laser power to avoid drifting over long hours of experiments.

The grating positions of the spectrometer are controlled by step motors coupled with mechanical arms ("sine bars") [Fig. 2.4] [4], which needs to be related to the wavelength of light imaged by the CCD. This is done by using "spectral lamps" that produce narrow, intense lines of UV to NIR wavelengths due to the excitation of various gases, commonly Hg, Ar, and Ne. Since the emission lines of these gases are well documented by the National Institute of Standards and Technology (NIST), we can readily relate the wavelength of these lines to the grating positions and CCD pixels using the so-called spectrometer equations. This calibration procedure is done semi-automatically across the entire UV-NIR spectrum by the computer software provided by Princeton Instrument (Winspec manual, Appendix C), which controls the CCD detector and AM-506 monochromator. Such global calibration usually has larger error bars, which can be locally calibrated in the spectral window of interest, again by spectral lamps. The ultimate spectral resolution is limited by the spectrometer's mechanics and CCD's pixel size, which is better than 0.02 nm at 435 nm wavelength (for 1800 grooves/mm gratings).

The polarization cube, lens, spectrometer, and detector's throughput all have non-linear wavelength and polarization dependences, which, if not accounted correctly, could lead to spurious excitation and polarization profile. This can be calibrated by measuring the flux through all of the above optics from a known white light source (standard candle). Since the flux from the lamp is known, by measuring the recorded intensity on the CCD, we can derive the combined throughput ratio of linearly polarized light at each wavelength, which we call a spectrometer's "response ratio." In our lab at Rutgers, we use a NIST certified spectral lamp to calibrate the combined throughput of the polarization cube, L_2 lens, spectrometer,

and CCD, for all individual gratings, grating positions, and cube orientations. A metallic flip mirror is placed in front of the cube polarizer [Fig. 2.2], which easily switches between the collimated light from the sample and from the spectral lamp.

Even when all lights and lasers are turned off, a small amount of background room light (usually from instrument and computer LED indicators) and CCD dark current can still contribute to the spectra. These contributions (about 0.3 counts/pixel/hour, or 3 counts/superpixel/min under 150×4 binning) are much smaller than the typical signal from most samples and are usually ignored. However, sometimes this is not entirely negligible compared to the sample signal and has to be carefully measured and subtracted from the signal before further analysis.

2.2.2 Cosmic Ray Rejection

In order to minimize readout noise in samples with weak signal, we have to take a long exposure time as possible. However, the earth surface is constantly under the bombardment of highly energized muons, typically created by the decay of pions in the upper atmosphere. These are very penetrating particles, thus very difficult to block by shielding. They deposit energy in the CCD detector via the Coulomb interaction as they traverse through the silicon sensor, which produce a usually large spike in the spectra [7]. After about 10–20 min, the spectra would be dominated by cosmic spikes, covering a large portion of the CCD detector. Once a pixel is covered by a cosmic spike, the information within that pixel is lost. Therefore, it is better to split the exposure time into several shorter consecutive "frames" and remove the spikes in each frame and then average the frames. Thus the number of spikes is still the same, but the amount of usable pixels is much more.

In practice, we take no longer than 5 min per frame, which typically contains less than 5 spikes in the spectra. There are many different strategies in removing the cosmic spikes, from simpler spacial or temporal filters to much more complicated wavelet transformation algorithms [8]. In our lab, we choose to use a temporal filter, requiring us to always take at least 3 consecutive frames per experiment. The removal of spikes is done automatically by a C++ code developed by Adrian Gozar [3], where we compare the data in each pixel across the frames and simply remove the data in a particular pixel in a particular frame, if we find that pixel to have a much higher photon counts ($> 5\sqrt{N}$, where N is the median counts of that pixel across the frames) than the same pixel in the other frames. In the end, we only average the data in the remaining pixels.

2.2.3 Optical Corrections

The signal recorded at the detector is in the unit of counts/second/pixel. This has to be converted into differential cross section and corrected for the optical constants

of the sample, before quantitative analysis of the data can be done. The detailed conversion between measurement and theory was first done by Loudon in 1965 [9], although discussions of optical corrections have already begun as early as 1951 [10]. Here, we follow the simplified semi-quantitative approach as given in Ref.[11, 12], where we convert the measured photon counts into the dimensionless "scattering efficiency" per unit solid angle per unit energy (in units of cm^{-1}), $\frac{d^2S}{d\Omega d\omega}$, which is a dimensionless quantity.

Due to the construction and calibration of grating spectrometers, we first convert the measured data (after subtracting CCD dark current and environmental background) into the cross section per unit wavelength, $\frac{d^2S'}{d\Omega' d\lambda}$, by normalizing the CCD count rate to laser power and response ratio. Here $d\Omega'$ is the solid angle defined by the collection lens L_1. This can be easily converted into per unit energy by noting that $\frac{d}{d(-\omega')} \sim \lambda^2 \frac{d}{d\lambda}$. Since we are usually interested in the Stokes process, we usually write $\omega = -\omega'$.

However, this quantity depends on the details of optical properties of the sample. Most importantly, due to refraction at the sample/vacuum interface, the solid angle inside the crystal, $d\Omega$, could be very different than the collection solid angle fixed by the lens, $d\Omega'$. In fact, one can easily see that

$$\frac{\Omega'}{\Omega} = \frac{1 - \cos\theta'}{1 - \cos\theta}. \tag{2.4}$$

For small θ' as in most experimental setups (notice not the case in micro-Raman setups where the NA of the objective is easily larger than 0.5), $d\Omega'$ can be approximated as $n(\lambda)^2 d\Omega$ (assuming vacuum outside sample), where $n(\lambda)$ is the refractive index. This could be quite sizable in many materials, for example, $n(\lambda) \sim 4$ for germanium in the visible range.

In addition, only a portion of incident photon transmits across vacuum/sample interface and the same for the scattered photon. Therefore, the real scattering efficiency in the sample should be $\frac{1}{(1-R(\lambda_L))(1-R(\lambda))}$ times larger than we measured. Lastly, we should account for the scattering volume in different samples, which is roughly $V_{eff} \sim \frac{D^2}{\alpha(\lambda_L)+\alpha(\lambda)}$, where D^2 is the laser spot size, and α is the absorption coefficient which determines the penetration depth of light in the sample. More comprehensive corrections are given in Ref. [13].

Combining the above corrections, we can calculate the scattering efficiency in the sample:

$$\frac{d^2S}{d\Omega d\omega} \sim n^2(\lambda) \frac{d^2S'}{d\Omega' d\omega} \frac{\alpha(\lambda_L) + \alpha(\lambda)}{D^2(1 - R(\lambda_L))(1 - R(\lambda))}. \tag{2.5}$$

2.2.4 Data Analysis

The data analysis of this monograph is mainly done in Mathematica and then exported into OriginPro for plotting. Since the Raman signals in this study are mostly small, it is important to carefully address the issue of noise, signal to noise ratio (S/N), and statistical analysis. The signal noise in our spectra comes from several sources, with mainly the following ones.

Photon Shot Noise

This is due to the discrete nature of photons, where the probability of collecting N photons with a particular energy within a fixed time interval is described by the Poisson distribution [14]:

$$P_\mu(N) = e^{-\mu}\frac{\mu^N}{N!}, \tag{2.6}$$

where μ is just the average number of photon counts we would expect, $\overline{N}$, if we repeat the finite time interval experiment infinitely many times (or equivalently, in a single experiment with infinitely long collection time). In this limit, the standard deviation (SD) of a Poisson distribution can be shown to be proportional to $\sqrt{\mu}$ [14]. Therefore, using the principle of maximum likelihood, the SD of any finite time experiment that counted N photons is just simply $\sqrt{N}$, i.e., S/N$= N/\sqrt{N}$ is also proportional to $\sqrt{N}$. Since the photon events are assumed to occur randomly in time (white noise in time domain), in order to achieve higher S/N, the length of exposure time we need increases quadratically. For reasonably large signal $\mu \gtrsim 10$, the photon events approach a normal (Gaussian) distribution around its mean value, and thus the SD of two distributions becomes identical, i.e., $G_{X=\mu,\sigma=\sqrt{\mu}}(N)$. This approximation is basically fulfilled in all our experiments, and thus we usually consider the data to be following a Gaussian distribution. Sometimes, the signal is extremely low and the uncertainty is too large to make a claim, and then we will have to either increase the laser power (at the cost of laser heating) or increase the number of frames in each experiment.

Vibration and Focus Drift

Due to cosmic spikes issue, we prefer averaging signal from many consecutive frames than to take a single long exposure. This assumes that each frame was taken under the *exact* same conditions, i.e., the signal is perfectly homogeneous in time. This is obviously not possible due to realistic concerns, such as temperature fluctuations, laser power fluctuations, vibrations, etc. While the temperature and laser power are easier to monitor in real time and compensate through software,

the focus and position of the laser spot drifting due to sample vibration are much more difficult to avert. The common practice is to setup all of the equipments on an optical table with pneumatic damper legs. However, the minute vibrations from pumping lines, liquid helium transfer line, and room air flow are unavoidable and will eventually lead to noticeable laser defocus and spot drift after roughly an hour. Therefore, we usually prefer to split a single long experiment into several 30 min shorter experiments, such that we can promptly adjust the drifting issues. This will of course introduce additional human errors, and therefore care has to be taken to check that the averaged signals between each 30 min experiments are consistent with each other within SD.

CCD Detector Noise

A charge-coupled device (CCD) is a photodetector composed of an array of top-gate capacitors on a semiconductor (usually silicon), where each capacitor works as a quantum well (pixels) that stores electrons proportional to the light intensity being illuminated [15]. The photons are absorbed from the back of the detector (in back illumination configuration) and are converted into electrons through photogeneration of electron–hole pairs across the semiconductor band gap. The photogenerated electrons are captured and integrated in the quantum well during light exposure and to be "readout" at a later time. There are two main sources of noise in a CCD device: (1) the "dark current," which is due to thermal generated charge carriers in each pixel at finite temperature. Thus the noise arising from the dark current can be reduced by lowering the operation temperature of the CCD detector and minimizing the readout pixels by using only the parts illuminated by the scattered light. Typically, the dark current can be reduced bellow 1 electron/pixel-hour in commercially available liquid nitrogen cooled silicon-based CCDs; (2) the readout noise, which comes from the uncertainties in the electrical measurement of a very small charge current, such as the charge stored in each pixel. This noise is contributed by many elements and can be somewhat reduced by better electronic design, for example, on-chip pre-amplifiers and more efficient analogue–digital converters, but it is impossible to entirely remove. In well-designed CCDs, the readout noise is as homogeneous in time as possible and therefore can be reduced by averaging many frames or increasing exposure time; (3) electronic interferences, such as power line voltage fluctuations, radio frequency interference, electronic noise from other power line sharing instruments, etc. The CCD readout signal is DC and usually within the microvolt range, which can easily couple to many sources of electronic interferences, making it very challenging for a precise measurement. In our lab, the CCD camera power is fed through a separate UPS system with line filter and connected to an isolated ground line. All of the cables are shielded by braided metal strands and using twisted pairs whenever possible; and (4) spikes due to energetic charged particles generated by cosmic rays. While intense cosmic spikes are easy to remove by taking multiple frames in every experiment as we discussed in the previous section, weak spikes comparable to the signal can be confusing and

hard to distinguish. Luckily, this almost never happens and can be further reduced by using minimal area of CCD detector.

Statistical Analysis

From the above discussion, it is clear that noise and therefore uncertainty are unavoidable in the experiment. The Raman scattering efficiency is almost always very small, meaning that only a small fraction of incident photon is inelastically scattered. If the temperature regime of interest is relatively high, e.g., above 20 K, then we can increase the S/N by increasing laser power. Since we use continuous wave laser with a pretty large spot, laser damage of the sample is usually not a consideration for most of our studies. However, most of the phenomena we are interested in can only be observed below 20 K, and thus we are usually limited to a few milliwatts of laser power. Therefore, it is important to design the experimental apparatus to be as stable as possible, such that we can increase the S/N by averaging more experiments or increasing exposure times.

At the end of the day, we would like to know the uncertainty in our signal and the confidence level of our claims. The error of the intensity associated within $\delta\lambda$ or $\delta\omega$ can be easily found from statistical analysis of signal in repeated experiments or frames. In most practical cases, the probability function of measurement value can be considered as a Gaussian distribution, and thus the *best estimates* can be easily computed following text books [14].

For example, let the secondary emission intensity recorded by a certain CCD pixel (in unit of photon counts) to be ν. This is of course only a theoretical value that we do not know. But following the above discussion, if ν is a reasonably large number, then the probability function of the measurement at this pixel, n, will follow a Gaussian distribution centered at ν with SD of σ:

$$G_{\nu,\sigma}(n) = \frac{1}{\sigma\sqrt{2pi}} e^{\frac{-(n-\nu)^2}{2\sigma^2}}. \tag{2.7}$$

Regretfully, since we do not know ν, we do not know σ either. However, the properties of the Gaussian distribution help us to estimate and put constraints on the most probable values of ν and σ from N repeated measurements. Let the value of the i-th measurement be n_i, then the best estimates of ν and σ would be $\tilde{n} \pm \sigma_{\tilde{n}}$ and $\tilde{\sigma} \pm \sigma_{\tilde{\sigma}}$, respectively. From the properties of Gaussian distribution, we know that [14]

$$\tilde{n} = \frac{1}{N}\sum_{i=1}^{N} n_i \tag{2.8}$$

$$\tilde{\sigma} = \sqrt{\frac{1}{N-1}\sum_{i=1}^{N}(n_i - \tilde{n})^2} \tag{2.9}$$

$$\sigma_{\tilde{n}} = \tilde{\sigma}/\sqrt{N} \tag{2.10}$$

$$\sigma_{\tilde{\sigma}} = \tilde{\sigma}/\sqrt{2(N-1)}\,. \tag{2.11}$$

One has to be careful when plotting or interpreting the error bars of data points, which are usually the averages of many measurements. The error bars could reflect either $\tilde{\sigma}$ or $\sigma_{\tilde{n}}$, depending on the content of the plot. $\tilde{\sigma}$ reflects the standard deviation of the measurements, where one would expect the results of the next measurement would likely be, whereas $\sigma_{\tilde{n}}$ reflects the uncertainty in our estimate of $\tilde{n}$, which is important for determining the confidence interval of the spectra, and therefore the significance of any claims that follow from it.

References

1. C.V. Raman, A new radiation. Indian J. Phys. **2**, 387–398 (1928)
2. I.L. Fabelinskiĭ, Seventy years of Raman scattering. Physics-Uspekhi **41**(12), 1229 (1998)
3. A.M. Gozar, Inelastic Light Scattering in Low Dimensional Quantum Spin Systems. PhD thesis. University of Illinois at Urbana-Champaign, 2004
4. C. Palmer, E.G. Loewen, *Diffraction Grating Handbook* (Newport Corporation, New York, 2005)
5. W. Hayes, R. Loudon, *Scattering of Light by Crystals* (Courier Corporation, Chelmsford, 2012)
6. N.H. Balshaw, *Practical Cryogenics – An Introduction to Laboratory Cryogenics* (Oxford Instruments Superconductivity Limited, Abingdon, 2001)
7. M. Fisher-Levine, A. Nomerotski, Characterising CCDs with cosmic rays. J. Instr. **10**(08), C08006 (2015)
8. Y. Tian, K.S. Burch, Automatic spike removal algorithm for Raman spectra. Appl. Spectrosc. **70**(11), 1861–1871 (2016). eprint: http://dx.doi.org/10.1177/0003702816671065
9. R. Loudon, Theory of the resonance Raman effect in crystals. J. Phys. France **26**(11), 677–683 (1965). https://doi.org/10.1051/jphys:019650026011067700
10. L.A. Woodward, J.H.B. George, Refractive index correction in relative Raman intensity measurements. Nature **167**(4240), 193–193 (1951). https://doi.org/10.1038/167193a0
11. M. Cardona, Resonance phenomena, in *Light Scattering in Solids II*, ed. by M. Cardona, G. Güntherodt (Springer, Berlin, 1982), pp. 45–49
12. J. Menéndez, Characterization of bulk semiconductors using Raman spectroscopy, in *Raman Scattering in Materials Science*, ed. by W.H. Weber, R. Merlin. Springer Series in Materials Science (Springer, Berlin, 2000), pp. 55–103
13. W. Richter, C.R. Becker, A Raman and far-infrared investigation of phonons in the rhombohedral V_2–VI_3 compounds Bi_2Te_3, Bi_2Se_3, Sb_2Te_3 and $Bi_2(Te_{1-x}Se_x)_3$ ($0 < x < 1$), $(Bi_{1-y}Sb_y)_2Te_3$ ($0 < y < 1$). Phys. Status Solidi (B) **84**(2), 619–628 (1977). https://doi.org/10.1002/pssb.2220840226
14. J. Taylor, *Introduction to Error Analysis, the Study of Uncertainties in Physical Measurements*, 2nd edn. (University Science Books, Sausalito, 1997)
15. S.M. Sze, K.K. Ng, *Physics of Semiconductor Devices*, 3rd edn. (Wiley, Hoboken, 2006)

Chapter 3
Raman Scattering in URu_2Si_2

Abstract In this chapter, I will introduce our Raman scattering study of the "hidden order" (HO) and antiferromagnetic (AFM) phases in URu_2Si_2, a heavy fermion material of undiminished interest in the condensed matter community for over thirty years. I will first give a short overview on the heavy fermion physics and the exotic phases in this compound, where focus will be given on the experimental results [Sect. 3.1]. Then I will describe typical sample preparation and characterization procedures, which are particularly important for detecting the electronic phases in URu_2Si_2 [Sect. 3.2]. In Sect. 3.3, I will present our Raman spectroscopic results in the pristine and Fe substituted $URu_{2-x}Fe_xSi_2$ samples, which are fully consistent with a minimal model that explains the origin of the unusual A_{2g} susceptibility in URu_2Si_2 [Sect. 3.4]. We will also discuss the origin of the collective mode in the ordered phase at low temperature and the interrelation between the HO and AFM phases.

The work in this chapter is done in collaboration with E.D. Bauer (LANL), R.E. Baumbach (NHMFL and FSU), Kristjan Haule (Rutgers), M.B. Maple (UCSD), and J.A. Mydosh (Leiden U.). The results on the symmetry breaking in the HO phase of pristine URu_2Si_2 are published in Ref. [1]. The results on the interrelation between the HO and AFM phases in $URu_{2-x}Fe_xSi_2$ are published in Ref. [2].

3.1 Introduction

3.1.1 Kondo Effect and Heavy Fermion Systems

The heavy fermion metals have been a constant source of emergent behavior related to their unconventional superconductivity and novel magnetism for more than 30 years. At the heart of the heavy fermion physics lie strong electron correlations, leading to variety of emergent phenomena, e.g., heavy Fermi liquid [3], quantum critical transitions [4, 5], multipolar orderings [6], and unconventional supercon-

H.-H. Kung, *Collective Excitations in the Antisymmetric Channel of Raman Spectroscopy*, Springer Theses, https://doi.org/10.1007/978-3-030-89332-3_3

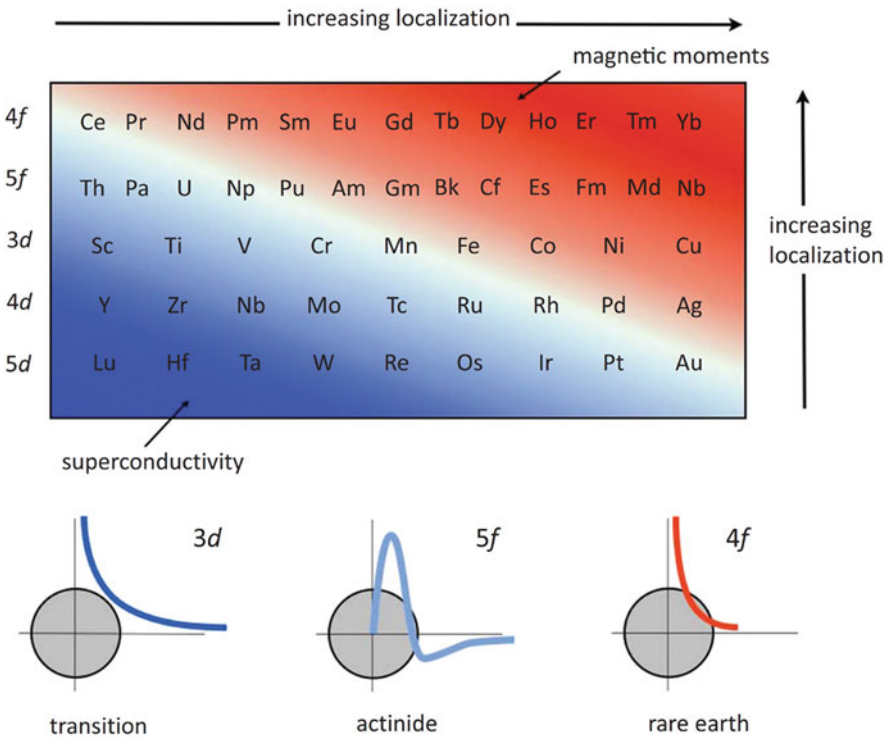

Fig. 3.1 The Kmetko–Smith diagram showing the degree of electron localization and itinerancy [9]. Figure adapted from Ref. [10]. The f-electrons are usually very localized, leading to magnetic ground states at low temperature, as opposed to d electrons which commonly form itinerant bands. However, along every row, there would be elements where the electrons behave dual character, leading to rich and unpredictable ground states at low temperature

ductivity [7, 8]. Figure 3.1 is a modified periodic table know as the Kmetko–Smith diagram, showing the degree of electron localization and itinerancy for d and f electrons. In general, f electrons are more localized than the d electrons due to the more positive nucleus. But higher principle quantum number also means more radial nodes in the electron wave function, thus increasing the orbital radius. The result is that the electrons in many elements (white region) possess a dual character of being partly localized and partly itinerant, leading to rich and unpredictable ground states at low temperature. Moreover, when strong interaction is introduced between the highly localized and partly filled f or d orbitals and the itinerant conduction bands from spd electrons, the result is a zoo of novel phenomena including the curious Kondo effect, non-Fermi liquid, unconventional superconductivity, and so on.

The Kondo Effect

Armed with the cryogenic techniques developed in Leiden University, experimentalists systematically studied temperature dependence of resistivity in metals. It was noted by W.J. de Haas in 1933 that good conductors, such as gold and copper, sometimes develop a strange resistivity minimum at very low temperature [11]. This phenomenon has been widely observed across many labs globally and is against the common belief that the resistivity of metal should decrease monotonically with decreasing temperature. One of the main complications to understanding the effect was due to various contradicting experimental reports on the role played by the impurities; namely, whether the impurity needs to be a particular element, or is it generic to any material possessing a certain (yet unknown) property? Physicists were clueless about this mysterious effect until Bernd Matthias and Myriam Sarachik at Bell Lab proved that the resistivity minima are associated with a trace amount of magnetic impurities in the metal [12–14]. More precisely, a nonmagnetic metal host mixed with trace amount of magnetic impurity would display the resistivity minimum if and only if the doped alloy is magnetic. The big question was when does local magnetic moment (1% Fe for example) in metallic alloy would induce global magnetism and when would not? How does a macroscopic electronic property such as the resistivity minimum has anything to do with the tiny local magnetic moments? Almost immediately, Philip W. Anderson also working in Bell Lab developed a model explaining the formation of local magnetic moments in metals [15], which is essential for solving this three decades-old problem.

Anderson's model elegantly combines the ideas of local Coulomb interaction and virtual bound states between free electron and local atomic orbitals. We use its simplest form, with one electron in the conduction band (*spd* orbital) and one electron from the f orbital as an example here:

$$H = \sum_{\sigma,k} \epsilon_k n_{\sigma,k} + \sum_{\sigma,k} (V_k c^\dagger_{\sigma,k} f_\sigma + V_k^* f^\dagger_\sigma c_{\sigma,k}) + \sum_\sigma \epsilon_f n_{f\sigma} + U n_{f\uparrow} n_{f\downarrow}. \quad (3.1)$$

The first three terms account for the virtual bound state with conduction electrons. Here, σ and k are, respectively, the spin and momenta quantum numbers, ϵ_k is the energy of a conduction band, and $n_{\sigma,k}$ is the conduction electron density. V_k is the hybridization matrix element between f orbitals and conduction band, $c^\dagger_{\sigma,k}$ and $f^\dagger_\sigma$ are creation operators for an electron in the conduction band and f orbital, respectively. The last two terms describe the local interaction in the atomic limit, where ϵ_f is the f orbital energy for single occupancy, $n_{f\sigma}$ is the density, and U is associated with on-site Coulomb energy for double occupancy. At the heart of Anderson's model is Coulomb's interaction of the f-orbitals, $U \sim \int_{r,r'} \rho_f(r)\rho_f(r')/|r - r'|$, where $\rho_f(r)$ is the electron density of the f-orbital at position r.

In the atomic limit, the energy cost of adding or removing one electron from the magnetic f^1 configuration is $\Delta E = U/2 \pm (\epsilon_f + U/2)$. That is, for larger and

positive $U > |U + 2\epsilon_f|$, the ground state would prefer the doubly degenerate and magnetic f^1 configuration. On the other extreme where we put $U = 0$, the "semi-core" f-electron can tunnel out to hybridize with the surrounding electron sea. The hybridization broadens the localized f-states to a finite width, $w(\epsilon) \sim \pi\rho(\epsilon)|V_k|^2$, where $\rho(\epsilon)$ is the density of states. Therefore, we see that the Coulomb interaction and hybridization are competing with each other for the ground state. Anderson concluded that, within the mean field limit, the critical Coulomb interaction is $U_c = \pi w_0$, where w_0 is the f-orbital broadening averaged over the conduction band width around the Fermi level [10]. For metallic hosts with higher density of states, w_0 is typically larger, and therefore the system will favor hybridization over a magnetic ground state. That is, the Fermi level will cross the very broadened and half-filled f-orbital, resulting in a nonmagnetic (because spin up and down are degenerate) and metallic phase. However, if one reduces w_0 such that $U > U_c$, then the relatively sharp spin up and down orbitals separated by U are split across the Fermi level. Therefore, local moments form and the metallic alloy becomes magnetic.

One of the most interesting results proving the Anderson model is the appearance of a third peak crossing the Fermi energy in the photoemission (particle removal) or the inverse photoemission (particle addition) spectra. This peak is also known as the "Kondo resonance," which arises purely due to interaction, and therefore the peak area is equal to the quasiparticle weight Z. The peak width is roughly the Kondo temperature T_K, which sets the crossover between local impurity behavior where the spin is free and the low temperature Kondo regime where the spin and conduction electrons are highly entangled. This peak intensity is set by the scattering phase shift at the E_F, which when combined with Friedel sum rule represents the number of f-electrons bound inside the resonance. The most remarkable feature here is that the Kondo resonance is guaranteed to peak around E_F with width about 1 meV, while the Coulomb interaction U giving rise to it is typically on the order of 10 eV.

The key consequence of Anderson's model is that the local magnetic moments would develop *antiferromagnetic* coupling with the conduction electron sea at low temperature when charge fluctuations are neglected, instead of the more intuitive ferromagnetic coupling. If we start from an isolated atomic limit where $V_k = 0$, then we are looking at local atomic physics where the dominating features are due to valence fluctuations. But as we turn on hybridization V_k while keeping U much larger than the conduction band width D, the f^2 configuration is integrated out by the so-called Hubbard operators, $X_{\sigma 0} = |f^1_\sigma\rangle\langle f^0|$ and $X_{\sigma\sigma'} = |f^1_\sigma\rangle\langle f^1_{\sigma'}|$, which does not allow double occupancy of the f-electrons. The Anderson model now reduces to the Hubbard model with infinite U:

$$H = \sum_{\sigma,k} \epsilon_k n_{\sigma,k} + \sum_{\sigma,k} (V_k c^\dagger_{\sigma,k} X_{0\sigma} + V_k^* X_{\sigma 0} c_{\sigma,k}) + \sum_\sigma \epsilon_f X_{\sigma\sigma'}. \tag{3.2}$$

This is equivalent to the high temperature regime where the local impurity is free to do a spin flip, with finite probability of hopping into the conduction sea.

However, if we keep lowering the temperature, the high energy degrees of freedom are continuously integrated out, leaving the f-electron set in the f^1

configuration and the local moment has only spin degrees of freedom. Then the local spin can only flip through virtual charge fluctuations, where the spin of the f-electron is exchanged with the spin of a conduction band electron. In this case, the energy of the singlet bound state between the f and conduction electron is lowered by $J \sim V_k^2[\frac{1}{\epsilon_f+U} - \frac{1}{\epsilon_f}]$. The low energy Hamiltonian is now reduced to the famous (single impurity) Kondo model:

$$H = \sum_{\sigma,k} \epsilon_k n_{\sigma,k} + \sum_{k,k'} J c^\dagger_{k\alpha} \hat{\sigma}_{\alpha\beta} c_{k',\beta} \cdot \hat{S}_f . \tag{3.3}$$

Here, $\hat{\sigma}_{\alpha\beta}$ measures the electron spin at the impurity site, and $\hat{S}_f = \frac{1}{2} f^\dagger_\alpha \hat{\sigma}_{\alpha\beta} f_\beta$ measures the spin of the f-electron.

Jun Kondo soon found out that when using Anderson's model to calculate the electron scattering in metals with dilute magnetic impurities, the scattering rate of conduction electrons has a logarithmic divergence at low temperature, leading to a resistivity minimum. The resistivity upturn eventually saturates when all local electrons form singlet virtual bound states with conduction electrons. Thus, the local magnetic moments are "Kondo screened" at low temperature. This is as if the magnetic moments of the local impurities "*dissolve*" into the conduction electron sea, leaving behind the spinless "Kondo singlets" or "Kondo holes" at local impurity sites [10].

Heavy Fermion

After finding the exact solutions to the Kondo Hamiltonian in the entire temperature range by Natan Andrei and Paul Weigman in 1980, the Kondo problem for dilute magnetic impurities in metals is completely solved. However, the physics is much more complicated when the magnetic atoms form a lattice that interacts strongly with the conduction electron sea, known as the Kondo lattice. The first well-studied Kondo lattice is probably the Kondo insulator SmB_6 in 1969 [16]. But the field did catch much interest until superconductivity was observed at about 0.5 K in $CeCu_2Si_2$ by Frank Steglich in 1979 [17], where superconductivity seems to emerge from a Fermi liquid like ground state with unusually heavy electron mass, i.e., heavy fermion liquid. I will only qualitatively describe the phenomenology in heavy fermion materials, where a comprehensive description of the heavy fermion physics can be found in monographs such as Ref. [18] and in some manybody physics textbooks such as Ref. [10].

The heavy fermion compounds often display a giant Sommerfeld coefficient ($\gamma = \lim_{T\to 0} C(T)/T \sim 450$–$1600\,\text{mJ/mol K}^2$, compared to roughly unity in normal metals) and a giant magnetic susceptibility at low temperatures ($\chi \sim 8$–50×10^{-3} emu/mol, compared to roughly 10^{-6} emu/mol in normal metals). The ratio of the two is proportional to the dimensionless quantity known as the Wilson ratio,

$$R_w = \frac{\pi^2 k_B^2 \chi}{g^2 \mu_B^2 J(J+1)\gamma} \sim \frac{218.7\chi}{\mu_{eff}\gamma},$$

which remains the same order of magnitude as unity across most heavy fermion metals. Notably, $R_w = 1$ is expected in a free electron gas model such as Fermi liquid but is typically larger than 1 due to electron correlations. Here, the extremely large effective mass and magnetic susceptibility all point to strong electron correlations, which eventually renormalize to quasiparticles that are closely described by the Fermi liquid theory. A trend was observed that with increasing Wilson ratio, the low temperature ground state seems to shift from superconductivity, to nonmagnetic metal, to long range ordered magnetism [19]. The observation suggests the competitive roles played by magnetism and superconductivity. Therefore, much focus has been put in understanding the magnetism in heavy fermion systems, which interestingly share several similarities; Most notably, they all possess a large antiferromagnetic susceptibility with a temperature dependence that qualitatively follows the Curie–Weiss law near the room temperature, $\chi \sim (T + \Theta)^{-1}$. The fit to Curie's law typically yields a relatively large effective moment around 2–5 μ_B at high temperatures, close to the free ion limit. Moreover, the separation between f-atoms is typically larger than 4 Å, above the "Hill limit" of about 3.25–3.50 Å, where the f-orbitals cease to overlap and long range ordered magnetism is predicted to prevail. This is quite surprising because the low temperature ground state of heavy fermions is not all long range ordered and sometimes not even magnetic. The origin of this contradiction is usually explained similar to the Kondo effect, where the local magnetic moment is dissolved into the conduction sea.

Within the Kondo model, the local magnetic moment at x_i induces Friedel oscillations in the nonlocal spin density, which again couples to a magnetic moment at x_j, thus giving rise to a long ranged conduction electron mediated magnetic interaction, known as the RKKY interaction. The typical energy scale for RKKY interaction in solid is $T_{RKKY} \sim J^2\rho$, where J is the effective single impurity Kondo coupling between local f orbital electrons and conduction band, and ρ is the conduction electron density of states. However, there is actually another energy scale in a Kondo lattice competing with T_{RKKY}, that is the Kondo energy, $T_K \sim D\exp[\frac{-1}{2J\rho}]$, where D is the conduction band width. If $J\rho$ is small, then RKKY interaction dominates the low temperature phase and typically favors an antiferromagnetic ground state [Fig. 3.2]. For large $J\rho$, however, Kondo interaction stabilizes a ground state where each magnetic atom resonantly scatters conduction electrons. Therefore, one can expect a quantum phase transition when $J\rho$ is at a critical value where RKKY and Kondo energy scales are comparable.

Due to Bloch's theorem, the *coherent* elastic scattering in the heavy fermion ground state should produce a renormalized quasiparticle band, with band width roughly equal to T_K. In a Kondo lattice, this new band can be understood as a hybridization of the local f states with the conduction band, as illustrated in Fig. 3.3 [21]. The hybridized bands have a narrow indirect gap, $\Delta_h \sim T_K$, and a larger direct gap $2v \sim \sqrt{DT_K}$. Due to the flatness of the bands near

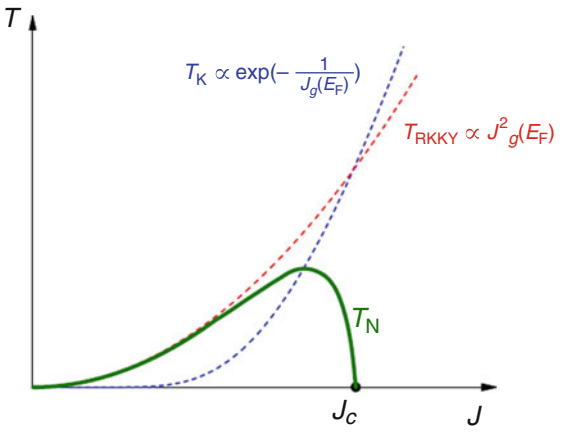

Fig. 3.2 The Doniach phase diagram illustrating the competition between the RKKY and Kondo energy scales in a Kondo lattice system [20]. With increasing J, the ground state typically shifts from an antiferromagnet to paramagnetic heavy Fermi liquid, resulting in a quantum critical point at $J = J_c$. Figure adapted from Ref. [20]

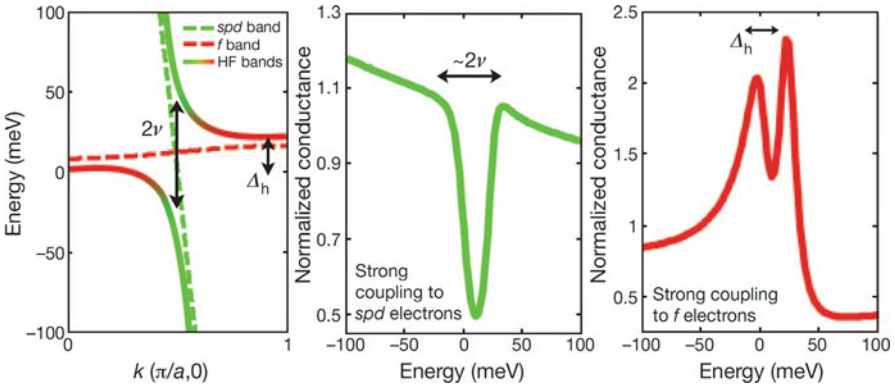

Fig. 3.3 Illustrations showing band dispersion and tunneling spectra of a Kondo lattice, adapted from Ref. [21]. (**a**) Schematic drawing of heavy quasiparticle dispersion showing the hybridization between local f states with the itinerant *spd* conduction band in a heavy fermion material below the coherence temperature, displaying direct (2ν) and indirect Δ_h hybridization gaps. (**b**, **c**) Computed tunneling spectra into the itinerant and localized electron bands. The interference between both tunneling channels (cotunneling) results in a Fano lineshape [24]. Figure adapted from Ref. [21]

Fermi surface, the Sommerfeld coefficient γ in heavy fermion systems is typically hundreds of times larger than in normal metals [3, 19], suggesting enhancement in the conduction electron effective mass and hence the name "heavy fermion." The drastic mass enhancement and direct band gap opening below the coherent temperature were confirmed by infrared spectroscopy measurements, where the mass enhancement $m^*/m \sim D/T_K$ was verified in many materials [3]. The low temperature resistivity possesses T^2 dependence as expected from Fermi liquid, and optical conductivity shows a renormalized Drude peak.

A remarkable feature predicted by the above picture is the Fermi surface volume expansion [22]. Without any hybridization, the Fermi surface is composed entirely of the conduction *spd*-electrons, which would enclose a volume not counting

the f-electrons. However, according to the Luttinger sum rule, the Fermi surface volume is determined by the number of valence electrons (including both local and conduction), independent of the interaction or local impurities involved. This is achieved through the Friedel sum rule, which claims that the number of valence electrons must be increased by the amount proportional to the interaction induced phase shift at the Fermi surface. Combining the two sum rules, one concludes that the hybridization must renormalize the *spd*-band in such a way that the Fermi surface encloses a larger volume consistent with both local and conduction electron counting. This is basically just another version of the Kondo resonance peak in the single impurity Kondo model. Here, the resonance peak at the Fermi energy originates from the flat part of the renormalized quasiparticle bands in Fig. 3.3, which results in the "double peak" structure in the density of states, as opposed to the single peak in the impurity model. Experimentally, it has been demonstrated by quantum oscillations that the Fermi surface in $CeRhIn_5$ expands to a larger volume after the antiferromagnetism is quenched by applying hydrostatic pressure [23]. The Kondo coupling constant J increases with pressure, such that the ground state shifts from antiferromagnetic to heavy fermion, and the Fermi surface volume also changes accordingly.

One of the main reasons for the interest in studying the heavy fermion metals is the very large discontinuity of specific heat, ΔC, across the superconducting transition temperature, T_c. In the standard BCS theory, $\Delta C = 1.43\gamma T_c \sim N(0)$, where $N(0)$ is the density of states at E_F. In many heavy fermion systems, such as the first example of heavy fermion superconductor, $CeCu_2Si_2$, $\Delta C \sim 500$ mJ/mol K, suggesting a huge value of density of states has been gapped out at the superconducting transition [17]. This is highly unusual, because in BCS theory we would expect $T_c \sim 1.13\omega_D \exp[-\frac{1}{VN(0)}]$. For heavy fermion superconductors, the Debye frequency ω_D and electron–phonon coupling potential V are comparable to many standard BCS superconductors. That is, the 3 orders of magnitude larger $N(0)$ implies that we should have a room temperature superconductor. However, the transition temperatures of heavy fermion superconductors are typically a disappointingly low number, regularly below 1 K. Therefore, it is highly desirable to understand the mechanisms for such "suppression" of T_c in these materials, in the hope that we might one day be able to drastically raise the transition temperature.

Although the thermodynamic and transport properties of many heavy fermion materials have been thoroughly studied in the 80s [19], and the electrodynamic response was more or less understood after the 90s from infrared spectroscopic studies [3]. Many details of the band hybridization and dynamical properties of the heavy electrons are still not fully understood even to date and remain an interesting and progressing field of study. Recent development of new experimental techniques, in particular the high resolution and dilution fridge temperature scanning tunneling spectroscopy (STS), has helped us understand the "composite" nature of the heavy fermions, which produces a characteristic Fano lineshape in the tunneling spectra [Fig. 3.3] [21, 25–27]. On the theoretical side, the development of dynamical mean field theory and relevant computational techniques has greatly helped our understanding and even predictive powers in the strongly correlated electron

systems [28–30]. Very recently, the topological properties in heavy electron systems rekindled physicists' interests in the field, leading to emergence of new concepts such as topological Kondo insulators [31].

URu_2Si_2

Among the many known exotic heavy fermion materials, URu_2Si_2 has been particularly interesting due to a mysterious nonmagnetic and non-structural phase transition at $T_{HO} = 17.5$K, also known as the hidden order (HO) transition [32]. URu_2Si_2 has body centered tetragonal structure characterized by the D_{4h} point group symmetry ($I4/mmm$ space group), as illustrated in Fig. 3.4. It can be seen from Fig. 3.1 that uranium sits at the border of locality and itinerancy in the Kmetko–Smith diagram, thus showing a dual character of localization and itinerancy. While it is commonly accepted that the uranium ions in URu_2Si_2 are in a mixed valence state between tetravalent $5f^2$ and trivalent $5f^3$ configurations [33], recent resonant X-ray emission spectroscopic studies strongly suggest a predominant $5f^2$ configuration [34]. This is also consistent with the results of DMFT+DFT calculation [35].

Notice, however, that the valence configuration does not directly imply the locality or itinerancy of the *5f* electrons at low temperature. As we have introduced in the previous section, the local f orbitals can be delocalized through Kondo hybridization, which conventionally assumes Krammers doublet ground state as in the $5f^3$ configuration. However, other less trivial versions of Kondo effect have also been proposed in materials with even number of electrons, such as two channel Kondo effects [37, 38]. URu_2Si_2 is believed to be one of these cases, where the most probable atomic configuration is two electrons from the $j = 5/2$ spin–orbit subshell, forming a multiplet of total angular momentum $J = 4$. This multiplet further splits into 5 singlet states $2A_{1g} \oplus A_{2g} \oplus B_{1g} \oplus B_{2g}$ and 2 doublet states $2E_g$

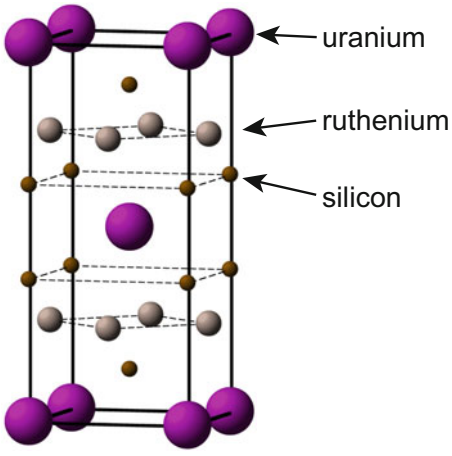

Fig. 3.4 Crystal structure of body centered tetragonal URu_2Si_2 in the paramagnetic state. Lattice constants are $a = 4.124$ Åand $c = 9.582$ Å at low temperature [36]

Table 3.1 The crystal field states of U-5*f* electrons with two electrons in the angular momentum $j = 5/2$ subshell, categorized by irreducible representation (IRR) of the D_{4h} group. These states have total angular moment $J = 4$ and magnetic quantum number M_j runs from $-4 \cdots 4$. The states on the right hand side are labeled by their M_j value, e.g., $|0\rangle \equiv |J = 4, M_j = 0\rangle$

IRR	state
A_{2g} (Γ_2)	$\|A2g\rangle = \frac{i}{\sqrt{2}}(\|4\rangle - \|-4\rangle)$
A_{1g} ($\Gamma_1^{(1)}$)	$\|A1g\rangle = \frac{\cos\theta}{\sqrt{2}}(\|4\rangle + \|-4\rangle) - \sin\theta\,\|0\rangle$
A_{1g} ($\Gamma_1^{(2)}$)	$\|\text{⊭}\rangle = \frac{\sin\theta}{\sqrt{2}}(\|4\rangle + \|-4\rangle) + \cos\theta\,\|0\rangle$
E_g ($\Gamma_{5,1}^{(1)}$)	$\|\text{⊭}\rangle = \cos\phi\,\|-3\rangle + \sin\phi\,\|1\rangle$
E_g ($\Gamma_{5,2}^{(1)}$)	$\|\not\text{⊭}\rangle = \cos\phi\,\|3\rangle + \sin\phi\,\|-1\rangle$
E_g ($\Gamma_{5,1}^{(2)}$)	$\|\not\text{⊲}\rangle = \sin\phi\,\|-3\rangle - \cos\phi\,\|1\rangle$
E_g ($\Gamma_{5,2}^{(2)}$)	$\|\text{⊲}\rangle = \sin\phi\,\|3\rangle - \cos\phi\,\|-1\rangle$
B_{1g} (Γ_3)	$\|\not\text{⊳}\rangle = \frac{1}{\sqrt{2}}(\|2\rangle + \|-2\rangle)$
B_{2g} (Γ_4)	$\|\not\text{↜}\rangle = \frac{i}{\sqrt{2}}(\|2\rangle - \|-2\rangle)$

under the tetragonal crystal electric field, as listed in Table 3.1. Note that fluctuations into other atomic configurations such as different valence or even into $j = 7/2$ subshell remain finite at all temperatures, which greatly increases the complexity and difficulty for a detailed theoretical description. Various versions of two channel Kondo effect have been proposed within this crystal field scheme [35, 39, 40].

3.1.2 *The Phase Diagrams of URu_2Si_2 and the Enigmatic "Hidden Order"*

Several reviews focused on the low temperature ordered phases in URu_2Si_2 have already been available [32, 41–50]. More general review of "122 type" uranium based heavy fermion systems is given in Ref. [51]. Ever since the first discovery of this material, many PhD students have either focused on this compound or included this as a major part of their thesis dissertation. The authors have particularly benefited from reading the dissertations of Collin Broholm [52], Jonathan Buhot [53], Lance Cooper [54], Elena Hassinger [55], and Maxwell Shapiro [56]. In the following, we will limit ourselves to the introduction of properties and experiments that we will later refer to in our Raman scattering study.

At room temperature, URu_2Si_2 is considered a bad metal, with conduction band (CB) electrons scattering off uranium ions incoherently as suggested by transport properties, which is quite conventional for a heavy fermion system [Fig. 3.5] [57, 58]. The resistivity shows a slight upturn upon cooling in the high temperature regime, followed by a drastic drop as the lattice coherence develops and the *5f* electrons hybridize with the conduction band, forming a heavy fermion band [36]. The magnetic susceptibility along *c*-axis follows Curie–Weiss law down to about 150 K, also showing a maximum around the same temperature as in resistivity at about 70 K, marking the coherence temperature T_{coh} [36].

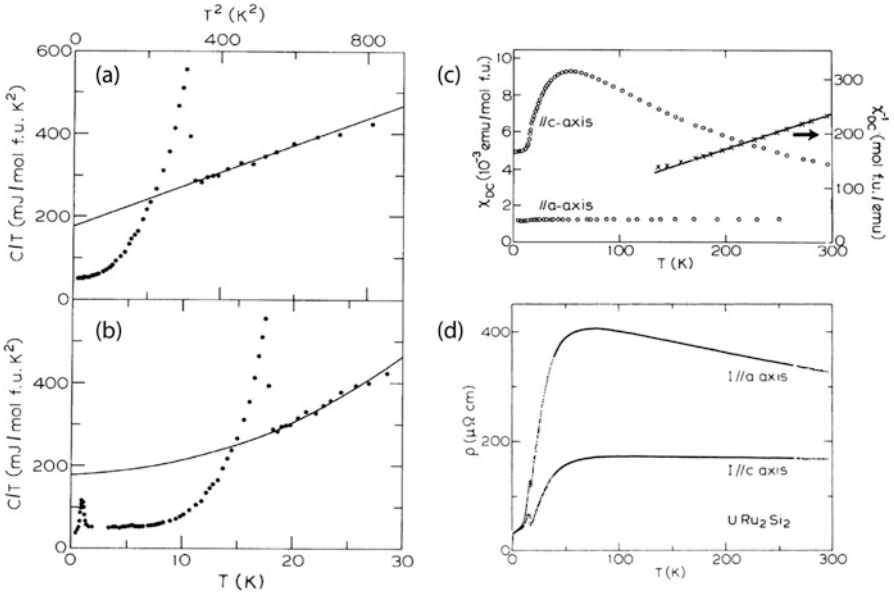

Fig. 3.5 (**a** and **b**) The specific heat data from Ref. [36] plotted as C/T vs. T^2. The λ-like anomaly at 17.5 K is characteristic of a second order phase transition. (**c**) Magnetic susceptibility from Ref. [36]. (**d**) Resistivity data from Ref. [57]

The Kondo hybridization and the formation of heavy bands are most clearly seen in the optical conductivity measurements [59–61]. Figure 3.6 shows temperature and frequency dependent optical conductivity data from Ref. [61]. Clear development of a narrow Drude peak below 5 meV is observed below T_{coh} (marked by the red arrows) in the a-axis, followed by a suppression between 10 and 50 meV due to the opening of hybridization gap.

Below a second order phase transition, URu_2Si_2 orders into two density wave-like phases involving long range ordering of the uranium-5f electrons when a critical parameter x is tuned [62], where x can be chemical substituent concentration [63, 64], pressure [65, 66], or magnetic field [67, 68]. We will denote the second order transition temperature to be $T_{DW}(x) \approx 18$ K. We note that the transition temperature for the special case of $x = 0$ is $T_{DW}(0) = T_{HO} = 17.5$ K.

At $x < x_c$, the system settles in the enigmatic "hidden order" (HO) phase [Fig. 3.5] [36, 69, 70], which transforms into an unconventional large moment antiferromagnetic (AFM) phase through a first order transition for $x > x_c$ [Fig. 3.7], in which uranium atoms carry a magnetic moment of about $0.4\,\mu_B/U$ [66, 71]. The moments are staggered along c-axis and are arranged ferromagnetically in-plane, as determined by neutron scattering [72, 73] and resonant elastic X-ray scattering (REXS) [74] [Fig. 3.8b].

It is deduced from C/T data that about 40% of the Fermi surface is gapped and the entropy change is about $0.2R \log 2$ per uranium, which is an order of magnitude

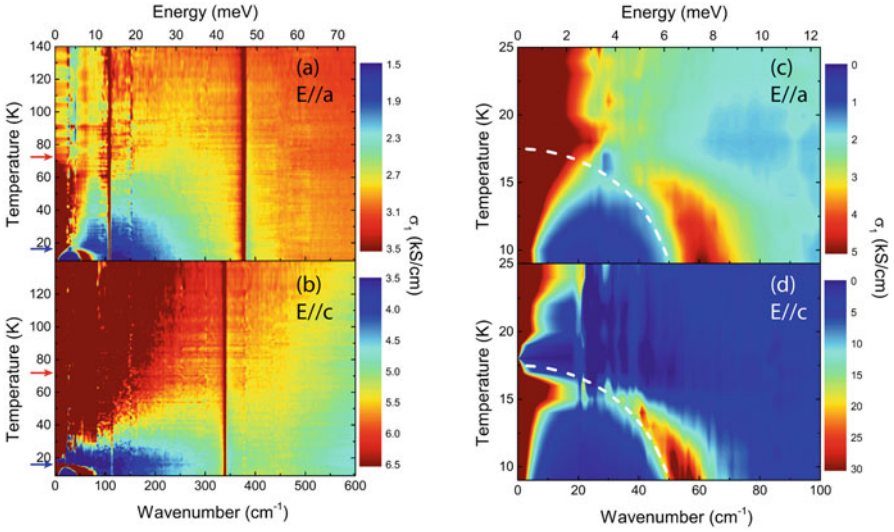

Fig. 3.6 (**a**) *a*-axis and (**b**) *c*-axis, optical conductivity data from Ref. [61]. The red and blue arrows indicate the coherence temperature T_{coh} and HO temperature T_{HO}, respectively. Enlarged low temperature optical conductivity along (**c**) *a*-axis and (**d**) *c*-axis. The white dashed line shows a BCS gap function with $T_c = 17.5$ K. Figure adapted from Ref. [61]

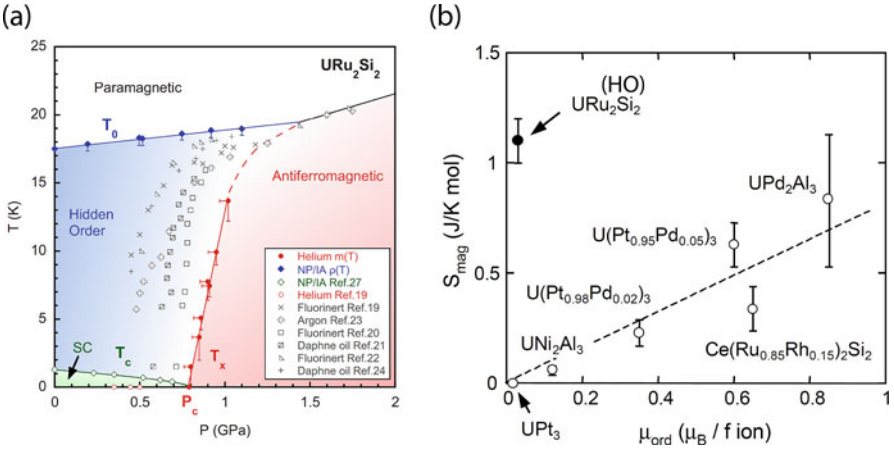

Fig. 3.7 (**a**) The pressure–temperature phase diagram for URu_2Si_2, adapted from Ref. [65]. The symbol "SC" stands for superconductivity, which is fully suppressed for $\geq P_c$ where antiferromagnetism appears. (**b**) Magnetic entropy S_{mag} versus ordered moment m_{ord} for several uranium compounds, figure adapted from Ref. [41]. The broken line is a guide to the eye

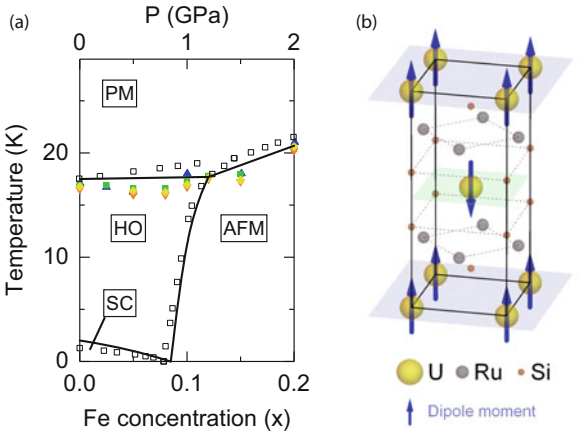

Fig. 3.8 The phase diagram of URu_2Si_2 system, where the black lines show the phase boundaries. (**a**) The measurements on the iron substituted $URu_{2-x}Fe_xSi_2$ crystals from neutron diffraction [80] (blue triangle), electrical resistivity [63] (green square), magnetic susceptibility [63] (purple triangle), and heat capacity [64] (yellow diamond) are overlaid with the neutron diffraction results for URu_2Si_2 under hydrostatic pressure [65] (open square) to show the similarity between the two tuning parameters. (**b**) The magnetic lattice structure in the ordered phases in URu_2Si_2, determined by neutron scattering [73] and resonant elastic X-ray scattering (REXS) [74]. In the HO phase, the local moment was determined to be less than $0.04\,\mu_B/U$ and in the pressurized AFM phase about $0.4\,\mu_B/U$. But the magnetic structure is determined to be the same as illustrated here

too large to be explained by the small magnetic moment of about $0.04\,\mu_B$ per uranium. Hall effect shows that carrier concentration decreased by about an order of magnitude across the transition, while in-plane resistivity increased less than 10% [75].

Below 1.5 K, a superconducting state, which likely breaks time reversal symmetry [76], emerges from the HO phase and is absent in AFM phase [Fig. 3.7] [65]. The HO and AFM phases are known to exhibit "adiabatic continuity" [77]; that is, both phases possess similar electronic properties [63, 78], and the Fermi surface practically shows no change across the phase boundary [77]. Furthermore, inelastic neutron scattering observed a dispersive collective excitation in the HO phase [66, 73] and recently in the AFM phase of pressurized URu_2Si_2 [79]. This raises the intriguing question of the symmetry relation between the two phases. However, experimental progress is hindered due to inherent constraints of low temperature pressurized experiments.

The availability of $URu_{2-x}Fe_xSi_2$ crystals [63, 64] made it possible to perform high resolution spectroscopic experiments at low temperature and ambient pressure in both the HO and AFM phases. With increasing iron concentration, the a-axis lattice constant decreases linearly while leaving the c-axis roughly unchanged [63]. Thus, iron substitution mimics the effect of applying small pressure or in-plane stress on the URu_2Si_2 lattice, and the iron (Fe) concentration, x, can be approximately treated as an effective "chemical pressure" [63]. Recently, the phase diagram

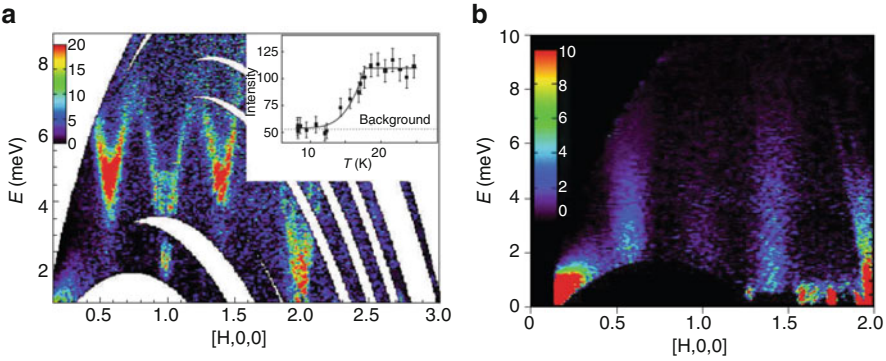

Fig. 3.9 Inelastic neutron scattering results at temperatures above and below the HO transition, from Ref. [84]. (**a**) The excitation spectrum in the HO phase (data measured at 1.5 K, just above the superconductivity) and (**b**) above the HO phase at 20 K. Notice the ungapped continuum of excitations at incommensurate wave vectors at 20 K

of $URu_{2-x}Fe_xSi_2$ single crystals has been determined [62, 64, 80–82], which resembles the low pressure phase diagram of pristine URu_2Si_2 [32, 65] [Fig. 3.8]. The inelastic neutron scattering measurements again illustrate the analogies of the AFM phase to the HO phase [82, 83], albeit differences remain relating to the existence of the resonance in the AFM state of pressurized [79, 83] or Fe substituted crystals [82].

In the paramagnetic phase above T_{HO}, inelastic neutron scattering (INS) detected a continuous spectrum at incommensurate wave vector $\mathbf{Q}_1 = (\pm 0.6, 0, 0)$ [84] [Fig. 3.9]. Below T_{HO}, this continuum is gapped at $\Delta_1 = 4\,\text{meV}$, and another excitation appears at commensurate wave vector $\mathbf{Q}_0 = (1, 0, 0)$ with energy gap $\Delta_0 = 2\,\text{meV}$ [72, 84, 85] [Fig. 3.9]. Application of hydrostatic pressure at low temperature showed that the commensurate mode is fully suppressed in AFM state, while the incommensurate mode hardens with increasing pressure [86]. Consistent results were obtained from Fe substituted crystals [82, 83].

Particular caution should be taken here with the conventions of the ordering vectors. Historically, the wave vectors of the *high temperature* BCT phase (the structure lattice) were given in the units of the *low temperature* ST phase (the density wave lattice) parameters, $a = 4.13\,\text{Å}$and $c = 9.58\,\text{Å}$. This was because of the observation of a small magnetic moment staggered along c-axis, with ordering vector $(0, 0, \frac{\pi}{c})\,\text{Å}^{-1}$, as shown in Fig. 3.8b. In the reciprocal lattice units of the ST phase, the ordering vector is written as $(0, 0, 1)$. However, the structural Brillouin zone (BCT) is twice the size of density wave Brillouin zone (ST), as clearly seen in Fig. 3.10. That is, the ordering vector $\mathbf{Q}_0 = (0, 0, 1)$ given in the ST reciprocal lattice units would have been $(0, 0, 1/2)$ if given in the structural lattice (BCT) units.

With the above clarification in mind, the "incommensurate" wave vector, $\mathbf{Q}_1$, is in fact a high symmetry point of the BCT Brillouin zone. In the reciprocal lattice units of the ST phase, $\mathbf{\Sigma}_{BCT} \equiv (\pm\frac{1}{2}[1 + \frac{a^2}{c^2}] \approx \pm 0.6, 0, 0)$, where a and c are lattice

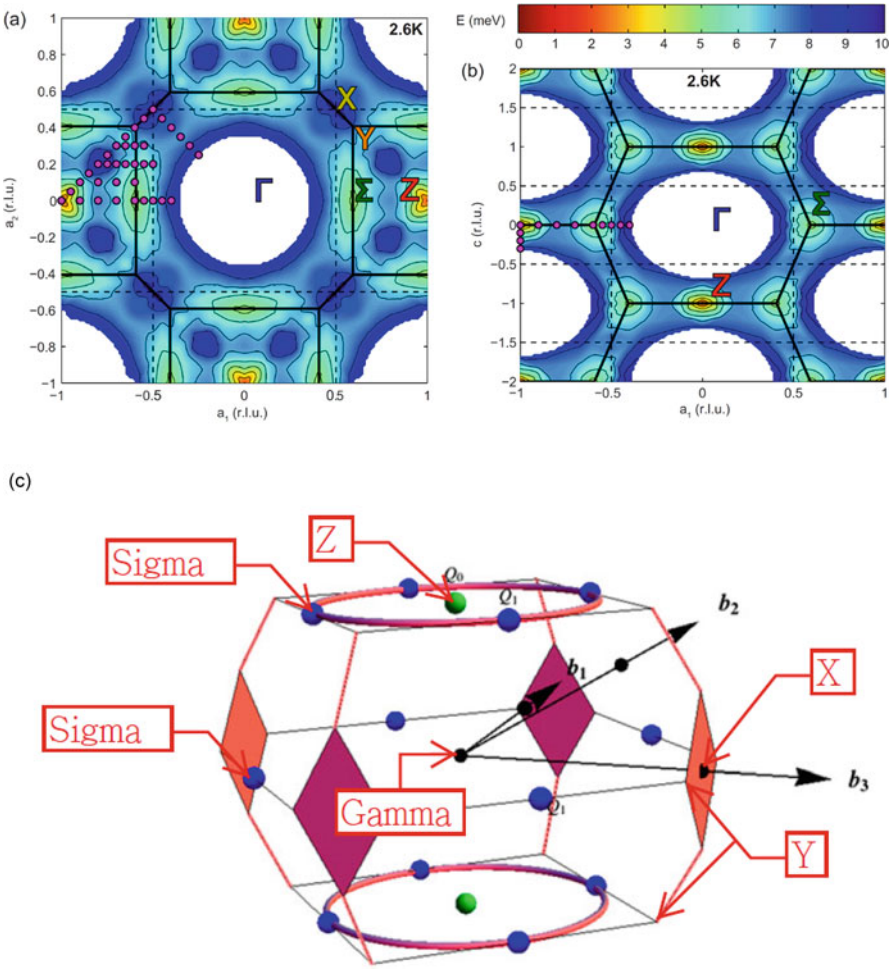

Fig. 3.10 Magnetic dispersion in HO phase (2.6 K) in (**a**) the *ab*-plane and (**b**) the *ac*-plane, measured by inelastic neutron scattering (INS) [87]. The heavy solid lines show the Brillouin zone boundaries of the high temperature paramagnetic body centered tetragonal (BCT) phase, where as the dotted lines show the low temperature simple tetragonal (ST) phase. The reciprocal lattice unit (r.l.u.) is given in the ST lattice parameters. (**c**) The BCT Brillouin zone, high symmetry points and where the commensurate (green balls) and incommensurate (blue balls) excitations were observed

parameters of the ST phase. As evident from Fig. 3.10, $(\pm 0.6, 0, 0)$ would also be equivalent to wave vectors such as $(\pm 0.4, 0, 1)$ in the second zone. Moreover, in the BCT Brillouin zone, the high symmetry point $\mathbf{Z} \equiv (0, 0, \pm 1)$ (given in the reciprocal lattice units of the ST phase as before) is equivalent to $(\pm 1, 0, 0)$ [Fig. 3.10].

Scanning tunneling microscopy (STM) reported Fano interference pattern in the differential conductance spectrum below 120 K and a 4–5 meV gap opening in the HO state [26, 27].

Optical conductivity in *a*-axis and *c*-axis both showed a density wave-like energy gap followed by a peak at about 65 cm^{-1} (8 meV), with BCS like temperature dependence [Fig. 3.6] [59–61, 88, 89].

Early Raman work reported quasielastic scattering in the antisymmetric A_{2g} channel, probing pseudovector like chiral excitations, which was attributed to spin fluctuations eventually condense to form the AFM phase [90]. As we explained in Chap. 1, the Raman response in this symmetry channel is usually negligible in materials without long range magnetic ordering. The fundamental reason is that the electronic polarizability tensors associated with most common excitations, such as phonons and plasmons, are symmetric with respect to reflections. However, it has previously been experimentally identified in nonmagnetic heavy element compounds due to crystal field excitations [91–93] and in some systems with exotic electronic ground states [94–96].

Several theories have been suggested to explain the HO phenomena [32], including the recently proposed hexadecapole order [35, 97], dynamical symmetry breaking [98, 99], E-type quadrupole order [100], rank-5 pseudo-spin density wave [101], under-screened Kondo effect [49, 102], rank-5 multipole order [103], modulated spin liquid [104], staggered spin–orbit order [105], and hastatic order [40, 106, 107]. Until now, there is still no consensus for the complete description of HO ground state [43].

Raman scattering offers unique features in the investigation of manybody quantum phenomena by simultaneously providing energy, symmetry, and lifetime information of collective excitations. While the ultimate goal in solving the "HO mystery" is to find the order parameter, answers to a few questions would have greatly constrain the phase space for possible theories. One of the most important questions is about the symmetry or symmetries that were removed at the phase transition. A typical second order phase transition is related to a reduction of group symmetry, which usually occurs through removing a combination of translation, rotation, and time reversal symmetry operators.

3.2 Material and Methods

Preparation of high quality single crystals with controlled chemical compositions has always been a critical factor for the understanding of physical phenomena and reproducibility of experiments in condensed matter physics. This is particularly important in the quest of the HO mystery due to the proximity of several electronic phases at low temperature. Small amount of residual stress in URu_2Si_2 results in puddles of antiferromagnetic regions in the crystal [71], leading to confusing observations in the early years [32].

At low temperature, the residual resistivity is dominated by the impurity or defect scatterings in URu_2Si_2. Therefore the resistivity ratio between the room temperature and the base temperature, ρ_{RT}/ρ_{base-T}, also known as the residual resistivity ratio (RRR), is often used as a characterization of crystal purity for metallic compounds. It is known that the superconducting transition temperature T_c in URu_2Si_2 is strongly affected by RRR [108, 109], not uncommon for nodal superconductors [110, 111]. On the other hand, the dependence of RRR with the HO transition temperature and the sharpness of the phase transition is much less obvious [108, 109]. Recently, C_4 symmetry breaking features were reported in the HO phase only in the samples with highest RRR values [112, 113]. However, the subtlety of these signatures seems inconsistent with the large entropy change and the robustness of the HO phase transition. Therefore, the C_4 symmetry breaking may have been due to secondary effect of an (unknown) primary order parameter.

Traditionally, large single crystals were grown by the Czochralski pulling method in the arc furnaces [36, 114]. In order to minimize the contribution from extrinsic impurity phases, several improvements have been made. First, the starting uranium has purity of only about 99.9% and is further purified by the so-called electro-refinement method, i.e., solid state electrotransport method under ultrahigh vacuum to remove trace amount of transitional metals such as iron and copper [115]. The as-grown crystals using refined uranium by the Czochralski pulling method have typical RRR over 10 and untraceable impurity levels [45]. The superconducting transition temperature T_{sc} in these as-grown samples is typically less than 1 K. The crystals are then followed by annealing process using the electro-refinement method in high vacuum for over 10 days, which was shown to significantly increase the RRR up to 1000 in some cases [116], and T_{sc} is increased to 1.5 K [109, 116].

3.2.1 Raman Studies

The $URu_{2-x}Fe_xSi_2$ single crystals used in this monograph are grown by the Czochralski method in a tetra-arc furnace in argon environment. The pristine crystals were further post-processed by electro-refinement as described in Ref. [45, 108, 116] and were provided by Dr. Ryan E. Baumbach and Dr. Eric D. Bauer from Los Alamos National Laboratory. The crystals with Fe substitution were provided by Dr. Sheng Ran, Dr. Noravee Kanchanavatee, and Dr. M. Brian Maple from University of California, San Diego. The quality of the synthesized single crystals was confirmed by X-ray diffraction measurements.

The Raman scattering data shown in the following are all collected from the *ab*-surface of $URu_{2-x}Fe_xSi_2$ single crystals. Unless otherwise given, the Raman data were acquired using 752.5 nm line of a Kr^+ laser for excitation. The scattered light was analyzed by a custom triple-grating spectrometer equipped with a liquid nitrogen cooled CCD detector. The scattered light intensities were corrected for the spectral response of the spectrometer and CCD. The laser spot size on the sample is roughly $50 \times 100\,\mu m^2$. All temperatures shown in the following are corrected for

	E	$2C_4$ (z)	C_2	$2C'_2$	$2C''_2$	i	$2S_4$	σ_h	$2\sigma_v$	$2\sigma_d$	linears, rotations	quadratic
$A_{1g}(\Gamma_1^+)$	1	1	1	1	1	1	1	1	1	1		x^2+y^2, z^2
$A_{2g}(\Gamma_2^+)$	1	1	1	-1	-1	1	1	1	-1	-1	R_z	
$B_{1g}(\Gamma_3^+)$	1	-1	1	1	-1	1	-1	1	1	-1		x^2-y^2
$B_{2g}(\Gamma_4^+)$	1	-1	1	-1	1	1	-1	1	-1	1		xy
$E_g(\Gamma_5^+)$	2	0	-2	0	0	2	0	-2	0	0	(R_x, R_y)	(xz, yz)
$A_{1u}(\Gamma_1^-)$	1	1	1	1	1	-1	-1	-1	-1	-1		
$A_{2u}(\Gamma_2^-)$	1	1	1	-1	-1	-1	-1	-1	1	1	z	
$B_{1u}(\Gamma_3^-)$	1	-1	1	1	-1	-1	1	-1	-1	1		
$B_{2u}(\Gamma_4^-)$	1	-1	1	-1	1	-1	1	-1	1	-1		
$E_u(\Gamma_5^-)$	2	0	-2	0	0	-2	0	2	0	0	(x, y)	

Fig. 3.11 The character table for the point group D_{4h}. The linear basis functions (x,y) and z denote vectors in and out of the *ab*-plane, respectively. Similarly, (R_x,R_y) and R_z are pseudovectors in and out of the *ab*-plane, respectively. The quadratic functions are also shown

laser heating. The power on the sample is about 10 mW for most temperatures and kept below 7 mW for the lowest temperatures to reduce laser heating.

$URu_{2-x}Fe_xSi_2$ single crystals have body centered tetragonal structure characterized by the D_{4h} point group symmetry ($I4/mmm$ space group), as illustrated in Fig. 3.4. In our measurements, we align the incident and scattered light along the *c*-axis of the crystal. Thus, the electric field of light is in-plane and transforms as the E_u irreducible representation of the D_{4h} point group 3.11. Therefore, the inelastically scattered light couples to excitations that transform as

$$E_u \otimes E_u = A_{1g} \oplus A_{2g} \oplus B_{1g} \oplus B_{2g}$$

irreducible representations. The basis functions of these representations are shown in Fig. 3.11. The A_{2g} symmetry channel is special in the sense that it only couples to the pseudovector like excitations, forbidden for phonons.

The symmetry of excitations is selected through varying the experimentally controlled combination of incident and scattered light directional vector and polarization, called the "scattering geometry" [details in Sect. 1.3]. We adopt Porto's notation to indicate the scattering geometries, $\mathbf{k}_i(\mathbf{e}_i\mathbf{e}_s)\mathbf{k}_s$, where the directional vector and polarization of incident (scattered) light are denoted by $\mathbf{k}_i$ and $\mathbf{e}_i$ ($\mathbf{k}_s$ and $\mathbf{e}_s$), respectively. Since we are only using quasi-backscattering geometry, we omit

the directional vector in the following. We use X, Y, X′, Y′, R, and L for shorthand notations of $\mathbf{e}_i$ and $\mathbf{e}_s$. X=[100] and Y=[010] are aligned along crystallographic a-axis, X′=[110] and Y′=[1$\bar{1}$0] are aligned 45° to the a-axis, and R=(X+iY)/$\sqrt{2}$ and L=(X-iY)/$\sqrt{2}$ are right and left circularly polarized, respectively.

The measured spectral intensity in the $\mathbf{e}_i\mathbf{e}_s$ scattering geometry, $I_{\mathbf{e}_i\mathbf{e}_s}(\omega, T)$, is related to the Raman response function, $\chi''_{\mathbf{e}_i\mathbf{e}_s}(\omega, T) \equiv \mathrm{Im}[\chi_{\mathbf{e}_i\mathbf{e}_s}(\omega, T)]$, by the following: $I_{\mathbf{e}_i\mathbf{e}_s}(\omega, T) = [1 + n(\omega, T)]\chi''_{\mathbf{e}_i\mathbf{e}_s}(\omega, T) + L(\omega, T)$, where $\chi_{\mathbf{e}_i\mathbf{e}_s}(\omega, T)$ is the Raman susceptibility, $n(\omega, T)$ is the Bose factor, and $L(\omega, T)$ is a background mainly resulting from luminescence of the sample.

We notice that other than the phononic contribution, the response in B_{1g} and B_{2g} symmetry channels is the same and weakly temperature dependent. This suggests that electronic Raman contributions in the B_{1g} and B_{2g} channels are negligibly small, and the measured spectral intensity in RL scattering geometry, $I_{RL}(\omega, T) = [1+n(\omega, T)][\chi''_{B1g}(\omega, T)+\chi''_{B2g}(\omega, T)]+L(\omega, T)$, is predominantly contributed by luminescent background. This background signal is very small in the near infrared excitation and can be approximated as a small constant.

3.2.2 *Characterization of Strain Free Areas*

Due to the proximity of the HO and AFM phases [Fig. 3.7], any small strain field in the crystal can induce small ∼50 nm size AFM puddles in the HO phase, which blurs fine spectroscopic features coming from the HO phase. Therefore, it is important not only to measure from a flat and clean surface as in most Raman scattering experiments but also to measure from a strain free area. In our experiment, the *ab*-plane residual resistivity ratio (RRR) for crystals from the same batch as used for this Raman scattering study is over 300 [109]. The cleaved samples were examined under a reflective Nomarski differential interference contrast (DIC) microscope to find a stress free area for Raman study. Our spectrometer is equipped with a "behind entrance slits" periscope as described in Sect. 2.1, which allows us to measure from the exact same spot predetermined by the Nomarski microscope.

The reflective Nomarski DIC microscope is commonly used by the semiconductor industry to optically image the surface roughness and defects [117]. In comparison to the more common bright field microscopy, the microscopic lattice deformation can be much more clearly distinguished in Nomarski DIC image [118] and hence a sensitive tool for finding an optically flat and strain free area on the crystal for Raman scattering studies. Figure 3.12 is a white light illuminated Nomarski microscope image of URu_2Si_2 single crystal, glued on a copper sample holder by epoxy and silver paint. The color gradients are proportional to the strain gradients on the sample surface induced by defects, steps, and impurity centers. The white arrows contrast two areas, both seem flat and featureless under bright field microscopy, while Normarski microscope clearly shows detailed differences due to minor crystal imperfections. The black rectangle is 100 by 200 μm, about twice the laser spot size of our experiment. The magnetic inclusions are known to exist in

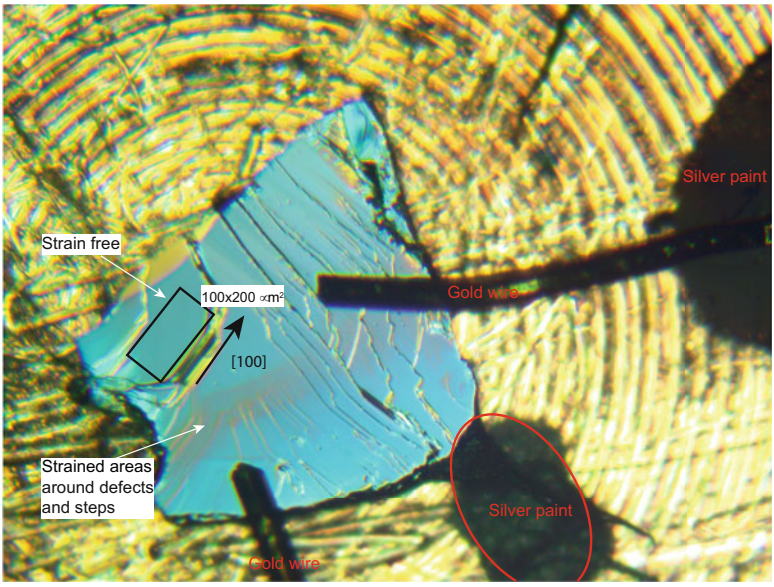

Fig. 3.12 Nomarski microscope image of URu_2Si_2 single crystal glued on a copper sample holder by epoxy and silver paint. The color gradients are proportional to the strain gradients on the sample surface induced by defects, step, and impurity centers. The white arrows contrast two areas, both seem flat and featureless under bright field microscopy. The gold wires are attached to the copper holder by conductive silver paint

bulk URu_2Si_2 under very small pressure or stress [65, 66], and thus it is crucial to study the intrinsic properties of the HO phase from a strain free area. The attached gold wires are glued to the copper holder by conductive silver paint to improve the thermal conductivity between the sample and copper holder.

3.3 Experiment and Results

Phase transitions are emergent phenomena in condensed matter materials that arise due to interactions between large quantity of particles. Despite the astronomical number of materials in this world, the "general behavior" of phase transitions is surprisingly similar. Experimentally, phase transitions are associated with divergence of some measurable quantity, such as heat capacitance, particle density, pressure, or magnetization. The phenomena are so common in nature, yet the concept remains one of the most puzzling fields in physics, and scientists are only starting to understand them in the recent hundred years. Theoretically, phase transitions occur as singularities in the partition function after taking the thermal dynamic limit [119]. Depending on the details of the singularity (or the way the measurable diverges), phase transitions can be sorted into a few categories [120].

In particular, a second order phase transition, e.g., ferromagnetic or superconducting transition, is associated with the emergence of an "order parameter" and spontaneous symmetry breaking. Above the phase transition temperature, both temporal and spatial short range fluctuations occur across the sample. Approaching the transition temperature, the fluctuations experience "critical slow down" as both the coherence time and length approach the thermal dynamic limit. Below the transition temperature, the fluctuations are quenched as some long range ordering form simultaneously and break the ground state symmetry of the high temperature phase. In the language of group theory, at least one symmetry operator is removed from the space group of the high temperature phase across a second order phase transition. To quantify the phase transition, one defines a measurable quantity, i.e., the order parameter ψ, that is only nonzero below the transition temperature. The Ginzburg–Landau free energy is then written as a function of ψ, and the thermal dynamic quantities can be derived from the free energy [121].

While the ultimate goal is to write down the partition function (microscopic theory) of a system, it is typical to use the Ginzburg–Landau theory for predicting the measurable properties of the system. This is because the partition functions defer from material to material, but the Ginzburg–Landau theory for a certain type of transition, e.g., superconductivity, can be very general and applies to many similar systems. In principle, infinitely many possible order parameters can arise due to a certain symmetry breaking. However, real materials embody many constraints, such as the lattice parameters and band structures, and therefore only allow a handful of imaginable order parameters. Thus, knowing the broken symmetry in a second order phase transition significantly reduces the complexity of the problem by constraining the allowed order parameters.

In our experiment, we will focus on the determination of symmetry breaking in the HO phase. Raman scattering is unique for simultaneously measuring the energy and symmetry of collective modes at the Brillouin zone center. Therefore, we study the *Raman selection rules* of two collective modes for determining the point group symmetry in the HO phase. (1) The 163 cm^{-1} B_{1g} phonon mode, corresponding to the lattice vibration of Ru atoms along c-axis and (2) a new mode of electronic origin with A_{2g} symmetry, which emerges only below the second order phase transition. The B_{1g} phonon is sensitive to the in-plane lattice C_4 rotational symmetry breaking. Furthermore, the Raman selection rule is capable of distinguishing the new Bravais lattice being orthorhombic (D_{2h}) or monoclinic (C_{2h}). We will show our low temperature data below and discuss in relation to the recent reports of C_4 symmetry breaking in the HO phase. The A_{2g} collective mode is typically associated with the magnetic Raman scattering [122]. Here, this mode is a new type of electronic Raman excitation, for which we will explain its origin and significance. Most importantly, by studying the Raman selection rules of this mode, we determine that the reflection symmetry is broken in the HO phase.

3.3.1 Phonon Modes

URu_2Si_2 crystallizes in the body centered tetragonal $ThCu_2Si_2$ structure type, with space group $I4/mmm$ (point group D_{4h}). The material contains 5 atoms in the primitive cell and therefore has a total of 15 phonon modes, with 3 acoustic (A_{2u}+E_u) and 12 optical bands. The U, Ru, and Si atoms occupy the 2a, 4d, and 4e Wyckoff positions, respectively, and it can be determined from the Bilbao crystallographic database that the optical phonons are half Raman active (A_{1g}+B_{1g}+2E_g) and half IR active ($2A_{2u}$+2E_u) [123, 124] (Fig. 3.13). The atomic displacements of each optical phonons are shown in Fig. 3.14, reproduced from Ref. [125]. We can see that the A_{1g} and B_{1g} phonons only involve the vibration of Si and Ru atoms, respectively. The role played by the lattice degrees of freedom has been studied by Raman scattering in the very early days of URu_2Si_2 [90]. It was concluded that the A_{1g} phonon intensity shows anomalous increase at low temperature, which may suggest strong electron–phonon coupling.

Recently, a detailed study of the lattice degrees of freedom from 2 to 300 K has been done by Raman scattering, IR spectroscopy, inelastic neutron scattering, and *ab initio* DFT calculations [125]. The study reproduced the anomalous temperature dependence of the A_{1g} phonon found in Ref. [90] and also reported a small energy softening of the B_{1g} phonon below about 100 K. The authors of Ref. [125] suggested a tendency toward lattice instability with orthorhombic distortion below 100 K, which is possibly related to the observation of a "pseudogap" in the E_g channel [126]. However, Ref. [125] found no phononic anomaly anywhere in the BZ across the HO transition. This study thereby put a strong constraint on the theoretical models explaining the HO phase transition, such that the order parameter must not couple to the lattice or at least couple in a manner that the phonons remain

Fig. 3.13 A table of the IR and Raman active phonons (acoustic modes not included), given the Wyckoff positions of the crystal structure of URu_2Si_2, determined from the Bilbao crystallographic database [123, 124]

IR Ative Modes

WP	A_{1g}	A_{1u}	A_{2g}	A_{2u}	B_{1g}	B_{1u}	B_{2g}	B_{2u}	E_u	E_g
4e	-	-	-	1	-	-	-	-	1	-
4d	-	-	-	1	-	-	-	-	1	-
2a	-	-	-	1	-	-	-	-	1	-

Infrared active Modes: $2A_{2u} + E_u$ (Acoustic modes not included)

Raman Active Modes

WP	A_{1g}	A_{1u}	A_{2g}	A_{2u}	B_{1g}	B_{1u}	B_{2g}	B_{2u}	E_u	E_g
4e	1	-	-		-	-	-	-		1
4d	-	-	-		1	-	-	-		1
2a	-	-	-		-	-	-	-		-

Raman active Modes: $A_{1g} + B_{1g} + 2E_g$

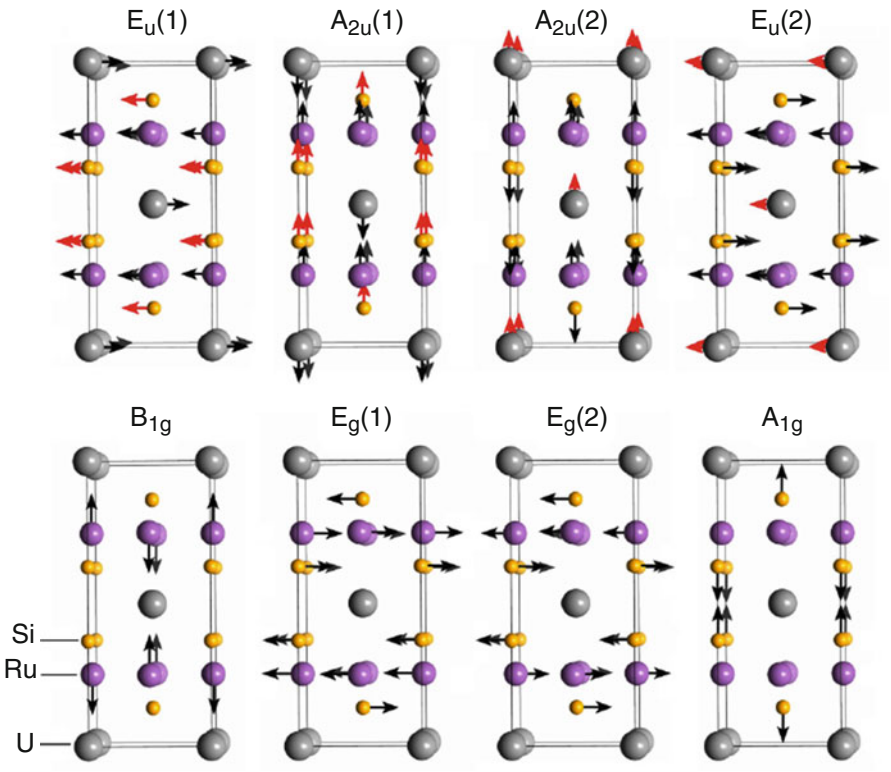

Fig. 3.14 The atomic displacement of the IR and Raman active phonons, where the arrows indicate the relative motions in a frozen time frame. Figure adapted from Ref. [125]

unaffected (energy, lifetime, and intensity) even with the strong electron–phonon couplings.

Figure 3.15 plots the Raman response function in the *XX* scattering geometry at 7 K, containing the B_{1g} phonon centered at 20 meV. In general, the phonon width is composed of its decay rate and inhomogeneous broadening due to stress field [125, 127]. Hence, the phonon width at low temperature is an indication of crystal quality. It has been demonstrated that stress field on the sample induces local AFM domains[32, 128]. Here, the deconvoluted full-width-at-half-maximum of the B_{1g} phonon is about 0.1 meV, smaller than the values reported elsewhere for this material[125, 127], indicating that the measured surface is single domain and stress free as it is required to study the symmetry of the order parameter in the HO phase.

Recently, a small lattice distortion was discovered by X-ray diffraction [129], where the observed orthorhombicity is 6.2×10^{-5}. In general, the broken fourfold rotational symmetry allows the B_{1g} phonon at 20.0 meV to leak into other channels. As illustrated in Fig. 3.15, the B_{2g} type lattice distortion reported in Ref. [129] would leave *X* and *Y* no longer aligned with crystallographic axes, leading to

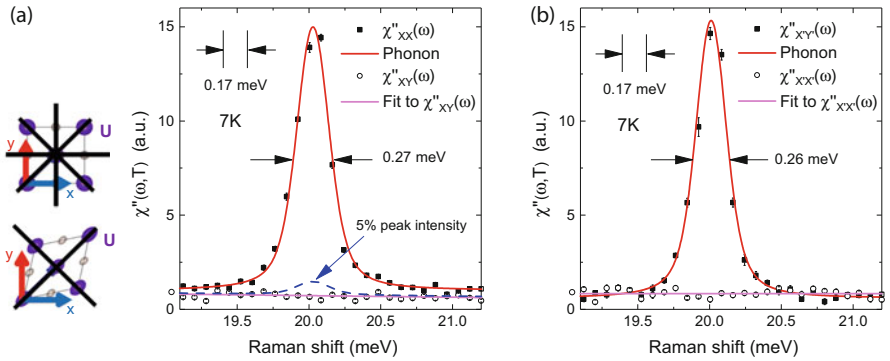

Fig. 3.15 (**a**) The Raman active B_{1g} phonon measured at 7 K in XX and XY scattering geometries and (b) in $X'X'$ and $X'Y'$ scattering geometries. The data were taken from the same surface as the rest of data presented in this report. The red curve is a fit of the Raman response function (**a**) in XX and (**b**) in $X'Y'$, scattering geometry (solid squares) containing the B_{1g} phonon, whereas the pink line is a fit to the Raman response function (**a**) in XY and (**b**) in $X'X'$, scattering geometry (open circles) containing no phonon. The deconvoluted full-width-at-half-maximum of the B_{1g} phonon is about 0.1 meV, close to resolution limitation of the instrument. There is no observable B_{1g} phonon leakage into other symmetry channels at 7 K, where a 5% phonon intensity is shown as guide to the eye (blue dashed line). The instrumental resolution is shown in the upper-left corner

intensity leakage of the B_{1g} phonon into the XY channel. However, within the experimental accuracy, no such orthorhombicity induced phonon leakage was observed in our data [Fig. 3.15a]. The absence of the phonon leakage is consistent with the tininess of the orthorhombicity observed by X-ray diffraction.

Similar argument can be extended to B_{1g} type of lattice distortion, which would allow finite intensity in the otherwise forbidden geometry $X'X'$. We also did *not* observe such feature experimentally [Fig. 3.15b]. The s/n of the data allows us to confidently rule out any C_4 breaking lattice distortion (orthorhombicity) in the *ab*-plane larger than 5%.

3.3.2 *Raman Response in the A_{2g} Symmetry Channel*

In Fig. 3.16, we plot the Raman response in the chiral A_{2g} channel where the most significant temperature dependence was observed. We show that $\chi''_{A2g}(\omega, T)$ displays enhancement of quasi-elastic scattering upon cooling.

At high temperatures, the Raman spectra exhibits a Drude line shape, $\chi''_{A2g}(\omega, T) \sim \frac{\omega\Gamma(T)}{\omega^2+\Gamma^2(T)}$, which in Ref. [90] was attributed to quasi-elastic scattering. The Drude line shape is due to incoherent scattering from the uranium crystal field states, and the maxima energy $\Gamma(T)$ reflects the scattering rate or the inverse quasiparticle lifetime. As temperature decreases, the coherent scattering leads to longer quasiparticle lifetime, thus decreasing $\Gamma(T)$. Below 70 K, the line

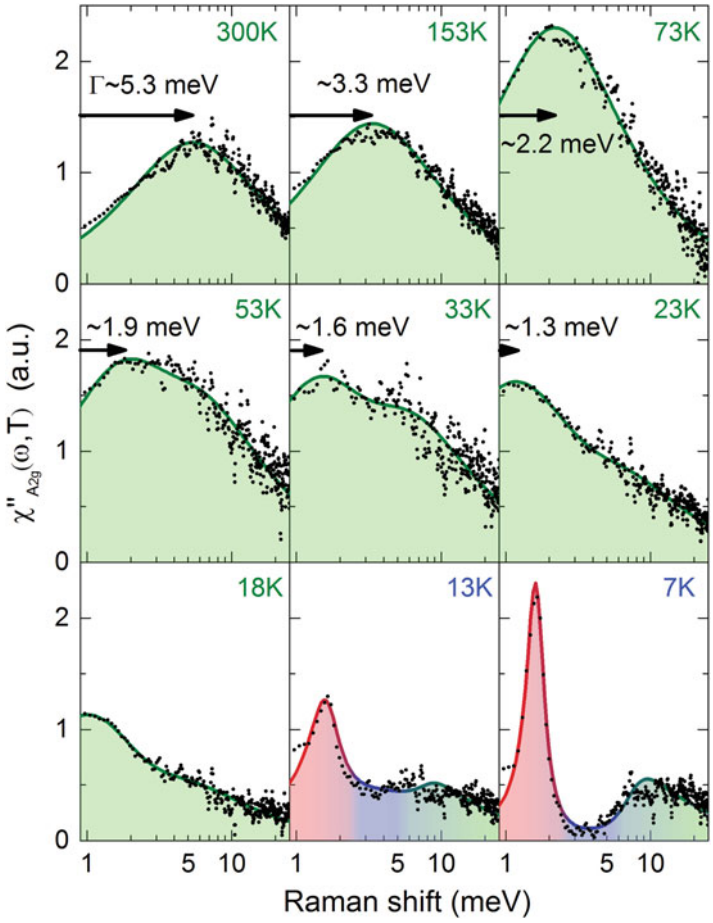

Fig. 3.16 The A_{2g} Raman response function decomposed from the spectra measured in the XY, $X'Y'$, and RL scattering geometries. The solid lines are guide to the eyes illustrating the narrowing of the Drude function[90, 130]: $\chi''_{A2g}(\omega, T) \sim \text{Im}\left[\frac{\omega}{\omega + i\Gamma(T)}\right]$, where $\Gamma(T)$ is the Drude scattering rate (indicated by the arrows), which decreases on cooling. Below 70 K, the Raman response deviates from the Drude function. Below T_{HO}, the Raman response shows a spectral weight suppression below 6 meV and the appearance of an in-gap mode at 1.6 meV (7 and 13 K)

shape deviates slightly from the Drude function, tracking the formation of the heavy fermion states by the hybridization of the itinerant conduction band and the U-5f states. In Fig. 3.16, the maximum in the Raman response function decreases from 5 meV at room temperature to 1 meV just above T_{HO}, reflecting the dramatic increase of the quasiparticle lifetime.

Further analysis of data in Fig. 3.16 by doing Krammers–Kronig transformation,

$$\chi'_{A2g}(0,T) = \frac{2}{\pi}\int_0^{25\,\mathrm{meV}} \left[\frac{\chi''_{A2g}(\omega,T)}{\omega}\right] d\omega, \tag{3.4}$$

reveals a striking resemblance between the Raman susceptibility in the A_{2g} channel, $\chi'_{A2g}(0,T)$, and the magnetic susceptibility. Figure 3.17 displays a comparison between $\chi'_{A2g}(0,T)$ (left axis) and the c-axis static magnetic susceptibility $\chi_c^m(T)$ (right axis), showing that the responses are proportional to each other at temperatures above T_{HO}.

Figure 3.18 shows the comparison between $\chi'_{A2g}(0,T)$ and $\chi_c^m(T)$ for a different iron concentration x in $URu_{2-x}Fe_xSi_2$ [64]. While there are discrepancies around the maxima at about 50–100 K, both quantities follow the same Curie–Weiss-like temperature dependence above about 100 K, followed by a suppression approaching the second order phase transition.

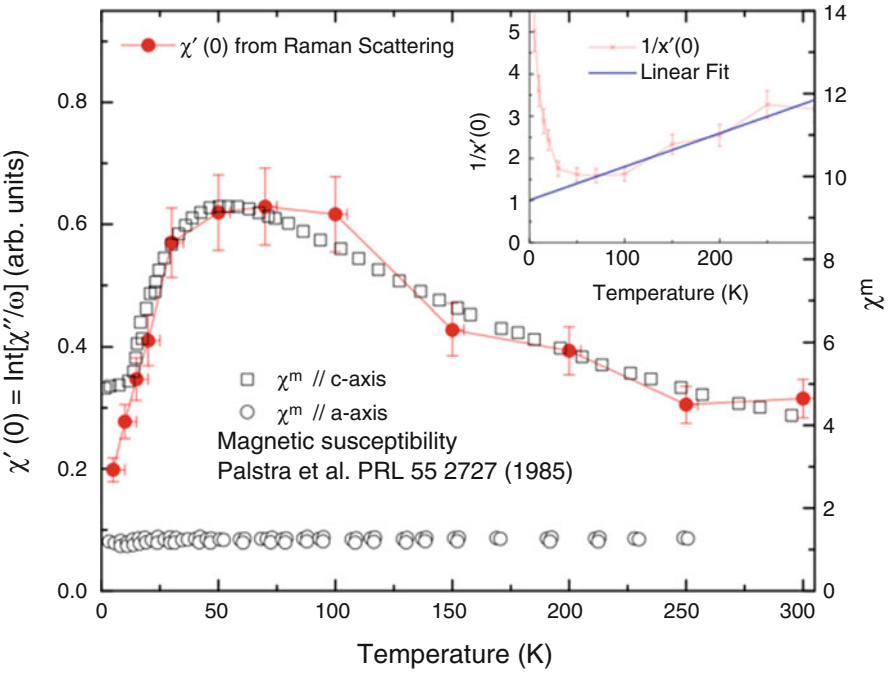

Fig. 3.17 Temperature dependence of the static Raman susceptibility in A_{2g} channel: $\chi'_{A2g}(0,T) = \frac{2}{\pi}\int_0^{25\,\mathrm{meV}}\left[\frac{\chi''_{A2g}(\omega,T)}{\omega}\right]d\omega$ (red dots), and the static magnetic susceptibility along c-axis and a-axis from Ref.[36] is plotted as blue squares and black circles, respectively. T_{HO} is marked by the dashed line

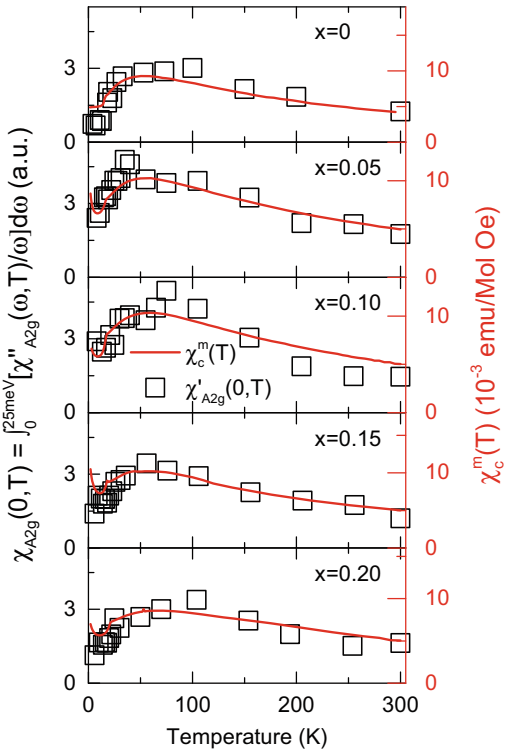

Fig. 3.18 The static Raman susceptibility in the A_{2g} symmetry channel (open squares) $\chi_{A2g}(0, T)$, compared with the magnetic susceptibility with field applied along the c-axis [64] (solid line)

The Curie–Weiss-like behavior above 100 K in static magnetic [64, 131] and Raman susceptibilities [1, 90, 132] suggests A_{2g} pseudovector-like instabilities at low temperature. Below about 50 K, the Kondo screening begins setting in [32, 59, 89, 131, 133] and the correlation length of the HO [134] or AFM [65, 128] phase builds at the ordering vector $Q_0 = (0, 0, 1)$; therefore, both the magnetic and Raman uniform susceptibilities start to decrease [Fig. 3.18]. Close to the transition temperature, both the HO and AFM order parameters fluctuate regardless of the low temperature ordering. However, the static magnetic susceptibility at Q_0 diverges only across the PM–AFM phase transition [65, 80], whereas it becomes "near critical" from the PM-HO phase [134]. Thus, HO is a nonmagnetic transition, but there is the "ghost" of AFM present. Here, we find that the temperature dependencies of the static A_{2g} Raman susceptibility $\chi_{A2g}(0, T)$ are similar and track $\chi_c^m(T)$ in all measured samples.

Below $T_{HO} = 17.5$ K, the A_{2g} Raman response function shows suppression of low energy spectral weight below 55 cm^{-1} (6.8meV) and the emergence of a sharp in-gap mode centered at 13 cm^{-1} (1.6 meV) [Fig. 3.16]. The temperature evolution of the gap and in-gap mode is most clearly seen in the colored intensity plot, where a mode at 1.6 meV appears sharply below T_{HO} without much temperature dependence [Fig. 3.19]. The low energy spectral weight gap suppression roughly follows Bardeen–Cooper–Schrieffer (BCS) gap function (white line in Fig. 3.19).

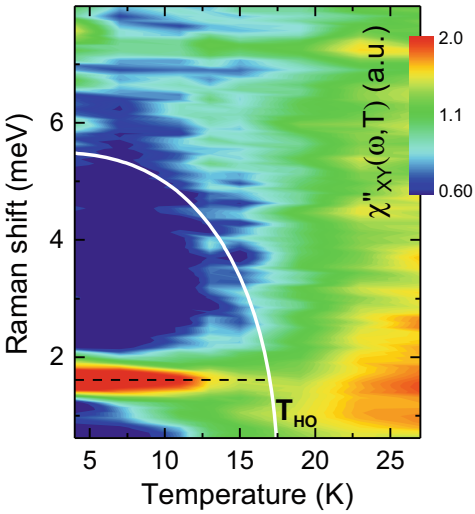

Fig. 3.19 Temperature dependence of the low frequency Raman response in the *XY* scattering geometry, dominantly comprised of A_{2g} excitations. The colors are coded in logarithmic scale. A gap-like suppression develops on cooling, and an in-gap mode at 1.6 meV (black dashed line) emerges below T_{HO}. The white line shows the temperature dependence of the BCS gap function

3.3.3 *The Reflection Symmetry Breaking in the "Hidden Order" State*

Figure 3.20 shows the Raman response in six scattering geometries at 7 K. The six scattering geometries are denoted as $\mathbf{e}_s\mathbf{e}_i$ =XX, XY, X'X', X'Y', RR, and RL, with $\mathbf{e}_i$ being the direction vector for incident light polarization and $\mathbf{e}_s$ being the scattered light polarization. X=[100] and Y=[010] are aligned along crystallographic axes, X'=[110] and Y'=[1$\bar{1}$0] are at 45° to the *a*-axis, and R=(X+*i*Y)/$\sqrt{2}$ and L=(X-*i*Y)/$\sqrt{2}$ are right and left circularly polarized light, respectively.

The intense in-gap mode is observed in all scattering geometries containing A_{2g} symmetry. In the most naive sense, the mode can be interpreted as a $\omega_0 = 1.6$ meV resonance between two quasi-localized crystal field states, which have symmetry difference of A_{2g}, e.g., between $|A_{1g}\rangle$ and $|A_{2g}\rangle$ states [132]. However, crystal field excitations in heavy element compounds appear gradually with decreasing temperatures [92, 93]. The abrupt appearance of the mode below the phase transition temperature is highly unusual for a crystal field excitation. We will explain the origin of this mode in the next section.

The most interesting and important feature in Fig. 3.20 is a much weaker intensity observed at the same energy of the A_{2g} mode in *XX* and $X'X'$ geometries, containing the excitations of the A_{1g} symmetry.

The data are fitted to a Lorentzian centered at 1.6 meV (convoluted by instrumental resolution). The intensities can be separated into distinct symmetry channels, $I_{A_{2g}} = (I_{XY} + I_{RR} - I_{X'X'})/2 = 2.6 \pm 0.1$, $I_{A_{1g}} = (I_{X'X'} + I_{RR} - I_{XY})/2 = 0.7 \pm 0.1$, $I_{B_{1g}} = (I_{X'Y'} + I_{XX} - I_{RR})/2 = 0.3 \pm 0.1$, and $I_{B_{2g}} = (I_{X'X'} + I_{XY} - I_{RR})/2 = 0.1 \pm 0.1$. Hence, the intensity ratio of A_{1g} to A_{2g} channels is $25 \pm 3\%$, B_{1g} to A_{2g} channels is $11 \pm 3\%$, and B_{2g} to A_{2g} channels is $3 \pm 3\%$.

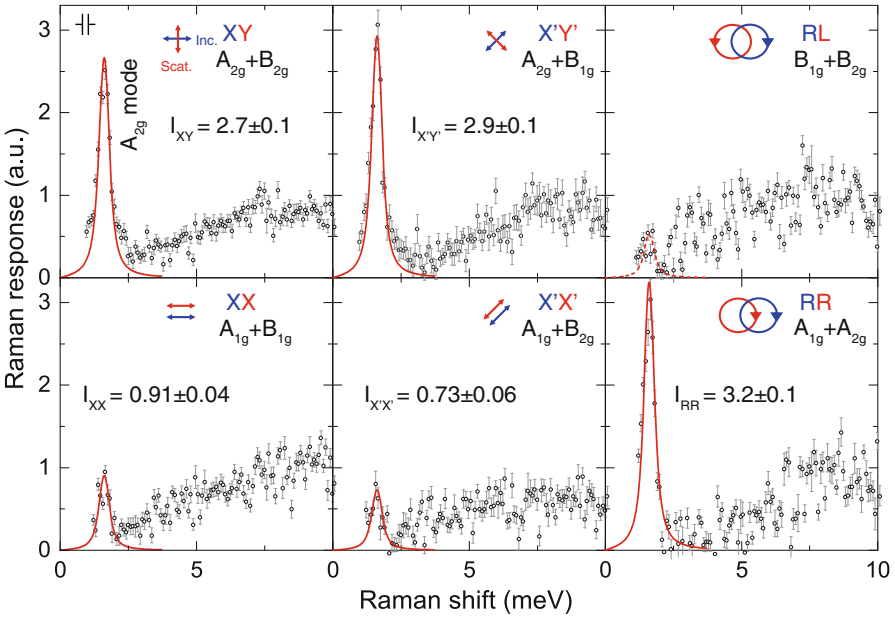

Fig. 3.20 The Raman response function in six scattering geometries at 7 K. The arrows in each panel show the linear or circular polarizations for incident (blue) and scattered (red) light. The irreducible representations for each scattering geometry are shown within the D_{4h} point group. The data are shown in black circles, where the error bars show one standard deviation. The red solid lines are fits of the in-gap mode to a Lorentzian, and the fitted intensity using the method of maximum likelihood is noted in each panel. The full width at half maximum of the in-gap mode is about 0.3 meV at 7 K (instrumental resolution of 0.17 meV is shown in the XY panel)

Therefore, we claim the observation of the 1.6 meV mode dominantly presenting in the A_{2g} symmetry channel with a weaker intensity "leakage" into the A_{1g} symmetry channel in the HO phase. Similarly, the small intensity in the B_{1g} channel could also be interpreted as small "leakage" of the collective mode from A_{2g} channel. However, the intensity borders on the noise level, and we do not intend to claim any observation in B_{1g} or B_{2g} channel.

The selection rules between scattering geometries and symmetries of Raman response are governed by the Raman tensors [Sect. 1.3] and summarized in Table 3.2. At the Γ point, collective modes have definite symmetries and therefore do not appear in more than one symmetry channel. However, due to spontaneous symmetry breaking, the point group symmetry of the system is reduced, and it is possible that one collective mode "leaks" into more than one symmetry channel. For example, upon the reduction of symmetry from point group D_{4h} to C_{4h}, the A_{1g} and A_{2g} irreducible representations merge into A_g, B_{1g} and B_{2g} merge into B_g, and E_g remains doubly degenerate [137]. Thus, a collective mode with "pure" A_{2g} symmetry of D_{4h} group should only appear in XY, $X'Y'$, and RR scattering geometries. But in the lower symmetry C_{4h} point group, there is no A_{2g} irreducible

Table 3.2 The Raman selection rules of URu_2Si_2 [135, 136]. Upon the reduction of symmetry from point group D_{4h} to C_{4h}, the A_{1g} and A_{2g} irreducible representations merge into A_g, B_{1g} and B_{2g} merge into B_g, and E_g remains doubly degenerate [137]

Scattering geometry	Irreducible representations	
	(D_{4h})	(C_{4h})
RR	$A_{1g} + A_{2g}$	A_g
RL	$B_{1g} + B_{2g}$	B_g
XX	$A_{1g} + B_{1g}$	$A_g + B_g$
YX	$A_{2g} + B_{2g}$	$A_g + B_g$
$X'X'$	$A_{1g} + B_{2g}$	$A_g + B_g$
$Y'X'$	$A_{2g} + B_{1g}$	$A_g + B_g$

Character table

$T > T_{HO}$ (D_{4h} group)

	E	$2C_4$	C_2	$2C'_2$	$2C''_2$	i	$2S_4$	σ_h	$2\sigma_v$	$2\sigma_d$	linears, rotation	quadratic
A_{1g}	1	1	1	1	1	1	1	1	1	1		x^2+y^2, z^2
A_{2g}	1	1	1	-1	-1	1	1	1	-1	-1	R_z	
B_{1g}	1	-1	1	1	-1	1	-1	1	1	-1		x^2-y^2
B_{2g}	1	-1	1	-1	1	1	-1	1	-1	1		xy
E_g	2	0	-2	0	0	2	0	-2	0	0	(R_x, R_y)	(xy, yz)

$T < T_{HO}$ (C_{4h} group)

	E	$2C_4$	C_2	i	$2S_4$	σ_h	linears, rotation	quadratic	
A_g	1	1	1	1	1	1	R_z	x^2+y^2, z^2	$A_{1g}+A_{2g}$
B_g	1	-1	1	1	-1	1		x^2-y^2, xy	$B_{1g}+B_{2g}$
E_g	2	0	-2	2	0	-2	(R_x, R_y)	(xy, yz)	E_g

D_{4h} group

Fig. 3.21 The character tables for the point group D_{4h} and C_{4h}, showing only parity even irreducible representations

representation any more. The previous A_{2g} of D_{4h} group is now reduced to A_g in C_{4h} group, which appears in all but RL scattering geometry in Table 3.2. Comparing the selection rules of C_{4h} group to Fig. 3.20, one can easily see that the symmetry properties of the collective mode are entirely consistent with C_{4h} point group. In fact, C_{4h} is the only point group consistent with our data.

Comparing the character tables (showing only parity even irreducible representations) for the point group D_{4h} and C_{4h} in Fig. 3.21, we see that the reflection symmetry operators, σ_d and σ_v (equivalently the out-of-plane rotation operators C'_2 and C''_2), have to be removed from the D_{4h} group. In other words, the *local* vertical and diagonal reflection symmetry operators at the uranium sites have to be removed. Therefore, the conclusion from the data shown in Fig. 3.20 is that the reflection symmetries are broken in the HO phase.

The tiny intensity leakage into the RL scattering geometry measures the strength of orthorhombic distortion caused by broken fourfold rotational symmetry. How-

ever, the signal in the *RL* geometry borders on the noise level and therefore is at most a subdominant order parameter induced by the broken reflection symmetries.

3.3.4 Iron Substitution Dependence of the A_{2g} Collective Mode

Albeit the distinct discrete symmetries are broken above and below the critical concentration x_c, we find that the A_{2g} collective mode continuously evolves with parameter x. In the HO phase, the mode energy decreases as x is increased, disappearing at the critical Fe concentration x_c. In the AFM phase, the collective mode again emerges in the same A_{2g} symmetry channel with the energy increasing with x. The continues transformation of this collective excitation, a photoinduced transition between the HO and AFM electronic phases, provides direct experimental evidence for a unified order parameter for both nonmagnetic and magnetic phases arising from the orbital degree of freedom of the uranium-5f electrons.

Figure 3.22 shows the temperature dependence of the Raman response in the eminent A_{2g} symmetry channel of the D_{4h} group. The upper panels of Fig. 3.22 show the intensity plots of the low energy Raman response $\chi''_{A2g}(\omega, T)$ below 30 K. Above $T_{\mathrm{DW}}(x)$ at about 18–20 K, a quasi-elastic peak (QEP) comprises most of the spectral weight for all samples, narrowing toward the transition. The observed QEP originates from overdamped excitations between quasidegenerate crystal field states [1, 35], and the narrowing of the QEP with cooling is due to the increase of excitation lifetime, related to the development of a hybridization gap and formation of a heavy Fermi liquid [59–61]. Our data show that this process is similar for both pristine and iron doped samples, regardless of the low temperature ordered phase

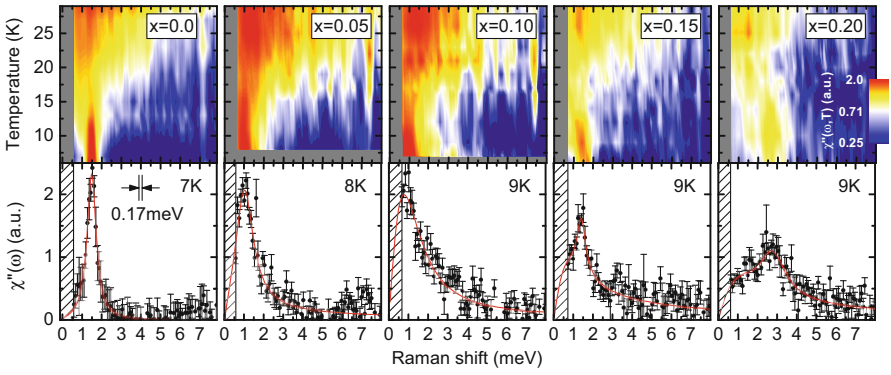

Fig. 3.22 Raman response in the A_{2g} symmetry channel, $\chi''_{A2g}(\omega, T)$, for $URu_{2-x}Fe_xSi_2$ below the second order phase transition temperature. The upper panels show intensity plots, where the intensities are color coded in logarithmic scale. The lower panels show the spectra at about half the transition temperature to emphasize the collective mode, where the error bars represent one standard deviation, and the red solid lines are guides to the eye

being HO or AFM phase. This indirectly shows that the Kondo hybridization cannot be a critical ingredient for distinguishing HO from AFM phase.

Below $T_{DW}(x)$, the most significant feature in the A_{2g} channel is a sharp collective mode. The sharpness of this resonance suggests the lack of relaxation channels due to the opening of an energy gap [59, 61, 62, 89]. In order to see the mode's lineshape more clearly, we plot $\chi''_{A2g}(\omega, T)$ for each Fe concentration x in the lower panels, with $T \approx T_{DW}(x)/2$. The lineshapes broaden with increasing x owing to the inhomogeneity of the local stress field, or unsuppressed relaxation channels introduced by doping that interact with the collective mode, which may also be related to the increasing continuum in the $x = 0.15$ and 0.2 spectra. In contrast to the monotonic broadening of the lineshape width, the collective mode frequency shows nonmonotonic behavior as function of x. The energy decreases with increasing x in the HO phase, until it vanishes below the instrumental resolution at $x = 0.10$, which is close to the HO and AFM phase boundary determined by elastic neutron scattering [80] and thermal expansion measurements [64]. The mode reappears in the AFM phase, where the energy increases with increasing x, and also appears in the same A_{2g} symmetry channel as in the HO phase.

3.3.5 *Excitation and Sample Dependence*

Figure 3.23a shows Raman response in the $X'Y'$ scattering geometry in the HO phase, measured with different excitation energies at about 8 K. All spectra were normalized by laser power, spectrometer response, and corrected for optical constants obtained from Ref. [61] [Chap. 2]. We demonstrate that the collective mode and the background have very different excitation profile as the conventional phonon. Figure 3.23b plots the integrated intensity of the A_{2g} collective mode (red) and the B_{1g} phonon (black) as function of excitation wavelength. The B_{1g} phonon

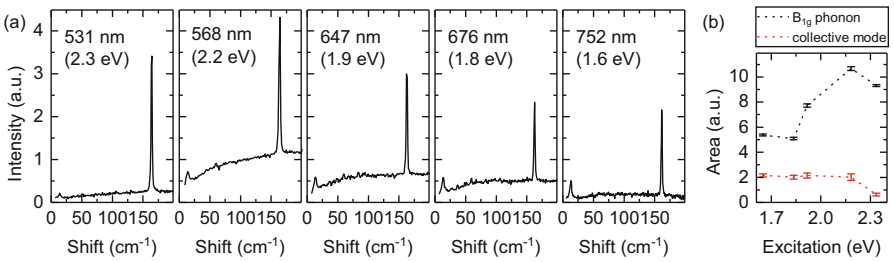

Fig. 3.23 (**a**) Low frequency secondary intensity in the $X'Y'$ scattering geometry, measured with different excitation energies in the HO phase (about 8 K). This includes contribution from both Raman response and photoluminescence background. All spectra were normalized by laser power, spectrometer response, and corrected for refractive index. (**b**) Integrated intensity of the A_{2g} collective mode (red) and the B_{1g} phonon (black) as function of excitation wavelength. Error bars are shown for one standard deviation

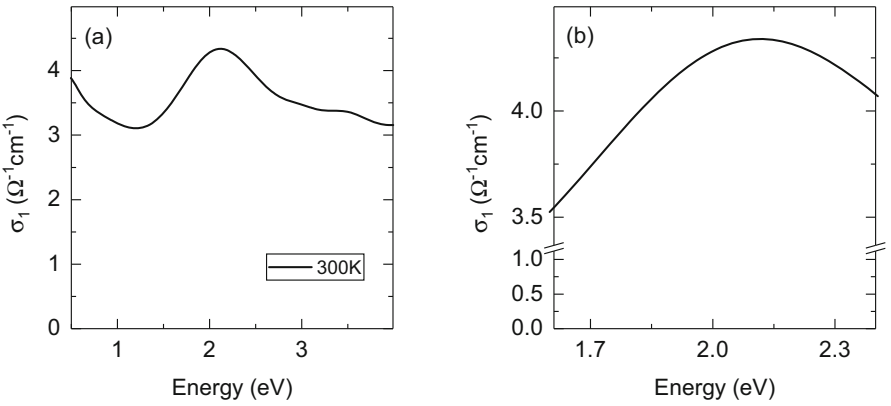

Fig. 3.24 (**a**) The *a*-axis optical conductivity of URu_2Si_2 from infrared to ultraviolet, measured at 300 K, from Ref. [61]. (**b**) Enlarged from panel (**a**) in the visible range between 1.6 and 2.4 eV

intensity seems to peak at around 2.2 eV, as reported in the dissertation of Dr. Buhot [Fig. 4.19 in Ref. [53]]. This may be due to the resonance enhancement from an interband transition, as suggested by the optical conductivity in Fig. 3.24 [61].

The A_{2g} collective mode has however a different profile, where the intensity is peaked at slightly longer wavelength than 676 nm. Notice that the spectrometer and CCD response is about 5 times larger around 550 nm than in 750 nm. Therefore despite the slightly larger signal in the NIR regime, the required spectra collection time is actually longer than 500–600 nm excitations. In most Raman experiments, one is usually tempted to pick the excitation where the signal (before normalizing to spectrometer and detector response) is the strongest. However, for the data analysis we employ here for URu_2Si_2, it is also important to minimize the photoluminescent contribution to the *scattering cross section*. For example, the Krammers–Kronig analysis applies to linear susceptibility functions, and therefore the photoluminescent background needs to be subtracted *before* the transformation. However, any subtraction of background introduces uncertainties, rendering the Krammers–Kronig analysis pointless if signal becomes comparable to the background. In fact, even by adjusting a simple linear background, one can get almost any temperature dependence for the "static susceptibility." Moreover, the analysis of "gap suppression" is meaningless unless either the luminescence background is known, or the background is negligibly small. In reality, the luminescent background has no reason to be linear or even any simple analytic function.

Unfortunately, it can be seen in Fig. 3.23a that the broad continuum has yet another excitation dependence different from the A_{2g} signal, peaking at around 568 nm. This broad background extends to much higher energies and is therefore assigned to be *mainly* due to photoluminescence, and it should be subtracted from the intensity before calculating Raman response. However, it must be emphasized here that there is no way to distinguish Raman response from photoluminescence

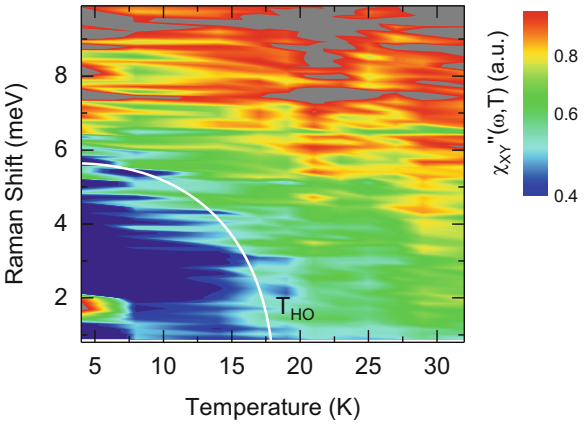

Fig. 3.25 Temperature dependence of the low frequency Raman response in the *XY* scattering geometry, taken from a different sample than in Fig. 3.19 and measured with 647 nm excitation. The colors are coded in logarithmic scale

for such broad continuum. Therefore, in our study [1, 138], we do the experiment with 752 nm excitation from Kr^+ ion laser, which contains minimal background.

Another challenging aspect of this study is to find a good sample *and* a good cleave. The residual resistivity ratio (RRR) from different batch of URu_2Si_2 crystals can differ from 20 to 700, likely due to varying degree of impurity concentrations and crystalline homogeneity [109]. Although the varying RRR does not greatly modify the HO temperature, it will likely introduce different inhomogeneous broadening in all spectroscopic features, such as phonons and collective modes. Figure 3.25 shows the temperature dependence of the low frequency Raman response in the *XY* scattering geometry, measured from a batch of samples with lower RRR. The RRR in this batch of samples ranges between 50 and 200, which is consistently lower compared to another batch of samples with RRR ≈200–600, where Fig. 3.19 was measured from. In all measured sample batches, T_{HO} is characterized by transport measurements and consistently found at 17.5 K.

Compared to Fig. 3.19, we first notice that the A_{2g} collective mode in Fig. 3.25 appears at significantly lower temperature, about 8 K. Surprisingly, the temperature dependence of the gap suppression is still consistent with T_{HO} characterized by transport measurements, indicating that the laser heating has been correctly accounted for in both figures. Also, the FWHM (deconvoluted for the instrumental resolution) of the A_{2g} peak is about 0.7 meV at 7 K, which is much broader than about 0.4 meV found in samples with higher RRR. Therefore, the reason for the seemingly weaker A_{2g} peak is likely just due to the inhomogeneous broadening. In fact, we found that the integrated intensity of the A_{2g} peak is roughly the same in all samples, resulting the *peak height* in low RRR samples to be much lower, hindering us to distinguish it from noise background. Another possible aspect is that Fig. 3.25 was measured with 647 nm, which has slightly higher background than in 752 nm, introducing higher uncertainty in background subtraction.

In all measured samples from three different sources, grown by the Czochralski method with and without electrorefinement, and also samples grown by molten indium flux method, we consistently find the A_{2g} peak to saturate at 1.6–1.7 meV in low temperature. On the other hand, we find that the FWHM of the peak fluctuates

between samples and even slightly varies for different spots on the same cleave. On average, we find the FWHM roughly between 0.4 and 0.5 meV in high RRR samples and about 0.7 meV in low RRR samples. In all measured samples, the phonon width is close to instrumental resolution limited and therefore cannot serve as a reliable standard for sample quality.

3.4 Discussion

We now discuss the origin and the observed doping dependence of the collective mode in the ordered phases within a phenomenological Ginzburg–Landau approach, based on a minimal model where the two order parameters for both HO and AFM phases can be constructed from $|A_{2g}\rangle$ and $|A_{1g}\rangle$ [35, 97]. This model has recently been directly confirmed by experiments using inelastic X-ray scattering [139–141] and resonant ultrasound spectroscopy [142].

3.4.1 The Minimal Model and the Hexadecapole Order Parameter

For low energy spectroscopy, it is sufficient to introduce a minimal model containing the two lowest energy states in Table 3.1, $|A_{2g}\rangle$ and $|A_{1g}\rangle$, separated by a small energy $\approx 30\,\mathrm{cm}^{-1}$. From this minimal model, Haule and Kotliar proposed an A_{2g} type local interaction operator, $\Psi(r) \equiv V\,\langle|A_{1g}\rangle\,\langle A_{2g}|\rangle_r$, with V being the interaction strength, and r is the lattice site [35]. This is a complex order parameter, where the real part is responsible for the condensation in the HO phase, and is proportional to the electric hexadecapolar order parameter: $\Psi_{HO} \sim \langle(J_xJ_y + J_yJ_x)(J_x^2 - J_y^2)\rangle \sim \langle J_+^4 - J_-^4\rangle$. A hexadecapolar order parameter breaks the reflection symmetries but does not couple to the lattice directly (in the first order), and thus no lattice distortion (such as C_4 symmetry breaking) is expected. It was pointed out in Ref. [143] that the A_{2g} local order parameter and the antiferro-staggering along c-axis with ordering vector $Q_{DW} = (0, 0, \frac{c}{2\pi})$ lower the group symmetry from the high temperature $I4/mmm$ (No. 139) to $P\bar{4}/mnc$ (No. 128).

This A_{2g} hexadecapolar order parameter alone cannot explain the C_4 rotational symmetry breaking observed in magnetic torque [112], X-ray diffraction [129], and elastoresistivity [113] experiments. However, notice that external magnetic field or strain can induce small C_4 symmetry breaking as explained in Ref. [143] from symmetry arguments or in Supplementary Materials in Ref. [1] from direct calculations by involving a small subdominant order parameter of different symmetry (B_{1g} was included for example).

Consider now the minimal model introduced above and the low energy sector of the purely real hexadecapolar order parameter, which is appropriate for the low energy spectroscopy. We can write an effective Hamiltonian as

$$\begin{array}{c|cc} H_0 & |A_{2g}\rangle & |A_{1g}\rangle \\ \hline |A_{2g}\rangle & 0 & V\sin\theta \\ |A_{1g}\rangle & V\sin\theta & \omega_0 \end{array} \tag{3.5}$$

where $|A_{2g}\rangle = \frac{i}{\sqrt{2}}(|4\rangle - |-4\rangle)$ with A_{2g} symmetry and $|A_{1g}\rangle = \frac{\cos\theta}{\sqrt{2}}(|4\rangle + |-4\rangle) - \sin\theta\,|0\rangle$ with A_{1g} symmetry are the singlet crystal field states of the U-5f electrons. Notice that we have absorbed the $\sin\theta$ factor into V in the main text.

From perturbation theory, the perturbed states up to second order in V are

$$\begin{aligned} |\mathrm{HO}\rangle &= \left(1 - \frac{V^2\sin^2\theta}{2\omega_0^2}\right)|A_{2g}\rangle + \frac{V\sin\theta}{\omega_0}|A_{1g}\rangle + \mathcal{O}(V^3) \\ |\beth\rangle &= \frac{-V\sin\theta}{\omega_0}|A_{2g}\rangle + \left(1 - \frac{V^2\sin^2\theta}{2\omega_0^2}\right)|A_{1g}\rangle + \mathcal{O}(V^3), \end{aligned} \tag{3.6}$$

where $|\mathrm{HO}\rangle$ is the HO ground state, and $|\beth\rangle$ (reads "veht") is the first excited state.

Notice that V can take up positive or negative values. In the following, we will use the notation:

$$\begin{aligned} |\mathrm{HO}^+\rangle &= \left(1 - \frac{V^2\sin^2\theta}{2\omega_0^2}\right)|A_{2g}\rangle + \frac{|V|\sin\theta}{\omega_0}|A_{1g}\rangle + \mathcal{O}(V^3) \\ |\mathrm{HO}^-\rangle &= \left(1 - \frac{V^2\sin^2\theta}{2\omega_0^2}\right)|A_{2g}\rangle - \frac{|V|\sin\theta}{\omega_0}|A_{1g}\rangle + \mathcal{O}(V^3) \end{aligned} \tag{3.7}$$

to distinguish the right- and left-handed states.

The mixing between $|A_{2g}\rangle$ and $|A_{1g}\rangle$ states by the hexadecapolar order parameter in HO phase is illustrated in Fig. 3.26. The resulted two states, $|\mathrm{HO}^+\rangle$ and $|\mathrm{HO}^-\rangle$,

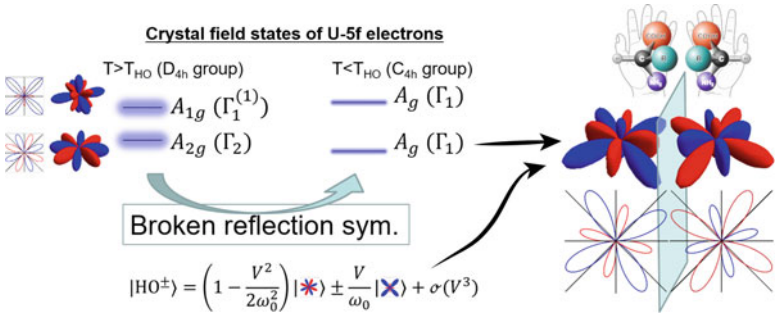

Fig. 3.26 The formation local chiral states, $|\mathrm{HO}^+\rangle$ and $|\mathrm{HO}^-\rangle$, in the HO phase due to reflection symmetry breaking and an A_{2g} type local interaction. The illustrations are meant to emphasize the symmetry of the wave function, where red and blue are positive and negative phases

cannot be transformed into one another by any remaining C_{4h} group operators. In particular, the two states are related to each other by a mirror reflection with an additional sign change: a property known as chirality (or handedness). The choice of either the right-handed or the left-handed state on a given uranium site, $|\mathrm{HO}^{+}\rangle$ or $|\mathrm{HO}^{-}\rangle$, defines the local chirality in the HO phase. Notice that these two degenerate states preserve the time reversal symmetry, carry no spin, and contain the same total charge but differ only in charge distribution, thus "hidden" from most experimental probes for decades.

3.4.2 The Ordering Vector

As we explained in Sect. 3.1, the order parameter was historically "believed" to be staggered in HO phase along $\mathbf{Q}_0 = (0, 0, 1)$ due to observation of a weak magnetic Bragg peak [73, 74]. However, since the magnetic feature is now attributed to extrinsic reasons, the question of whether translational symmetry being broken or not is back on the table. In particular, if the ordering is truly magnetic and along $\mathbf{Q}_0$ as shown in Fig. 3.8b, then one would expect certain periodicity of the magnetic dispersion. That is, the Z point of the BCT zone $(\pm 1, 0, 0)$ will become the Γ point $(0, 0, 0)$ in the HO phase [Fig. 3.10]. Also, the Σ point of the BCT zone $(\pm 0.6, 0, 0)$ should be equal to $(\pm 0.4, 0, 0)$ in the ordered phase. However, the inelastic neutron scattering results show that both magnetic and lattice excitations (phonons) obey the structural lattice periodicity (BCT zone) in the HO phase [87].

The Brillouin zone folding predicted for an ordering vector $\mathbf{Q}_0$ was recently observed in the HO phase by angle resolved photoemission spectroscopy (ARPES) [144]. The electronic band periodicity changes from BCT in the paramagnetic phase into ST in the HO phase, suggesting the formation of some density wave. The observed density wave gap $\sim$ 7 meV is consistent with the optical conductivity results [88], and the estimated gapping of density of states at Fermi surface could account for the entropy lost measured by heat capacitance. Thus, it seems clear that the ordering is electronic origin and does not break the lattice periodicity.

Besides the ARPES results [144], we show in the following that the Raman spectroscopy results also suggest ordering along $\mathbf{Q}_0$ (Fig. 3.27).

Detailed studies of the temperature dependence of the energy and FWHM of the 1.6 meV sharp A_{2g} mode by Buhot et al. [132], and its comparison to the collective mode observed by inelastic neutron scattering at Q_0 [85], revealed that the two modes measured at very different crystal momentum is likely the same mode. This is a "smoking gun" evidence of unit cell doubling along c-axis, i.e., the ordering vector is indeed $Q_0 = (0, 0, 1)$ as in the AFM phase. Thus the HO ground state is the staggering of local symmetry breaking order parameters, forming "some kind" density wave as suggested by infrared spectroscopy [88] and ARPES measurements [144].

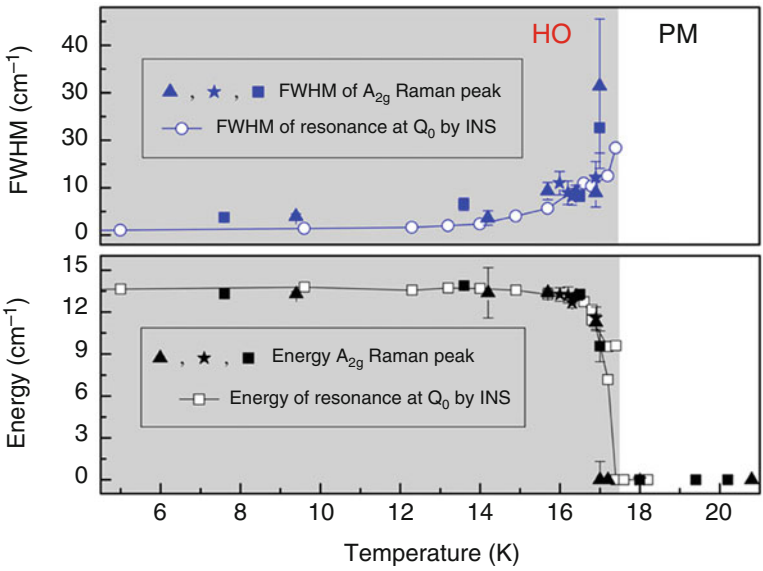

Fig. 3.27 The comparison between the A_{2g} collective mode in Raman scattering and Q_0 mode in inelastic neutron scattering, adapted from Ref. [132]. The figure compares the temperature dependence of the energy and FWHM of the A_{2g} Raman peak (full symbols) and the Q_0 mode measured by inelastic neutron scattering (open symbols) [85]. The full symbols (stars, triangle, and square) are extracted from various measurements on different samples from the same batch. The gray area corresponds to the temperature range of the HO phase

However, detailed studying of phonon branches by inelastic neutron scattering showed that within experimental sensitivity no evidence of translational symmetry breaking in any direction is observed [87]. This means that the long range ordered HO ground state does not induce any periodic lattice distortion, which is a very strange case since the phononic thermal conductivity [145] and linear thermal expansion coefficients [64] all show drastic change across the HO phase transition. In conclusion, the HO ground state must be an electronic ordering, which although couples strongly to lattice, and does not induce lattice distortion.

The most intuitive explanation to reconcile the above experiments would be to have *c*-axis staggering of an electric multipolar order parameter, which breaks the reflection symmetries on uranium sites, but does not induce any lattice distortion. Within the crystal group of URu_2Si_2, a hexadecapole (rank 4 electric multipole) is the choice in the lowest order. Notice that the interaction between rank 4 multipoles is not necessarily weak. For example, dotriacontapole (rank 5) is the dominant interaction in PrO_2, even stronger than dipoles [6].

3.4.3 The $\chi''_{A2g}(\omega, T)$ Continuum

The Raman response above T_{HO} can be described within a low energy minimal model suggested in Ref. [35] that contains two singlet states of A_{2g} and A_{1g} symmetries, split by an energy ω_0. In the following, we denote the singlet states of A_{2g} and A_{1g} symmetries by $|A_{2g}\rangle$ and $|A_{1g}\rangle$; the conduction band is labeled $|CB\rangle$. At high temperatures, the crystal field states are quasidegenerate in energy and localized at the uranium f shells in space. The incoherent excitation between the two states thus leads to a broad Drude like quasi-elastic peak as in Fig. 3.16, where the inverse excitation lifetime determines the peak maxima $\Gamma(T)$.

The proportionality between $\chi'_{A2g}(0, T)$ and $\chi^m_c(0, T)$ in Fig. 3.17 can be understood by noting that both susceptibilities probe A_{2g} excitations [Fig. 3.11]. This is because the Raman susceptibility in A_{2g} channel can be expressed by

$$\chi_{A_{2g}}(\omega) \propto \int \langle O_{A_{2g}}(\tau) O^{\dagger}_{A_{2g}}(0)\rangle e^{i\omega\tau} d\tau, \tag{3.8}$$

where $O_{A_{2g}}$ is the Raman operator in the A_{2g} channel. The magnetic susceptibility along z-axis is

$$\chi^m_z(\omega) \propto \int \langle J_z(\tau) J_z(0)\rangle e^{i\omega\tau} d\tau. \tag{3.9}$$

Here, J_z can be approximated by the orbital angular momentum operator L_z. Notice that $O_{A_{2g}}$ and L_z both couple to wave functions that transform as A_{2g} representation in D_{4h} group and thus differ only in the structure of the bare vertex. Therefore, we have the following relations:

$$\begin{aligned}
\langle A2g|O_{A_{2g}}|A2g\rangle &= \langle A2g|J_z|A2g\rangle = 0 \\
\langle A1g|O_{A_{2g}}|A1g\rangle &= \langle A1g|J_z|A1g\rangle = 0 \\
\langle A1g|O_{A_{2g}}|A2g\rangle &= \beta \langle A1g|J_z|A2g\rangle = i\alpha \\
\langle CB|O_{A_{2g}}|A2g\rangle &= \beta' \langle CB|J_z|A2g\rangle = i\alpha',
\end{aligned} \tag{3.10}$$

where α, β, α', and β' are real numbers. We see that the matrix elements of $O_{A_{2g}}$ and J_z operators are proportional to each other within the minimal model. This explains the proportionality between $\chi'_{A2g}(0, T)$ and $\chi^m_c(0, T)$ in Fig. 3.17.

The extreme anisotropy between a- and c-axis magnetic susceptibility also follows from this minimal model. The in-plane magnetic susceptibility is probed by a E_g symmetry operator in D_{4h} group [137], which does not couple to excitations between the $|A_{2g}\rangle$ and $|A_{1g}\rangle$ states. Thus, the predicted in-plane magnetic susceptibility χ^m_a is zero.

3.4.4 The Chirality Density Wave

The result of antiferro-staggering of the chiral states, $|\mathrm{HO}^+\rangle$ or $|\mathrm{HO}^-\rangle$, along c-axis is a chirality density wave [Fig. 3.28]. The staggered condensate can be approximated by a form

$$|\psi_{\mathrm{HO}}\rangle = \prod_{r=A\ site} |\mathrm{HO}_r^+\rangle \times \prod_{r=B\ site} |\mathrm{HO}_r^-\rangle\,. \tag{3.11}$$

Note that $|A_{2g}\rangle$ is the lowest energy crystal field state in the HO phase, and thus $|\mathrm{HO}_r^{\pm}\rangle$ at uranium site r is dominantly $|A_{2g}\rangle$, with a small admixture of $|A_{1g}\rangle$, i.e., $|\mathrm{HO}^{\pm}\rangle = \cos\theta\,|A_{2g}\rangle \pm \sin\theta\,|A_{1g}\rangle$. $\theta \equiv \arcsin(V/\omega_0)$, where ω_0 is the splitting between the lowest lying crystal field states in the minimal model, and V is the order parameter strength in the HO phase.

If we assume that in the AFM phase, the ordering of the crystal field states switches, i.e., the $|A_{1g}\rangle$ is the lowest energy crystal field state. Moreover, we let the AFM order parameter be the imaginary part of the complex local interaction, $\Psi(r) \equiv V\,\langle |A_{1g}\rangle\,\langle A_{2g}|\rangle_r$, which is proportional to the magnetic dipole operator: $\Psi_{AFM} \sim \langle J_z\rangle$. The new local wave functions in the AFM phase are $|\mathrm{AFM}^{\pm}\rangle \approx \cos\theta'\,|A_{1g}\rangle \pm i\sin\theta'\,|A_{2g}\rangle$. Here, $\theta' \equiv \arcsin(V'/\omega_0)$, and V' is the order parameter strength in the AFM phase. Since the mixing is purely imaginary, the charge distribution on the uranium site does not break any spatial symmetry; instead, it acquires nonzero out-of-plane magnetic moments and thereby breaks time reversal

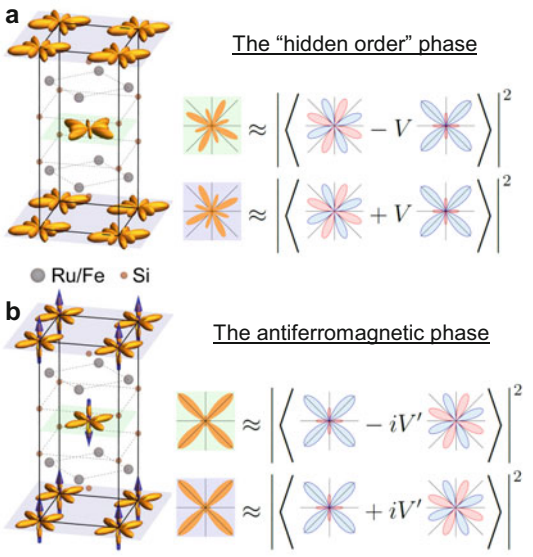

Fig. 3.28 The crystal structure of $URu_{2-x}Fe_xSi_2$ in (**a**) the HO and (**b**) the AFM phases. Illustrations capturing the symmetries of the charge distributions of the ground state wave functions are placed at the uranium atomic sites. On the right are illustrations showing the in-plane structures of the wave functions

symmetry. The staggering of these local states along Q_0 forms an antiferromagnetic lattice, as illustrated in Fig. 3.28. The Néel-type condensate takes the form

$$|\psi_{\mathrm{AFM}}\rangle = \prod_{r=A\ site} |\mathrm{AFM}_r^+\rangle \times \prod_{r=B\ site} |\mathrm{AFM}_r^-\rangle\,. \tag{3.12}$$

The two apparently competing orders, the chirality density wave and the antiferromagnetic state, are constructed by mixing the two orbital wave functions on uranium sites with a real or an imaginary phase factor, $\sin\theta$ or $i\sin\theta'$, thus unifying the two order parameters.

3.4.5 *Ginzburg–Landau Theory*

Based on the A_{2g} complex order parameter, Haule and Kotliar built a phenomenological Ginzburg–Landau theory to explain the phase diagram of URu_2Si_2 [97]. The Ginzburg–Landau theory is later slightly modified by Kusunose and Harima to improve the agreement with experiments [143] and recently expanded by Boyer and Yakovenko to account for "low field training" experiments [76, 146].

The Ginzburg–Landau free energy takes the form

$$F[\Psi] = \Psi^T \hat{A} \Psi + \beta \left(\Psi^T \Psi\right)^2 + \gamma \left(\Psi^T \hat{\sigma}_1 \Psi\right)^2, \tag{3.13}$$

where $\Psi^T \equiv \begin{pmatrix} \psi_{\mathrm{HO}} & \psi_{\mathrm{AFM}} \end{pmatrix}$, $\hat{A} \equiv \begin{pmatrix} \alpha_{HO} & 0 \\ 0 & \alpha_{AFM} \end{pmatrix}$, with α_{HO} and α_{AFM} vanish at the critical temperature, and $\hat{\sigma}_1 \equiv \begin{pmatrix} 0 & 1 \\ 1 & 0 \end{pmatrix}$ is the Pauli matrix. γ ensures a finite energy barrier between the two phases and hence the phase separation between the HO and AFM phases [128].

A schematic of the Ginzburg–Landau free energy at various special points in the phase diagram of URu_2Si_2 is shown in Fig. 3.29. Below the second order phase transition T_{DW}, two global and two local minima develop on ψ_{HO} and ψ_{AFM} axes due to spontaneous discrete symmetry breaking, where the minima characterize the ground states in the HO and AFM phases, respectively. At the critical doping in the ordered phase [Fig. 3.29f], the four minima are degenerate, but the barrier between the minima remains finite due to the γ term in Ginzburg–Landau functional [Eq. (3.13)]. Therefore the transition between the HO and LMAF phases is of the first order, and the coexistence of both phases is allowed, explaining the LMAF puddles that have been observed in the HO phase [147, 148].

Here, the free energy parameters are introduced following the recipes given Refs. [97, 143, 146] with adjustments to match the phase diagram in Fig. 3.29. All energies and temperatures are given in the units of Kelvin, and all pressure units are in GPa. The quadratic couplings are defined as

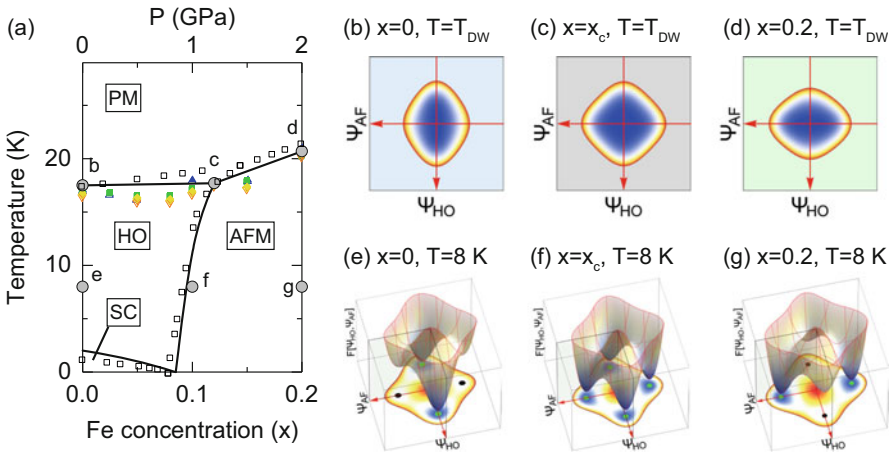

Fig. 3.29 (**a**) The phase diagram of URu_2Si_2 system, as shown in Fig. 3.8. (**b**)–(**g**) Schematics of the Ginzburg–Landau free energy at various special points in the phase diagram [solid gray circles in (**a**)]. ψ_{HO} and ψ_{AFM} are the real and imaginary part of the hexadecapole order parameter, respectively [35, 97, 143]

$$\alpha_{HO}(\omega_0, T, P) \equiv -\frac{1}{2} J_{HO}(\omega_0, P) + \tilde{\alpha}_{HO}(\omega_0, T, P)$$

and

$$\alpha_{AFM}(\omega_0, T, P) \equiv -\frac{1}{2} J_{AFM}(\omega_0, P) + \tilde{\alpha}_{AFM}(\omega_0, T, P),$$

where $\omega_0 = 35\,\mathrm{K}$ is the effective energy separation between the singlet states in the minimal model, T is temperature, and P can be either hydrostatic pressure or effective chemical pressure.

$$J_{HO}(\omega_0, P) = \frac{\omega_0(1 + a_1 P)}{\tanh\left(\frac{\omega_0}{2T_{HO}}\right)}$$

and

$$J_{AFM}(\omega_0, P) = \frac{\omega_0(1 + a_2 P)}{\tanh\left(\frac{\omega_0}{2T_N}\right)}$$

are the effective nearest neighbor exchange constants, with $T_{HO} = 17.5\,\mathrm{K}$ and $T_N = 15.5\,\mathrm{K}$.

$$\tilde{\alpha}_{HO}(\omega_0, T, P) = \frac{1}{2}\omega_0 \coth\left(\frac{\omega_0}{2T}\right)(1 - a_3 P)$$

and

$$\tilde{\alpha}_{AFM}(\omega_0, T, P) = \frac{1}{2}\omega_0 \coth\left(\frac{\omega_0}{2T}\right)(1 + a_3 P)$$

are the effective on-site couplings.

$$\beta(\omega_0, P) = \frac{\omega_0\left[\sinh\left(\frac{\omega_0}{T}\right) - \frac{\omega_0}{T}\right]\cosh^2\left(\frac{\omega_0}{2T}\right)}{8\sinh^4\left(\frac{\omega_0}{2T}\right)}$$

is the quartic coupling.

3.4.6 *Origin of the A_{2g} Collective Modes in URu_2Si_2*

Having established the x dependence of the Ginzburg–Landau free energy landscape, we are finally at a place to discuss the origin of the A_{2g} collective modes in the HO and AFM phases. As we mentioned in Sect. 3.3, the local picture of explaining the A_{2g} mode as crystal field excitation between $|A_{2g}\rangle$ and $|A_{1g}\rangle$ is too naive, completely ignoring the effect of phase transition that mixes these two states. Moreover, the condensate of these local orbital states implies off-site coupling, which results in a dispersive collective mode as observed by inelastic neutron scattering [72].

Therefore, the more accurate description of the A_{2g} collective mode should be an exciton carrying quadrapolar moment, which has the symmetry of the subdominant phase (e.g., $|\psi_{\mathrm{AFM}}\rangle$ when the system orders in the HO phase). This mode propagates through the crystal that orders with the dominant symmetry (e.g., $|\psi_{\mathrm{HO}}\rangle$). Likewise, when the ground state is $|\psi_{\mathrm{AFM}}\rangle$, the propagating exciton is of $|\psi_{\mathrm{HO}}\rangle$ symmetry. However, we will see below that at the Γ point, the local description actually captures the basic symmetry properties of the excitation and is appropriate for describing the symmetry breaking as we have done in Sect. 3.3. The symmetry difference between the two condensates is mainly A_{2g}, with a small admixture of A_{1g}; hence, such exciton can be detected by Raman in the A_{2g} channel and explains the sharp resonance shown in Fig. 3.19.

The energy of the collective mode at the Γ point then simply corresponds to the energy separation between the dominant long range order (e.g., $|\psi_{\mathrm{HO}}\rangle$ in the HO phase) and the sub-dominant order (e.g., $|\psi_{\mathrm{AFM}}\rangle$). Or equivalently, the energy difference between the Ginzburg–Landau free energy minima along ψ_{HO} and ψ_{AFM} axes in Fig. 3.29, which is vanishingly small at the critical Fe concentration and even away from this point, is much smaller than the size of the gap [62, 82]. Comparison of this energy difference with the A_{2g} mode is shown in Fig. 3.30. A very good agreement can be seen without any parameter adjustments.

The intensities of the collective modes in each symmetry channel can also be calculated from the matrix elements, $\langle\psi_{\mathrm{AFM}}| O_\mu |\psi_{\mathrm{HO}}\rangle$, where O_μ is the Raman

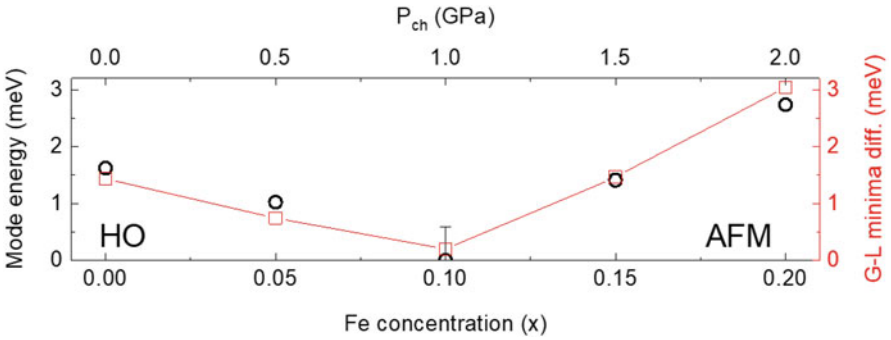

Fig. 3.30 The A_{2g} mode energy is plot against iron concentration x and compared to the energy difference between the Ginzburg–Landau free energy minima along ψ_{HO} and ψ_{AFM} axes in Fig. 3.29

operator in the μ symmetry channel. At the Γ point (long wavelength limit), without the loss of generality, we can consider the wave functions at site r,

$$|\psi_{\mathrm{HO}}\rangle_r = |\mathrm{HO}\rangle = \left(1 - \frac{V^2 \sin^2\theta}{2\omega_0^2}\right)|A_{2g}\rangle + \left(\frac{V \sin\theta}{\omega_0}\right)|A_{1g}\rangle + \mathcal{O}(V^2) \tag{3.14}$$

$$|\psi_{\mathrm{AFM}}\rangle_r = |\mathrm{AFM}\rangle = \left(1 - \frac{V'^2 \sin^2\theta'}{2\omega_0^2}\right)|A_{1g}\rangle + \left(\frac{iV' \sin\theta'}{\omega_0}\right)|A_{2g}\rangle + \mathcal{O}(V'^2). \tag{3.15}$$

To illustrate the symmetry selection rule in Raman scattering, we consider the simplest case where $V = V'$ and $\theta = \theta'$. In the HO phase, the matrix element in the A_{2g} channel is then

$$\begin{aligned}
&\langle \mathrm{AFM}| O_{A2g} |\mathrm{HO}\rangle \\
&= \left(1 - \frac{V^2 \sin^2\theta}{\omega_0^2}\right)\langle A_{1g}| O_{A2g} |A_{2g}\rangle + \left(\frac{iV^2 \sin^2\theta}{\omega_0^2}\right)\langle A_{2g}| O_{A2g} |A_{1g}\rangle + \mathcal{O}(V^4) \\
&= \langle A_{1g}| O_{A2g} |A_{2g}\rangle - \frac{V^2 \sin^2\theta}{\omega_0^2}\left(\langle A_{1g}| O_{A2g} |A_{2g}\rangle - i\langle A_{2g}| O_{A2g} |A_{1g}\rangle\right) + \mathcal{O}(V^4) \\
&= \left(1 - \frac{(1+i)V^2 \sin^2\theta}{\omega_0^2}\right)\langle A_{1g}| O_{A2g} |A_{2g}\rangle + \mathcal{O}(V^4).
\end{aligned} \tag{3.16}$$

We have used in the above $\langle A_{2g}| O_{A2g} |A_{2g}\rangle = \langle A_{1g}| O_{A2g} |A_{1g}\rangle = 0$ by symmetry selection rules and $\langle A_{1g}| O_{A2g} |A_{2g}\rangle = -\langle A_{2g}| O_{A2g} |A_{1g}\rangle$ by the fact that $\langle A_{1g}| O_{A2g} |A_{2g}\rangle$ is purely imaginary. Therefore, the intensity of collective mode in the A_{2g} channel is

$$I_{A2g} \sim |\langle \text{AFM}| O_{A2g} |\text{HO}\rangle|^2 = \left(1 - \frac{2V^2 \sin^2\theta}{\omega_0^2}\right) |\langle A_{1g}| O_{A2g} |A_{2g}\rangle|^2 + \mathcal{O}(V^4). \tag{3.17}$$

Similarly, the matrix element in the A_{1g} channel is

$$\langle \text{AFM}| O_{A1g} |\text{HO}\rangle = \frac{iV \sin\theta}{\omega_0} \langle A_{2g}| O_{A1g} |A_{2g}\rangle + \frac{V \sin\theta}{\omega_0} \langle A_{1g}| O_{A1g} |A_{1g}\rangle + \mathcal{O}(V^3). \tag{3.18}$$

We have used in the above $\langle A_{1g}| O_{A1g} |A_{2g}\rangle = \langle A_{2g}| O_{A1g} |A_{1g}\rangle = 0$ by symmetry selection rules. Therefore, the "leakage" intensity of the collective mode in the A_{1g} channel is

$$I_{A1g} \sim |\langle \text{AFM}| O_{A1g} |\text{HO}\rangle|^2 = \left(\frac{V^2 \sin^2\theta}{\omega_0^2}\right) |\langle A_{1g}| O_{A1g} |A_{1g}\rangle + i \langle A_{2g}| O_{A1g} |A_{2g}\rangle|^2 + \mathcal{O}(V^4). \tag{3.19}$$

Thus, the intensity in the A_{1g} channel is proportional to the square of the order parameter, $V^2 \sin^2\theta$, providing an indication of the symmetry breaking in the HO phase. Comparison of I_{A2g} to I_{A1g} is however difficult, because the evaluation of the expectation values depends on the details of the intermediate states and the laser excitation energy.

3.5 Summary

Summarizing this chapter, we used polarization resolved low temperature Raman spectroscopy to study the broken symmetry and collective modes in the long range ordered phases of $URu_{2-x}Fe_xSi_2$. By studying the temperature dependent Raman response, we observed a collective mode appearing in the A_{2g} symmetry channel below the second order phase transition, in both HO and AFM phases. The mode energy continuously evolves with increasing x, decreasing from 1.7 meV in the HO phase to almost zero at the HO/AFM phase boundary, and reappears with increasing energy in the AFM phase. The mode's evolution provides direct evidence for unified order parameter for both HO and AFM phases arising from the orbital degrees of freedom of the uranium-5f electrons.

While the long range ordering and broken time reversal symmetry in the pressurized and chemically substituted phases are undoubtedly due to AFM, the broken symmetry in the HO phase has been haunting the condensed matter physics community for many years. By carefully analyzing the Raman response in all available scattering geometries in the HO phase, we conclude that the reflection

symmetries σ_v and σ_d must be broken. Therefore, the HO must have a ground state breaking the local chirality at uranium sites. Moreover, the A_{2g} mode is also observed by inelastic neutron scattering at finite momentum, Q_0, suggesting the lattice translational symmetry is also broken along c-axis, resulting in a chirality density wave.

In our study, we find that the uranium-5f orbitals in URu_2Si_2 can arrange into orders with broken chirality or time reversal symmetry. While such orders are competing for the same phase space at low temperature, they are also subtly connected and were here unified into a common order parameter, which are almost degenerate in energy. Here, we propose that the "unrealized" phase is also the first excited state and can be probed through inelastic light scattering. The low energy excitations in the Ginzburg–Landau theory are usually Goldstone modes, but here we detected a new type of collective mode which corresponds to the oscillation between the HO and AFM phases.

This is by no means the end to the story of the HO in URu_2Si_2. A direct experimental verification to the chiral wave function, $|HO\rangle$, is still yet to be done. Whether the Raman active collective mode observed in the AFM phase is indeed related to the HO phase, and why is it absent in the inelastic neutron scattering data? How does the Raman collective mode in the HO phase soften toward the AFM phase? Is it a first or second order phase boundary? Is there a quantum critical point at the phase boundary? Most importantly, how generic are the phenomena we observed in the URu_2Si_2 system? Can we reproduce the HO in other heavy fermion systems? Are we able to describe or even predict the HO by *ab initio* calculations? Knowing the symmetry of the order parameter is just a small step forward, and there are still many unanswered questions lying in front of us.

References

1. H.-H. Kung et al., Chirality density wave of the "hidden order" phase in URu_2Si_2. Science **347**(6228), 1339–1342 (2015). https://doi.org/10.1126/science.1259729
2. H.-H. Kung et al., Analogy between the "Hidden Order" and the orbital antiferromagnetism in $URu_{2-x}Fe_xSi_2$. Phys. Rev. Lett. **117**, 227601 (2016). https://doi.org/10.1103/PhysRevLett.117.227601
3. L. Degiorgi, The electrodynamic response of heavy-electron compounds. Rev. Mod. Phys. **71**, 687–734 (1999). https://doi.org/10.1103/RevModPhys.71.687
4. J.D. Thompson, Z. Fisk, Progress in heavy-fermion superconductivity: Ce115 and related materials. J. Phys. Soc. Jpn. **81**(1), 011002 (2012). https://doi.org/10.1143/JPSJ.81.011002
5. J.L. Sarrao, J.D. Thompson, Superconductivity in cerium- and plutonium-based '115' materials. J. Phys. Soc. Jpn. **76**(5), 051013 (2007). https://doi.org/10.1143/JPSJ.76.051013
6. P. Santini et al., Multipolar interactions in f-electron systems: the paradigm of actinide dioxides. Rev. Mod. Phys. **81**, 807–863 (2009). https://doi.org/10.1103/RevModPhys.81.807
7. R. Joynt, L. Taillefer, The superconducting phases of UPt$ 3$. Rev. Mod. Phys. **74**, 235–294 (2002). https://doi.org/10.1103/RevModPhys.74.235
8. C. Pfleiderer, Superconducting phases of f -electron compounds. Rev. Mod. Phys. **81**(4), 1551–1624 (2009). https://doi.org/10.1103/RevModPhys.81.1551

9. J.L. Smith, E.A. Kmetko, Magnetism or bonding: a nearly periodic table of transition elements. J. Less Common Met. **90**(1), 83–88 (1983)
10. P. Coleman, *Introduction to Many-Body Physics* (Cambridge University Press, Cambridge, 2015). https://doi.org/10.1017/CBO9781139020916
11. W.J. De Haas, J. De Boer, G.J. Van den Berg, The electrical resistance of gold, copper and lead at low temperatures. Physica **1**(7–12), 1115–1124 (1934). https://doi.org/10.1016/S0031-8914(34)80310-2
12. M.P. Sarachik, E. Corenzwit, L.D. Longinotti, Resistivity of Mo-Nb and Mo-Re alloys containing 1% Fe. Phys. Rev. **135**, A1041–A1045 (1964). https://doi.org/10.1103/PhysRev.135.A1041
13. B.T. Matthias et al., Magnetic moment of transition metal atoms in dilute solution and their effect on superconducting transition temperature. Phys. Rev. Lett. **5**, 542–544 (1960). https://doi.org/10.1103/PhysRevLett.5.542
14. A.M. Clogston et al., Local magnetic moment associated with an iron atom dissolved in various transition metal alloys. Phys. Rev. **125**, 541–552 (1962). https://doi.org/10.1103/PhysRev.125.541
15. P.W. Anderson, Localized magnetic states in metals. Phys. Rev. **124**, 1–53 (1961). https://doi.org/10.1103/PhysRev.124.41
16. A. Menth, E. Buehler, T.H. Geballe, Magnetic and semiconducting properties of SmB_6. Phys. Rev. Lett. **22**, 295–297 (1969). https://doi.org/10.1103/PhysRevLett.22.295
17. F. Steglich et al., Superconductivity in the presence of strong Pauli paramagnetism: $CeCu_2Si_2$. Phys. Rev. Lett. **43**, 1892–1896 (1979). https://doi.org/10.1103/PhysRevLett.43.1892
18. A.C. Hewson, *The Kondo Problem to Heavy Fermions*. Cambridge Studies in Magnetism (Cambridge University Press, Cambridge, 1997)
19. G.R. Stewart, Heavy-fermion systems. Rev. Mod. Phys. **56**(4), 755–787 (1984). https://doi.org/10.1103/RevModPhys.56.755
20. F. Steglich et al., Magnetism, f-electron localization and superconductivity in 122-type heavy-fermion metals. J. Phys. Condensed Matter **24**(29), 294201 (2012). https://doi.org/10.1088/0953-8984/24/29/294201
21. P. Aynajian et al., Visualizing heavy fermions emerging in a quantum critical Kondo lattice. Nature **486**(7402), 201–206 (2012). https://doi.org/10.1038/nature11204
22. R.M. Martin, Fermi-surface sum rule and its consequences for periodic Kondo and mixed-valence systems. Phys. Rev. Lett. **48**, 362–365 (1982). https://doi.org/10.1103/PhysRevLett.48.362
23. H. Shishido et al., A drastic change of the Fermi surface at a critical pressure in "CeRhIn5: dHvA" study under pressure. J. Phys. Soc. Jpn. **74**(4), 1103–1106 (2005). https://doi.org/10.1143/JPSJ.74.1103
24. M. Maltseva, M. Dzero, P. Coleman, Electron cotunneling into a Kondo lattice. Phys. Rev. Lett. **103**, 206402 (2009). 10.1103/PhysRevLett.103.206402
25. M.H. Hamidian et al., How Kondo-holes create intense nanoscale heavy-fermion hybridization disorder. Proc. Natl. Acad. Sci. **108**(45), 18233–18237 (2011). https://doi.org/10.1073/pnas.1115027108. eprint. http://www.pnas.org/content/108/45/18233.full.pdf
26. A.R. Schmidt et al., Imaging the Fano lattice to 'hidden order' transition in URu_2Si_2". Nature (London) **465**(7298), 570–576 (2010). https://doi.org/10.1038/nature09073
27. P. Aynajian et al., Visualizing the formation of the Kondo lattice and the hidden order in URu_2Si_2. Proc. Natl. Acad. Sci. U. S. A. **107**(23), 10383–10388 (2010). https://doi.org/10.1073/pnas.1005892107
28. A. Georges et al., Dynamical mean-field theory of strongly correlated fermion systems and the limit of infinite dimensions. Rev. Mod. Phys. **68**, 13–125 (1996). https://doi.org/10.1103/RevModPhys.68.13
29. G. Kotliar et al., Electronic structure calculations with dynamical mean-field theory. Rev. Mod. Phys. **78**, 865–951 (2006). https://doi.org/10.1103/RevModPhys.78.865
30. D.N. Basov et al., Electrodynamics of correlated electron materials. Rev. Mod. Phys. **83**, 471–541 (2011). https://doi.org/10.1103/RevModPhys.83.471

31. M. Dzero et al., Topological Kondo insulators. Annu. Rev. Condens. Matter Phys. **7**(1), 249–280 (2016). https://doi.org/10.1146/annurev-conmatphys-031214-014749
32. J.A. Mydosh, P.M. Oppeneer, Colloquium: hidden order, superconductivity, and magnetism: the unsolved case of URu_2Si_2. Rev. Mod. Phys. **83**(4), pp. 1301–1322 (2011). And references therein. https://doi.org/10.1103/RevModPhys.83.1301
33. J.R. Jeffries et al., Degree of 5f electron localization in URu_2Si_2: electron energy-loss spectroscopy and spin-orbit sum rule analysis. Phys. Rev. B **82**(3), 033103 (2010). https://doi.org/10.1103/PhysRevB.82.033103
34. K.O. Kvashnina et al., Resonant X-ray spectroscopy of uranium intermetallics at the $M_{4,5}$ edges of uranium. Phys. Rev. B **95**, 245103 (2017). https://doi.org/10.1103/PhysRevB.95.245103
35. K. Haule, G. Kotliar, Arrested Kondo effect and hidden order in URu_2Si_2. Nat. Phys. **5**(11), 796–799 (2009). https://doi.org/10.1038/nphys1392
36. T.T.M. Palstra et al., Superconducting and magnetic transitions in the heavy-fermion system URu_2Si_2. Phys. Rev. Lett. **55**, 2727–2730 (1985). https://doi.org/10.1103/PhysRevLett.55.2727
37. D.L. Cox, Quadrupolar Kondo effect in uranium heavy-electron materials? Phys. Rev. Lett. **59**, 1240–1243 (1987). 10.1103/PhysRevLett.59.1240
38. D.L. Cox, A. Zawadowski, Exotic Kondo effects in metals: magnetic ions in a crystalline electric field and tunneling centres. Adv. Phys. **47**(5), 599–942 (1998). https://doi.org/10.1080/000187398243500
39. A.I. Tóth, G. Kotliar, Hexadecapolar Kondo effect in $\mathbf{U}Ru_2\mathbf{Si}_2$? Phys. Rev. Lett. **107**, 266405 (2011). https://doi.org/10.1103/PhysRevLett.107.266405
40. P. Chandra, P. Coleman, R. Flint, Hastatic order in the heavy-fermion compound URu_2Si_2". Nature (London) **493**, 621–626 (2013). https://doi.org/10.1038/nature11820
41. H. Amitsuka et al., Hidden order and weak antiferromagnetism in URu_2Si_2. Phys. B Condensed Matter **312**, 390 (2002). https://doi.org/10.1016/S0921-4526(01)01343-6
42. N. Harrison et al., Metamagnetism, quantum criticality, hidden order and crystal electric fields in URu_2Si_2. Physica B: Condensed Matter 346, 92 (2004). https://doi.org/10.1016/j.physb.2004.01.027
43. J.A. Mydosh, P.M. Oppeneer, Hidden order behaviour in URu_2Si_2 (A critical review of the status of hidden order in 2014). Philos. Mag. **94**(32–33), 3642–3662 (2014). And references therein. https://doi.org/10.1080/14786435.2014.916428
44. N. Kanchanavatee et al., Enhancement of the hidden order/large moment antiferromagnetic transition temperature in the $URu_{2-x}Os_xSi_2$ system. Philos. Mag. **94**(32–33), 3681–3690 (2014). https://doi.org/10.1080/14786435.2014.886022
45. Y. Haga et al., Single crystal growth and characterization of URu_2Si_2. Philos. Mag. **94**(32–33), 3672–3680 (2014). https://doi.org/10.1080/14786435.2014.974711
46. C. Tabata et al., X-ray backscattering study of crystal lattice distortion in hidden order of URu_2Si_2. Philos. Mag. **94**(32–33), 3691–3701 (2014). https://doi.org/10.1080/14786435.2014.952701
47. F. Bourdarot, S. Raymond, L.-P. Regnault, Neutron scattering studies on URu_2Si_2. Philos. Mag. **94**(32–33), 3702–3722 (2014). https://doi.org/10.1080/14786435.2014.935513
48. T. Durakiewicz, Photoemission investigations of URu_2Si_2. Philos. Mag. **94**(32–33), 723–3736 (2014). https://doi.org/10.1080/14786435.2014.937783
49. P.S. Riseborough, S.G. Magalhães, E.J. Calegari, Signatures of broken spin-rotational invariance in the "Hidden Ordered" compound URu_2Si_2? Philos. Mag. **94**(32–33), 3820–3837 (2014). https://doi.org/10.1080/14786435.2014.952256
50. P. Thalmeier, T. Takimoto, H. Ikeda, Itinerant multipolar order in URu_2Si_2 and its signature in magnetic and lattice properties. Philos. Mag. **94**(32–33), 3863–3876 (2014). https://doi.org/10.1080/14786435.2013.861615
51. O. Stockert et al., Superconductivity in Ce- and U-based "122" heavy-fermion compounds. J. Phys. Soc. Jpn. **81**(1), 011001 (2012). https://doi.org/10.1143/JPSJ.81.011001. eprint

52. C.L. Broholm, Magnetic fluctuations in heavy Fermion systems: a neutron scattering study of UPt_3, U_2Zn_{17} and URu_2Si_2. PhD thesis. The University of Copenhagen, 1989
53. J. Buhot, Ordres cachés et magnétisme étudiés par spectroscopie Raman en conditions extrêmes. PhD thesis. Université Paris Diderot-Paris 7, 2015
54. S.L. Cooper, Light Scattering Studies of Heavy Fermion and High Tc Superconductors. PhD thesis. University of Illinois at Urbana-Champaign, 1988
55. E. Hassinger, Pressure-temperature phase diagram of URu_2Si_2 by accalorimetry and resistivity measurements. PhD thesis. Heidelberg University, 2007
56. M.C. Shapiro, Elastoresistivity as a Probe of Electronically Driven Rotational Symmetry Breaking and Its Application to the Hidden Order State in URu_2Si_2. PhD thesis. Stanford University, 2016
57. T.T.M. Palstra, A.A. Menovsky, J.A. Mydosh, Anisotropic electrical resistivity of the magnetic heavy-fermion superconductor URu_2Si_2. Phys. Rev. B **33**, 6527–6530 (1986). https://doi.org/10.1103/PhysRevB.33.6527
58. M.W. McElfresh et al., Effect of pressure on competing electronic correlations in the heavy-electron system URu_2Si_2. Phys. Rev. B **35**, 43–47 (1987). https://doi.org/10.1103/PhysRevB.35.43
59. W.T. Guo et al., Hybridization gap versus hidden-order gap in URu_2Si_2 as revealed by optical spectroscopy. Phys. Rev. B **85**, 195105 (2012). https://doi.org/10.1103/PhysRevB.85.195105
60. R.P.S.M. Lobo et al., Optical conductivity of URu_2Si_2 in the Kondo liquid and hidden-order phases. Phys. Rev. B **92**, 045129 (2015). https://doi.org/10.1103/PhysRevB.92.045129
61. N. Bachar et al., Detailed optical spectroscopy of hybridization gap and hidden order transition in high-quality URu_2Si_2 single crystals. Phys. Rev. B **94**, 235101 (2016). https://doi.org/10.1103/PhysRevB.94.235101
62. J.S. Hall et al., Electrodynamics of the antiferromagnetic phase in URu_2Si_2. Phys. Rev. B **92**, 195111 (2015). https://doi.org/10.1103/PhysRevB.92.195111
63. N. Kanchanavatee et al., Twofold enhancement of the hidden-order/large moment antiferromagnetic phase boundary in the $URu_{2-x}Fe_xSi_2$ system. Phys. Rev. B **84**, 245122 (2011). https://doi.org/10.1103/PhysRevB.84.245122
64. S. Ran et al., Phase diagram and thermal expansion measurements on the system $URu_{2-x}Fe_xSi_2$. Proc. Natl. Acad. Sci. U. S. A. **113**(47), 13348–13353 (2016). https://doi.org/10.1073/pnas.1616542113
65. N.P. Butch et al., Antiferromagnetic critical pressure in URu_2Si_2 under hydrostatic conditions. Phys. Rev. B **82**, 060408 (2010). https://doi.org/10.1103/PhysRevB.82.060408
66. F. Bourdarot et al., Magnetic properties of URu_2Si_2 under uniaxial stress by neutron scattering. Phys. Rev. B **84**(18), 184430 (2011). https://doi.org/10.1103/PhysRevB.84.184430
67. M. Jaime et al., High magnetic field studies of the hidden order transition in URu_2Si_2". Phys. Rev. Lett. **89**, 287201 (2002). https://doi.org/10.1103/PhysRevLett.89.287201
68. D. Aoki et al., Field reentrance of the hidden order state of URu_2Si_2 under pressure. J. Phys. Soc. Jpn. **78**(5), 053701 (2009). https://doi.org/10.1143/JPSJ.78.053701
69. M.B. Maple et al., Partially gapped Fermi surface in the heavy-electron superconductor URu_2Si_2. Phys. Rev. Lett. **56**, 185–188 (1986). https://doi.org/10.1103/PhysRevLett.56.185
70. W. Schlabitz et al., Superconductivity and magnetic order in a strongly interacting Fermi-system: URu_2Si_2. Z. Phys. B **62**, 171–177 (1986). https://doi.org/10.1007/BF01323427
71. H. Amitsuka et al., Pressure–temperature phase diagram of the heavy-electron superconductor. J. Magn. Magn. Mater. **310**(2), Part 1, 214–220 (2007). https://doi.org/10.1016/j.jmmm.2006.10.008
72. C. Broholm et al., Magnetic excitations in the heavy-fermion superconductor URu_2Si_2. Phys. Rev. B **43**, 12809–12822 (1991). https://doi.org/10.1103/PhysRevB.43.12809
73. C. Broholm et al., Magnetic excitations and ordering in the heavy-electron superconductor URu_2Si_2. Phys. Rev. Lett. **58**, 1467–1470 (1987). https://doi.org/10.1103/PhysRevLett.58.1467
74. E.D. Isaacs et al., X-ray magnetic scattering in antiferromagnetic URu_2Si_2. Phys. Rev. Lett. **65**, 3185–3188 (1990). https://doi.org/10.1103/PhysRevLett.65.3185

75. J. Schoenes et al., Hall-effect and resistivity study of the heavy-fermion system URu_2Si_2. Phys. Rev. B **35**, 5375–5378 (1987). https://doi.org/10.1103/PhysRevB.35.5375
76. E.R. Schemm et al., Evidence for broken time-reversal symmetry in the superconducting phase of URu_2Si_2. Phys. Rev. B **91**, 140506 (2015). https://doi.org/10.1103/PhysRevB.91.140506
77. Y.J. Jo et al., Field-induced Fermi surface reconstruction and adiabatic continuity between antiferromagnetism and the hidden-order state in URu_2Si_2. Phys. Rev. Lett. **98**, 166404 (2007). https://doi.org/10.1103/PhysRevLett.98.166404
78. E. Hassinger et al., Temperature-pressure phase diagram of URu_2Si_2 from resistivity measurements and ac calorimetry: hidden order and Fermi-surface nesting. Phys. Rev. B **77**, 115117 (2008). https://doi.org/10.1103/PhysRevB.77.115117
79. T.J. Williams et al., Gapped excitations in the high-pressure antiferromagnetic phase of URu_2Si_2. Phys. Rev. B **95**, 195171 (2017). https://doi.org/10.1103/PhysRevB.95.195171
80. P. Das et al., Chemical pressure tuning of URu_2Si_2 via isoelectronic substitution of Ru with Fe. Phys. Rev. B **91**, 085122 (2015). https://doi.org/10.1103/PhysRevB.91.085122
81. M.N. Wilson et al., Antiferromagnetism and hidden order in isoelectronic doping of URu_2Si_2. Phys. Rev. B **93**, 064402 (2016). https://doi.org/10.1103/PhysRevB.93.064402
82. N.P. Butch et al., Distinct magnetic spectra in the hidden order and antiferromagnetic phases in $URu_{2-x}Fe_xSi_2$. Phys. Rev. B **94**, 201102 (2016). https://doi.org/10.1103/PhysRevB.94.201102
83. T.J. Williams et al., Hidden order signatures in the antiferromagnetic phase of $U(Ru_{1-x}Fe_x)_2Si_2$. Phys. Rev. B **95**, 104440 (2017). https://doi.org/10.1103/PhysRevB.95.104440
84. C.R. Wiebe et al., Gapped itinerant spin excitations account for missing entropy in the hidden-order state of URu_2Si_2. Nat. Phys. **3**(2), 96–99 (2007). https://doi.org/10.1038/nphys522
85. F. Bourdarot et al., Precise study of the resonance at $Q_0 = (1, 0, 0)$ in URu_2Si_2. J. Phys. Soc. Jpn. **79**(6), 064719 (2010). https://doi.org/10.1143/JPSJ.79.064719
86. A. Villaume et al., Signature of hidden order in heavy fermion superconductor URu_2Si_2: resonance at the wave vector $Q_0 = (1; 0; 0)$. Phys. Rev. B **78**, 012504 (2008). https://doi.org/10.1103/PhysRevB.78.012504
87. N.P. Butch et al., Symmetry and correlations underlying hidden order in URu_2Si_2. Phys. Rev. B **91**, 035128 (2015). https://doi.org/10.1103/PhysRevB.91.035128
88. D.A. Bonn, J.D. Garrett, T. Timusk, Far-infrared properties of URu_2Si_2. Phys. Rev. Lett. **61**, 1305–1308 (1988). https://doi.org/10.1103/PhysRevLett.61.1305
89. J.S. Hall et al., Observation of multiple-gap structure in hidden order state of URu_2Si_2 from optical conductivity. Phys. Rev. B **86**, 035132 (2012). https://doi.org/10.1103/PhysRevB.86.035132
90. S.L. Cooper et al., Magnetic excitations and phonon anomalies in URu_2Si_2. Phys. Rev. B **36**(10), 5743–5746 (1987). https://doi.org/10.1103/PhysRevB.36.5743
91. J.A. Koningstein, O.S. Mortensen, Experimental observation of an antisymmetric Raman scattering tensor. Nature **217**(5127), 445–446 (1968). https://doi.org/10.1038/217445a0
92. H. Rho, M.V. Klein, P.C. Canfield, Polarized Raman scattering studies of crystal-field excitations in $ErNi_2B_2C$. Phys. Rev. B **69**, 144420 (2004). https://doi.org/10.1103/PhysRevB.69.144420
93. H. Rho, M.V. Klein, P.C. Canfield, Crystal-field excitations and spin-phonon interactions in $DyNi_2B_2C$: Raman scattering study. Phys. Rev. B **82**, 064423 (2010). https://doi.org/10.1103/PhysRevB.82.064423
94. R. Liu et al., Novel Raman-active electronic excitations near the charge transfer gap in insulating cuprates. Phys. Rev. Lett. **71**, 709–3712 (1993). https://doi.org/10.1103/PhysRevLett.71.3709
95. E. Riccardi et al., Gate-dependent electronic Raman scattering in graphene. Phys. Rev. Lett. **116**, 066805 (2016). https://doi.org/10.1103/PhysRevLett.116.066805
96. H.-H. Kung et al., Chiral spin mode on the surface of a topological insulator. Phys. Rev. Lett. **119**, 136802 (2017). https://doi.org/10.1103/PhysRevLett.119.136802
97. K. Haule, G. Kotliar, Complex Landau-Ginzburg theory of the hidden order in URu_2Si_2. Europhys. Lett. **89**(5), 57006 (2010)

98. S. Elgazzar et al., Hidden order in URu_2Si_2 originates from Fermi surface gapping induced by dynamic symmetry breaking. Nat. Mater. **8**(4), 337–341 (2009). https://doi.org/10.1038/nmat2395
99. P.M. Oppeneer et al., Spin and orbital hybridization at specifically nested Fermi surfaces in URu_2Si_2. Phys. Rev. B **84**(24), 241102 (2011). https://doi.org/10.1103/PhysRevB.84.241102
100. P. Thalmeier, T. Takimoto, Signatures of hidden-order symmetry in torque oscillations, elastic constant anomalies, and field-induced moments in URu_2Si_2. Phys. Rev. B **83**(16), 165110 (2011). https://doi.org/10.1103/PhysRevB.83.165110
101. J.G. Rau, H.-Y. Kee, Hidden and antiferromagnetic order as a rank-5 superspin in URu_2Si_2. Phys. Rev. B **85**(24), 245112 (2012). https://doi.org/10.1103/PhysRevB.85.245112
102. P.S. Riseborough, B. Coqblin, S.G. Magalhães, Phase transition arising from the under-screened Anderson lattice model: a candidate concept for explaining hidden order in URu_2Si_2. Phys. Rev. B **85**(16), 165116 (2012). https://doi.org/10.1103/PhysRevB.85.165116
103. H. Ikeda et al., Emergent rank-5 nematic order in URu_2Si_2. Nat. Phys. **8**(7), 528–533 (2012). https://doi.org/10.1038/nphys2330
104. C. Thomas et al., Three-dimensional modulated spin liquid model applied to URu_2Si_2. Phys. Rev. B **87**, 014422 (2013). https://doi.org/10.1103/PhysRevB.87.014422
105. T. Das, Spin-orbit density wave induced hidden topological order in URu_2Si_2. Sci. Rep. **2**, 596 (2012). https://doi.org/10.1038/srep00596
106. R. Flint, P. Chandra, P. Coleman, Basal-plane nonlinear susceptibility: a direct probe of the single-ion physics in URu_2Si_2. Phys. Rev. B **86**, 155155 (2012). https://doi.org/10.1103/PhysRevB.86.155155
107. P. Chandra, P. Coleman, R. Flint, Hastatic order in URu_2Si_2: hybridization with a twist. Phys. Rev. B **91**, 205103 (2015). https://doi.org/10.1103/PhysRevB.91.205103
108. T.D. Matsuda et al., Details of sample dependence and transport properties of URu_2Si_2. J. Phys. Soc. Jpn. **80**(11), 14710 (2011). https://doi.org/10.1143/JPSJ.80.114710
109. R.E. Baumbach et al., High purity specimens of URu2Si2 produced by a molten metal UX technique. Philos. Mag. **94**(32–33), 3663–3671 (2014). https://doi.org/10.1080/14786435.2014.895876
110. Y. Kasahara et al., Exotic superconducting properties in the electron-hole-compensated heavy-fermion "Semimetal" URu_2Si_2. Phys. Rev. Lett. **99**, 116402 (2007). https://doi.org/10.1103/PhysRevLett.99.116402
111. A.P. Mackenzie, Y. Maeno, The superconductivity of Sr_2RuO_4 and the physics of spin-triplet pairing. Rev. Mod. Phys. **75**, 657–712 (2003). https://doi.org/10.1103/RevModPhys.75.657
112. R. Okazaki et al., Rotational symmetry breaking in the hidden-order phase of URu_2Si_2. Science **331**(6016), 439–442 (2011). https://doi.org/10.1126/science.1197358
113. S.C. Riggs et al., Evidence for a nematic component to the hidden-order parameter in URu_2Si_2 from differential elastoresistance measurements. Nat. Commun. **6**, 6425 (2015)
114. A. Menovsky, J.J.M. Franse, Crystal growth of some rare earth and uranium intermetallics from the melt. J. Crystal Growth **65**(1), 286–292 (1983). https://doi.org/10.1016/0022-0248(83)90062-3
115. Y. Haga et al., Purification of uranium metal using the solid state electrotransport method under ultrahigh vacuum. Jpn. J. Appl. Phys. **37**(6R), 3604 (1998)
116. T.D. Matsuda et al., Super clean sample of URu_2Si_2. J. Phys. Soc. Jpn. **77**(Suppl. A), 362–364 (2008). https://doi.org/10.1143/JPSJS.77SA.362. eprint
117. M. Pluta, Nomarski's DIC microscopy: a review. *Proc. SPIE* **1846** (1994). https://doi.org/10.1117/12.171873
118. W. Lang, *Nomarski Differential Interference-Contrast Microscopy* (Zeiss Information, Oberkochen, 1968)
119. K. Huang, *Statistical Mechanics* (Wiley, London, 1963)
120. M.W. Zemansky, R.H. Dittman, *Heat and Thermodynamics: An Intermediate Textbook*. International Series in Pure and Applied Mathematics (McGraw-Hill, New York, 1997)
121. R.K. Pathria, P.D. Beale, *Statistical Mechanics* (Elsevier Science, Oxford, 1996)

122. W. Hayes, R. Loudon, *Scattering of Light by Crystals* (Courier Corporation, Chelmsford, 2012)
123. E. Kroumova et al., Bilbao crystallographic server: useful databases and tools for phase-transition studies. Phase Trans. Multinat. J. **76**(1–2), 155–170 (2003). https://doi.org/10.1080/0141159031000076110
124. M.I. Aroyo et al., Crystallography online: Bilbao crystallographic server. Bulgar. Chem. Commun. **43**(2), 183–197 (2011)
125. J. Buhot et al., Lattice dynamics of the heavy-fermion compound URu_2Si_2. Phys. Rev. B **91**, 035129 (2015). https://doi.org/10.1103/PhysRevB.91.035129
126. J. Buhot et al., Anisotropic Kondo pseudogap in URu_2Si_2. Phys. Rev. B **101**, 245103 (2020). https://doi.org/10.1103/PhysRevB.101.245103
127. J. Buhot et al., Raman scattering study of the lattice dynamic of URu_2Si_2 and sample's preparation. English. J. Korean Phys. Soc. **62**(10), 1427–1430 (2013). https://doi.org/10.3938/jkps.62.1427
128. P.G. Niklowitz et al., Parasitic small-moment antiferromagnetism and nonlinear coupling of hidden order and antiferromagnetism in URu_2Si_2 observed by Larmor diffraction. Phys. Rev. Lett. **104**(10), 106406 (2010). https://doi.org/10.1103/PhysRevLett.104.106406
129. S. Tonegawa et al., Direct observation of lattice symmetry breaking at the hidden-order transition in URu_2Si_2. Nat. Commun. **5** (2014). https://doi.org/10.1038/ncomms5188
130. A. Zawadowski, M. Cardona, Theory of Raman scattering on normal metals with impurities. Phys. Rev. B **42**, 10732–10734 (1990). https://doi.org/10.1103/PhysRevB.42.10732
131. C. Pfleiderer, J.A. Mydosh, M. Vojta, Pressure dependence of the magnetization of URu_2Si_2. Phys. Rev. B **74**, 104412 (2006). 10.1103/PhysRevB.74.104412
132. J. Buhot et al., Symmetry of the excitations in the hidden order state of URu_2Si_2. Phys. Rev. Lett. **113**, 266405 (2014). https://doi.org/10.1103/PhysRevLett.113.266405
133. J. Levallois et al., Hybridization gap and anisotropic far-infrared optical conductivity of URu_2Si_2. Phys. Rev. B **84**, 184420, 184420 (2011). https://doi.org/10.1103/PhysRevB.84.184420
134. P.G. Niklowitz et al., Role of commensurate and incommensurate low-energy excitations in the paramagnetic to hidden-order transition of URu_2Si_2. Phys. Rev. B **92**, 115116 (2015). https://doi.org/10.1103/PhysRevB.92.115116
135. L.N. Ovander, The form of the Raman tensor. Opt. Spectrosc. **9**, 302 (1960)
136. M. Cardona, Resonance phenomena, in *Light Scattering in Solids II*, ed. by M. Cardona, G. Güntherodt (Springer, Berlin, 1982), pp. 45–49
137. G.F. Koster, *Properties of the Thirty-Two Point Groups*. Massachusetts Institute of Technology Press Research Monograph (M.I.T. Press, Cambridge, 1963)
138. H.-H. Kung et al., Surface vibrational modes of the topological insulator Bi_2Se_3 observed by Raman spectroscopy. Phys. Rev. B **95**, 245406 (2017). https://doi.org/10.1103/PhysRevB.95.245406
139. M. Sundermann et al., Direct bulk-sensitive probe of 5f symmetry in URu_2Si_2. Proc. Natl. Acad. Sci. U. S. A. **113**(49), 13989–13994 (2016). https://doi.org/0.1073/pnas.1612791113
140. M. Sundermann et al., Impact of Fe substitution on the electronic structure of URu_2Si_2 (2020). arXiv. Preprint arXiv:2005.03946
141. A. Amorese et al., From antiferromagnetic and hidden order to Pauli paramagnetism in UM_2Si_2 compounds with $5f$ electron duality. Proc. Natl. Acad. Sci. **117**(48), 30220–30227 (2020). https://doi.org/10.1073/pnas.2005701117
142. S. Ghosh et al., One-component order parameter in URu_2Si_2 uncovered by resonant ultrasound spectroscopy and machine learning. Sci. Adv. **6**(10), eaaz4074 (2020). https://doi.org/10.1126/sciadv.aaz4074
143. H. Kusunose, H. Harima, On the hidden order in URu_2Si_2 – antiferro hexadecapole order and its consequences. J. Phys. Soc. Jpn. **80**(8), 084702 (2011). https://doi.org/10.1143/JPSJ.80.084702
144. C. Bareille et al., Momentum-resolved hidden-order gap reveals symmetry breaking and origin of entropy loss in URu_2Si_2. Nat. Commun. **5** (2014). https://doi.org/10.1038/ncomms5326

145. P.A. Sharma et al., Phonon thermal transport of URu_2Si_2: broken translational symmetry and strong-coupling of the "Hidden Order" to the lattice. Phys. Rev. Lett. **97**, 156401 (2006). https://doi.org/10.1103/PhysRevLett.97.156401
146. L. Boyer, V.M. Yakovenko, et al., A model for metastable magnetism in the hidden-order phase of URu_2Si_2. Ann. Phys. (New York) **388** (2018). https://doi.org/10.1016/j.aop.2017.11.024
147. K. Matsuda et al., Spatially inhomogeneous development of antiferromagnetism in URu_2Si_2: evidence from ^{29}Si NMR under pressure. Phys. Rev. Lett. **87**, 087203 (2001). https://doi.org/10.1103/PhysRevLett.87.087203
148. M. Yokoyama et al., Competition between hidden order and antiferromagnetism in URu_2Si_2 under uniaxial stress studied by neutron scattering. Phys. Rev. B **72**, 214419 (2005). https://doi.org/10.1103/PhysRevB.72.214419

Chapter 4
Secondary Emission in Bi_2Se_3

Abstract In this chapter I will present our study of the secondary emissions (radiation) in a prototypical 3D topological insulator (TI) material, Bi_2Se_3. I will begin with a short overview on the physics of 3D TIs, with focus on the properties of the spin polarized surface states (Sect. 4.1.2). In Sect. 4.2, I will present our Raman spectroscopic results on the bulk and surface phonon modes in Bi_2Se_3, for which we identified the symmetries and self-energies and discussed the excitation dependence of them. In Sect. 4.3, I will present our electronic Raman scattering results in the much higher energy regime, where we observed a chiral spin mode as collective spin–flip excitations of the surface Dirac fermions. In Sect. 4.4, I will present our photoluminescence study of Bi_2Se_3, where we show a highly circular polarized surface exciton as a result of chiral spin texture in the surface states. Finally, I will make a brief summary of our study and its implications in Sect. 4.5.

The work in this chapter was done in collaboration with S.-W. Cheong (Rutgers), A.F. Kemper (NCSU), L.S. Levitov (MIT), S. Maiti (U. Florida), D.L. Maslov (U. Florida and NHMFL), R. Merlin (U. Michigan), and S. Oh (Rutgers).

The phononic study that focused on the surface phonons of Bi_2Se_3 is published in [1]. The Raman study of the chiral spin mode on the surface of Bi_2Se_3 is published in [2], and the photoluminescence (PL) study of the chiral excitons in Bi_2Se_3 is published in [3].

4.1 Introduction

Since ancient times, humans have been using physical properties, such as electrical conductivity, magnetism, hardness, color, etc., to classify the materials around us. Based on the electrical transport properties, we can broadly divide materials into two classes, i.e., the conducting metals where the conductivity increases as temperature decreases, and the nonconductive insulators with exponentially decreasing conductivity with decreasing temperature. One of the great triumphs of

H.-H. Kung, *Collective Excitations in the Antisymmetric Channel of Raman Spectroscopy*, Springer Theses, https://doi.org/10.1007/978-3-030-89332-3_4

condensed mater physics in the last century is to understand the differences between these two classes of materials based on the electronic "band theory."

If we think about it, the electronic properties in solids are not trivial to describe at all. For example, the electrical transport is not well-defined in a single atom or molecule and only becomes relevant when we consider many atoms closely packed such that their electronic wave functions overlap with each other. To describe such "collective" behaviors, we need to consider the many electrons as a whole instead of ascribing them to each atoms, and this is the central idea behind the band theory. In a solid, the electrons lose their single particle identities due to the very high density and long ranged Coulomb interaction with each other. The collective movements of electrons renormalizes into propagating waves called "Bloch waves," where the eigen-energies are neither discrete local states nor a simple parabola as free electrons. Instead, the atomic energy levels merge to form electronic bands, where dispersions are determined by the crystal symmetry, orbital characters, chemical bondings, etc.

Within this context, if the chemical potential (Fermi energy, E_F) situates inside an energy gap where no states are allowed, then it is a band insulator, otherwise a metal [4]. The most well-known insulator is perhaps the vacuum, with a gap of about 1 MeV below the electron–hole continuum, i.e., the minimum energy required for the "interband transition" that creates an electron–hole pair (Fig. 1.2). Whereas in a metal, it only requires infinitesimally small amount of energy to create an electron–hole pair through the "intraband transition," which is responsible for the charge transport. That is, there exists a connection between the band structures and electrical transport properties, which justifies the classification of metal versus insulator.

The band theory can be verified experimentally by angle resolved photoemission spectroscopy (ARPES), which directly maps the dispersion of quasiparticle states [5]. In the past century, physicists have been able to explain most of the material properties using the band theory. The development of such microscopic theories has allowed us to precisely control materials' properties by fine-tuning the band structure and chemical potential. It is fair to say that the foundation of the digital revolution we enjoy today is built upon the deep understanding of the band theory. Although physicists are still struggling to understand the metal-insulator transition and some other exotic phenomena due to the strong electron–electron interaction in some transitional metal oxides [6], the situation of the band theory is in general satisfactory for most systems.

However, toward the end of the past century, the discovery of quantum Hall effect opened the gateway to an entirely new phase of matter that does not fit into our traditional classification of materials [7]. In this new phase of matter, the bulk can be made insulated while the boundary is metallic by simply tuning carrier density and magnetic field, without breaking any space group symmetry. These materials are termed "topological" where the conductive boundary states are protected by global symmetries, rather than the detailed crystalline surface structures and electron filling as in non-topological band insulators.

In particular, the proposal and realization of 3D topological insulators (TIs) have attracted major interest in the condensed matter physics community into this emerging field. In these materials, the conductive 2D surface states are protected by the time reversal symmetry (TRS) and guaranteed to exist without any external magnetic field. Microscopically, these topological boundary states originate from strong spin–orbit coupling (SOC) in the bulk, which abruptly terminates at the crystalline boundary. Due to the symmetry protection, these states are extremely robust unlike their non-topological counterparts, and the transport properties are mainly governed by the "topological invariant" rather than the fine prints in the bulk band structures [8].

Make no mistake, the topological invariant themselves are also derived from the bulk band structures, but in a much more abstract way such that the details of the bands do not affect the outcome. In other words, we may put the materials through extreme conditions (such as magnetic field, temperature, pressure, chemical doping, etc.), and the topological boundary states and their associated transport properties would often remain unchanged, as long as the "topology" of the bands is unchanged. This is obviously a very nice property for electronic device design and applications. However, the original proposals have been limited to 2D systems, which are more difficult to manufacture and verify experimentally.

In the past decade, major developments have been made in the understanding of 3D materials' boundary properties based on their bulk band topology near the Fermi energy [8], immediately raising great interests in the condensed matter physics community. Materials that possess nontrivial band topologies and surface states are termed "topological materials." Just like metal versus insulators, topological materials can be further classified into different categories based on the topological invariants, and many of them are already experimentally verified [9–11]. Broadly speaking, depending on the bulk band structure at the Fermi level, topological materials can be separated into topological insulators and topological semimetals. The interesting aspects of the topological boundary states in three-dimensional (3D) TIs will be discussed in more detail later; see Sect. 4.1.2.

During the transition from a trivial band insulator to a topological insulator, there must exist a critical point at which the conduction and valence band intersect each other at a few nodal points or 1D nodal lines (either open arcs or closed loops) in the Brillouin zone. Depending on the symmetry and dimension of the system under study, the topology of these band crossing points can be further classified. For example, graphene can be considered as one of the simplest kinds of topological semimetal, i.e., a 2D Dirac semimetal. Around the nodes, the quasiparticles are described by the linearly dispersing bulk bands and topological boundary states. A variety of anomalous transport and optical properties have been predicted and some realized in various kinds of 3D topological semimetals [10, 11]. These exotic properties not only provide test beds for our current understanding of condensed matter theory but also possess promising applications in optoelectronics and spintronics.

The subject of topological band theory studies the relationships between topological boundary states and the bulk using only first principle calculations and lattice

symmetries. This is a very active and largely unexplored field, with new results appearing almost every day and many challenges lying ahead. In the following sections, we will focus on a particular kind of topological material, i.e., the 3D topological insulators.

4.1.1 Band Topology in Solids

The topological invariants are ultimately derived from the *bulk* band structures, which originate from the chemistry and symmetries of the lattice. Just as in geometrical topology that studies the properties that are preserved during deformation of objects, band topology is concerned with properties that are conserved as we continuously deform the bulk band structures. The widely used example is that a doughnut and a coffee mug both contain one open hole in it, which corresponds to the "genus" $g = 1$ that remains unchanged as we continuously deform the two objects into each other. Therefore, that hole is a topological property that cannot be easily removed, unless we cut the doughnut open with a knife or break off the coffee mug handle. In topological materials, the "doughnut hole" is reflected on the boundary, where *metallic* states must exist regardless of how we deform the bulk band structure through external perturbations or charge doping (within the range of bulk band gap). Note that not all boundary states in a topological material are topologically protected, there could be trivial states that coexist. Just like cutting the doughnut into halves, removing the topological boundary states also requires something dramatic, which is different for each topological class. In 3D topological insulators, this means applying magnetic field strong enough such that the Zeeman splitting is comparable to the spin–orbit coupling (SOC) or decrease the SOC strength significantly, which are not physically possible in most cases. Therefore, we often refer to the topological surface states as protected by time reversal symmetry.

Note that not all topological materials require strong SOC, but in the case of TIs, SOC plays a central role and therefore we should do a small detour and discuss it briefly now. The SOC is a relativistic effect that is present both in a single atom and also on the extended Bloch waves in solids. That is, SOC can be derived from the relativistic Dirac equations by keeping terms on the order of $1/c^2$. However, we can capture the essence of SOC in the atomic limit by the following simple arguments. In the rest frame of the electron in an atom, the SOC originates from the effective magnetic field acting on the electron by the nucleus.

$$\mathbf{B} = -\frac{\mathbf{v} \times \mathbf{E}}{c^2}$$

Let $\mathbf{E} = -\nabla_r V\hat{r} = \frac{\mathbf{r}}{er}\frac{\partial U}{\partial r}$ and $\mathbf{v} = \hat{p}/m$, and we can further simplify the equation to the more familiar form:

$$\mathbf{B} = \frac{1}{emc^2}\left(\frac{1}{r}\frac{\partial U}{\partial r}\right)\mathbf{r} \times \mathbf{p}.$$

Note that the electric potential gradient $\partial U/\partial r$ is proportional to the nucleus charge to the 4th-power, Z^4, and therefore tend to be important only in heavy elements. The last term $\mathbf{r} \times \mathbf{p}$ is nothing other than the orbital angular momentum, L, and therefore SOC is not present in s-orbitals. The SOC interaction Hamiltonian for atomic orbitals is then

$$H_{SOC} = \frac{\mu_B}{\hbar mec^2}\left(\frac{1}{r}\frac{\partial U}{\partial r}\right)\mathbf{L} \cdot \mathbf{S}. \tag{4.1}$$

While the SOC in solids must ultimately be related to the atomic limit and thus have the same order of magnitude, it is not straightforward to derive a general equation for solids. This is because of the extremely diverse chemical compositions and spatial symmetries in solids. It is however possible to formulate effective models for many general cases, such as the Dresselhaus effect and the Bychkov–Rashba effect [12]. A detailed discussion and derivation of these effects are beyond the scope of this thesis, and we will only use the results throughout the rest of the chapter.

In 3D topological insulators, there are 4 topological invariants, $(\nu_0; \nu_1, \nu_2, \nu_3)$, each taking value 0 or 1, with 1 being topologically nontrivial. Fu, Kane, and Mele came up with a simple method to compute these invariants [13, 14]:

$$(-1)^{\nu_i} = \prod_{j=1}^{n} \delta_j, \tag{4.2}$$

where $n = 8$ for ν_0 and $n = 4$ for the rest, and the product $\delta_{j1} \times \delta_{j2}$ determines the time reversal polarization at time reversal invariant momentum (TRIM) Λ_j. Here, Λ_{j1} and Λ_{j2} are 2 momenta that project onto the same point on a particular surface, on which we are interested in the surface states' spectra. For example, the k-points (1,0,0) and (1,0,1) both project onto the same point on the (0,0,1) surface. We also see that ν_0 is a special invariant, which involves all 8 TRIM in 3D and characterizes a "strong TI." That is, any of the surfaces is guaranteed to host topological surface states, which are also robust against weak time reversal invariant perturbations. If $\nu_0 = 0$, the other 3 invariants can still independently take nonzero values and predict at least one surface with topological states.

Although $\delta_j = \pm 1$ is in general not easy to compute, for lattices with inversion symmetry, δ_j simplifies to the product of the parity eigenvalues of all valence bands evaluated at TRIM Λ_j [13]. Nontrivial surface states arise due to the "band inversion" at TRIM points in the BZ as depicted in Fig. 4.1. The bulk conduction and valence bands are separated by a band gap, as derived from DFT calculations without including SOC. Assuming that the two bands have different parity eigenvalues (with respect to the inversion symmetry operator), denoted by

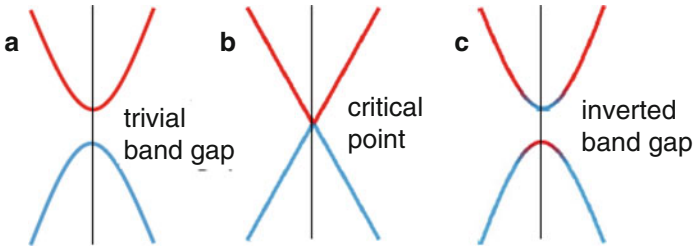

Fig. 4.1 From left to right are illustrations of "band inversion" due to increasing spin orbit coupling strength (figure adapted from [8]). (**a**) Band insulator where the conduction and valence bands with opposite parity eigenvalues are separated by a trivial band gap. With increasing SOC, the gap closes in (**b**) and eventually crosses each other and opens up a nontrivial band gap due to avoided crossing. As a result, the orbital character at the high symmetry point is inverted

red and blue colors, the inclusion of SOC will decrease the band gap at some high symmetry k-points given the proper orbital characters [15]. Once the gap becomes negative, the band crossing points can be hybridized and open up a gap in the bulk due to "avoided crossing." The parity at the high symmetry point is then inverted, giving an additional negative sign to δ_j, which leads to nonzero ν_i. Outside the crystal, the topological invariant is necessarily zero, because vacuum is a trivial "insulator" for electrons. As a consequence of the "bulk–boundary correspondence" [16, 17], the band gap must goes to zero at the bulk–vacuum interface, i.e., gapless surface states are guaranteed by the topology of the bulk bands.

4.1.2 Topological Surface States

It should be emphasized that every bulk material has its surface (boundary) states, which arise simply due to the abrupt change of electronic potential at the bulk–vacuum boundary. This argument applies both to the electronic and lattice degree of freedom, as illustrated in Sect. 4.2, comparing the surface to bulk states. In general, the long lived Bloch states inside the bulk of the crystal are solutions to the periodic Schrödinger's equation. These solutions are no longer valid at the crystal interface due to the breakdown of lattice periodicity [18, 19]. The eigenstates (electronic or phononic) satisfying the surface boundary conditions are localized states at the surface and exponentially decay into the bulk, as illustrated in Fig. 4.2. Namely, the eigen-energies of the surface states are entirely within the bulk band gap. Note that this is very different than a bulk state that extends to the surface. The main difference is that the bulk states will more often than not have finite k_z dependence, while surface states do not. If the surface states are not energetically well-separated from the bulk bands, then the hybridization between surface and bulk bands results in the so-called surface resonance, as illustrated in the third column of Fig. 4.2. Typically

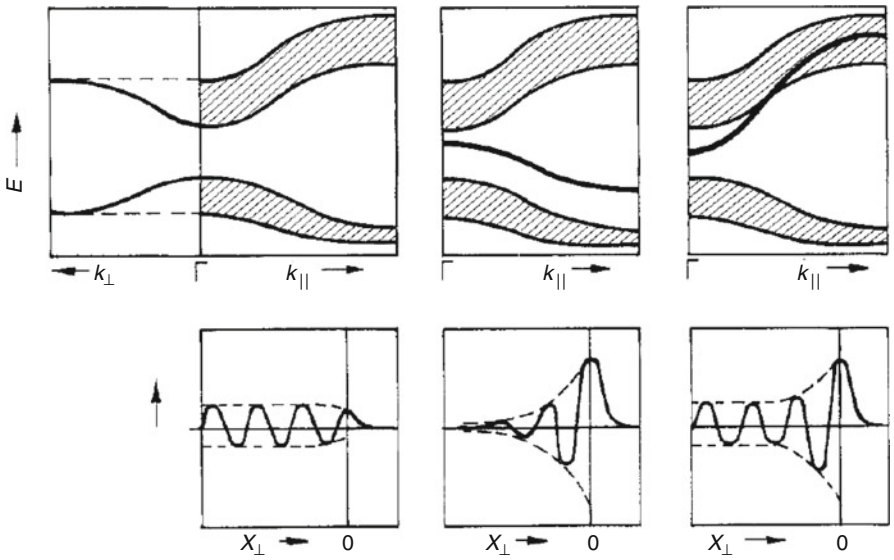

Fig. 4.2 Illustrations of the electron bands/states and wave functions at the crystal–vacuum interface, reproduced from [19]. (Top row) From left to right are the electronic band structures for bulk bands, surface states, and surface resonance, respectively. The shaded areas are the bulk bands of all k_z values projected onto the surface BZ, where k_z is the momenta along the out-of-plane direction. They are reproduced in the center and right columns to illustrate the positions of the bulk bands, where the surface state/resonance is denoted by the thick line. (Bottom row) The electronic wave functions associated with the top band structures

this happens if the surface state and bulk band satisfy certain symmetry constraints (see, for example, [20]). In a surface resonance, the state has finite intensity through the whole bulk but is enhanced at the surface.

The non-topological surface states or resonances are highly sensitive to the details of the crystal's surface structures, such as the termination of the atomic layers, surface reconstruction and dangling bonds. Whereas the topological surface states are a necessity of the material's band topology that does not care about the details of the surface structure. In fact, the topological surface states are extremely robust and not easily destroyed by surface doping, which is useful to distinguish the topological from trivial surface states that could coexist in topological insulators [21, 22].

The 3D TIs and trivial (band) insulators are similar to each other in the sense that both of their Fermi energies (E_F) are within the bulk band gap (Fig. 4.3). But in the case of a 3D TI, there are additional gapless surface states inside the bulk band gap that intersects E_F at the "Dirac point." These additional states support 2D conducting channels at the surface and are protected from nonmagnetic impurity scatterings due to time reversal symmetry [13]. The topological surface states in a 3D TI are described by the Hamiltonian:

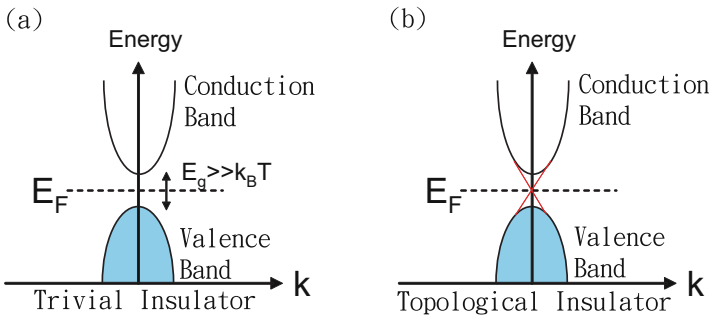

Fig. 4.3 (**a**) Illustration of the typical band structure of a trivial insulator. Colored area denotes bands filled by electrons. Valence band is totally filled, while the conduction band is empty. They are separated by a band gap E_g, which is much larger than the thermal energy k_BT. The dash line depicts the position of Fermi level E_F. (**b**) The band structure of an ideal topological insulator. The gapless surface states are denoted by the red lines

$$H(\mathbf{k}) = \frac{k^2}{2m^*}\sigma_0 + v_F\boldsymbol{\sigma}\cdot\mathbf{k}, \tag{4.3}$$

where m^* is the effective mass, v_F is the Fermi velocity, $\boldsymbol{\sigma} = (\sigma_x, \sigma_y, \sigma_z)$ are the Pauli matrices, σ_0 is the 2×2 unit matrix, and $\mathbf{k} = (-k_y, k_x, \frac{\lambda}{2v_F}[k_+^3 + k_-^3])$ with $k_\pm \equiv k_x \pm ik_y$. The z component of $\mathbf{k}$ describes hexagonal warping of the surface states away from the Dirac point [23].

The energy dispersion of the surface states described by Eq. (4.3) is

$$E_\pm(\mathbf{k}) = \frac{k^2}{2m^*} \pm \sqrt{v_F^2k^2 + \lambda^2k^6\cos^2(3\theta)}, \tag{4.4}$$

where $\pm$ corresponds to the upper and lower Dirac cones, and θ is the azimuth angle of in-plane momentum $\mathbf{k}$ with respect to the x axis ($\Gamma - K$). To the lowest order expansion in k, the dispersion is linear with the wave vector k, $E = v_F\hbar k$, where v_F is Fermi velocity. Due to its linear dispersion, the *rest mass* of Dirac Fermion near Dirac point is zero. Their wave function must be described by Dirac equation rather than Schrödinger equation. The charge carriers in the surface states are also called "Dirac fermions." One direct consequence of zero effective mass is the well-defined chirality

$$h \equiv \sigma\cdot\mathbf{p} = \pm 1, \tag{4.5}$$

where σ is Pauli matrix and $\mathbf{p}$ is momentum unit vector. For typical particles with nonzero mass, $\mathbf{p}$ depends on the observer's reference frame and may even change sign if the observer is moving faster than the particle. Therefore, chirality is not well-defined for massive particles. But the eigenvalue of chirality operator is irrelevant to the observer's reference frame when acting on wave functions described by Dirac

equation. Therefore, the chirality of Dirac fermion is well-defined and the surface states are referred to as "chiral states."

A consequence of well-defined chirality is the suppression of the $2k_F$-scatterings (backscattering). Since chirality is a conserved physical quantity in topological insulators, electrons moving in opposite direction are required to have opposite spins (from Eq. 4.5). Therefore, backscattering is suppressed since it requires higher energy to flip electron spins [24]. This predicts a higher mobility for the conductive topological surface states as compared to usual surface states. However, one should note that the spin-momentum texture does *not* exclude scattering from any other angles, e.g., 175 degrees. To date, the observed electronic transport properties of the topological surface states are in general quite similar to usual 2D electronic states, except for the weak anti-localization [25, 26], and quantum interference effects [27].

Another consequence of the linear dispersion is the π-shift in Berry's phase, γ [28]. We know that electrons in crystals moving in a closed trajectory at constant energy in momentum space gain an additional phase called Berry's phase that is zero in typical conductors and π in massless Dirac materials (without considering spin–orbit coupling). Further consideration of spin–orbit interaction (which is non-negligible in topological insulators) will modify this π shift in Berry's phase [25]. The exact value of this phase shift can be experimentally determined through Shubnikov–de Haas oscillations [26, 29].

4.1.3 The Band Structure in Bi_2Se_3

$Bi_{1-x}Sb_x$, Bi_2Se_3, and Bi_2Te_3 were first theoretically predicted to be 3D topological insulators [13, 15]. Later on, the 2D surface state of $Bi_{1-x}Sb_x$ was experimentally confirmed using Angle Resolved Photoemission Spectroscopy (ARPES) [30]. Soon after, Bi_2Se_3 [31] and Bi_2Te_3 [32] were also experimentally confirmed by ARPES. Calculated band structure of Bi_2Se_3 is shown in Fig. 4.4a, where the warmer color denotes a higher density of states (DOS). The gapless states with linear dispersion can be seen crossing bulk band gap. The center white line denotes the position of Fermi surface. Experimental result of Bi_2Se_3 from ARPES is shown in Fig. 4.4b. The color code denotes ARPES spectra height, which is proportional to electron DOS. The yellow areas are bands with high DOS, indicating the position of bulk bands, and the lower one and upper one are valence band and conduction band, respectively. The white dotted line marks the position of the Fermi level. A red colored, gapless band with almost linear dispersion can be seen inside the bulk band gap. The electron cyclotron mass can be estimated from the energy dispersion in Fig. 4.4b. The cyclotron effective mass is usually defined as [4]

$$m_c = \frac{\hbar^2}{2\pi}\frac{\partial A}{\partial E}, \tag{4.6}$$

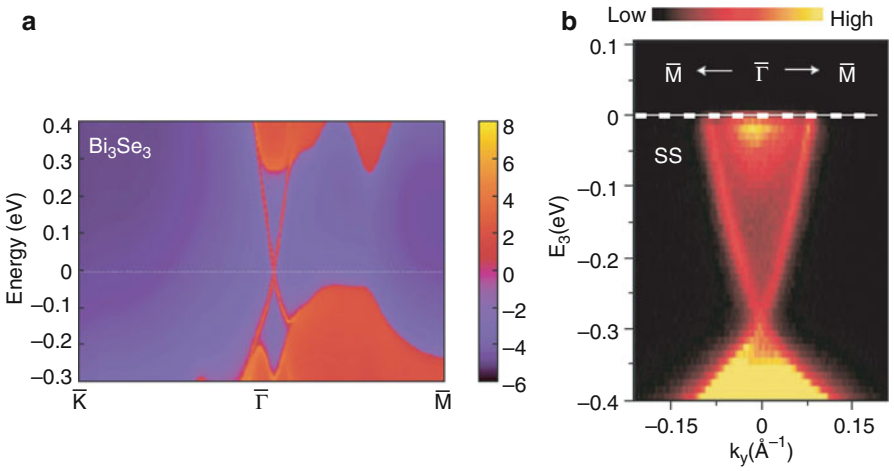

Fig. 4.4 (**a**) Theoretical work based on first principle calculations from [15]. The warmer color indicates higher electron DOS, and the blue regions are bulk band gap. The upper and lower irregular red regions are the bulk conduction and valence bands, respectively. A linear dispersed gapless surface state can be seen inside the bulk band gap. (**b**) The ARPES measurement of surface electronic band structure from [31]. The warmer color denotes higher electron DOS, and the black region is bulk band gap. The upper and lower yellow regions are bulk conduction and valence bands, respectively. The white dash line marks the position of Fermi level. A red colored, gapless band with nearly linear dispersion can be seen inside the bulk band gap

where A is k-space area enclosed by the orbit and E is the energy. Combine the above equation with the linear dispersion relation of Dirac fermions, $E = v_F \hbar k$, it can be shown that $m_c = \hbar k / v_F$. Therefore, the cyclotron mass is zero at Dirac point. The Fermi velocity estimated from Fig. 4.4b is $\sim 4.6 \times 10^5$ m/s, and the cyclotron mass in surface states near E_F is $\sim 0.25\, m_0$ ($k_F \sim 0.1$ Å^{-1} and $E_F \sim 300$ meV), where m_0 is the free electron mass. For the electrons at the bottom of conduction band in Fig. 4.4b (assume parabolic dispersion, $E = \hbar^2 k^2 / (2m_c)$), the estimated cyclotron mass $m_c \sim 0.12\, m_0$ for electrons near E_F ($k_F \sim 0.04$ Å^{-1} and $E_F \sim 50$ meV).

The crystal structure of Bi_2Se_3 is shown in Fig. 4.5 (figure from [15]). The primitive lattice vectors are denoted as t_1, t_2, and t_3. It has layered structure with a triangular lattice within one layer. Each unit cell consists of five-atom layers along the **c**-axis, which is known as a quintuple layer (indicated by the red square). The lattice atoms in a quintuple layer have three different positions, denoted as A, B, and C. The thickness of each quintuple layer is about 1 nm, and the coupling force between quintuple layers is weak (van der Waals type).

One of the most important feature of the surface state is its spin texture. The electron spins of the surface states are predicted to be in-plane and perpendicular to the momentum (see Fig. 4.6a). The red arrows denote spin direction of each point on the intersection of Fermi surface and Dirac cone. Those spin textures have been verified by ARPES (Fig. 4.6b–d). Figure 4.6b is the top view of the Dirac

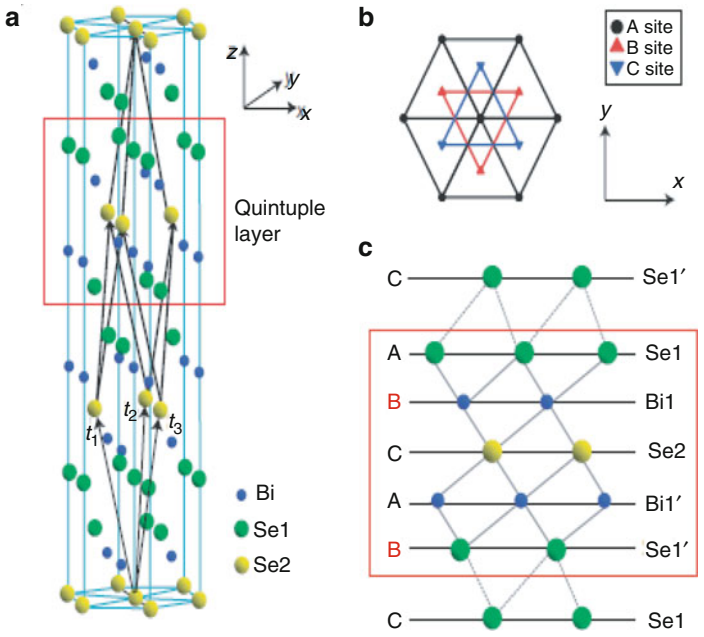

Fig. 4.5 (**a**) Crystal structure of Bi_2Se_3 with three primitive lattice vectors denoted as t_1, t_2, and t_3. A quintuple layer is indicated by the red square. (**b**) Top view along the z-direction. The lattice atoms in a quintuple layer have three different positions, denoted as A, B, and C. (**c**) Side view of the quintuple layer, which is about 1 nm thick. Figure adapted from [15]

cone intersection with Fermi surface, where the yellow arrows are the expected spin orientation. The inner white area is the bottom of bulk conduction band, but a darker ring with radius $\sim 0.1\,\text{Å}^{-1}$ is the intersection of Dirac cone with Fermi level. Figure 4.6c and d shows the measured spin polarizations along the k_x direction (z direction is defined as out of plane). No clear signal can be seen in x and z components. But in the y component, a clear peak of opposite sign and equal value at $k_x \sim \pm 0.1\,\text{Å}^{-1}$ can be seen, which is in accord with the position of Dirac cone edge. This observation agrees well with the theoretical prediction [14]. We can understate this spin texture in a simple way. We know that, due to relativistic effect, moving charge carriers in their rest frame will experience an effective magnetic field $\mathbf{B}_{eff} \sim \mathbf{v}_F \times \mathbf{E}$, where $\mathbf{v}_F$ is Fermi velocity of the charge carriers, and $\mathbf{E}$ is the electric field exerted on the charge carriers in crystal's rest frame. This effect is more pronounced in systems with strong spin–orbit coupling. When considering the carriers confined on the surface of a crystal, those carriers will only experience an effective electric field $\mathbf{E}_s$ along out-of-plane direction from symmetry argument. Therefore, the effective magnetic field will be pointing along in-plane direction and perpendicular to $\mathbf{v}_F$. Electrons moving on the surface will then tend to line up their spins with $\mathbf{B}_{eff}$ in order to minimize Zeeman energy, which is proportional to $\sigma \cdot \mathbf{B}_{eff}$. From this point of view, charge carriers moving in opposite direction

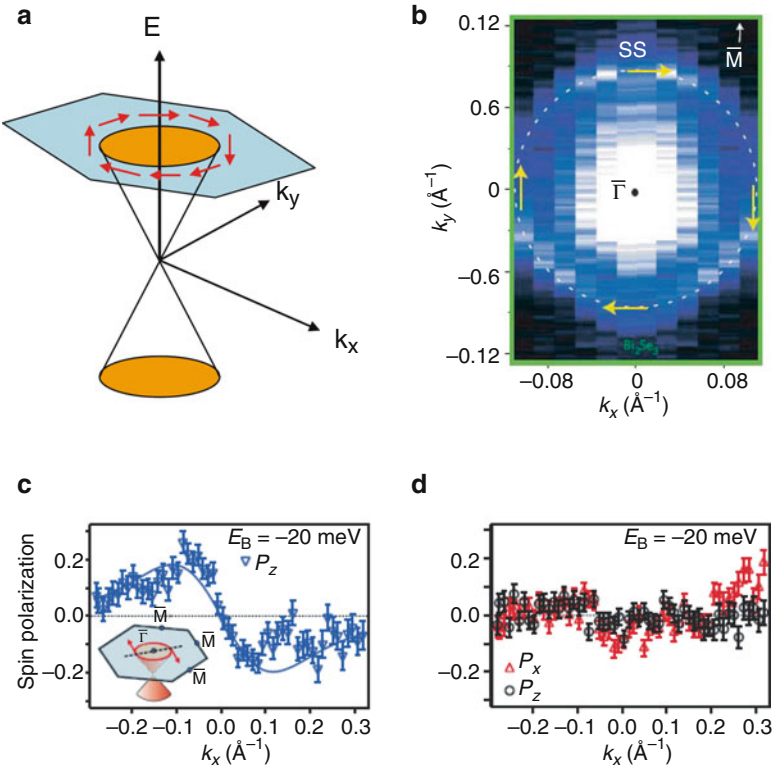

Fig. 4.6 (**a**) Schematic drawing of Bi_2Se_3 surface state spin texture near Fermi energy (denoted by the blue hexagon). The red arrows denote spin direction of each point on the intersection of Fermi surface and Dirac cone. (**b**) ARPES result from [31]. The inner white area is the bottom of bulk conduction band. A darker ring with radius ~0.1 $Å^{-1}$ is the intersection of Dirac cone with Fermi surface. The yellow arrows denote the spin directions. (**c**) and (**d**) are the spin polarizations along k_x, with z defined as the out-of-plane direction. Figure adapted from [21]. No clear signal can be seen in x and z components. But in the y component, a clear peak of opposite sign and equal value at $k_x \sim \pm 0.1$ $Å^{-1}$ can be seen, which is in accord with the position of Dirac cone

will have their spin polarization inverted. Because the effective field is pointing along opposite direction on the opposite surface, spin polarization of charge carriers moving in the same direction but on opposite surface will also be inverted.

Kane and Mele developed an easy way to distinguish nontrivial topological insulators (such as Bi_2Se_3) from trivial ones (band insulator) using a special topological invariant, Z_2 [8, 13]. They found that for a material with Fermi level inside band gap, Z_2 can only be 0 (trivial insulator) or 1 (nontrivial topological insulator). Z_2 can be easily determined by counting the number of Dirac pairs inside the band gap and then take modulo 2. For materials with $Z_2 = 1$, the gapless surface states are protected from weak disorder and nonmagnetic impurities by time

reversal symmetry (TRS). For materials with $Z_2 = 0$, the surface states can be easily destroyed by a small perturbation and become trivial insulators.

4.1.4 Materials and Methods

Table 4.1 lists 6 Bi_2Se_3 single crystals and films measured in this study. The single crystals were grown by modified Bridgman method. Mixtures of high-purity bismuth (99.999%) and selenium (99.999%) with the mole ratio Bi : Se = 2 : 3 were heated up to 870 °C in sealed vacuum quartz tubes for 10 h and then slowly cooled to 200 °C with rate 3 °C/h, followed by furnace cooling to room temperature. The thin film samples were epitaxially grown on Al_2O_3 (0001) substrates in a custom designed molecular beam epitaxy (MBE) chamber [29, 33]. They were immediately transferred into a cryostat after taking out of MBE chamber. Notice that the light penetration depth in Bi_2Se_3 within energy range of current study is about 10 nm [34]. Therefore, the signal is dominated by scattering from the first few QLs of Bi_2Se_3, and the scattering volume in the superlattice samples is practically the same as bulk.

Bi_2Se_3 has a rhombohedral crystal structure with the D_{3d} point group symmetry. The irreducible representations and Raman selection rules are given in Table 4.2. With five atoms in a primitive unit cell, there are a total of three acoustic and 12 optical bulk phonon branches. At the Γ-point, the irreducible representations of the Raman active phonons are $2A_{1g} + 2E_g$, and the infrared active phonons are $2A_{2u} + 2E_u$ [35, 36], where the corresponding atomic displacements are shown in Fig. 4.7. These bulk phonon modes have been measured by Raman and infrared spectroscopies [35–46], and the values reported in [37] and [40] are listed in Table 4.3.

The crystal naturally cleaves along the (111) surface terminated at Se atoms, forming optically flat QLs weakly bonded by van der Waals force [35]. The surface QL has the symmorphic $P6mm$ wallpaper group symmetry (two-dimensional crystallographic point group C_{6v}) [48–50]. Since the surface layer phonon modes in Bi_2Se_3 are not perfectly localized and decay into the bulk, it is more appropriate to analyze our experimental results within the layer group $P3m1$ (crystallographic

Table 4.1 The list of single crystal and films measured in this study

Sample #	Composition	Description	Growth
#2	Bi_2Se_3	50 QL thick film	MBE
#8	$(Bi_2Se_3)_m(In_2Se_3)_n$	50 nm superlattice with (m,n)=(5,5)	MBE
#10	$(Bi_2Se_3)_m(In_2Se_3)_n$	50 nm superlattice with (m,n)=(10,5)	MBE
#13	$Bi_{1.95}In_{0.05}Se_3$	Single crystal with indium doping	Bridgman
#14	Bi_2Se_3	Pristine single crystal	Bridgman
#A	Bi_2Se_3	Pristine single crystal	Bridgman

Table 4.2 The Raman selection rules in the bulk and on the surface of Bi_2Se_3 [51, 52]. Upon the reduction of symmetry from point group D_{3d} to C_{3v}, the A_{1g} and A_{2u} irreducible representations merge into A_1, A_{2g} and A_{1u} merge into A_2, and E_g and E_u merge into E [53]. Note that the surface phonon and electron wave functions are characterized by different symmetry groups [49] and thus follow different selection rules

Scattering geometry	Bulk (D_{3d})	Surface phonon (C_{3v})	Surface electron (C_{6v})
RR	$A_{1g} + A_{2g}$	$A_1 + A_2$	$A_1 + A_2$
RL	$2E_g$	$2E$	$2E_2$
XX	$A_{1g} + E_g$	$A_1 + E$	$A_1 + E_2$
YX	$A_{2g} + E_g$	$A_2 + E$	$A_2 + E_2$

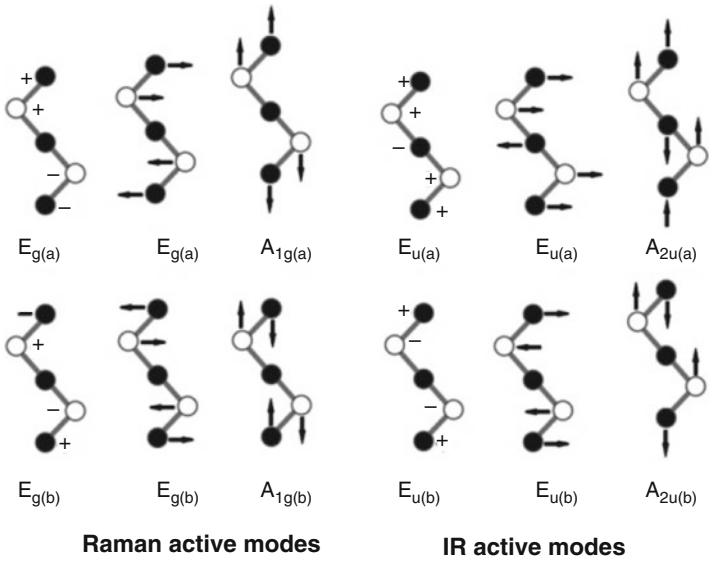

Fig. 4.7 Schematic drawing of the atomic displacements corresponding to the optical phonon modes in Bi_2Se_3 at the BZ center. The black and white spheres correspond to Bi and Se atoms, respectively. The $\pm$ signs denotes movements in the direction perpendicular to the paper. Figure adapted from [47]

point group C_{3v}, which is a subgroup containing common symmetry operators of D_{3d} and C_{6v} groups) [49].

All Raman scattering measurements are taken from *ab* surfaces freshly cleaved or grown immediately prior to the measurements. Samples #2–14 are measured in a quasi-backscattering geometry in a continuous He-flow optical cryostat. A glove bag with controlled dry nitrogen gas environment was sealed to the cryostat loading port. After purging the bag to the desired conditions, the single crystals were cleaved in the glove bag immediately before loading into the cryostat for cooling, without exposure to air. We use λ_L =532 nm solid state laser for excitation, where the spot

Table 4.3 The summary of the bulk and surface phonon mode energies. This work's data is compared to the spectroscopic and DFT computation studies reported in the literature. All values are given in units of cm^{-1}

	Experiment		Calculation	
Symmetry	This work	Literature	LDA+SOI [75]	GGA+SOI [47]
$A_{1g}^{(1)}$	75	73 [39, 40, 43, 46]	77	64
$A_{1g}^{(2)}$	180	175 [39, 40, 43, 46]	176	167
$E_g^{(1)}$	39	39 [39, 40, 43, 46]	41	39
$E_g^{(2)}$	137	133 [39, 40, 43, 46]	139	124
$A_{2u}^{(1)}$	–	N/A	139	137
$A_{2u}^{(2)}$	–	N/A	161	156
$E_u^{(1)}$	–	61 [37]	80	65
$E_u^{(2)}$	–	133 [37]	131	127
$A_1^{(1)}$	60	68 [68]	N/A	N/A
$A_1^{(2)}$	136	129 [40]	N/A	N/A
$A_1^{(3)}$	158	160 [40, 71]	N/A	N/A
$A_1^{(4)}$	173	N/A	N/A	N/A
$E^{(1)}$	67	68 [40]	N/A	N/A
$E^{(2)}$	126	125 [40]	N/A	N/A

size is roughly 50 μm. The scattered light was analyzed and collected by a custom triple-grating spectrometer equipped with a liquid nitrogen cooled CCD detector.

The irreducible representations of the D_{3d} and C_{3v} groups corresponding to these scattering geometries are listed in Table 4.2. Notice that in both the D_{3d} and C_{3v} groups, the phonon intensities do not depend on the orientation of the crystallographic axis. The notations X and Y have no reference to the crystallographic a and b axes.

4.2 Surface Phonons

Theoretical modeling of surface lattice dynamics was first developed by Lifshitz and Rosenzweig [54, 55] and later expanded by various workers [56–59]. The basic idea is to consider the free surface as a perturbation of an infinite lattice and therefore to derive the surface modes from the spectrum of bulk vibrations. As a result, the frequencies of atomic vibration modes at the surface are modified to a smaller value than in the bulk at the Brillouin zone center (Γ point). If there is a gap in the phonon density of state (DOS) and with large enough distortion, the surface phonon DOS can be entirely separated from the bulk [54, 57]. Such modes are long lived and localized at the surface, where the dispersion can be quite different than the bulk [60]. However, it is often experimentally challenging to distinguish surface signal from the overwhelmingly stronger intensity contribution of the bulk. Moreover, if the surface vibration mode is not completely gapped out from the bulk

spectrum, then the surface and bulk modes are indistinguishable. Instead, the "bulk phonon" acquires only a slight energy shift near the crystal surface. Notice that the surface modes originate from abrupt termination of the lattice restoring force across bulk–vacuum interface in a semi-infinite crystal and should not be confused with the phonons in quasi-2D ultrathin samples, which are almost decoupled from the underlying substrate of a different material [38, 39, 42, 44, 61].

While the bulk phonon modes have been extensively studied in Bi_2Se_3 single crystals [35–46], only a few papers have reported studies of the surface vibration modes. Zhu and coworkers observed strong Kohn anomaly at about $2k_F$ using helium atom scattering (HAS) [62] and deduced the interaction between surface phonon and the Dirac electrons to be much stronger than the values previously reported by angle-resolved photoemission spectroscopy (ARPES) measurements [63–66], suggesting that the electron–phonon coupling on TI surface may be more complex than anticipated. Time-resolved ARPES study of single crystals reported the observation of one A_{1g} bulk phonon at about 74 cm^{-1}, and an additional mode with slightly lower energy that couples much stronger to the surface states, consistent with what was suggested by transport measurements [67]. This mode was interpreted as a surface phonon associated with the observed A_{1g} bulk phonon [68]. However, alternative results have also been reported [65, 66, 69, 70], suggesting the existence of multiple phononic decaying channels that may depend on the details of sample preparation. Electron energy loss spectroscopy (EELS) study has distinguished a weak mode at about 160 cm^{-1} in Bi_2Se_3, which was assigned to the surface vibration mode associated with an A_{1g} bulk phonon [71]. The Raman scattering work on bulk single crystal [40] and exfoliated nano-crystals reported several additional features, and they were attributed to infrared active phonon modes becoming Raman active due to inversion symmetry breaking at crystal surface [38, 44].

4.2.1 Results

Raman spectroscopy is a conventional tool for studying surface phonon modes [72, 73]. The advantages of Raman spectroscopy is the wider accessible energy range compared with HAS, much higher energy resolution compared to EELS, and the additional information on the symmetries of the phonon modes. We focus our study on the bulk single crystals, which are unexposed to air or any chemicals. In addition to the four Raman active bulk phonons, we observed 6 additional modes with about 20–100 times weaker intensities compared to the bulk phonons (Fig. 4.8). By comparing the data to the results obtained by the complementary spectroscopic techniques and the calculations, we assign the observed additional modes to surface phonons arising from out-of-plane lattice distortion near the crystal–film interface.

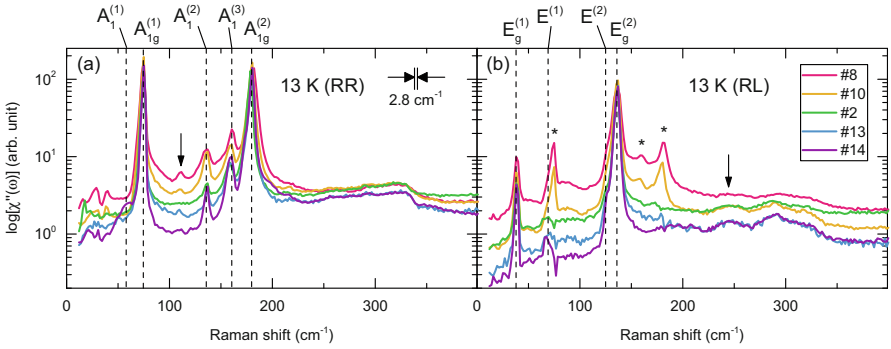

Fig. 4.8 The Raman response function $\chi''(\omega)$ measured in the (**a**) RR and (**b**) RL scattering geometry at 13 K with 532 nm excitation from various Bi_2Se_3 samples as described in Table 4.1, plotted on a semi-log scale. The dashed lines label the observed phonon modes as tabulated in Table 4.3. (**a**) The mode at 110 cm^{-1} indicated by arrow is due to the phonon signal from α-In_2Se_3 layers [74]. The asterisks mark the phonon modes with A_{1g} and A_1 symmetries, which appear in RL geometry due to indium atom diffusion. The instrumental resolution of 2.8 cm^{-1} is shown

Sample Dependences

Figure 4.8 shows the Raman response function $\chi''(\omega)$, taken at 13 K with 532 nm excitation, plotted on a semi-log scale. In order to confirm the tiny features of surface modes, we compared the results from bulk crystals and MBE films. Figure 4.8a and b is measured with the RR and RL scattering geometries, respectively (Table 4.2). The dashed lines label the observed phonons as tabulated in Table 4.3. The strong modes at 72 and 174 cm^{-1} in RR scattering geometry are the bulk A_{1g} phonons of Bi_2Se_3 (Fig. 4.8a), and the strong modes centered at 37 and 132 cm^{-1} in RL are the bulk E_g phonons (Fig. 4.8b), consistent with the previous Raman studies [39, 40] and calculations [75].

The broad feature at about 330 cm^{-1} in RR is possibly due to second-order scattering of the $A_{1g}^{(2)}$ phonon, broadened due to the large downward dispersion of the phonon branch [75]. Similarly, the broad feature observed around 300 cm^{-1} in RL is assigned to two-phonon excitation, $A_{1g}^{(2)} + E_g^{(2)}$. The broad feature at about 245 cm^{-1} (Fig. 4.8b, marked by arrow) was previously assigned to the 2D stretching mode of Se atoms on the surface [76]. However, we do not observe the reported resonance effect of this mode with near-infrared excitation (Fig. 4.9). Notice that this mode's energy is also consistent with the two-phonon excitation of $A_{1g}^{(2)} + E_g^{(1)}$.

In order to distinguish the broad features from electronic origin, such as excitations from the topological surface states, we compared the results with indium doped Bi_2Se_3 in Fig. 4.8. Indium doping was shown to increase the carrier density and suppress the topological surface states in Bi_2Se_3 [29, 77]. Here, we collected data from bulk single crystals and MBE grown In_2Se_3/Bi_2Se_3 superlattices, where indium doping is achieved through diffusion in the superlattices [78]. In all indium

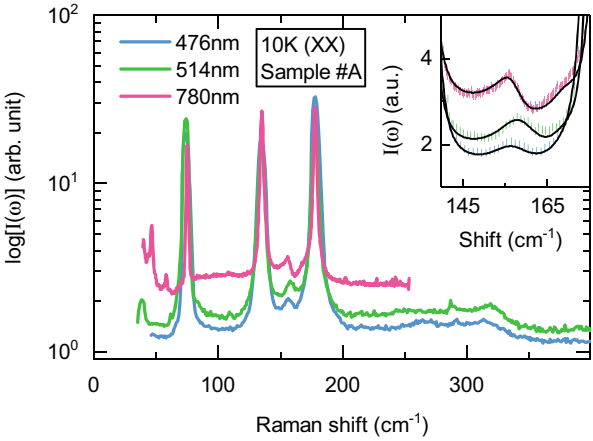

Fig. 4.9 The excitation dependence of scattering intensity in the XX polarization geometry, measured at 10 K from a bulk Bi_2Se_3 single crystal, plotted on a semi-log scale. The blue, green, and pink lines correspond to laser excitation energy of 476, 514, and 780 nm, respectively. Inset: enlarged plot around the $A_1^{(3)}$ mode. The black lines are fit to Fano line shape in Eq. (4.7)

doped samples, the broad features show the same intensity, suggesting their origin unrelated to the topological surface states. This feature is slightly weaker in the superlattice sample #8, despite that the first-order phonon modes are still sharp and strong. However, this is likely mainly due to the indium atom diffusion into the Bi_2Se_3 layer, which breaks the translation symmetry and therefore further broadens the multi-phonon mode. The diffused indium atoms also lower the local crystal symmetry in the Bi_2Se_3 layers, which therefore allows vibration modes with A_{1g} and A_1 symmetries to appear in the RL geometry, which is otherwise forbidden for the crystal symmetry of Bi_2Se_3 (Fig. 4.8b, marked by asterisks). The small feature at 110 cm^{-1} in RR is due to a strong phonon of α-In_2Se_3 layers [74] (indicated by arrow in Fig. 4.8a).

In addition to the strong bulk first-order Raman phonons and the broad features, we see additional sharp modes that are about 20 times weaker than the bulk phonons. In Fig. 4.8a, two such features at 136 and 158 cm^{-1} are seen in all samples in RR scattering geometry, labeled $A_1^{(2)}$ and $A_1^{(3)}$, respectively. In the bulk single crystal sample #14, we observed a mode at about 60 cm^{-1}, which we label as $A_1^{(1)}$. We associate these three features with vibration modes at the crystal surface, to be discussed in the RR polarization for the Sample #14 in the next section. We also noticed several sharp features below 50 cm^{-1} in samples #8 and #10 in RR, which are possibly zone folded phonons. In the RL scattering geometry, we observed two weak features at 67 and 126 cm^{-1}, labeled $E^{(1)}$ and $E^{(2)}$, respectively (Fig. 4.8b). The energies of these modes are close to the strong bulk phonons and therefore require higher resolution to distinguish them.

Excitation Dependences

In Fig. 4.9 are the Raman spectra of the bulk sample at different excitation wavelengths at 10 K. The spectra were obtained in the XX polarization. As in Fig. 4.8,

we observe an additional peak at 158 cm^{-1}, which we refer to as $A_1^{(3)}$. However, note that the mode is more asymmetric when 780 nm excitation wavelength is used. While the bulk phonons show little resonance effect, the $A_1^{(3)}$ phonon displays antisymmetric line shape with 780 nm excitation, reminiscent of a Fano line shape [79] (Fig. 4.9, inset). This is an indication that the $A_1^{(3)}$ phonon is interacting with a continuum. This was overlooked in the previous Raman studies and may be related to the 20 meV "kink" in the topological surface state's energy dispersion curve reported by some ARPES measurements [69, 70].

The observation of Fano line shape is a clear evidence for the existence of underlying electronic continuum in the A_1 symmetry channel, which interacts with the $A_1^{(3)}$ phonon [79, 80]. The excitation dependence also suggests resonance enhancement of the electronic continuum with near-infrared wavelength, consistent with the reported surface states at about 1.6 eV above the Fermi energy [81, 82]. Fitting the 780 nm data with Eq. 4.48 in [80]:

$$I(\omega) = \frac{\pi\rho T_e^2(\omega_0 - \omega - VT_p/T_e)^2}{(\omega_0 - \omega + V^2R)^2 + (\pi V^2\rho)^2} \tag{4.7}$$

yields electron–phonon interaction strength $V \approx 2.6\,\text{cm}^{-1}$, and phonon energy $\omega_0 \approx 158\,\text{cm}^{-1}$. Here we assumed that the electron DOS ρ is a constant in the relevant energy window and neglected the real part of the electronic Green's function R. T_p and T_e are the phonon and electronic continuum Raman transition matrix elements, respectively.

Symmetries of the Phonon Modes

To further understand the observed phonon modes, we measure the Raman response in four scattering geometries of the D_{3d} and C_{3v} point group as listed in Table 4.2 (Fig. 4.10a). The intensity contributed by each symmetry channel in different scattering geometries is dictated by the Raman tensors [51, 52], and the results for D_{3d} and C_{3v} groups are listed in Table 4.2. Therefore, by obtaining polarized Raman spectra in four proper scattering geometries, we can separate the measured Raman response from each symmetry channel.

$$\begin{aligned}
\chi''_{A1g}(\omega) + \chi''_{A1}(\omega) &= \chi''_{\text{XX}}(\omega) - \frac{1}{2}\chi''_{\text{RL}}(\omega) \\
\chi''_{A2g}(\omega) + \chi''_{A2}(\omega) &= \chi''_{\text{YX}}(\omega) - \frac{1}{2}\chi''_{\text{RL}}(\omega) \\
\chi''_{Eg}(\omega) + \chi''_{E}(\omega) &= \frac{1}{2}\chi''_{\text{RL}}(\omega).
\end{aligned} \tag{4.8}$$

The results are shown in Fig. 4.10b. We notice that no lattice vibrational mode is observed in the A_{2g} and A_2 symmetry channels. This is because the Raman

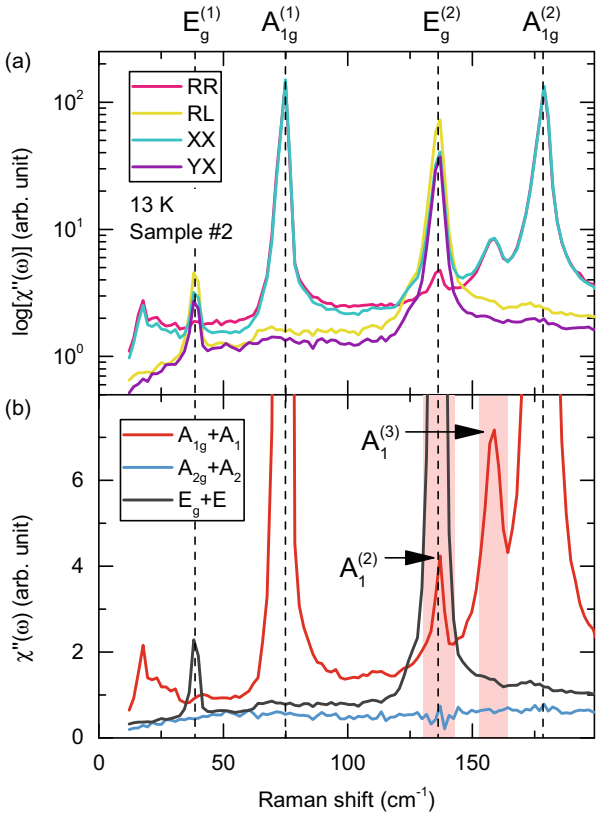

Fig. 4.10 (**a**) The Raman spectra taken in all four scattering geometries at 13 K with 532 nm excitation from a Bi_2Se_3 thick film, plotted on a semi-log scale. (**b**) The Raman response of different symmetry channels, obtained from data in (**a**). The bulk phonons are marked by dashed lines, whereas the surface modes are indicated by arrows and shaded in red

tensors for these two channels are antisymmetric and commonly correspond to pseudovector-like excitations [51, 83, 84], which is forbidden for phononic Raman scattering in Bi_2Se_3. Since the signals in A_{2g} and A_2 channels are expected to be zero, we can claim that all vibration modes appearing in RR have either A_{1g} or A_1 symmetry (Table 4.2).

The $A_1^{(2)}$ mode happens to have energy very close to the $E_g^{(2)}$ phonon, making it particularly difficult for spectroscopic experiments to distinguish. Here, we utilize the symmetry properties to separately detect them with polarized light. The polarization leakage of optical elements is precisely measured and removed (Appendix), and thereby excluding the possibility of $A_1^{(2)}$ being a trivial polarization leakage from the $E_g^{(2)}$ phonon.

To distinguish surface modes that are particularly weak and close in energy to the bulk phonons, we take high resolution spectra from a carefully prepared bulk crystal

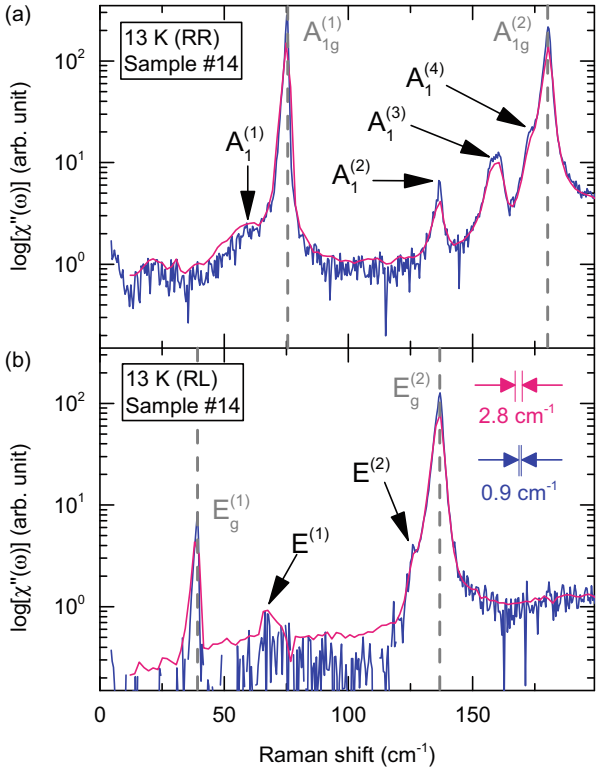

Fig. 4.11 The Raman spectra taken in the (**a**) RR and (**b**) RL scattering geometry at 13 K with 532 nm excitation from a bulk Bi_2Se_3 single crystal are plotted on a semi-log scale. The red and blue curves correspond to instrumental resolution of 2.8 and 0.9 cm^{-1} (as shown in (**b**)), respectively. The bulk phonons are marked by gray dashed lines

#14, cleaved in nitrogen environment. We show in Fig. 4.11 the spectra taken at 13 K in RR and RL scattering geometries, where the smoother low resolution (2.8 cm^{-1}) data is overlapped with the high resolution (0.9 cm^{-1}) spectra. Besides the more pronounced $A_1^{(2)}$ and $A_1^{(3)}$ modes already visible in Fig. 4.10, we see a few additional features in the high resolution data: (1) A mode centered at 173 cm^{-1} appearing as a shoulder to the $A_{1g}^{(2)}$ bulk phonon in RR geometry (Fig. 4.11a), which we designate as $A_1^{(4)}$. (2) Another mode centered at 126 cm^{-1} appearing as a shoulder to the $E_g^{(2)}$ bulk phonon in RL geometry (Fig. 4.11b), which we designate as $E^{(2)}$. (3) The mode $A_1^{(3)}$ shows broadened peak structure. This cannot be due to splitting of an A-symmetry phonon, e.g., lowering of symmetry, since A_1 is a one-dimensional representation. This can be explained as due to Fano interference, which become more pronounced with infrared excitation (Fig. 4.9).

Removal of Polarization Leakage

Due to the weakness of the surface vibration modes in Raman spectroscopy, possible polarization leakage arising from optical elements has to be carefully measured and removed, in order to avoid confusion with the weak surface modes.

The degree of leakage is determined from the $A_{1g}^{(1)}$ and $A_{1g}^{(2)}$ bulk phonons of single crystal samples at room temperature. The removal of polarization leakage is done by subtracting intensity from the orthogonal polarization geometry, i.e., $\chi''_{\mathrm{YX}}(\omega) = \overline{\chi''_{\mathrm{YX}}}(\omega) - \alpha \cdot \overline{\chi''_{\mathrm{XX}}}(\omega)$, where $\overline{\chi''_{\mathrm{YX}}}(\omega)$ and $\overline{\chi''_{\mathrm{XX}}}(\omega)$ are raw data taken in YX and XX polarization geometries, respectively, and α is the leakage ratio due to the limitations of polarization optics. It is reasonable to suggest that the same ratio also applies to XX polarization geometry: $\chi''_{\mathrm{XX}}(\omega) = \overline{\chi''_{\mathrm{XX}}}(\omega) - \alpha \cdot \overline{\chi''_{\mathrm{YX}}}(\omega)$. Similarly, we have $\chi''_{\mathrm{RL}}(\omega) = \overline{\chi''_{\mathrm{RL}}}(\omega) - \beta \cdot \overline{\chi''_{\mathrm{RR}}}(\omega)$ and $\chi''_{\mathrm{RR}}(\omega) = \overline{\chi''_{\mathrm{RR}}}(\omega) - \beta \cdot \overline{\chi''_{\mathrm{RL}}}(\omega)$ for the circularly polarized geometries, where β is the leakage ratio due to the limitations of the broadband quarter wave plate and alignment of the Berek compensator. The ratios α and β are in general a weak function of ω, but in a narrow energy window as in this study, they can be safely assumed as constants. In order to avoid confusion from contributions of surface phonons, we chose YX and RL geometries as our reference for the determination of α and β. In these two geometries, only $E_g^{(1)}$ and $E_g^{(2)}$ bulk phonons are expected to be present, the E symmetry surface modes are extremely weak and close to the bulk phonons (Fig. 4.11), and therefore they do not raise concern for the determination of α and β.

In Fig. 4.12, we show spectra of unprocessed raw data and polarization leakage removed results taken at 300 K from the *ab* surface of a Bi_2Se_3 thick film in black and red lines, respectively. The leakage intensity of $A_{1g}^{(1)}$ and $A_{1g}^{(2)}$ bulk phonons in raw data taken with YX and RL geometries can be fully removed with leakage ratios $\alpha = 0.004$ and $\beta = 0.015$, respectively. These values are within the specification of used broadband polarization optics.

The value of α depends only on the wavelength of light, and therefore the same value $\alpha = 0.004$ is used for all samples and temperatures measured with 532 nm excitation. The value of β depends critically on the alignment of the Berek compensator, which may vary between experiments and has to be determined using the method described above in each experiment. In this study, the value of β is always within the range 0.015 ± 0.005.

4.2.2 Discussion

At the crystal surface of Bi_2Se_3, the lattice structure is distorted along *c*-axis due to the abrupt reduction of the interlayer van der Waals force that binds the crystal together and is calculated by density functional theory (DFT) to be about 10% along *c*-axis [68]. Additionally, the observation of two-dimensional electron gas

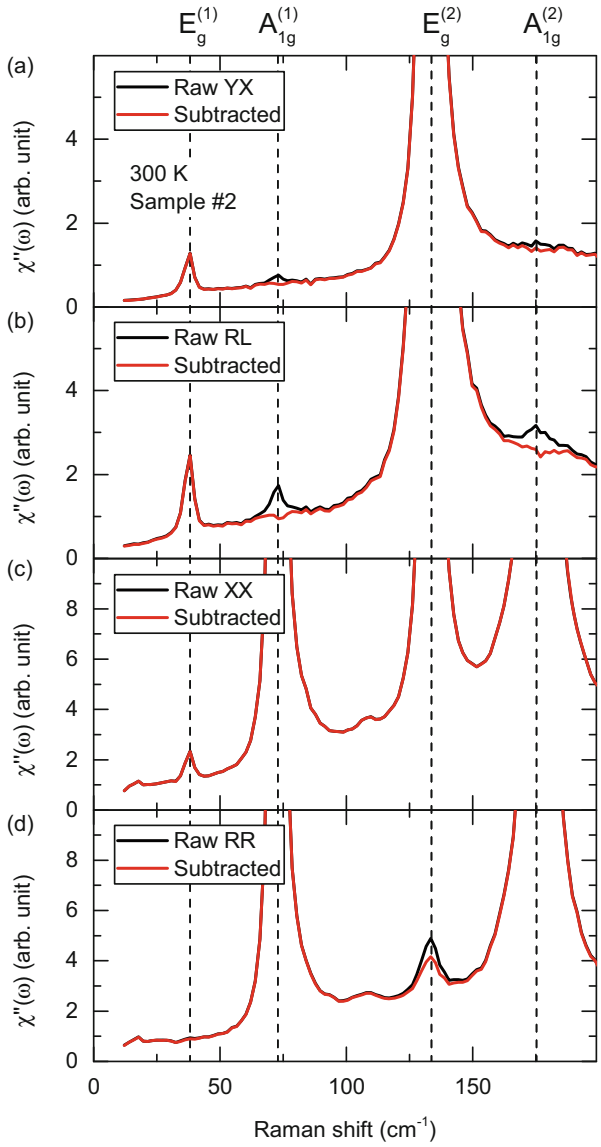

Fig. 4.12 Comparison of raw data and polarization leakage removed spectra, taken in (**a**) YX, (**b**) RL, (**c**) XX, and (**d**) RR polarization geometry from the *ab* surface of sample #2 at 300 K, with 532 nm excitation

formed on Bi_2Se_3 surface also supports the picture of subsurface van der Waals gap expansion [85–87]. However, finite phonon DOS exist across the entire energy range in Bi_2Se_3 [75], allowing the surface modes to decay into bulk phonon modes. Therefore, the surface mode is not entirely "peeled off" from the bulk bands. Then

the hybridization between surface and bulk bands results in a "surface resonance" with slightly lower energy than the bulk phonon, as illustrated in Fig. 4.2. This is markedly a different interpretation from the previous reports, where additional phonon peaks were observed in exfoliated flakes of only a few QLs thickness. In these thin samples, there is little sense in distinguishing surface from bulk, as signal from each layer contributes to distinct peaks. This is well-studied in few layers of graphite and graphene samples [88]. We can clearly see this effect in our thinnest sample #8, where the phonons are broadened to the extent that one cannot distinguish bulk from surface resonance peaks. But with increasing thickness, a clear intensity "shoulder" develops that signifies the formation of bulk phonon bands and the separation of surface resonance at the BZ center.

Due to inversion symmetry breaking at the crystal interface, the surface resonances from the Raman active A_{1g} and IR active A_{2u} phonons are both expected to appear in the A_1 symmetry (C_{3v} group), corresponding to out-of-plane atomic motion. The energies of such surface modes are usually slightly lower than the corresponding bulk phonons. This is consistent with the four A_1 modes we observed (Fig. 4.11a). From the energies of these A_1 modes, we conclude that $A_1^{(1)}$ and $A_1^{(4)}$ are associated with the bulk phonon modes $A_{1g}^{(1)}$ and $A_{1g}^{(2)}$, respectively. The measured energy of the $A_1^{(1)}$ mode is somewhat different than the previously reported value of $68\,\mathrm{cm}^{-1}$ by time-resolved ARPES [68] but close to what was suggested by transport measurements [67]. We believe that this difference may be partly due to surface quality variation. ARPES measured sample is usually cleaved in ultrahigh vacuum, whereas the surface in this study is cleaved in nitrogen environment. This may also explain why this mode was not observed in the MBE samples (Fig. 4.8), where the sample is unavoidably exposed to air for a few minutes during the transfer between MBE chamber and Raman cryostat. The $A_1^{(4)}$ mode appears as a shoulder to the $A_{1g}^{(2)}$ bulk phonon, requiring higher resolution to distinguish from the bulk mode, and therefore was overlooked in the previous Raman study [40].

In comparison, the surface modes $A_1^{(2)}$ and $A_1^{(3)}$ have higher intensity and are better resolved. One possibility for this difference is that the bulk counterparts of these resonances are the IR active $A_{2u}^{(1)}$ and $A_{2u}^{(2)}$ phonons, as the measured energy is close to the calculated values (Table 4.3). Since these bulk modes are not Raman active, we were able to better resolve the surface resonance. Another possibility is that the phonon DOS is practically zero at these energies in the A_1 symmetry channel, and the surface vibration modes are truly localized. Distinguishing these two scenarios is in fact experimentally nontrivial, especially since the experimental values of the $A_{2u}^{(1)}$ and $A_{2u}^{(2)}$ bulk phonon energies are yet unknown.

Since the in-plane symmetries are mainly preserved as the DFT calculated atomic surface distortion is purely out of plane [68], one would not expect surface phonon with E symmetry (C_{3v} group) for Bi_2Se_3. However, the in-plane bonding potential is also modified by having distortion along c-axis, and therefore the phonon frequency at surface is still slightly different than the bulk value. If the modification

is tiny, the E modes are expected to be weak and close to the bulk phonons. In Fig. 4.8b and 4.11b, we can see hints of two additional modes, labeled by $E^{(1)}$ and $E^{(2)}$. The energies of these modes are in fact close to the measured values of $E_u^{(1)}$ and $E_u^{(2)}$ bulk phonons [36, 37] and are consistent with the previous Raman study [40] (Table 4.3). However, the frequency of E_1 is slightly higher than $E_u^{(1)}$, which is against the expectation from a surface resonance. This may reflect the fact that this is an in-plane mode, orthogonal to the lattice distortion direction. Or, this may be indicative of nontrivial electron–phonon interaction with the surface states, and worth further studying.

4.3 Chiral Spin Modes

Ferromagnetic systems and partially spin-polarized Fermi liquids support collective spin excitations (spin waves), in which all electron spins respond coherently to external fields, and the "glue" that correlates the phases of individual spins is provided by the exchange interaction. In nonmagnetic materials where inversion symmetry is broken but time-reversal invariance remains intact, strong spin-orbit coupling (SOC) may play the role of an effective magnetic field, which locks electron spins and momenta into textures. This phenomenon is encountered in three-dimensional (3D) topological insulators (TIs), which harbor topologically protected surface states [13, 15, 30, 32, 89]. The surface band structures of TIs have been a focus of intense studies, both from the fundamental point-of-view [8, 90–95] and for potential spintronics device applications [96–103]. However, the many-body interactions leading to collective effects still remain largely unexplored. An essential aspect of this physics is an interplay between the Coulomb interaction and SOC, which is expected to give rise to a new type of collective spin excitations—chiral spin waves [104–110].

The spectrum of topological surface states (Eq. 4.4) consists of hexagonally warped electron- and hole-like Dirac cones of opposite chirality. A light-induced excitation from the occupied state in the hole cone to an empty state in the electron cone is accompanied by a spin-flip of the quasiparticle (Fig. 4.13b). Such direct transitions form a continuum that starts at the threshold energy ω_- (Fig. 4.13c) [111, 112].

Due to the Pauli exclusion principle, two electrons in the triplet state avoid each other, thus reducing the energy of the Coulomb repulsion. Therefore, the repulsive Coulomb interaction between electrons translates into an attractive exchange interaction between their spins, leading to bound states below the continuum of spin-flip excitation, i.e., chiral spin modes. In general, there are three such modes (red curves in Fig. 4.13c), which correspond to linearly polarized oscillations of the magnetic moment in the absence of the external magnetic field [106, 107, 109]. At $q = 0$, there is a doubly degenerate mode with an in-plane magnetic moment and a transverse mode with an out-of-plane moment, with energies $\omega_{s,||}$ and $\omega_{s,\perp}$,

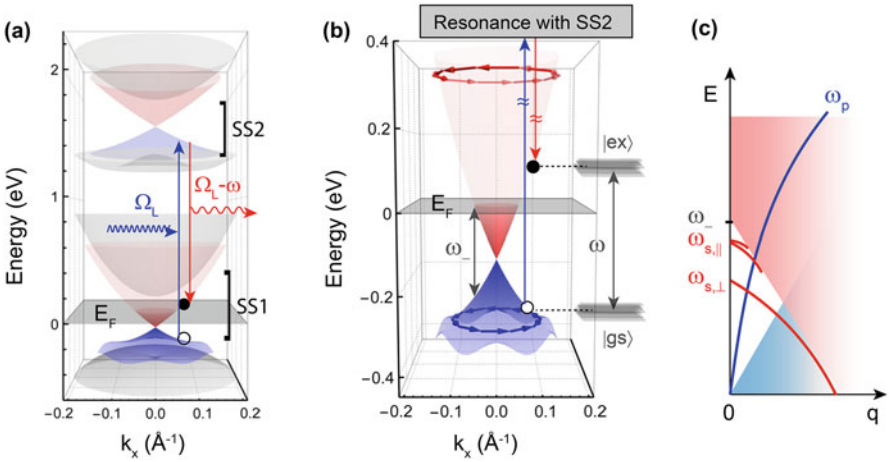

Fig. 4.13 (**a**) The band structure of Bi_2Se_3 around the Brillouin zone center, reconstructed from ARPES results in [81, 113]. The low-energy Dirac cones of surface states (SS1) are described by Eq. (4.4) with parameters $m^* \approx 0.066\,\mathrm{eV}^{-1}\mathrm{Å}^{-2}$, $v_1 \approx 2.4\,\mathrm{eVÅ}$, and $v_w \approx 25\,\mathrm{eVÅ}^3$. The upper and lower Dirac cones of opposite chirality are shown in red and blue, whereas the bulk bands are shown in gray. A pair of unoccupied surface Dirac cones (SS2) resides about 1.8 eV above SS1 [81]. The arrows illustrate a resonant Raman process stimulated by an incoming photon with energy Ω_L, in which an electron is promoted from the lower to the upper Dirac cone of SS1, through resonant scattering via the intermediate states, SS2. The energy difference between the excited and ground state defines the Raman shift, ω. (**b**) Enlarged view of SS1 around E_F with arrows showing the spin textures, where ω_- is the threshold energy for direct transitions between occupied states in the lower Dirac cone and available states of the upper cone. (**c**) Schematic dispersions of the particle–hole continua in the spin (red) and charge (blue) channels, surface plasmon [114] (blue line), and collective spin modes [106] (red lines)

respectively. Because the chiral spin modes are below the continuum, they are expected to remain long-lived even at elevated temperatures [115]. These modes are in essence (zero-field) spin waves that can be measured by resonant Raman scattering because they couple to the electromagnetic field through antisymmetric Raman tensors [109].

4.3.1 Results

As-grown Bi_2Se_3 is usually electron doped due to naturally formed Se vacancies [116]. In this study, we use characterized samples with low carrier concentration. The Fermi energy (E_F) is determined by scanning tunneling spectroscopy to be about 150 meV above the Dirac point of SS1 (Fig. 4.13b) [117].

The polarized Raman spectra were acquired in a quasi-backscattering geometry from the *ab* surface of Bi_2Se_3 single crystals grown by modified Bridgman method.

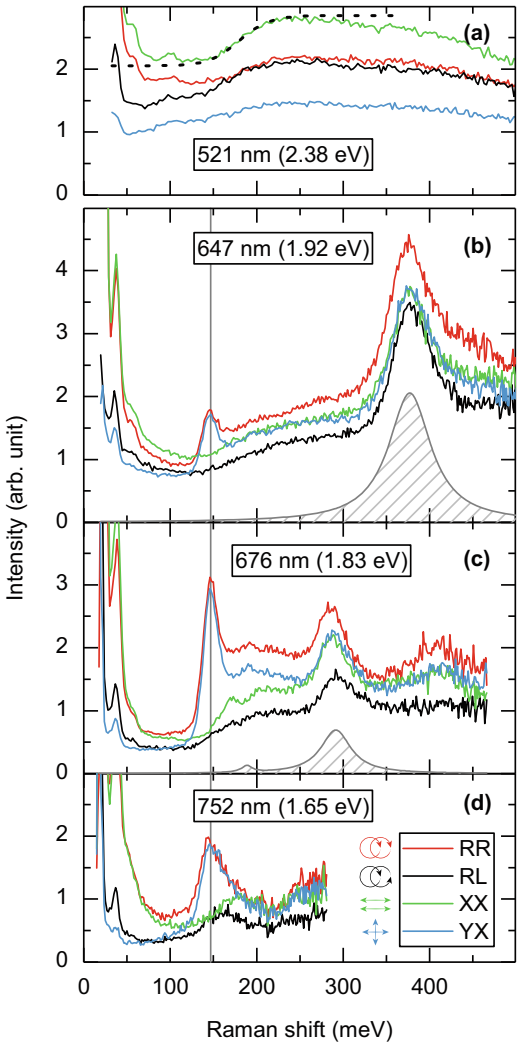

Fig. 4.14 The intensities of secondary emission are measured in circular and linear (with respect to crystallographic axes) scattering polarization geometries, as shown pictorially next to the figure legend in panel (**d**), at 24 K with (**a**) 521, (**b**) 647, (**c**) 676, and (**d**) 752 nm excitations. The vertical solid gray line indicates the sharp 150 meV peak, most pronounced for the incident photon energy of 1.83 eV, which is the closest to the energy difference between SS1 and SS2 (Fig. 4.13a). The dotted black line in (**a**) is a guide to the eye showing the energy threshold for the surface-to-bulk excitations. The hatched areas in (**b**) and (**c**) are Lorentzian fits to the excitonic photoluminescence peaks

We use 521, 647, 676, and 752 nm lines of a Kr^+ laser for excitation, where the spot size is roughly $50 \times 50\,\mu m^2$ and the power is about 10 mW. The scattered light is analyzed by a custom triple-grating spectrometer.

Excitation Profile

In Fig. 4.14, we show spectra of secondary emission for four scattering geometries employing both linear and circular polarizations. Of the four excitations, the 521 nm one is the farthest from near-resonant transition between SS1 and SS2, while the

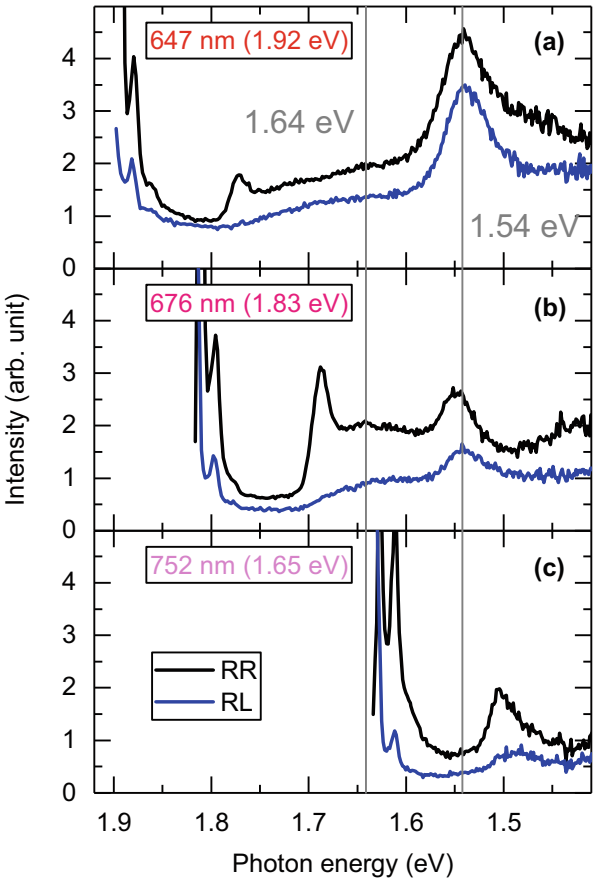

Fig. 4.15 Secondary emission intensity measured in RR and RL polarization geometries at 24 K for (**a**) 647, (**b**) 676, and (**c**) 752 excitation energies, plotted against scattered photon energy. The gray solid line marks 1.54 and 1.64 eV, where the exciton peaks centers' coincide for 647 and 676 nm excitations, indicating that the peaks are due to photoluminescence of excitonic states

676 nm one is the closest. The spectra contain contributions from electronic Raman scattering and exciton photoluminescence. The latter is present for all polarizations and can be subtracted from the spectra. The signal below 50 meV is dominated by phonon modes that are discussed elsewhere [1].

Luminescent Background Subtraction

Figure 4.15 shows the intensity of secondary emission measured with RR and RL polarizations at 24 K for 647, 676, and 752 excitation energies, plotted as function of emission photon energy. The exciton emission centers at 1.54 eV for 647 and

676 nm excitations and has about the same intensity for both RR and RL scattering geometries. Another small peak is at 1.64 eV for both excitation and is likely another state related to the 1.54 eV exciton.

In typical materials, exciton states have energies lower than the interband transition edge by the amount of the binding energy. The excited electron–hole pairs relax to the exciton states, which eventually decay back to the ground state through photon emission if symmetry allows. In some cases, if the photon emission is not allowed and the exciton is said to be "dark." The exciton peaks are absent for 752 nm excitation spectra, suggesting that the corresponding interband transition has a threshold of about 1.8 eV, which puts the binding energy to about 0.3 eV.

Bi_2Se_3 is commonly understood as a small gap semiconductor with the Fermi surface close to the bulk conduction band edge, therefore the observation of a well-defined exciton peak in the near-infrared range is quite surprising, suggesting an optical band gap of about 1.8 eV, much larger than the semiconductor gap. Since direct gap is required for exciton radiative emission, the most probable interband transition is between the M-shaped bulk valence band and a W-shaped conduction band about 1.5 eV above the Fermi energy [81] (Fig. 4.13a). The exciton most likely forms below the band minima at $|k| \approx 0.1$ Å^{-1}.

To remove photoluminescence background from the measured spectra, we fit the 1.54 and 1.64 eV exciton peaks with a Lorentzian function, as shown by the hatched peaks in Fig. 4.14. We also subtract a small constant background from all spectra to account for other photoluminescence contribution.

Temperature Dependence

The most interesting feature of the spectra is a sharp peak around 150 meV observed in the XY and RR geometries. The peak is the strongest for the 676 nm excitation, which is in near resonance with the transition between SS1 and SS2, thus confirming the surface origin of the observed signal.

In order to better understand the origin of the 150 meV peak, we subtract the photoluminescence contributions and then utilize the symmetry properties of the Raman tensors to separate the measured spectra into the E_2, A_1, and A_2 symmetry channels of C_{6v} point group (Table 4.2). In Fig. 4.16, we plot the temperature dependence of Raman response $\mathcal{R}(\omega, T)$ in three symmetry channels. It is clearly seen that the 150 meV peak is associated with the A_2 symmetry channel. The continuum broadens and becomes invisible above 150 K, but the peak is still well-defined even at $T = 300$ K. The temperature dependences of the chiral spin mode intensity (area under the peak), FWHM, and energy (peak center) are shown in Fig. 4.17. The parameters are obtained from fitting the data to the Lorentzian line shape. The width of the spin mode saturates below about 150 K, indicating that the main damping mechanism of the spin mode is likely due to disorder. In general, the energy and width of the chiral spin mode is well-described by the theoretical simulation that incorporates finite temperature effects only via thermal smearing of the Fermi functions and neglects inelastic damping mechanisms. The decreasing

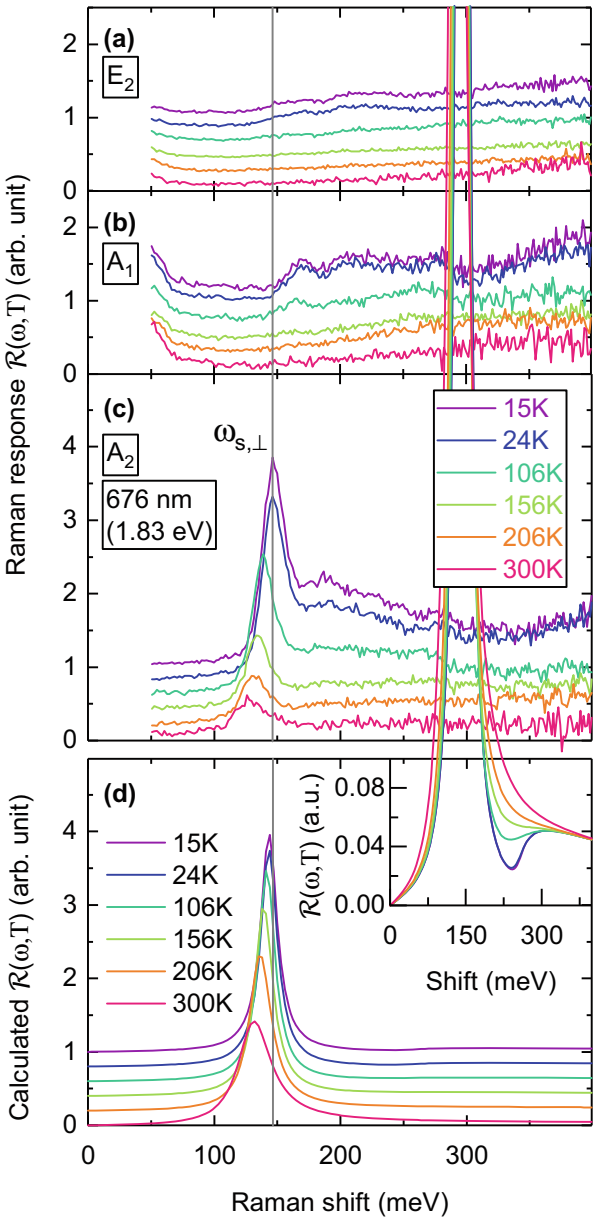

Fig. 4.16 Temperature dependence of the symmetry-separated Raman response $\mathcal{R}(\omega, T)$ in the (**a**) E_2, (**b**) A_1, and (**c**) A_2 symmetry channels, measured with the near-resonant 676 nm excitation. The photoluminescence background was subtracted from the raw data. The gray solid line locates the position of the sharp peak that is present only in the A_2 channel. (**d**) Calculated $\mathcal{R}(\omega, T)$ in the A_2 channel with the dimensionless interaction coupling constant $u \approx 0.6$ and impurity broadening of $\Gamma = 8$ meV was extracted from the data and used in the calculation. The lines are shifted vertically for clarity. Inset: Zoom-in of the calculated $\mathcal{R}(\omega, T)$ without vertical shift, showing the spin-flip continuum with a threshold energy of 260 meV

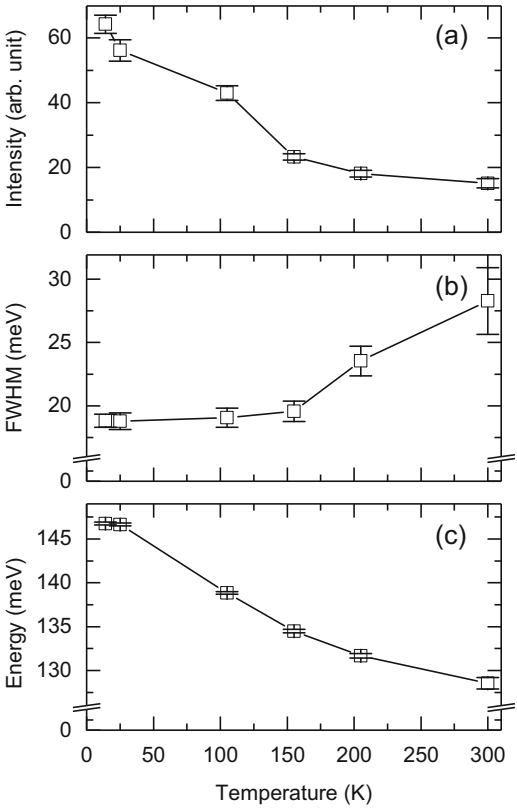

Fig. 4.17 Temperature dependence of (**a**) the intensity, (**b**) full width at half maximum (FWHM), and (**c**) peak center of the chiral spin mode in Fig. 4.16 by fitting to a Lorentzian line shape. The error bars reflect one standard deviation of the fit

intensity at elevated temperatures is not captured in the above temperature effects and is likely an indication of unaccounted spin decay channels, such as through the surface phonons [1].

4.3.2 Discussion

The basis functions of the A_2 representation of C_{6v} transform as the z component of the angular momentum, which is a pseudovector [53]. This suggests that the observed peak in the A_2 channel corresponds to a spin mode (marked by $\omega_{s,\perp}$ in Fig. 4.13c) with an out-of-plane magnetic moment (also a pseudovector).

To quantify the assignment of the 150 meV peak to the out-of-plane chiral spin mode, we calculate the Raman response of surface chiral states. We are interested in spin-flip resonant Raman processes between states near the Fermi level in SS1 and the states in SS2. Two resonance transitions are possible: an electron from the lower cone of SS1 can be transferred into either the lower cone or upper cone of SS2 and can come back to the upper cone of SS1, producing a particle–hole pair.

A characteristic feature of Bi_2Se_3 is that the lower cones of SS1 and SS2 are almost perfectly nested: a fit to the ARPES data in [81, 113] gives $v_1 = 2.4\,\text{eVÅ}$ and $v_2 = 2.0\,\text{eVÅ}$. Therefore, the "hole-to-hole" transition in the Raman vertex is essentially dispersionless, and the corresponding transition probability is enhanced by a factor of $\approx 1/(E_g - \Omega_L)^2$, whereas the "hole-to-electron" term is small. This explains why only one resonance is observed in the experiment.

The Raman response function in the A_2 symmetry channel can now be written as

$$\mathcal{R}(\omega, T) \propto \chi''_{zz}(\omega, T)/(E_g - \Omega_L)^2, \tag{4.9}$$

where χ''_{zz} is the imaginary part of the zz component of the spin susceptibility tensor and has a continuum of spin-flip excitations and a pole corresponding to a transverse collective mode, $\omega_{s,\perp}$ (Fig.4.13). A simple result for the frequency of this mode can be obtained if one neglects hexagonal warping and considers the weak-coupling limit. In this case, $\omega_{s,\perp} = 2E_F\left[1 - 2\exp(-4/u)\right]$, where $u \equiv UE_F/2\pi\hbar v_1^2 \ll 1$ is the dimensionless coupling constant [2].

For a more general case, which includes the realistic band structure and finite temperature, the Raman response has to be evaluated numerically. The results of this calculation are shown in Fig. 4.16d. With the band structure parameters obtained from ARPES measurements [113], the only two fitting parameters are the exchange coupling constant, fixed at $u \approx 0.6$ to reproduce the mode frequency at 15 K, and the impurity scattering rate chosen as $\Gamma = 8$ meV. Comparison of the measured and computed spectra (Fig. 4.16c and d, correspondingly) shows that the model well describes not only the overall shape of the signal but also its evolution with the temperature. In the sample measured, the threshold for the spin-flip continuum is supposed to be at $\omega_- \approx 260$ meV. However, the onset of this continuum is difficult to observe because its spectral weight is transferred into the collective mode; in the inset of Fig. 4.16d, we show a zoom into the computed crossover region between the collective mode and the continuum.

A quantitative agreement between the theory and experiment gives us confidence in that the observed 150 meV sharp peak in the A_2 symmetry channel is indeed a transverse chiral spin mode. The fact that the measured intensity decreases with increasing temperature faster than the calculated spectra is an indication of unaccounted spin decay channels at elevated temperatures, e.g., through interaction with surface phonons [1].

Transitions Between Surface States and Bulk Bands

In Fig. 4.14, the spectrum for the non-resonant 521 nm excitation shows no sharp peaks but a broad feature with an onset at about 200 meV. This energy scale corresponds to the onset of transitions between the surface Dirac cone and the bulk states. Such transitions do not need to flip spins and thus appear also in the XX scattering geometry, which contains the fully symmetric channel.

Figure 4.18 is a realistic illustration of the Bi_2Se_3 band structure reconstructed from ARPES measurements [113]. The surface state dispersion is [23]

$$E_{SS}(\mathbf{k}) = \Delta + \frac{k^2}{2m^*} \pm \sqrt{v_F^2 k^2 + \left(\frac{2v_3}{v_F}\right)^2 k^6 \cos^2 3\theta}$$
$$\approx \Delta + \frac{k^2}{2m^*} \pm v_F k + 2\left(\frac{v_3^2}{v_F}\right) k^5 \cos^2(3\theta) \tag{4.10}$$

where $\pm$ denote the upper and lower Dirac cones and θ is the azimuth angle of momentum $\mathbf{k}$ with respect to the x axis ($\Gamma - K$). Fitting data in [113] to Eq. (4.10) gives $m^* \approx 0.066\,\mathrm{eV^{-1}\AA^{-2}}$, $v_F \approx 2.4\,\mathrm{eV\AA}$, and $v_3 \approx 25\,\mathrm{eV\AA^3}$. One can readily see that the energy of a direct transition from the lower to upper Dirac cone is $2\sqrt{v_F^2 k^2 + (\frac{2v_3}{v_F})^2 k^6 \cos^2(3\theta)}$. In samples measured, Δ is determined by tunneling spectroscopy [117] to be about $-150\,\mathrm{meV}$, and therefore the Fermi momentum $k_F \approx 0.054\,\mathrm{\AA^{-1}}$ along k_x, thus resulting in a threshold energy $\omega_- \approx 260\,\mathrm{meV}$.

The direct transition energy between SS1 and the bulk conduction band is given by $\epsilon(\mathbf{k}) = E_{CB}(\mathbf{k}) - E_{SS}(\mathbf{k})$, where $E_{SS}(\mathbf{k})$ is given by Eq. (4.10), and the bulk conduction band dispersion follows a quasi-2D parabolic model [118]:

$$E_{CB}(\mathbf{k}) = E_0 + \frac{k_{||}^2}{2m_{||}^*} + \frac{k_\perp^2}{2m_\perp^*}, \tag{4.11}$$

where $E_0 \approx 130\,\mathrm{meV}$ is determined by E_F and the relative position between SS1 and bulk conduction band minimum [113, 117], $m_{||}^* \approx 0.03\,\mathrm{eV^{-1}\AA^{-2}}$ is the in-plane effective mass, determined from fitting the ARPES data in [113] to quadratic

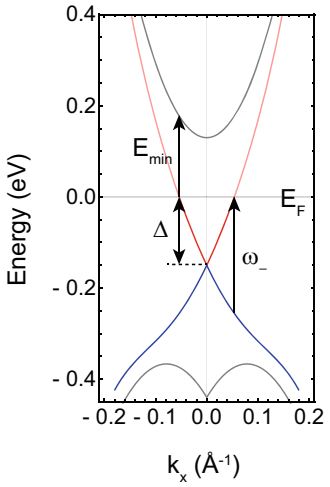

Fig. 4.18 Transitions between surface states and bulk conduction band. Band structure near the Γ point and Fermi surface, reconstructed from ARPES measurements [113]. The blue and red lines denote the lower and upper Dirac cones, respectively, whereas the bulk bands are shown in gray. In the measured sample, the Dirac point is about 150 meV below the Fermi energy E_F

dispersion. In the measured sample where $k_F \approx 0.054\,\text{Å}^{-1}$ along k_x, the threshold energy $E_{\min} \approx 180\,\text{meV}$, similar to what was observed in Fig. 4.14a.

4.4 Photoluminescence

As we have demonstrated in the previous section, spin–orbit coupling (SOC) can play a central role in emerging phenomena in condensed matter physics, e.g., 3D topological insulators (TIs) [13, 15, 21, 32], valleytronics [119–121] and Ising superconductivity [122, 123]. In this section, we show surprising results where two photoluminescence (PL) peaks are observed in the visible range in Bi_2Se_3. Figure 4.20a shows the right and left circularly polarized (CP) secondary emission spectra, indicated by $I_{\text{RR}}(\omega, T)$ and $I_{\text{RL}}(\omega, T)$, respectively. At low temperature, two PL peaks were detected in the visible range, where the peak center energies remain fixed with changing excitation. While broad PL features are not uncommon even in metals, a well-defined PL peak usually requires a minimum in the *e–h* band, which is unexpected to appear in the visible range for a small gap semiconductor, such as Bi_2Se_3.

The peak structure in the PL spectra is usually an evidence of fixed energy *e–h* bound states, known as excitons, that couple to the electromagnetic field through radiative decays. Due to phase relaxation during the thermalization of *e–h* pairs and the formation of excitons, the PL is usually unpolarized.

4.4.1 Circular Polarized Photoluminescence

Polarized PL is an indication of excitons favoring certain "optical orientation" than the other, which is usually due to underlying symmetry breaking in the system, leading to removal of band degeneracies. For example, spin polarization of electron bands can be induced by SOC through Rashba [124] and Dresselhaus [125] effects in solids without inversion symmetry, or in crystals with specific atomic site asymmetries [126]. The spin polarized energy bands lead to various novel collective phenomena, e.g., chiral spin modes [115] and chiral excitons [127], posing an emerging playground for studying interplay between spin and other degrees of freedom in solids [120]. In particular, the chiral excitons in TMD monolayers display a high degree of "optical orientation," allowing them to be efficiently and selectively excited by CP photons [120, 128, 129], with applications in optospintronics [129, 130].

The study of exciton's "optical orientation" through measuring polarized PL spectra dates back to the early 1970s [131–133], as an efficient way of probing the spin polarizations of electron bands in III–V and II–VI semiconductors [134]. The excitons originating from spin polarized electrons and holes are characterized

by its azimuth angular momentum, $S_z = \pm 1$. The oppositely oriented excitons are thus independently excited by circularly polarized photon of opposite helicity [135]. Since the electronic bands are spin polarized, the exciton orientation is preserved during thermalization, eventually leading to CP PL at electron–hole (e–h) recombination. Therefore, studying the polarized PL spectra is particularly interesting in a TI material, where information of the surface state spin dynamics is particularly important due to its potential application in spintronics [96, 103].

4.4.2 Results

In Bi_2Se_3, the large Rashba SOC on the surface results in three spin polarized bands at the Brillouin zone center (Γ-point), shown as red lines in Fig. 4.19a: the topologically protected surface Dirac cone at the Fermi level (SS1) [21, 89], the

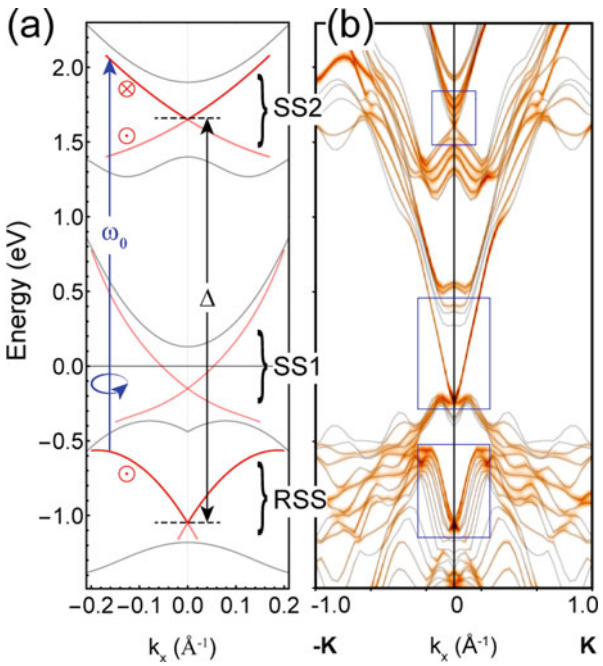

Fig. 4.19 The band structure around BZ center in Bi_2Se_3. (**a**) The electronic band structure near the Γ point was inferred from ARPES measurements and DFT calculations [81, 87]. The Rashba surface states (RSS) and the unoccupied topological surface states (SS2) are in red, with the in-plane spin orientations denoted by ⊙ and ⊗. The topological surface states (SS1) near Fermi energy (E_F) are shown in light red. The bulk bands do not contribute to the CP PL and are shown in gray. (**b**) DFT calculated band structure in a slab geometry with 32 Åvacuum layer, shown along the Γ-K cut of the Brillouin zone, with spectral weight projected onto the top quintuple layer for $J_z = 1/2$. The blue squares highlight the three surface bands labeled in (**a**)

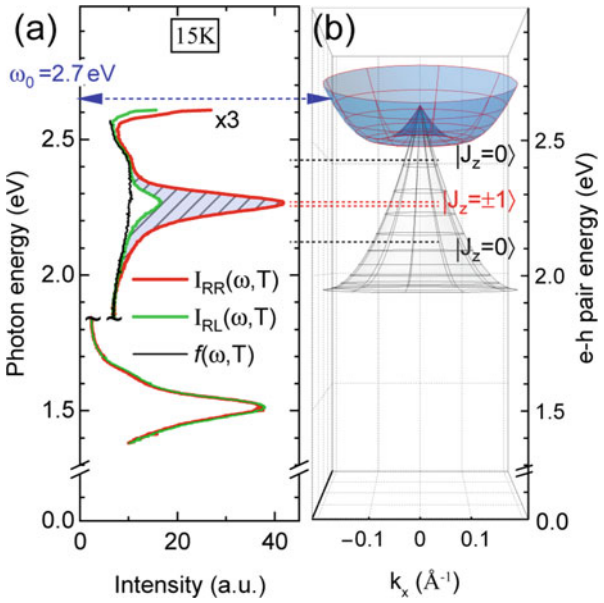

Fig. 4.20 Photoluminescence spectra and noninteracting e–h continuum of relevant interband transitions. (**a**) The CP PL spectra measured at 14 K, with right-CP 2.65 eV excitation. Right- and left-CP PL are designated by $I_{RR}(\omega, T)$ in red and $I_{RL}(\omega, T)$ in green, respectively. The black line shows unpolarized PL background, $f(\omega, T)$. The intensity in the 1.8–2.6 eV range is multiplied by factor of 3 for clarity. (**b**) The dispersion relation of non-interacting electron–hole pairs for possible transitions from RSS to SS2, with zero momentum transfer. The only transition consistent with excitation energy used in this study is shown in blue, while others are shown in gray. With finite interaction, the excitonic bound states form below the band minimum and are denoted by the total angular momenta of the electron–hole pairs, J_z

high energy unoccupied surface states (SS2) [81], and the fully occupied Rashba surface states (RSS) [87, 136].

In the following, we use continuous wave visible laser light to promote resonant interband transition between RSS and SS2 (Fig. 4.19a) and study polarized secondary emission spectra in the backscattering geometry. All of the results reported below are reproducible in the "time reversed" geometry, i.e., switching the excitation polarization leads to switching of PL polarization with the same spectral line shape, and so we will henceforth focus on the results with right-CP excitation.

In Fig. 4.20a, we can further separate $I_{RR}(\omega, T)$ and $I_{RL}(\omega, T)$ into two spectral contributions: (1) a broad unpolarized emission band, $f(\omega, T)$, and (2) a narrower peak that is almost fully polarized, with intensity defined as $\mathcal{L}_R(\omega, T) = I_{RR}(\omega, T) - f(\omega, T)$. We note that $f(\omega, T)$ and $\mathcal{L}_R(\omega, T)$ inherit distinct line shapes and therefore likely originate from different photoemission processes. We will henceforth focus on the polarized PL, $\mathcal{L}_R(\omega, T)$.

The broad unpolarized background $f(\omega, T)$ can be easily removed from the spectra as detailed in the following. With right circularly polarized (CP) excitation, the measured photoluminescence (PL) intensities can be decomposed into two parts:

$$I_{\mathrm{RR}}(\omega, T) = \mathcal{L}_R(\omega, T) + f(\omega, T),$$
$$I_{\mathrm{RL}}(\omega, T) = \mathcal{L}_L(\omega, T) + f(\omega, T), \tag{4.12}$$

where $\mathcal{L}_R(\omega, T)$ and $\mathcal{L}_L(\omega, T)$ denote right- and left-CP PL, respectively, and $f(\omega, T)$ denotes the featureless unpolarized broad background. We assume an energy independent depolarization ratio $r(T) = \frac{\mathcal{L}_L(\omega,T)}{\mathcal{L}_R(\omega,T)}$. Inserting $r(T)$ into the above expression of $I_{\mathrm{RL}}(\omega, T)$, we can write the unpolarized emission as

$$f(\omega, T) = \frac{I_{\mathrm{RL}}(\omega, T) - r(T) \cdot I_{\mathrm{RR}}(\omega, T)}{1 - r(T)}. \tag{4.13}$$

Then, $r(T)$ was estimated by imposing that $f(\omega, T)$ is a smooth function, and we arrive at

$$\mathcal{L}_R(\omega, T) = \frac{I_{\mathrm{RR}}(\omega, T) - I_{\mathrm{RL}}(\omega, T)}{1 - r(T)}. \tag{4.14}$$

Excitation Profile

In Fig. 4.20a, we see that a small fraction of $\mathcal{L}_R(\omega, T)$ is also present in the orthogonal polarization, $\mathcal{L}_L(\omega, T) = I_{\mathrm{RL}}(\omega, T) - f(\omega, T) \equiv r(T)\mathcal{L}_R(\omega, T)$, where $r(T)$ is a "depolarization ratio." We find that the depolarization ratio $r(T) \approx 0.1$ for single crystals measured with 2.6 eV excitation and increase to about 0.3 with 2.8 eV excitation (Fig. 4.21c). Such high degree of CP PL can only be explained by spin polarized bands resulting from SOC, which is only possible on the surface states due to the inversion symmetric bulk crystal structure of Bi_2Se_3.

Figure 4.21b shows the integrated PL intensity, $\int_{1.95}^{2.46\,eV} [I_{\mathrm{RR}}(\omega, T) - I_{\mathrm{RL}}(\omega, T)]d\omega$, versus excitation measured at about 15 K. Within the energy range where we see the CP PL, the only possible surface transition is from RSS to SS2. Figure 4.21c plots the depolarization ratio $r(T)$ against excitation energy. Assuming that the depolarization process is largely due to energy relaxation in the *e–h* continuum, then a linear extrapolation of $r(T)$ to zero suggests the *e–h* band minimum at 2.48 eV, which is very close to the noninteracting *e–h* energy estimated from the band structure (Fig. 4.20b). Below this energy, 2D excitons can only be resonantly excited, and the "hot luminescence" from the excitons is in principle 100% polarized. In this study, we will only discuss the PL from excitons created through *e–h* pairs.

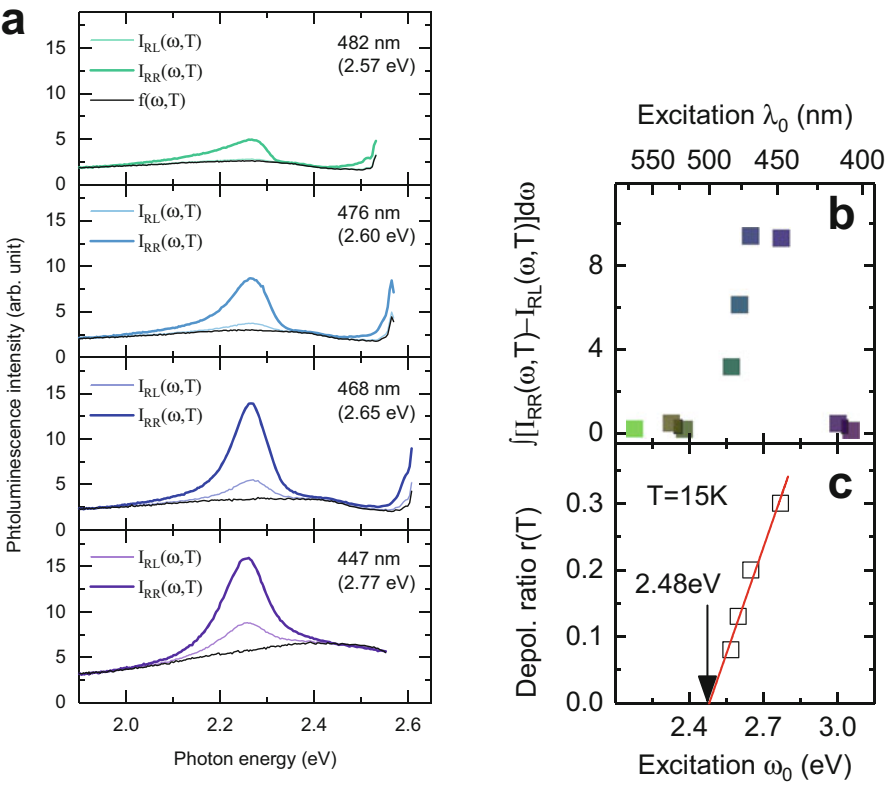

Fig. 4.21 (**a**) PL intensity measured at about 15 K is plotted against photon energy for 4 different excitations: ω_0 =2.57, 2.60, 2.65, and 2.77 eV. The light and dark colored lines denote $I_{RL}(\omega, T)$ and $I_{RR}(\omega, T)$, respectively. The smooth background $f(\omega, T)$ is plotted as black lines. (**b**) The integrated polarized PL intensity, $\int_{1.95}^{2.46\,eV}[I_{RR}(\omega, T)-I_{RL}(\omega, T)]d\omega$ (shaded in blue in Fig. 4.20a) versus excitation energy measured at about 15 K. (**c**) The depolarization ratio $r(T \approx 15\,K)$ is plotted against excitation energy. The red line is a linear extrapolation to $r(T) = 0$, suggesting a minimum excitation energy of 2.48 eV

The band minimum suggests the binding energy for the exciton states, denoted by $|E_1^{R/L}\rangle$ in Fig. 4.20b, to be about 0.2 eV. However, this is an underestimation of the electron–hole continuum edge. Because part of the depolarization is likely due to magnetic impurity scattering or local strain on the sample [137]. Thus the binding energy could be slightly higher than 0.2 eV.

To illustrate the unusual behaviors of the polarized exciton PL, it is perhaps suitable to contrast it with the PL data of a more common exciton. Figure 4.22 shows excitation dependence of PL of Bi_2Se_3 in a more extended energy regime, measured at about 15 K with 7 different excitations. We see that besides the highly polarized exciton PL emission at about 2.3 eV, there is another (much stronger) PL peak centered at about 1.5 eV, emitting with the same intensity of right- and left-CP

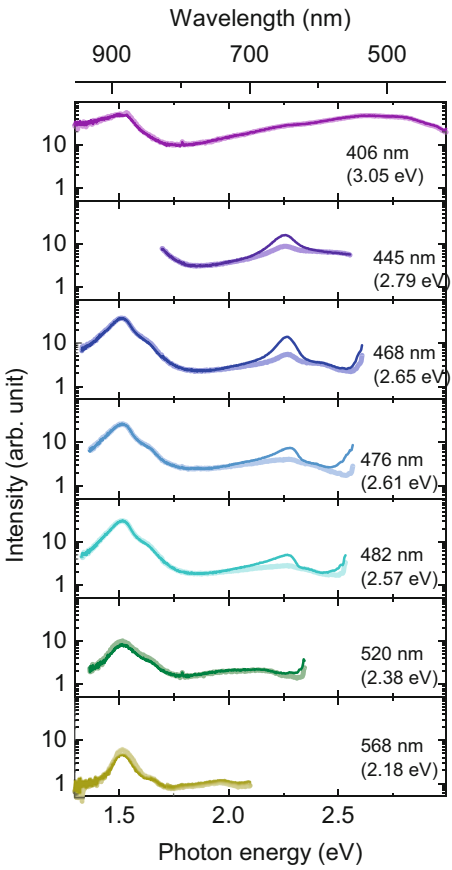

Fig. 4.22 PL intensity measured at about 15 K is plotted against photon energy for 7 different excitations. The intensities are shown in log scale. The light and dark colored lines denote $I_{RL}(\omega, T)$ and $I_{RR}(\omega, T)$, respectively

light, and it appears in all excitations. The line shape of this exciton is Lorentzian (symmetric), which is in contrast to the highly asymmetric line shape of the CP PL near 2.6 eV excitations. Figure 4.23 shows the excitation dependence of the integrated PL intensity of the 1.52 eV exciton, which shows monotonic increase of intensity with higher energy excitations. This is quite from the excitation profile of the 2.26 eV CP PL in Fig. 4.21b, which shows clear resonance around 2.7 eV excitation. The above comparisons show that the CP PL is unusual even within Bi_2Se_3, and new theory is required to understand this phenomenon.

Temperature Dependence

Figure 4.24a shows temperature dependence of $\mathcal{L}_R(\omega, T)$ for Bi_2Se_3 single crystal. While the PL is much stronger at low temperature, the polarized emission is present even at room temperature. Interestingly, we find that $r(T)$ remains about 0.1 up to room temperature. This demonstrates that while temperature has effects on the

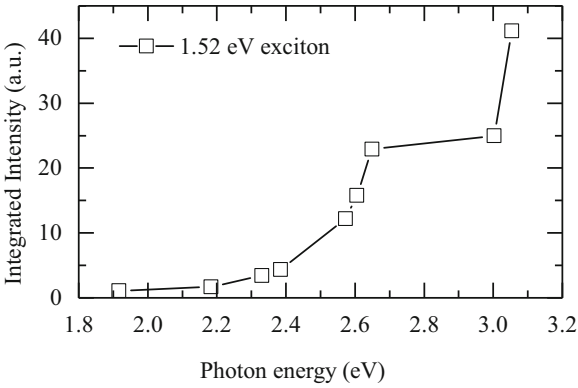

Fig. 4.23 Excitation dependence of the integrated PL intensity of the 1.52 eV exciton, plotted against photon energy

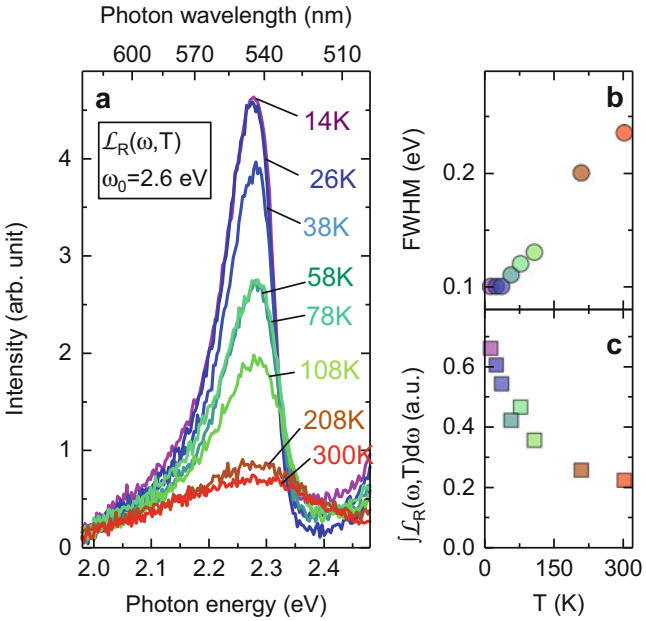

Fig. 4.24 Temperature dependence of CP PL measured with 2.6 eV right-CP excitation. (**a**) The intensity of the polarized PL, $\mathcal{L}_R(\omega, T)$, is plotted against photon energy for various temperatures. (**b**) The temperature dependence of the FWHM of the polarized PL. (**c**) The temperature dependence of the integrated intensity of the polarized PL, $\int \mathcal{L}_R(\omega, T)\, d\omega$

exciton lifetime and population, it has little impact on the polarization of the exciton emission.

Another interesting anomaly of the observed exciton emission is its line shape. Conventional phonon assisted exciton emission results in asymmetric broadening toward the high energy tail, and the extent of the broadening is larger at elevated temperatures [138], where both of them are in contrast to our observations in Bi_2Se_3.

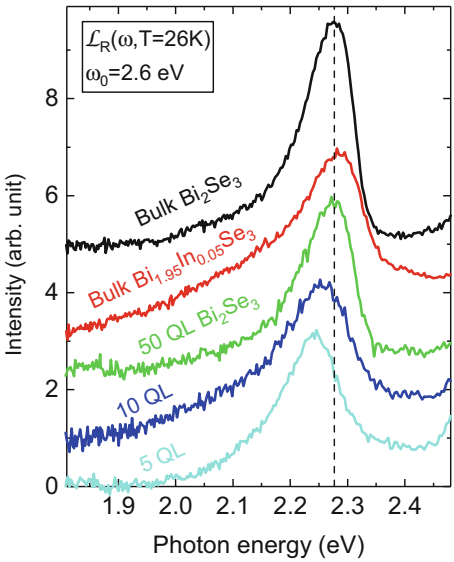

Fig. 4.25 $\mathcal{L}_R(\omega, T)$ is plotted against photon energy for different Bi_2Se_3 samples, measured with 2.6 eV right-CP excitation at 26 K. Spectra are shifted vertically for clarity. Dashed line is a guide to the eye indicating the PL peak center of the bulk Bi_2Se_3 single crystal

Sample Dependence

Further experiments done on MBE grown Bi_2Se_3 thin films of different thickness show qualitatively the same PL line shape, intensity and the depolarization ratio $r(T)$ as in single crystals (Fig. 4.25). This shows that the observed polarization preserving PL is indeed an intrinsic property of Bi_2Se_3.

The PL peak in bulk $Bi_{1.95}In_{0.05}Se_3$ crystal shows slight broadening compared to the pristine Bi_2Se_3 crystals, which could be due to increased inhomogeneity level from indium substitution. The PL peaks in the superlattice samples show lower energy compared to the bulk Bi_2Se_3, which could be due to changes of the band structures in the thin samples. The superlattice samples also present slight broadening, which could be due to increased inhomogeneity from indium diffusion into the Bi_2Se_3 layers.

The fact that the polarized PL intensity is unaffected by Bi_2Se_3 thickness seems to suggest a 3-dimensional (3D) nature of the exciton. However, the penetration depth of Bi_2Se_3 around 2.6 eV is about 10 nm [34]. In the backscattering geometry, the PL or scattered light intensity is again attenuated inside the crystal. The effective penetration depth is then about 5 nm (5 QL), reaching the 2D limit of Bi_2Se_3 [15]. Therefore, the optical experiment in the visible range is effectively a surface probe for Bi_2Se_3, and we cannot distinguish the surface from bulk contributions by studying sample thickness dependence.

Polarization Dependence

We plot in Fig.4.26 the PL spectra measured with different polarization geometries, which helps to elucidate the nature of the observed PL in Bi_2Se_3. The polarized PL with right-CP excitation (Fig. 4.26a) and left-CP excitation (Fig. 4.26b) show the same line shape in the time reversed channels. This suggests that there exist two degenerate exciton states, which can be excited by right- and left-CP light, separately. The decaying process of these exciton preserves angular momentum and therefore emits only PL in the same polarization as the excitation photon. For symmetry reasons, we denote the degenerate exciton states as $|E_1^R\rangle$ and $|E_1^L\rangle$, which couples to right- and left-CP light, respectively.

To test the quantum coherence between states $|E_1^R\rangle$ and $|E_1^L\rangle$, we excite the sample with linearly polarized light. In Fig. 4.26c, $I_{\mathrm{XR}}(\omega, T)$ and $I_{\mathrm{XL}}(\omega, T)$ coincide with each other. This suggests that the linearly polarized excitation being decomposed into right- and left-CP light can independently excite $|E_1^R\rangle$ and $|E_1^L\rangle$.

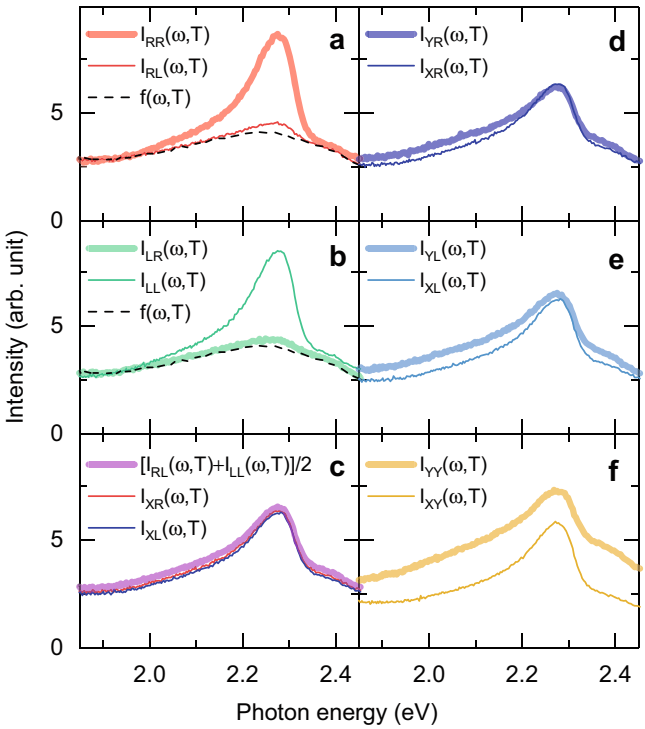

Fig. 4.26 Polarization dependence of PL measured at 26 K, with 2.6 eV right-CP excitation. (**a**) The thick and thin curves show the right- and left-handed PL spectra under right-CP and (**b**) left-CP excitation. The black curve shows a featureless unpolarized broad background. Panels (**c**)–(**e**) compare CP PL spectra excited with linearly polarized light. (**f**) Comparison of the spectra with excitation polarization parallel and cross to the PL polarization

The two types of excitons have independent but similar decay channels, such that the emitted PL acquires the same line shape and intensity. Such process does not allow any dependence on the orientation of the linearly polarized excitation, as linear light can be decomposed into circular light up to a total phase difference. The above argument is confirmed in Fig. 4.26d and e, where orthogonal linear light is used for excitation. The resulted CP PL show roughly the same intensity and line shape for both circular polarizations.

Moreover, the fact that $I_{\mathrm{XL}}(\omega, T)$ coincides with $[I_{\mathrm{RL}}(\omega, T) + I_{\mathrm{LL}}(\omega, T)]/2$ suggests that the quantum coherence is not preserved in the decay process of the exciton (Fig. 4.26c). With linearly polarized light, both $|E_1^R\rangle$ and $|E_1^L\rangle$ are simultaneously excited. The left-CP emission will therefore mainly come from $|E_1^L\rangle$, with small proportion from depolarized emission of $|E_1^R\rangle$. If $|E_1^L\rangle$ and $|E_1^R\rangle$ are phase coherent, then due to interference, the combined PL intensity will not be the same as the intensity obtained by individually exciting them, i.e., $I_{\mathrm{XL}}(\omega, T) \neq [I_{\mathrm{RL}}(\omega, T) + I_{\mathrm{LL}}(\omega, T)]/2$. In our experiment, we have never observed such interference phenomena.

This effect is particularly evident by exciting with the linearly polarized light while also probing the linearly polarized PL. Figure 4.26f shows comparison of spectra with the excitation polarization being parallel and cross to the PL polarization. Apart from the overall intensity change, the PL peak is present in both spectra with roughly the same strength. This is in contrast to the PL of valley excitons in some TMD monolayers, where the PL polarization is always parallel to the polarization of excitation photon [139], which is explained as a demonstration of quantum phase coherence in the decaying channels of both types of valley excitons. Here, the polarization dependence of PL in Bi_2Se_3 implies incoherent decay processes. As a result, $|E_1^L\rangle$ and $|E_1^R\rangle$ act as independent but polarization preserving emitters.

4.4.3 Chiral 2D Excitons

The observation of polarization preserving PL resonance can be readily understood in terms of a 2D chiral exciton, i.e., an electron–hole bound state originating from spin polarized surface states, as illustrated in Fig. 4.27. To explain how gapless Dirac particles can result in a formation of a discrete two-particle bound state, we present a model that involves an optically excited electron in SS2 and a hole state in RSS, as shown in Fig. 4.19a. Neglecting the high order warping terms, we model the Hamiltonians as

$$\begin{aligned} H_{SS2}(\mathbf{p}) &= \Delta + v\mathbf{p}\cdot\boldsymbol{\sigma}_e, \\ H_{RSS}(\mathbf{p}) &= -\frac{\mathbf{p}^2}{2m_h} - \alpha\mathbf{p}\cdot\boldsymbol{\sigma}_h, \end{aligned} \tag{4.15}$$

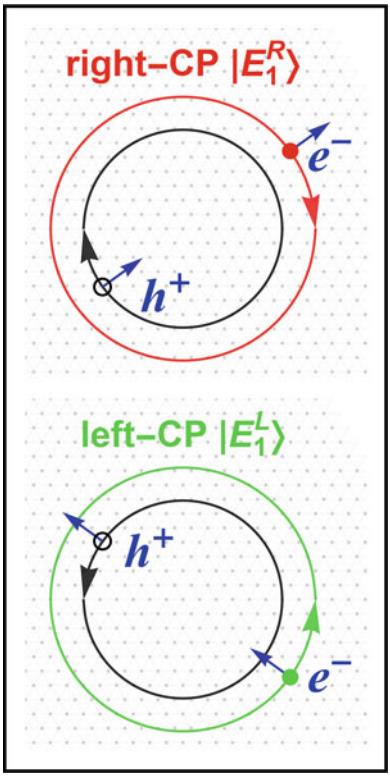

Fig. 4.27 Illustration of the chiral 2D excitons. The doubly degenerate excitonic states ($|E_1^R\rangle$ and $|E_1^L\rangle$) are shown, where a Dirac fermion from SS2, denoted in red and green, orbits a quasiparticle hole from RSS (shown in black open circle), with the spin polarization denoted by blue arrows. The exciton emissions from $|E_1^R\rangle$ and $|E_1^L\rangle$ are right- and left-CP, respectively. Interchange between these two states requires backscattering and spin flip and therefore is not allowed

where Δ is the energy difference between RSS and SS2, v is the Dirac velocity, m_h is the effective mass of the hole, α is Rashba coefficient, and 2D momentum $\mathbf{p}$ is measured from the Γ point. We note that Rashba spin-orbit interaction is of the form $\alpha(\boldsymbol{\sigma}_h \times \mathbf{p}) \cdot \hat{z}$ (similarly for the Dirac states with the substitution $\alpha \to v$ and $\boldsymbol{\sigma}_h \to \boldsymbol{\sigma}_e$). However this structure is equivalent to that in Eq. (4.15) after relabeling spin components as $\sigma_x \to \sigma_y$, $\sigma_y \to -\sigma_x$.

We model the non-interacting electron–hole pair by the two-body Hamiltonian $H_{eh}(\mathbf{p}) = H_{SS2}(\mathbf{p}_+) - H_{RSS}(\mathbf{p}_-)$, where $\mathbf{p}_\pm = \mathbf{p} \pm \frac{1}{2}\mathbf{k}$ and $\mathbf{k}$ is the exciton momentum. For zero momentum transfer ($\mathbf{k} = 0$), the eigenvalues of $H_{eh}(\mathbf{p})$ have W-shaped dispersion resembling a multi-layer Mexican hat (Fig. 4.20b). Crucially, the two-body bands originating from $H_{eh}(\mathbf{p})$ are bounded from below for any parameter values v and α due to the presence of the $\mathbf{p}^2$ term with $m_h > 0$. We therefore expect the two-particle bound state originating due to Coulomb attraction between electron and hole to be a discrete state positioned below the Mexican hat bottom layer band edge. This somewhat a counter-intuitive behavior, which arises despite the Dirac conduction band being unbounded, is illustrated in Fig. 4.20b. As we will see below, the characteristic momenta of this bound state are defined by the Mexican hat rim radius.

Excitonic Bound States

The formation of a discrete bound state may seem to be at odds with the fact that the energy spectrum of massless Dirac fermions spans the entire continuum $-\infty < \epsilon < \infty$, leaving no room for discrete states at any energy. The only known exception to this picture are the discrete complex-energy states arising in the so-called atomic collapse regime [140]. Here, in contrast, we predict bound states with discrete real-valued energies. Such states arise because an electron in the conduction band can bind to a hole in the valence band such that the electron and the hole are moving with roughly the same velocity, $\mathbf{v}_e(\mathbf{p}) = \mathbf{v}_h(\mathbf{p})$. In this case the (possibly large) kinetic energies of the electron and the hole have no impact on the formation of the bound state. The condition $\mathbf{v}_e(\mathbf{p}) = \mathbf{v}_h(\mathbf{p})$ defines the Mexican hat bottom, in agreement with the discussion above. As we will see, if the condition $\mathbf{v}_e(\mathbf{p}) = \mathbf{v}_h(\mathbf{p})$ is fulfilled on a circle in momentum space, the bound states can arise even for an arbitrarily weak attraction potential.

The quantum state and the binding energy of this chiral 2D exciton can be obtained with the help of the two-particle Schrödinger equation:

$$\epsilon \psi_{eh}(\mathbf{r}) = \left(H_{eh}(\mathbf{p}) + V(\mathbf{r})\right) \psi_{eh}(\mathbf{r}), \tag{4.16}$$

where $V(\mathbf{r})$ is the electron–hole interaction potential. Here, $\psi_{eh}(\mathbf{r})$ describes the exciton wave function, and for the sake of simplicity, we focus on the case of zero net exciton momentum ($\mathbf{k} = 0$), which is sufficient for the direct optical transitions discussed here.

To understand the general properties of the resulting discrete states, in particular their spin structure, it is instructive to replace the interaction potential by a model short-range attraction $V(\mathbf{r}) = -\lambda\delta(\mathbf{r})$, which in fact provides a good approximation for the Coulomb interaction screened by conduction electrons in Bi_2Se_3. The bound states for this problem can be readily obtained using the T-matrix approach, giving an equation for eigen-energies of the form:

$$1 = \lambda Z(\epsilon, \mathbf{k}), \tag{4.17}$$

$$Z(\epsilon, \mathbf{k}) = -\sum_{\mathbf{p}} \frac{1}{\epsilon - \Delta - \frac{\mathbf{p}_+^2}{2m_h} - v\mathbf{p}_+ \cdot \boldsymbol{\sigma}_e - \alpha \mathbf{p}_- \cdot \boldsymbol{\sigma}_h + i0},$$

where $\sum_{\mathbf{p}}$ denotes integration $\int \frac{d^2p}{(2\pi\hbar)^2}$. Equation (4.17) can be evaluated explicitly, giving a closed-form algebraic equation for exciton spectrum. In the Supplementary Materials of [3], we show that the discrete states exist for any attraction strength $\lambda > 0$, no matter how weak.

At $\mathbf{k} = 0$, $H_{eh}(\mathbf{p})$ possesses azimuthal symmetry, allowing us to understand the spin structure of Eq. (4.17) on general symmetry grounds. The eigenstates must have definite projection of the angular momenta z component, $\sigma_e^z = \pm 1$ and $\sigma_h^z = \pm 1$. Strictly speaking, exciton states have to be classified within the

surface symmetry group, which is C_{6v} for actual Bi_2Se_3 or $C_{\infty v}$ for a rotationally invariant Hamiltonian. At Γ point, both RSS and SS2 transform as the Γ_7 double group representation of the C_{6v} point group. Extending the symmetry argument to states near the Γ point, the 2D exciton states arising from Eq. (4.17) must have the symmetries [53]: $\Gamma_7 \times \Gamma_7 = \Gamma_1 + \Gamma_2 + \Gamma_5$, or equivalently in Mulliken symbols: $A_1 + A_2 + E_1$.

Inspecting the exciton wave functions, we find that the two $|J_z = 0\rangle$ states are fully symmetric with respect to all symmetry operators of both C_{6v} and $C_{\infty v}$ groups and therefore belong to the A_1 irreducible representation. On the contrary, the doubly degenerate $|J_z = \pm 1\rangle$ states belong to the E_1 representation, which transform as an in-plane electric dipole. Here, neither the orbital angular momentum nor the spin is a good quantum number, and the states should be labeled by the total angular momentum. The lowest energy state with $J_z = 0$ takes the form: $|A_1^1\rangle = \frac{1}{\sqrt{2}}(|\uparrow_e\downarrow_h\rangle - |\downarrow_e\uparrow_h\rangle)$. The excited state with the $J_z = 0$ component has the form: $|A_1^2\rangle = \frac{1}{\sqrt{2}}(|\uparrow_e\downarrow_h\rangle + |\downarrow_e\uparrow_h\rangle)$. The A_1 representation transforms as an electric dipole along c-axis, and therefore $|A_1\rangle$ is optically active only when excited from the ac surface.

In contrast, the states with $J_z = \pm 1$ have the E_1 symmetry, which transforms as in-plane electric dipoles and therefore couples to the circularly polarized light in backscattering geometry from the ab surface. Hence, we label the $J_z = \pm 1$ states as $|E_1^R\rangle = |\uparrow_e\uparrow_h\rangle$ and $|E_1^L\rangle = |\downarrow_e\downarrow_h\rangle$, populated by right- and left-CP light, respectively. It can be shown that these two states are degenerate and intermediate to the energies of the $|J_z = 0\rangle$ states, as we illustrated in Fig. 4.20b. Crucially, only the $|E_1^R\rangle$ and $|E_1^L\rangle$ are optically active, whereas both $|A_1^1\rangle$ and $|A_1^2\rangle$ are "invisible" in our experiment. This possibly explains the unusual line shape of exciton resonance with a pronounce tail on the long wavelength side, which can be due to emission from a "dark" state through high order terms beyond dipole approximation.

Optical Orientation of Chiral 2D Excitons

The polarization preserving PL arises as a direct result of the symmetry properties of the constructed 2D excitons. Within the backscattering geometry of our experiment, circularly polarized light can only promote excitations with $\Delta J_z = \pm 1$. Assuming no cross-relaxation between $J_z = 0$ and $J_z = \pm 1$ states, we expect a single PL peak arising from recombination of the $J_z = \pm 1$ exciton, which is consistent with our data. However, one would expect that inelastic scattering with phonons would couple the $|J_z = +1\rangle$ and $|J_z = -1\rangle$ states, which could cause an increase of $r(T)$ with increasing incident photon energy. In Fig. 4.22, we see only a moderate increase of $r(T)$ even if the incident photon energy is about 300 meV above the Mexican hat minimum (Fig. 4.20). This is because the interchange between the two states involves spin–flip as illustrated in Fig. 4.27 and therefore is unfavored for interaction with nonmagnetic impurities or full symmetric phonons.

We knew from the previous Sect. 4.2 that nonsymmetric surface phonons in Bi_2Se_3 are weak, and hence J_z remains approximately conserved during the energy relaxation. Hence this explains the exceptionally high degree of polarization observed in all samples and up to room temperature. It would be interesting to study in the future the interaction between the chiral exciton and other asymmetric collective modes, such as the Dirac plasmons and chiral spin modes, which might be the main relaxation channels for the chiral excitons.

4.5 Summary

In summary, we have studied the secondary emissions in the 3D TI Bi_2Se_3 single crystal and thin films, in the energy range of 0.5 meV to 1.5 eV. Within this energy regime, we have observed three surface originated phenomena, which is a particularly interesting topic in this material (Sect. 4.1.2).

Below 50 meV, the spectra is dominated by Raman scattering from lattice vibration normal modes (phonons, second-order phonons, etc.). Compared to the DFT calculated bulk phonon bands, we observed in total four additional out-of-plane and possibly 2 in-plane surface vibrational modes, where we tabulate the energies and symmetries in Table 4.3. These modes all have energies very close to the bulk values where the bulk phonon DOS is not zero, and therefore they were assigned to surface resonances. Thanks to the high energy resolution and sensitivity, we were able to resolve an additional $A_1^{(4)}$ mode that has not been previously observed. This completes all of the possible surface resonances that can be observed in Bi_2Se_3, and a proper symmetry analysis has been given.

Above 100 meV, the Raman spectra is basically flat with little signal, except for a new collective mode at 150 meV in the chiral A_2 symmetry channel of C_{6v} group. This mode is only observed under surface resonance energy of 1.8 eV and is identified as transverse chiral spin mode: a collective spin-flip excitation of the surface Dirac fermions. The high energy secondary emission spectra are overlapped with two PL peaks at about 1.5 and 2.3 eV. The 2.3 eV peak is almost fully circularly polarized parallel to the polarization of the excitation photon. We propose a 2D excitonic model where two energetically degenerate electron–hole bound states form on the surface of Bi_2Se_3.

The results we presented here demonstrate a way of studying the dynamical response of Dirac fermions and their many-body interactions through optical measurement. In the future, experiments should be done on the excitation dependence of the surface resonances, which might further reveal the relation between phononic and electronic degrees of freedom on the surface of TIs. In addition, the magnetic field dependence of the chiral spin mode and exciton would help understand the spin–spin correlations in TIs. Due to the particular interests this material has in spintronics, magnonics, optoelectronics, and quantum computing [129, 130, 141–147], our results may have important applications beyond scientific curiosities.

References

1. H.-H. Kung et al., Surface vibrational modes of the topological insulator Bi_2Se_3 observed by Raman spectroscopy. Phys. Rev. B **95**, 245406 (2017). https://doi.org/10.1103/PhysRevB.95.245406
2. H.-H. Kung et al., Chiral spin mode on the surface of a topological insulator. Phys. Rev. Lett. **119**, 136802 (2017). https://doi.org/10.1103/PhysRevLett.119.136802
3. H.-H. Kung et al., Observation of chiral surface excitons in a topological insulator Bi_2Se_3. Proc. Natl. Acad. Sci. **116**(10), 4006–4011 (2019). https://doi.org/10.1073/pnas.1813514116
4. N.W. Ashcroft, N.D. Mermin, *Solid State Physics*. HRW international editions. Holt, Rinehart and Winston (1976)
5. A. Damascelli, Probing the electronic structure of complex systems by ARPES. Physica Scripta **2004**(T109), 61 (2004). https://doi.org/10.1238/Physica.Topical.109a00061
6. N.F. Mott, The basis of the electron theory of metals, with special reference to the transition metals. Proc. Phys. Soc. A **62**(7), 416 (1949)
7. K.v. Klitzing, G. Dorda, M. Pepper, New method for high-accuracy determination of the fine-structure constant based on quantized hall resistance. Phys. Rev. Lett. **45**, 494–497 (1980). https://doi.org/10.1103/PhysRevLett.45.494
8. A. Bansil, H. Lin, T. Das, *Colloquium*: Topological band theory. Rev. Mod. Phys. **88**, 021004 (2016). https://doi.org/10.1103/RevModPhys.88.021004
9. M.Z. Hasan, S.-Y. Xu, G. Bian, Topological insulators, topological superconductors and Weyl fermion semimetals: discoveries, perspectives and outlooks. Physica Scripta **2015**(T164), 014001 (2015)
10. N.P. Armitage, E.J. Mele, A. Vishwanath, Weyl and Dirac semimetals in three-dimensional solids. Rev. Modern Phys. **90**(1), 015001 (2018). https://doi.org/10.1103/RevModPhys.90.015001
11. B. Yan, C. Felser, Topological materials: Weyl semimetals. Annu. Rev. Condens. Matter Phys. **8**, 337–354 (2017). https://doi.org/10.1146/annurev-conmatphys-031016-025458
12. M.I. Dyakonov, A.V. Khaetskii, *Spin Physics in Semiconductors*, vol. 1 (Springer, 2008). https://doi.org/10.1007/978-3-540-78820-1
13. L. Fu, C.L. Kane, E.J. Mele, Topological insulators in three dimensions. Phys. Rev. Lett. **98**, 106803 (2007). https://doi.org/10.1103/PhysRevLett.98.106803
14. L. Fu, C.L. Kane, Topological insulators with inversion symmetry. Phys. Rev. B **76**, 045302 (2007). https://doi.org/10.1103/PhysRevB.76.045302
15. H. Zhang et al., Topological insulators in Bi_2Se_3, Bi_2Te_3 and Sb_2Te_3 with a single Dirac cone on the surface. Nature Phys. **5**, 438 (2009). https://doi.org/10.1038/nphys1270
16. B.I. Halperin, Quantized Hall conductance, current-carrying edge states, and the existence of extended states in a two-dimensional disordered potential. Phys. Rev. B **25**, 2185–2190 (1982). https://doi.org/10.1103/PhysRevB.25.2185
17. A.M. Essin, V. Gurarie, Bulk-boundary correspondence of topological insulators from their respective Green's functions. Phys. Rev. B **84**, 125132 (2011). https://doi.org/10.1103/PhysRevB.84.125132
18. A. Zangwill. *Physics at Surfaces* (Cambridge University Press, 1988)
19. B. Feuerbacher, R.F. Willis, Photoemission and electron states at clean surfaces. J. Phys. C Solid State Phys. **9**(2), 169 (1976). https://doi.org/10.1088/0022-3719/9/2/007
20. K. Fukutani et al., Symmetry-protected surface state on Mo(112). J. Phys. Condens. Matter **26**(15), 155501 (2014). https://doi.org/10.1088/0953-8984/26/15/155501
21. D. Hsieh et al., A tunable topological insulator in the spin helical Dirac transport regime. Nature **460**(7259), 1101–1105 (2009). https://doi.org/10.1038/nature08234
22. P.D.C. King et al., Large tunable Rashba spin splitting of a two-dimensional electron gas in Bi_2Se_3. Phys. Rev. Lett. **107**, 096802 (2011). https://doi.org/10.1103/PhysRevLett.107.096802
23. L. Fu, Hexagonal warping effects in the surface states of the topological insulator Bi_2Te_3. Phys. Rev. Lett. **103**, 266801 (2009). https://doi.org/10.1103/PhysRevLett.103.266801

24. P. Roushan et al., Topological surface states protected from backscattering by chiral spin texture. Nature **460**(7259), 1106–1109 (2009). https://doi.org/10.1038/nature08308
25. A.A. Taskin, Y. ichi Ando, Berry phase of nonideal Dirac fermions in topological insulators. Phys. Rev. B **84**, 035301 (2011). https://doi.org/10.1103/PhysRevB.84.035301
26. M.J. Brahlek, Atomic scale engineering of topological materials". PhD thesis. Rutgers University, 2014. https://doi.org/10.7282/T3TM78KB
27. J.G. Checkelsky et al., Quantum interference in macroscopic crystals of nonmetallic Bi_2Se_3. Phys. Rev. Lett. **103**, 246601 (2009). https://doi.org/10.1103/PhysRevLett.103.246601
28. G.P. Mikitik, Yu.V. Sharlai, Manifestation of Berry's phase in metal physics. Phys. Rev. Lett. **82**, 2147–2150 (1999). https://doi.org/10.1103/PhysRevLett.82.2147
29. M. Brahlek et al., Topological-metal to band-insulator transition in $(Bi_{1-x}In_x)_2Se_3$ thin films. Phys. Rev. Lett. **109**, 186403 (2012). https://doi.org/10.1103/PhysRevLett.109.186403
30. D. Hsieh et al., A topological Dirac insulator in a quantum spin Hall phase. Nature **452**(7190), 970–974 (2008). https://doi.org/10.1038/nature06843
31. Y. Xia et al., Observation of a large-gap topological-insulator class with a single Dirac cone on the surface. Nature Phys. **5**(6), 398–402 (2009). https://doi.org/10.1038/nphys1274
32. Y.L. Chen et al., Experimental realization of a three-dimensional topological insulator, Bi_2Te_3. Science **325**(5937), 178–181 (2009). https://doi.org/10.1126/science.1173034
33. N. Bansal et al., Thickness-independent transport channels in topological insulator Bi_2Se_3 thin films. Phys. Rev. Lett. **109**, 116804 (2012). https://doi.org/10.1103/PhysRevLett.109.116804
34. J.W. McIver et al., Control over topological insulator photocurrents with light polarization. Nat. Nanotechnol. **7**(2), 96–100 (2012). https://doi.org/10.1038/nnano.2011.214
35. H. Köhler, C.R. Becker, Optically active lattice vibrations in Bi_2Se_3. Physica Status Solidi (b) **61**(2), 533–537 (1974). https://doi.org/10.1002/pssb.2220610218
36. W. Richter, C.R. Becker, A Raman and far-infrared investigation of phonons in the rhombohedral V_2–VI_3 compounds Bi_2Te_3, Bi_2Se_3, Sb_2Te_3 and $Bi_2(Te_{1-x}Se_x)_3$ $(0 < x < 1)$, $(Bi_{1-y}Sb_y)_2Te_3$ $(0 < y < 1)$. Physica Status Solidi (b) **84**(2), 619–628 (1977). https://doi.org/10.1002/pssb.2220840226
37. A.D. LaForge et al., Optical characterization of Bi_2Se_3 in a magnetic field: Infrared evidence for magnetoelectric coupling in a topological insulator material. Phys. Rev. B **81**, 125120 (2010). https://doi.org/10.1103/PhysRevB.81.125120
38. S.Y.F. Zhao et al., Fabrication and characterization of topological insulator Bi_2Se_3 nanocrystals. Appl. Phys. Lett. **98**(14), 141911 (2011). https://doi.org/10.1063/1.3573868
39. J. Zhang et al., Raman spectroscopy of few-quintuple layer topological insulator Bi_2Se_3 nanoplatelets. Nano Lett. **11**(6), 2407–2414 (2011). https://doi.org/10.1021/nl200773n
40. V. Gnezdilov et al., Helical fluctuations in the Raman response of the topological insulator Bi_2Se_3. Phys. Rev. B **84**, 195118 (2011). https://doi.org/10.1103/PhysRevB.84.195118
41. Y. Kim et al., Temperature dependence of Raman-active optical phonons in Bi_2Se_3 and Sb_2Te_3. Appl. Phys. Lett. **100**(7), 071907 (2012). https://doi.org/10.1063/1.3685465
42. J. Humlíček et al., Raman and interband optical spectra of epitaxial layers of the topological insulators Bi_2Te_3 and Bi_2Se_3 on BaF_2 substrates. Physica Scripta **2014**(T162), 014007 (2014). https://doi.org/10.1088/0031-8949/2014/T162/014007
43. B. Irfan et al., Temperature dependent Raman scattering studies of three dimensional topological insulators Bi_2Se_3. J. Appl. Phys. **115**(17), 173506 (2014). https://doi.org/10.1063/1.4871860
44. M. Eddrief et al., Low-temperature Raman fingerprints for few-quintuple layer topological insulator Bi_2Se_3 films epitaxied on GaAs. Nanotechnology **25**(24), 245701 (2014). https://doi.org/10.1088/0957-4484/25/24/245701
45. Y. Yan et al., Surface-facet-dependent phonon deformation potential in individual strained topological insulator Bi_2Se_3 nanoribbons. ACS Nano **9**(10), 10244–10251 (2015). https://doi.org/10.1021/acsnano.5b04057
46. X. Zhang et al., Review on the Raman spectroscopy of different types of layered materials. Nanoscale **8**, 6435–6450 (2016). https://doi.org/10.1039/C5NR07205K

47. W. Cheng, S.-F. Ren, Phonons of single quintuple Bi_2Te_3 and Bi_2Se_3 films and bulk materials. Phys. Rev. B **83**, 094301 (2011). https://doi.org/10.1103/PhysRevB.83.094301
48. T. Terzibaschian, B. Enderlein, The irreducible representations of the two-dimensional space groups of crystal surfaces. Theory and applications. Physica Status Solidi (b) **133**(2), 443–461 (1986). https://doi.org/10.1002/pssb.2221330202
49. J. Li, J.J. Tu, J.L. Birman, Symmetry predicted transitions in 3D topological insulators. Solid State Commun. **163**, 11–14 (2013). https://doi.org/10.1016/j.ssc.2013.03.010
50. R.-J. Slager et al., The space group classification of topological band insulators. Nature Phys. **9**(2), 98–102 (2013). https://doi.org/10.1038/nphys2513
51. L.N. Ovander, The form of the Raman tensor. Opt. Spectrosc. **9**, 302 (1960)
52. M. Cardona, Resonance phenomena, in *Light Scattering in Solids II*, ed. by M. Cardona, G. Güntherodt (Springer, Berlin, 1982), pp. 45–49
53. G.F. Koster, *Properties of the Thirty-Two Point Groups*. Massachusetts Institute of Technology Press Research Monograph (MIT Press, 1963)
54. I.M. Lifshitz, L.N. Rosenzweig, Dynamics of lattice filling half-space (Russian). Zh. Eksp. Teor. Fiz. **18**, 1012 (1948)
55. I.M. Lifshitz, Some problems of the dynamic theory of non-ideal crystal lattices. Il Nuovo Cimento **3**(4), 716–734 (1956). https://doi.org/10.1007/BF02746071
56. R.F. Wallis, Effect of free ends on the vibration frequencies of one-dimensional lattices. Phys. Rev. **105**, 540–545 (1957). https://doi.org/10.1103/PhysRev.105.540
57. R.F. Wallis, Theory of surface modes of vibration in two- and three-dimensional crystal lattices. Phys. Rev. **116**, 302–308 (1959). https://doi.org/10.1103/PhysRev.116.302
58. G. Benedek, L. Miglio, The Green's function method in the surface lattice dynamics of ionic crystals, in *Surface Phonons*, ed. by W. Kress, F.W. de Wette. (Springer, Berlin, Heidelberg, 1991), pp. 37–66. https://doi.org/10.1007/978-3-642-75785-3_3
59. R.F Wallis, Surface phonons: theoretical developments. Surface Science **299**, 612–627 (1994)
60. M.J. Lagos et al., Mapping vibrational surface and bulk modes in a single nanocube. Nature **543**(7646), 529–532 (2017)
61. V. Chis et al., Vibrations in binary and ternary topological insulators: First principles calculations and Raman spectroscopy measurements. Phys. Rev. B **86**, 174304 (2012). https://doi.org/10.1103/PhysRevB.86.174304
62. X. Zhu et al., Interaction of phonons and Dirac fermions on the surface of Bi_2Se_3: A strong Kohn anomaly. Phys. Rev. Lett. **107**, 186102 (2011). https://doi.org/10.1103/PhysRevLett.107.186102
63. X. Zhu et al., Electron-phonon coupling on the surface of the topological insulator Bi_2Se_3 determined from surface-phonon dispersion measurements. Phys. Rev. Lett. **108**, 185501 (2012). https://doi.org/10.1103/PhysRevLett.108.185501
64. C. Howard et al., Anomalous behavior in the phonon dispersion of the (001) surface of Bi_2Te_3 determined from helium atom-surface scattering measurements. Phys. Rev. B **88**, 035402 (2013). https://doi.org/10.1103/PhysRevB.88.035402
65. R.C. Hatch et al., Stability of the Bi_2Se_3(111) topological state: Electron-phonon and electron-defect scattering. Phys. Rev. B **83**, 241303 (2011). https://doi.org/10.1103/PhysRevB.83.241303
66. Z.-H. Pan et al., Measurement of an exceptionally weak electron-phonon coupling on the surface of the topological insulator Bi_2Se_3 using angle-resolved photoemission spectroscopy. Phys. Rev. Lett. **108**, 187001 (2012). https://doi.org/10.1103/PhysRevLett.108.187001
67. M.V. Costache et al., Fingerprints of inelastic transport at the surface of the topological insulator Bi_2Se_3: Role of electron-phonon coupling. Phys. Rev. Lett. **112**, 086601 (2014). https://doi.org/10.1103/PhysRevLett.112.086601
68. J.A. Sobota et al., Distinguishing bulk and surface electron-phonon coupling in the topological insulator Bi_2Se_3 using time-resolved photoemission spectroscopy. Phys. Rev. Lett. **113**, 157401 (2014). https://doi.org/10.1103/PhysRevLett.113.157401
69. C. Chen et al., Tunable Dirac fermion dynamics in topological insulators. Scientific Reports **3**, 2411 (2013)

70. T. Kondo et al., Anomalous dressing of Dirac fermions in the topological surface state of Bi_2Se_3, Bi_2Te_3, and cu-doped Bi_2Se_3. Phys. Rev. Lett. **110**, 217601 (2013). https://doi.org/10.1103/PhysRevLett.110.217601
71. A. Kogar et al., Surface collective modes in the topological insulators Bi_2Se_3 and $Bi_{0.5}Sb_{1.5}Te_{3-x}Se_x$. Phys. Rev. Lett. **115**, 257402 (2015). https://doi.org/10.1103/PhysRevLett.115.257402
72. N. Esser, W. Richter, Raman scattering from surface phonons, in *Light Scattering in Solids VIII*, ed. by M. Cardona, G. Güntherodt (Springer, Berlin, 1999), pp. 96–168
73. M. Liebhaber et al., Surface phonons of the Si(111)-(7 × 7) reconstruction observed by Raman spectroscopy. Phys. Rev. B **89**, 045313 (2014). https://doi.org/10.1103/PhysRevB.89.045313
74. R. Lewandowska et al., Raman scattering in α-In_2Se_3 crystals. Mater. Res. Bull. **36**(15), 2577–2583 (2001). https://doi.org/10.1016/S0025-5408(01)00746-2
75. B.-T. Wang, P. Zhang, Phonon spectrum and bonding properties of Bi_2Se_3: Role of strong spin-orbit interaction. Appl. Phys. Lett. **100**(8), 082109 (2012)
76. Y.D. Glinka et al., Thickness tunable quantum interference between surface phonon and Dirac plasmon states in thin films of the topological insulator Bi_2Se_3. J. Phys. Condens. Matter **27**(5), 052203 (2015)
77. L. Wu et al., A sudden collapse in the transport lifetime across the topological phase transition in $(Bi_{1-x}In_x)_2Se_3$. Nature Phys. **9**(7), 410–414 (2013)
78. H. Dong Lee et al., Indium and bismuth interdiffusion and its influence on the mobility in In_2Se_3/Bi_2Se_3. Thin Solid Films **556**, 322–324 (2014). https://doi.org/10.1016/j.tsf.2014.01.082
79. U. Fano, Effects of configuration interaction on intensities and phase shifts. Phys. Rev. **124**, 1866–1878 (1961). https://doi.org/10.1103/PhysRev.124.1866
80. M.V. Klein, Electronic Raman scattering, *Light Scattering in Solids I,* ed. by M. Cardona, G. Güntherodt (Springer, Berlin, 1983), pp. 169–172
81. J.A. Sobota et al., Direct optical coupling to an unoccupied Dirac surface state in the topological insulator Bi_2Se_3. Phys. Rev. Lett. **111**, 136802 (2013). https://doi.org/10.1103/PhysRevLett.111.136802
82. D. Niesner et al., Unoccupied topological states on bismuth chalcogenides. Phys. Rev. B **86**, 205403 (2012). https://doi.org/10.1103/PhysRevB.86.205403
83. B.S. Shastry, B.I. Shraiman, Raman scattering in Mott-Hubbard systems. Int. J. Mod. Phys. B **5**, 365–388 (1991). https://doi.org/10.1142/S0217979291000237
84. D.V. Khveshchenko, P.B. Wiegmann, Raman scattering and anomalous current algebra in Mott insulators. Phys. Rev. Lett. **73**, 500–503 (1994). https://doi.org/10.1103/PhysRevLett.73.500
85. M. Bianchi et al., Coexistence of the topological state and a two-dimensional electron gas on the surface of Bi_2Se_3. Nat. Commun. **1**, 128 (2010)
86. M. Bianchi et al., The electronic structure of clean and adsorbate-covered Bi_2Se_3: an angle-resolved photoemission study. Semicond. Sci. Technol. **27**(12), 124001 (2012)
87. T.V. Menshchikova, S.V. Eremeev, E.V. Chulkov, On the origin of two-dimensional electron gas states at the surface of topological insulators. JETP Lett. **94**(2), 106 (2011)
88. A.C. Ferrari, Raman spectroscopy of graphene and graphite: Disorder, electron–phonon coupling, doping and nonadiabatic effects. Solid State Commun. **143**(1-2), 47–57 (2007). https://doi.org/10.1016/j.ssc.2007.03.052
89. M.Z. Hasan, J.E. Moore, Three-dimensional topological insulators. Annu. Rev. Condens. Matter Phys. **2**(1), 55–78 (2011). https://doi.org/10.1146/annurev-conmatphys-062910-140432
90. Y.H. Wang et al., Observation of Floquet-Bloch states on the surface of a topological insulator. Science **342**(6157), 453–457 (2013). https://doi.org/10.1126/science.1239834
91. Z.-H. Zhu et al., Photoelectron spin-polarization control in the topological insulator Bi_2Se_3. Phys. Rev. Lett. **112**, 076802 (2014). https://doi.org/10.1103/PhysRevLett.112.076802

92. L. Wu et al., Quantized Faraday and Kerr rotation and axion electrodynamics of a 3D topological insulator. Science **354**(6316), 1124 (2016). https://doi.org/10.1126/science.aaf5541
93. C. Jozwiak et al., Spin-polarized surface resonances accompanying topological surface state formation. Nat. Commun. **7**, 13143 (2016)
94. W. Li et al., Origin of the low critical observing temperature of the quantum anomalous Hall effect in V-doped $(Bi, Sb)_2Te_3$ film. Scientific Reports **6**, 32732 (2016)
95. Y. Shao et al., Faraday rotation due to surface states in the topological insulator $(Bi_{1-x}Sb_x)_2Te_3$. Nano Letters **17**(2), 980–984 (2017). https://doi.org/10.1021/acs.nanolett.6b04313
96. D. Pesin, A.H. MacDonald, Spintronics and pseudospintronics in graphene and topological insulators. Nat. Mater. **11**(5), 409–416 (2012). https://doi.org/10.1038/nmat3305
97. Y. Xu et al., Observation of topological surface state quantum Hall effect in an intrinsic three-dimensional topological insulator. Nature Phys. **10**(12), 956 (2014)
98. Y. Fan et al., Electric-field control of spin–orbit torque in a magnetically doped topological insulator. Nat. Nanotechnol. **11**, 352 (2016). https://doi.org/10.1038/nnano.2015.294
99. Y. Wang et al., Topological surface states originated spin-orbit torques in Bi_2Se_3. Phys. Rev. Lett. **114**, 257202 (2015). https://doi.org/10.1103/PhysRevLett.114.257202
100. B. Scharf et al., Tunneling planar hall effect in topological insulators: Spin valves and amplifiers. Phys. Rev. Lett. **117**, 166806 (2016). https://doi.org/10.1103/PhysRevLett.117.166806
101. K. Kondou et al., Fermi-level-dependent charge-to-spin current conversion by Dirac surface states of topological insulators. Nature Phys. **12**(11), 1027–1031 (2016)
102. J. Tian et al., Observation of current-induced, long-lived persistent spin polarization in a topological insulator: A rechargeable spin battery. Science Advances **3**(4), (2017). https://doi.org/10.1126/sciadv.1602531
103. Y. Ando, M. Shiraishi, Spin to charge interconversion phenomena in the interface and surface states. J. Phys. Soc. Jpn. **86**(1), 011001 (2017). https://doi.org/10.7566/JPSJ.86.011001
104. A. Shekhter, M. Khodas, A.M. Finkel'stein, Chiral spin resonance and spin-Hall conductivity in the presence of the electron-electron interactions. Phys. Rev. B **71**, 165329 (2005). https://doi.org/10.1103/PhysRevB.71.165329
105. A. Ashrafi, D.L. Maslov, Chiral spin waves in Fermi liquids with spin-orbit coupling. Phys. Rev. Lett. **109**, 227201 (2012). https://doi.org/10.1103/PhysRevLett.109.227201
106. S. Maiti, V. Zyuzin, D.L. Maslov, Collective modes in two- and three-dimensional electron systems with Rashba spin-orbit coupling. Phys. Rev. B **91**, 035106 (2015). https://doi.org/10.1103/PhysRevB.91.035106
107. S. Maiti, M. Imran, D.L. Maslov, Electron spin resonance in a two-dimensional Fermi liquid with spin-orbit coupling. Phys. Rev. B **93**, 045134 (2016). https://doi.org/10.1103/PhysRevB.93.045134
108. F. Perez et al., Spin-orbit twisted spin waves: Group velocity control. Phys. Rev. Lett. **117**, 137204 (2016). https://doi.org/10.1103/PhysRevLett.117.137204
109. S. Maiti, D.L. Maslov, Raman scattering in a two-dimensional Fermi liquid with spin-orbit coupling. Phys. Rev. B **95**, 134425 (2017). https://doi.org/10.1103/PhysRevB.95.134425
110. A. Kumar, D.L. Maslov, Effective lattice model for the collective modes in a Fermi liquid with spin-orbit coupling. Phys. Rev. B **95**, 165140 (2017). https://doi.org/10.1103/PhysRevB.95.165140
111. E. Riccardi et al., Gate-dependent electronic Raman scattering in graphene. Phys. Rev. Lett. **116**, 066805 (2016). https://doi.org/10.1103/PhysRevLett.116.066805
112. O. Kashuba, V.I. Fal'ko, Signature of electronic excitations in the Raman spectrum of graphene. Phys. Rev. B **80**, 241404 (2009). https://doi.org/10.1103/PhysRevB.80.241404
113. M. Nomura et al., Relationship between Fermi surface warping and out-of-plane spin polarization in topological insulators: A view from spin- and angle-resolved photoemission. Phys. Rev. B **89**, 045134 (2014). https://doi.org/10.1103/PhysRevB.89.045134
114. S. Raghu et al., Collective modes of a Helical liquid. Phys. Rev. Lett. **104**, 116401 (2010). https://doi.org/10.1103/PhysRevLett.104.116401

115. S. Maiti, D.L. Maslov, Intrinsic damping of collective spin modes in a two-dimensional Fermi liquid with spin-orbit coupling. Phys. Rev. Lett. **114**, 156803 (2015). https://doi.org/10.1103/PhysRevLett.114.156803
116. F.-T. Huang et al., Nonstoichiometric doping and Bi antisite defect in single crystal Bi_2Se_3. Phys. Rev. B **86**, 081104 (2012). https://doi.org/10.1103/PhysRevB.86.081104
117. J. Dai et al., Toward the intrinsic limit of the topological insulator Bi_2Se_3. Phys. Rev. Lett. **117**, 106401 (2016). https://doi.org/10.1103/PhysRevLett.117.106401
118. E. Lahoud et al., Evolution of the Fermi surface of a doped topological insulator with carrier concentration. Phys. Rev. B **88**, 195107 (2013). https://doi.org/10.1103/PhysRevB.88.195107
119. K.F. Mak et al., Atomically thin MoS_2: A new direct-gap semiconductor. Phys. Rev. Lett. **105**, 136805 (2010). https://doi.org/10.1103/PhysRevLett.105.136805
120. X. Xu et al., Spin and pseudospins in layered transition metal dichalcogenides. Nature Phys. **10**(5), 343–350 (2014)
121. J.R. Schaibley et al., Valleytronics in 2D materials. Nat. Rev. Mater. **1**, 16055 (2016)
122. J.M. Lu et al., Evidence for two-dimensional Ising superconductivity in gated MoS_2. Science **350**(6266), 1353–1357 (2015). https://doi.org/10.1126/science.aab2277
123. X. Xi et al., Ising pairing in superconducting $NbSe_2$ atomic layers. Nature Phys. **12**(2), 139–143 (2016)
124. E.I. Rashba, Properties of semiconductors with an extremum loop 1 cyclotron and combinational resonance in a magnetic field perpendicular to the plane of the loop. Sov. Phys.-Solid State **2**, 1109–1122 (1960)
125. G. Dresselhaus, Spin-orbit coupling effects in zinc blende structures. Phys. Rev. **100**, 580–586 (1955). https://doi.org/10.1103/PhysRev.100.580
126. X. Zhang et al., Hidden spin polarization in inversion-symmetric bulk crystals. Nature Phys. **10**(5), 387–393 (2014)
127. D. Xiao et al., Coupled spin and valley physics in monolayers of MoS_2 and other Group-VI dichalcogenides. Phys. Rev. Lett. **108**, 196802 (2012). https://doi.org/10.1103/PhysRevLett.108.196802
128. Q. Liu, X. Zhang, A. Zunger, Intrinsic circular polarization in centrosymmetric stacks of transition-metal dichalcogenide compounds. Phys. Rev. Lett. **114**, 087402 (2015). https://doi.org/10.1103/PhysRevLett.114.087402
129. K.F. Mak, J. Shan, Photonics and optoelectronics of 2D semiconductor transition metal dichalcogenides. Nat. Photon. **10**(4), 216–226 (2016)
130. M. Gmitra, J. Fabian, Graphene on transition-metal dichalcogenides: A platform for proximity spin-orbit physics and optospintronics. Phys. Rev. B **92**, 155403 (2015). https://doi.org/10.1103/PhysRevB.92.155403
131. R.R. Parsons, Band-to-band optical pumping in solids and polarized photoluminescence. Phys. Rev. Lett. **23**, 1152–1154 (1969). https://doi.org/10.1103/PhysRevLett.23.1152
132. A.I. Ekimov, V.I. Safarov, Optical orientation of carriers in interband transitions in semiconductors. Sov. J. Exp. Theor. Phys. Lett. **12**, 198 (1970)
133. A. Bonnot, R. Planel, C. Benoit à la Guillaume, Optical orientation of excitons in CdS. Phys. Rev. B **9**, 690–702 (1974). https://doi.org/10.1103/PhysRevB.9.690
134. I. Žuti ć, J. Fabian, S. Das Sarma, Spintronics: Fundamentals and applications. Rev. Mod. Phys. **76**, 323–410 (2004). https://doi.org/10.1103/RevModPhys.76.323
135. R. Planel, C.B. Guillaume, Optical orientation of excitons, in *Optical Orientation*, Chap. 8, ed. by F. Meier, B.P. Zakharchenya (Elsevier Science Ltd., 1984), p. 353
136. K. Miyamoto et al., The gigantic Rashba effect of surface states energetically buried in the topological insulator Bi_2Te_2Se. New J. Phys. **16**(6), 065016 (2014)
137. Y. Liu et al., Tuning Dirac states by strain in the topological insulator Bi_2Se_3. Nature Phys. **10**(4), 294–299 (2014)
138. D. Kovalev et al., Free exciton emission in GaN. Phys. Rev. B **54**, 2518–2522 (1996). https://doi.org/10.1103/PhysRevB.54.2518
139. A.M. Jones et al., Optical generation of excitonic valley coherence in monolayer WSe_2. Nat. Nanotechnol. **8**(9), 634–638 (2013)

140. A.V. Shytov, M.I. Katsnelson, L.S. Levitov, Atomic collapse and quasi-Rydberg states in graphene. Phys. Rev. Lett. **99**, 246802 (2007). https://doi.org/10.1103/PhysRevLett.99.246802
141. A. Najmaie, E.Ya. Sherman, J.E. Sipe, Generation of spin currents via Raman scattering. Phys. Rev. Lett. **95**, 056601 (2005). https://doi.org/10.1103/PhysRevLett.95.056601
142. L. Fu, C.L. Kane, Superconducting proximity effect and Majorana fermions at the surface of a topological insulator. Phys. Rev. Lett. **100**, 096407 (2008). https://doi.org/10.1103/PhysRevLett.100.096407
143. V.V. Kruglyak, S.O. Demokritov, D. Grundler, Magnonics. J. Phys. D Appl. Phys. **43**(26), 264001 (2010)
144. J. Alicea, New directions in the pursuit of Majorana fermions in solid state systems. Rep. Progress Phys. **75**(7), 076501 (2012)
145. A.V. Chumak et al., Magnon spintronics. Nature Phys. **11**(6), 453–461 (2015)
146. R.K. Dumas, J. Akerman, Spintronics: Channelling spin waves. Nat. Nanotechnol. **9**(7), 503–504 (2014)
147. S. Urazhdin et al., Nanomagnonic devices based on the spin-transfer torque. Nat. Nanotechnol. **9**(7), 509–513 (2014)

Chapter 5
Conclusion

Abstract In this monograph, we used Raman scattering to identify collective excitations in the "chiral" symmetry channel in two completely different nonmagnetic systems: the HO phase of heavy fermion metal URu_2Si_2 and the surface states of 3D topological insulator Bi_2Se_3.

In URu_2Si_2, the collective mode arises from the uranium *5f* electrons orbital degrees of freedom, crystal field states. However, due to the partly localized and itinerant characters of uranium electrons, the crystal field excitations in URu_2Si_2 are overdamped and difficult to observe experimentally, as in many other uranium compounds. Indeed, due to Kondo hybridization with the conduction band electrons, the local crystal field picture often fails to explain the low temperature phases in heavy electron materials. However, the "arrested Kondo effect" in URu_2Si_2 is a special case where the local degrees of freedom reemerge and become important at low temperature [1]. The spontaneous symmetry breaking results the system in a chiral ground state, where the *5f* electron orbital states reorganize and order in real space to form a "chirality density wave" [1, 2]. One of the contributions in this monograph is to identify a collective mode out of this ground state and how it evolves across the temperature-doping phase diagram [3]. Both temperature and doping evolution of this mode match the low temperature phase diagram of URu_2Si_2, and the mode energy is fully consistent with the Ginzburg–Landau model by Haule and Kotliar [3–6]. The mode observed in Raman scattering of URu_2Si_2 appears only below the phase transition, which is very different from usual crystal field transitions that are already observable above the phase transition, and the linewidth gradually sharpen at low temperature due to reduced relaxation channels. The particular symmetry dependence of this collective mode allows us to identify the symmetry breaking in the HO phase, which strongly constraints the allowed order parameters for the HO phase. Thus, we demonstrate the unique property of Raman spectroscopy in determining the symmetry of collective modes, which is very useful when studying symmetry breaking and phase transitions in solids.

In Bi_2Se_3, the "stage setting" is very different than in URu_2Si_2. Here we do not have any f-orbitals or localized states at the Fermi level to worry about. But instead,

H.-H. Kung, *Collective Excitations in the Antisymmetric Channel of Raman Spectroscopy*, Springer Theses, https://doi.org/10.1007/978-3-030-89332-3_5

the strong SOC on the crystal surface collaborates with time reversal symmetry to produce a pair of 2D surface Dirac cones at Fermi energy around Γ point. The Dirac electrons possess a chiral spin texture, which has intrigued many studies in the recent years [7–10]. While the spin polarization and surface band structure have been well established, the spin correlation between the Dirac fermions is actually very little known. The main contribution in this monograph is to use Raman scattering to identify a mode in the chiral symmetry channel, which corresponds to the collective "spin-flip" excitation out of the surface's chiral ground state [11]. This mode is known as a "chiral spin mode" and is in fact generic to many systems with strong SOC [12, 13]. However, it has never been so cleanly observed in zero field at such high temperature and also never been observed from the surface states of a 3D TI. A chiral spin mode is similar to a magnetic bound state, which peels off from the "spin-flip" transition continuum due to finite interaction, and thus is a fantastic tool to measure the spin correlation between Dirac fermions. In order to selectively enhance the signal from the surface, we tune the excitation energy to resonantly promote interband transitions into unoccupied surface states. This innovative surface selective resonant Raman scattering paves new ways of studying the surface states in Bi_2Se_3 using optical methods [11].

We hope that the work presented in this thesis would inspire future studies in the condensed matter physics community, introducing polarization resolved Raman spectroscopy as a powerful tool to characterize the collective modes in solids. In particular, the sensitivity in the fully antisymmetric channel presents a unique tool to study chiral excitations in a wide range of systems. Besides materials with time reversal symmetry breaking, we argue that antisymmetric Raman excitations could be expected whenever reflection symmetries are broken or if the ground state has a chiral spin texture. These properties encompass a large group of materials that are interesting to the current research, and we believe the studies we present in this thesis would be a useful starting point for future researchers.

References

1. K. Haule, G. Kotliar, Arrested Kondo effect and hidden order in URu_2Si_2. Nature Phys. **5**(11), 796–799 (2009). https://doi.org/10.1038/nphys1392
2. H.-H. Kung et al., Chirality density wave of the "hidden order" phase in URu_2Si_2. Science **347**(6228), 1339–1342 (2015). https://doi.org/10.1126/science.1259729
3. H.-H. Kung et al., Analogy between the "Hidden Order" and the orbital antiferromagnetism in $URu_{2-x}Fe_xSi_2$. Phys. Rev. Lett. **117**, 227601 (2016). https://doi.org/10.1103/PhysRevLett.117.227601
4. K. Haule, G. Kotliar, Complex Landau-Ginzburg theory of the hidden order in URu_2Si_2. Europhys. Lett. **89**(5), 57006 (2010)
5. H. Kusunose, H. Harima, On the hidden order in URu_2Si_2 – antiferro hexadecapole order and its consequences. J. Phys. Soc. Jpn. **80**(8), 084702 (2011). https://doi.org/10.1143/JPSJ.80.084702
6. L. Boyer, V.M. Yakovenko, et al., A model for metastable magnetism in the hidden-order phase of URu_2Si_2. Ann. Phys. (New York) **388** (2018). https://doi.org/10.1016/j.aop.2017.11.024

7. M.Z. Hasan, C.L. Kane, *Colloquium* : Topological insulators. Rev. Mod. Phys. **82**, 3045–3067 (2010). https://doi.org/10.1103/RevModPhys.82.3045
8. M.Z. Hasan, S.-Y. Xu, G. Bian, Topological insulators, topological superconductors and Weyl fermion semimetals: discoveries, perspectives and outlooks. Physica Scripta **2015**(T164), 014001 (2015)
9. A. Bansil, H. Lin, T. Das, *Colloquium*: Topological band theory. Rev. Mod. Phys. **88**, 021004 (2016). https://doi.org/10.1103/RevModPhys.88.021004
10. Y. Ando, M. Shiraishi, Spin to charge interconversion phenomena in the interface and surface states. J. Phys. Soc. Jpn. **86**(1), 011001 (2017). https://doi.org/10.7566/JPSJ.86.011001
11. H.-H. Kung, et al. Chiral spin mode on the surface of a topological insulator. Phys. Rev. Lett. **119**, 136802 (2017). https://doi.org/10.1103/PhysRevLett.119.136802
12. S. Maiti, D.L. Maslov, Intrinsic damping of collective spin modes in a two-dimensional Fermi liquid with spin-orbit coupling. Phys. Rev. Lett. **114**, 156803 (2015). https://doi.org/10.1103/PhysRevLett.114.156803
13. S. Maiti, D.L. Maslov, Raman scattering in a two-dimensional Fermi liquid with spin-orbit coupling. Phys. Rev. B **95**, 134425 (2017). https://doi.org/10.1103/PhysRevB.95.134425